Université du Québec
Institut National de la Recherche Scientifique
Centre Énergie, Matériaux et Télécommunications

GENERALIZED TALBOT EFFECT

THEORY AND APPLICATION TO ADVANCED OPTICAL WAVE PROCESSING

Par

Luis Romero Cortés

Thèse présentée pour l'obtention du grade de
Doctorat en Télécommunication, Ph.D.

Jury d'évaluation

Examinateur externe	José Capmany Universitat Politècnica de València (Spain)
Examinateur externe	Michael E. Durst Middlebury College (USA)
Examinateur interne	François Vidal Institut National de la Recherche Scientifique (Canada)
Directeur de recherche	José Azaña Institut National de la Recherche Scientifique (Canada)

A la memoria de mis abuelos

In memory of my grandparents

Acknowledgement

We choose to go to the Moon in this decade and do the other things, not because they are easy, but because they are hard.

– *John Fitzgerald Kennedy*, Rice University speech, September 12th, 1962.

The years I have spent developing the work reported in this dissertation, studying the physics, working out the math and fighting with the experiments in the lab, have been without a doubt, the most stressful, mentally exhausting and physically taxing that I can remember. They were also the most enlightening, and through them, I am today a fundamentally different person than I was the day I set foot in Montreal. Curiosity and the desire to see and do cool stuff have been and still are powerful driving forces in my life; however, more often than not, over the course of these past few years the motivation to keep going came from my family, friends and colleagues. If the reader finds this dissertation useful, or in any way interesting, entertaining or of any value, the people featured in these paragraphs are to be thanked for it.

Starting with my supervisor, Prof. José Azaña, to whom I am deeply indebted for his support and guidance, but most of all for his consistent willingness to listen to my inputs and ideas, and to take them into consideration, whatever the topic or situation. For that, beyond my admiration as a researcher, he has my most sincere respect, both as a supervisor and as a fellow, and I count myself among the lucky ones who had the privilege of working with him.

My family; my parents, Rafaela Cortés and Manuel Romero, my sister, Ana Romero, and my grandparents, Encarnación Limón, Antonio Romero, Rafaela Cuadri and Alberto Cortés, to whose memory I wish to dedicate these pages. Without their unconditional love, support and encouragement I would surely not have made it this far.

My colleagues from INRS; Dr. Maurizio Burla, Dr. Reza Maram, Dr. Reza Ashrafi, Dr. Bo Li, Dr. Lei Lei, Dr. María del Rosario Fernández Ruiz, Dr. Hamed Pishvai Bazargani, Dr. Mohamed Seghilani, Dr. Xiao-Zhou Li, Benjamin Crockett, Jeonh Hyun Huh, Jinwoo Jeon, Saikrishna Reddy and Robin Helsten. My supervised students, Yoann Atlas, Line Rahal, Ines Hamam, Ahmed Boubaker, and Antonin Deville. Prof. Hugues Guillet de Chatellus, from CNRS in Grenoble, France, with whom I had the immense pleasure of sharing nine enlightening months of productive work and a lot of fun; Profs. James van Howe, from Augustana College, in Illinois, USA, and Carlos Rodríguez Fernández-Pousa, from Universidad Miguel Hernández, in Elche, Spain, as well as Juan Pastor Graells, from Universidad de Alcalá, in Alcalá de Henares, Spain, with whom I shared very interesting and stimulating conversations and work time. Working alongside these people has been one heck of an experience.

All the friends I have made in Montreal over the years. Such an amazing city, so vibrant, yet so cozy, with so much to offer, makes for the perfect place to make and keep good friends. All my friends from Spain, most of them now scattered all around the world.

I would also like to thank the Natural Sciences and Engineering Research Council of Canada (NSERC), the Fonds de recherche du Québec – Nature et technologies (FRQNT), and the Institut National de la Recherche Scientifique – Énergie, Matériaux et Télécommunications (INRS–EMT), for providing the funding which allowed me to undertake this Ph.D. Additionally, I thank the people, institutions and companies that lent us equipment during the course of the experiments reported in this dissertation; Profs. Sohphie LaRochelle, from Université Laval, in Québec, Canada, and David V. Plant, from McGill University in Montreal, Canada; Tektronix, Inc. and Keysight Technologies, Inc.

Finally, I feel that some people with whom I have shared important moments of my life these past years deserve a special shout-out.

Ana, my sister, for always being there for me, no matter the situation, the time or the distance.

Mauri, for making me feel at home, over 0.018 light-seconds away from home.

Reza, for being a great mentor, a fantastic colleague and an even better friend.

Alex, for caring so much about me, and for being such a good friend.

Inma, for being as good as they come, and for always remembering everything.

Piotr, for keeping me grounded and decidedly excited about the future at the same time.

Elena, for making my life worth living for so many years, bittersweet as it might be to remember.

To all these people, I owe a great deal of gratitude. This has been a real challenge, impossible to accomplish without their support, encouragement and inspiration. To all of you, thank you sincerely,

Luis Romero Cortés

Abstract

The capability to generate precisely-timed periodic trains of optical pulses has pushed forward many fields of science and technology. Periodic optical waves are key to disciplines such as optical communications and computing, optical signal processing, sensing, spectroscopy, nonlinear and quantum optics, and many others.

Periodic optical waveforms can be generated through electro-optical means, external modulation of continuous-wave lasers, and through mode-locking, perhaps one of the most significant recent advances in optical science and technology. Mode-locking is the process by which the different longitudinal modes oscillating in a laser cavity are tightly locked in phase, giving rise to the repetitive emission of a light pulse, i.e., a periodic pulse train. The spectrum of such a signal is a collection of equally-spaced discrete frequency components, known as a frequency comb for the characteristic comb-like shape of its power spectrum. Currently, optical frequency combs are the most precise man-made clocks in history. These signals are used in a myriad of fundamental and applied disciplines, and they are the key enabling factor of many scientific and technological fields, ranging from high-resolution spectroscopy of molecules and atoms, to next-generation optical communication systems and the astronomical search for exo-planets.

The separation between adjacent frequency components of a frequency comb, known as the free spectral range (FSR), is the inverse of the repetition period of the corresponding pulse train in the time domain representation of the signal. This is a fundamental parameter from an application viewpoint. Not only most applications of periodic optical signals require their periodicity to be fixed with precision (for instance, the rate at which information is transmitted in a telecommunication system, and processed in a computing system, is strongly related to the pulse period of the clock signal), but distinct applications require fundamentally different orders of magnitude. As an example, typical atomic and molecular spectroscopy applications require combs with FSR values in the MHz regime, while astronomical spectrographic measurements, as well as applications aimed at arbitrary waveform generation and processing, are performed with frequency combs in the GHz regime.

Conventional, well-established approaches for periodicity control through manipulation of pulse trains and frequency combs include spectral amplitude filtering and temporal pulse picking (or time gating). The main drawback of these approaches is their low energy efficiency, as they rely on directly discarding signal energy. Additionally, these methods suffer from practical implementation shortcomings. The amplitude filtering method needs high-finesse filters, with tight design and operational requirements (e.g., precise spectral alignment between the filter and the comb), in order to achieve signals with high quality. Similarly, the imperfect suppression of undesired pulses in pulse picking techniques results in spectral line-to-line amplitude fluctuations of the obtained comb. The relatively low extinction ratio of current electro-optic intensity modulators often forces to use optical gates based on nonlinear effects (incurring in even higher energy inefficiency), or optical switches based on semiconductor optical amplifiers and acousto-optic modulators (with typically low operation speeds). Precise timing between the pulse train and the pulse picking gate also becomes a critical factor for a correct pulse suppression.

Another fundamental metric for the applicability of periodic optical waveforms is related to their noise content. Indeed, our ability to detect signals or events and to extract information contained therein is ultimately limited by the strength of said signal and that of the noise content of the measurement. Noise is ubiquitous, and its origin mechanisms are often random and difficult to control. In the particular case of periodic optical signals, the aforementioned techniques for periodicity control typically result in the degradation of the signal-to-noise ratio of the waveform of interest. This is mainly due to the fact that a large amount of energy from the input signal is deliberately thrown away (e.g., in the form of line suppression by spectral amplitude filtering of frequency combs, or pulse rejection by temporal amplitude gating of pulse trains).

Versatile methods to control the pulse period of optical trains and the FSR of frequency combs with high energy efficiency and low signal degradation based on passive, linear processes are highly desired. Periodicity control methods for optical signals based on phase-only manipulations – temporal phase modulation and/or spectral phase filtering – are particularly attractive solutions to the problem, as these techniques recycle the energy of the input signal, rather than discarding part of it, redistributing it to form the desired output signal.

Several techniques for periodicity control through phase-only manipulations have been proposed. In particular, an important set of these techniques relies on periodic phase transformations based on the theory of Talbot self-imaging. Realizations of Talbot phenomena have been reported across several observation domains, including time and frequency (for pulse trains and frequency combs respectively), and although the phenomenon has been extensively studied, a description that unifies its manifestations across all observation domains is still missing.

The main goal of this dissertation is to propose a universal method for arbitrary, energy-preserving control of the period of repetitive optical signals, through the development of a unified mathematical description of the Talbot effect in Fourier-dual representation domains of waves. Such a generalization of the phenomenon is presented in Chapter 3, followed by the formulation of the aforementioned universal periodicity control model. Chapters 4 and 5 present experimental demonstrations of arbitrary, energy-preserving control of the repetition period of temporal pulse trains, and the FSR of frequency combs, respectively. In both chapters, the properties of the method to increase the signal energy over the level of incoherent noise propagating alongside are analyzed. The proposed method is indeed capable of redistributing the energy content of the signals of interest, producing an effect of passive amplification, thus avoiding the need for conventional active gain mechanisms (which are known to amplify both the signal and its noise content, and typically inject additional external noise contributions to the signal).

Finally, Chapter 6 presents experimental examples and applications of the developed period control method to the spectra of arbitrary, aperiodic signals. In particular, two applications are reported: (i) a method for introducing reversible frequency gaps (frequency bands free of energy in the spectrum of a wave) to the spectrum of isolated optical waveforms, allowing for implementation of a novel technique for invisibility cloaking; and (ii) a method for compressing the spectra of modulated sequences of short pulses, while preserving the temporal shape of the pulses (including pulse duration), thus combining the performance advantages and robustness of short pulses for transferring and processing information with the convenience of frequency-domain multiplexing and processing operations.

Considering the wide range of application of periodic temporal and spectral waveforms (e.g., trains of pulses and frequency combs), interest in the methods reported in this dissertation can be foreseen across many different fields. A particularly appealing feature of the proposed methods for pulse period/FSR control is that they offer a high flexibility and energy efficiency. Furthermore, this project could inspire the development of new applications that would take advantage of the energy redistribution strategies for the design of signal processing systems and techniques.

Résumé

Cette section fournit un bref résumé des motivations de ce projet de thèse de doctorat, ainsi que les principaux concepts développés dans cette thèse. Ceux-ci incluent la généralité de la condition de Talbot et la méthode universelle pour le contrôle de période des signaux temporels et spectraux répétitifs. Des exemples expérimentaux de démonstration de manipulation de période de trains d'impulsions et de peignes de fréquence sont rapportés. Enfin, quelques conclusions du travail sont discutées brièvement.

0.1 Introduction

Les signaux optiques périodiques sont d'une importance fondamentale pour une myriade de domaines scientifiques et technologiques. Les trains d'impulsions optiques (signaux optiques temporellement périodiques) et leur contrepartie spectrale, les peignes de fréquence optique (signaux optiques spectralement périodiques) sont le facteur clé de plusieurs disciplines fondamentales et appliquées, telles que la spectroscopie à haute résolution, y compris la mesure et la synchronisation de temps de haute précision, la calibration spectrographique de haute précision des mesures astronomiques, la génération et traitement de formes d'ondes arbitraires à haute résolution, entre autres. La Fig. 0.1 illustre la relation entre un train d'impulsions et son spectre, un peigne de fréquence.

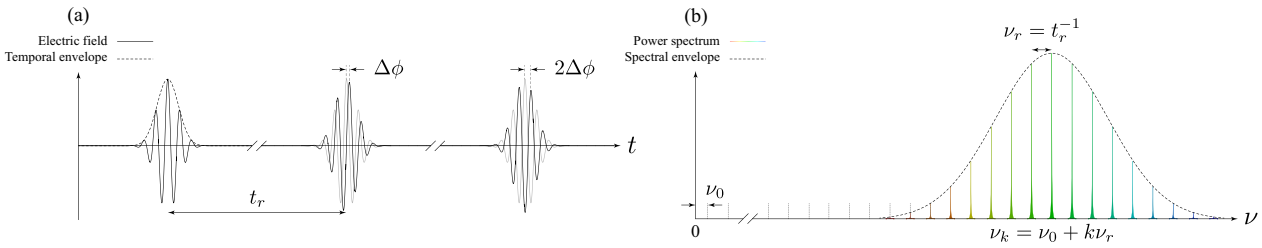

Figure 0.1 – Relation entre un train d'impulsions et son spectre en peigne de fréquence. Les paramètres de (a) un train d'impulsions et (b) sa représentation en peigne de fréquence sont liés par la transformée de Fourier, où l'enveloppe spectrale en peigne est donnée par la transformée de Fourier de l'enveloppe temporelle d'une impulsion. Le FSR du peigne est l'inverse de la période d'impulsion temporelle. Si la fréquence de décalage est différente de zéro, l'enveloppe temporelle du train d'impulsions subit un décalage, $\Delta\phi = 2\pi\nu_0\nu_r^{-1}$, par rapport à la porteuse optique sous-jacente. Ceci est connu comme le décalage entre enveloppe et porteuse. Les symboles t et ν représentent les variables de temps et de fréquence, respectivement.

Un grand nombre de ces applications nécessitent des trains périodiques et précis d'impulsions optiques courtes, généralement générées par des lasers à modes verrouillés. L'un des paramètres clés de ces signaux est leur période de répétition – la période d'impulsion du train, et l'intervalle spectral libre du peigne correspondant (la séparation de fréquence entre les lignes de peigne appelée FSR[1], pour 'Free spectral range' en

[1]Pour assurer l'uniformité des abréviations entre ce résumé et la thèse, nous retenons les abréviations en anglais

anglais). La plupart des applications exigent que ces paramètres soient fixés avec précision. Par exemple, la vitesse à laquelle l'information est transmise dans un système de télécommunication et traitée dans un système informatique, est fortement liée à la période d'impulsion du signal d'horloge. De plus, des applications distinctes nécessitent des ordres de grandeur fondamentalement différents. À titre d'exemple, les applications de spectroscopie atomique et moléculaire nécessitent des peignes de fréquence avec un FSR typiquement dans le régime MHz, tandis que les mesures spectrographiques astronomiques, ainsi que les applications de génération et de traitement de formes d'ondes arbitraires, sont réalisées avec des peignes dans le régime GHz.

Un autre facteur fondamental des signaux périodiques pour leur utilisation pratique est l'énergie par impulsion d'un train d'impulsions, et la puissance de crête de ligne dans un peigne de fréquence. Les applications de trains d'impulsions telles que le pompage optique nécessitent des niveaux élevés de puissance d'impulsion de crête. De plus, ceci est lié au rapport signal sur bruit (SNR pour 'signal-to-noise ratio' en anglais) du signal, un paramètre clé pour de nombreuses disciplines, de la spectroscopie aux communications optiques.

Le contrôle de la période des signaux optiques périodiques dans les deux domaines de temps et de fréquence avec un rendement énergétique élevé est donc critique. Les méthodes visant à manipuler la période des formes d'onde répétitives peuvent être classées en deux groupes: Techniques qui affectent le mécanisme de génération du signal pour obtenir la période désirée, et techniques qui manipulent le signal déjà généré et transforment sa période.

Dans la première catégorie, la miniaturisation d'une cavité laser réduit efficacement le temps d'aller-retour des photons dans le résonateur. Le verrouillage de modes de telles cavités courtes peut générer des trains d'impulsions avec des taux de répétition très élevés; cependant, ces approches souffrent de lacunes critiques, telles que les faibles largeurs de bande d'émission et l'instabilité à des taux de répétition élevés. Les cavités des micro-résonateurs intégrées peuvent atteindre des largeurs de bande d'émission élevées, mais au prix d'une accordabilité très limitée du FSR, d'une non-uniformité d'intensité, et d'un bruit de fréquence dans les modes de peigne. Une solution alternative est l'utilisation du verrouillage de modes harmonique, où plusieurs impulsions sont maintenues en même temps par la cavité résonnante, augmentant ainsi le taux de répétition. Cependant, cette technique est confrontée à d'importants défauts de performance et de mise en œuvre, notamment une mauvaise stabilité à long terme, l'émission d'impulsions avec des valeurs énergies inégales, et une émission de salves empêchant la formation d'un spectre de peigne de fréquence.

Dans la deuxième catégorie, la période d'un signal répétitif peut être modifiée par des opérations de traitement du signal. Ceux-ci sont effectués sur le signal optique lui-même, en dehors de la cavité laser, et par conséquent, ils ont tendance à être plus polyvalents, car pratiquement n'importe quel signal peut être ciblé, indépendamment de sa source. De telles opérations impliquent la manipulation du signal dans le domaine temporel - modulation temporelle - et / ou la manipulation de son spectre de fréquence - le filtrage spectral. Parmi les approches traditionnelles bien établies pour le contrôle de la périodicité à travers la manipulation des trains d'impulsions et des peignes de fréquence on trouve le filtrage d'amplitude spectrale et le prélèvement d'impulsions temporelles (représentés dans la Fig. 0.2)

Dans ceux-ci, l'élimination directe de $r-1$ impulsions (ligne de peigne) sur chaque r impulsions (lignes de peigne) consécutives produit une augmentation de r-fois de la période d'impulsion (FSR du peigne), et une réduction égale du FSR du peigne (période d'impulsion).

Le principal inconvénient de ces approches est leur faible efficacité énergétique, car les deux méthodes impliquent le rejet délibéré d'une fraction $1 - r^{-1}$ de l'énergie du signal original, entraînant une perte d'énergie qui augmente avec le facteur r. L'amplification peut alors devenir nécessaire, entraînant ainsi la dégradation du SNR, inévitable dans les processus d'amplification active classique.

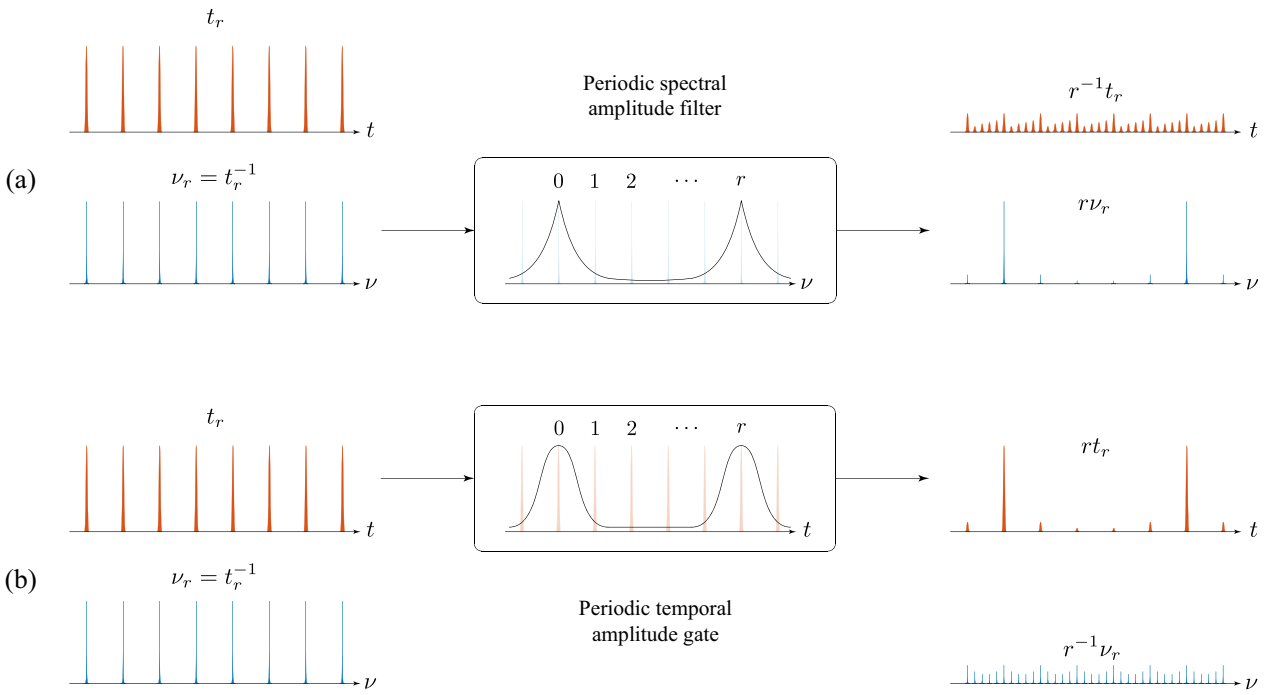

Figure 0.2 – Méthodes de traitement du signal pour le contrôle de période par manipulation directe de l'énergie. Méthodes traditionnelles de contrôle de la périodicité pour les trains d'impulsions optiques et de peignes de fréquence optiques : a) filtrage spectral d'amplitude et b) prélèvement d'impulsion par temporisation (l'exemple montré illustre un facteur de multiplication $r = 5$).

De plus, ces méthodes souffrent de défauts de mise en œuvre pratiques. Le procédé de filtrage d'amplitude nécessite des filtres de haute finesse, avec des exigences de conception et de fonctionnement stricts (par exemple, un alignement spectral précis entre le filtre et le peigne), afin d'obtenir des signaux de haute qualité temporelle et spectrale. Les lignes de peigne non supprimées se traduiront par des fluctuations d'amplitude impulsion à impulsion résiduelle dans le domaine temporel (voir Fig. 0.2(a)). De même, la suppression imparfaite des impulsions indésirables dans les techniques de prélèvement d'impulsions se traduit par des fluctuations spectrales d'amplitude ligne à ligne du peigne obtenu (voir Fig. 0.2(b)).

Le taux d'extinction relativement faible des modulateurs d'intensité électro-optiques actuels oblige souvent à utiliser des portes optiques basées sur des effets non linéaires (entraînant une inefficacité énergétique encore plus élevée), ou des commutateurs optiques basés sur des amplificateurs optiques à semi-conducteurs et des modulateurs acousto-optiques (avec des vitesses de fonctionnement qui sont généralement faibles).

Enfin, dernier point mais non des moindres, la nature même de ces techniques force le facteur r à être nécessairement un entier. Ceci est dû au fait que l'on ne peut supprimer qu'un nombre entier d'impulsions/lignes. Les facteurs fractionnaires de multiplication/division de période sont donc inaccessibles par des méthodes de filtrage d'amplitude et de prélèvement d'impulsions.

Les solutions de traitement du signal au problème de contrôle de périodicité basé sur des manipulations de phase seulement; modulation de phase temporelle et/ou filtrage de phase spectrale (voir Fig. 0.3) sont particulièrement intéressantes, car les transformations de phase recyclent l'énergie totale transportée par le signal cible dans un signal de sortie qui satisfait aux spécifications requises.

Un ensemble important de techniques de contrôle de période basées sur des transformations de phase seule repose sur la théorie de l'auto-imagerie de Talbot. De tels procédés ont été développés pour réaliser la multiplication et/ou la division de la période de répétition des trains d'impulsions par des facteurs ar-

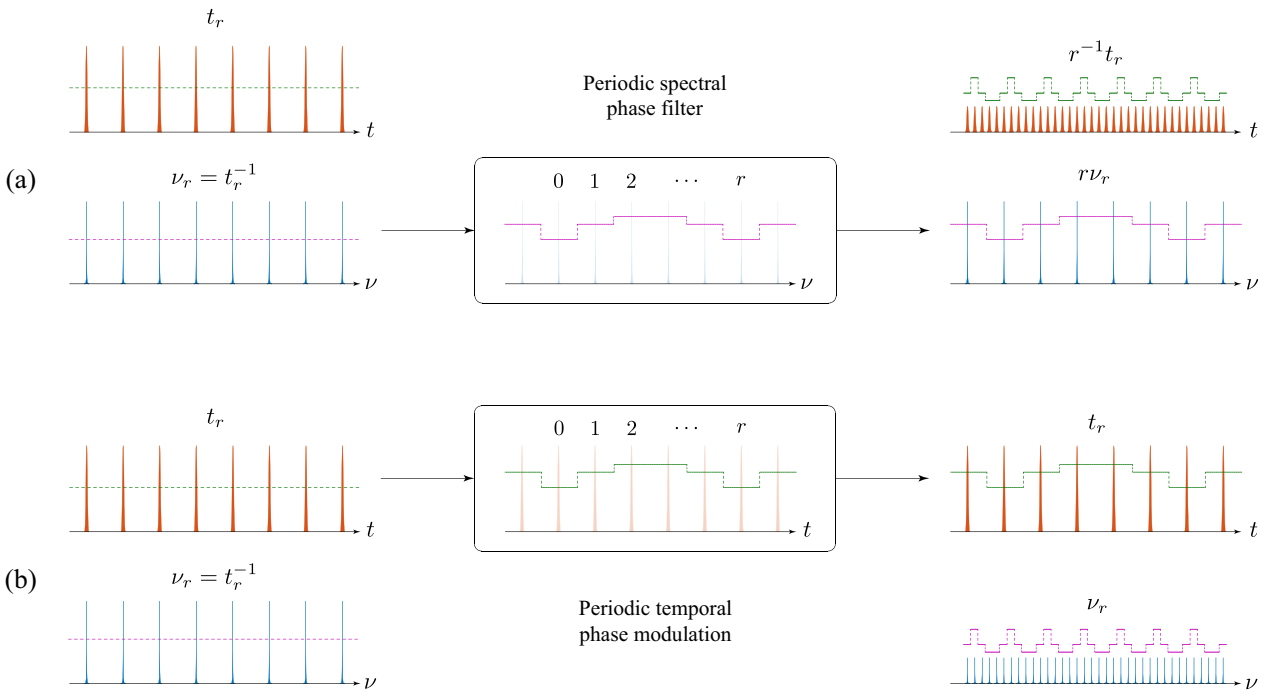

Figure 0.3 – Méthodes de traitement du signal pour le contrôle de période par manipulation de phase uniquement Exemples de (a) division de période d'impulsion (multiplication du taux de répétition) par filtrage périodique de phase spectrale et (b) division du FSR par modulation périodique de phase temporelle (les profils de phase temporelle et spectrale sont représentés en pointillés). La période de répétition est, dans les deux cas, divisée par un nombre entier ($r = 5$ dans l'exemple montré), et les variations de phase subsistent dans les deux domaines temps et fréquence dans les deux situations.

bitraires (entiers ou fractionnaires). De même, des méthodes basées sur l'effet Talbot ont également été rapportées pour réaliser une division du FSR des peignes de fréquence par des facteurs entiers tout en préservant l'énergie du peigne. Ces approches préservent idéalement l'énergie totale du signal d'intérêt, permettant même de réduire l'impact du bruit grâce à une redistribution cohérente de l'énergie.

Cependant, les solutions proposées implémentent uniquement la transformation de période ciblée dans un seul domaine de représentation. Les systèmes définis pour le contrôle du taux de répétition des impulsions impliquent une combinaison de modulation de phase temporelle et de filtrage de phase spectrale (par exemple, par propagation dispersive), et généralement ils n'implémentent pas le contrôle du FSR dans le spectre de peigne de fréquence associé. De même, les conceptions destinées au contrôle du FSR consistent en une combinaison inversée (réciproque) de manipulations de phase, à savoir filtrage de phase spectrale et modulation de phase temporelle, mais elles n'implémentent généralement pas le contrôle du taux de répétition sur le train d'impulsions correspondant. Dans les deux cas, les variations de phase résiduelles restent non compensées dans le domaine réciproque (voir Fig. 0.3).

0.2 Motivation

0.2.1 Définition du projet

L'objectif principal de cette thèse est de *proposer une méthode universelle pour contrôler la période des signaux optiques répétitifs, de telle sorte que l'énergie véhiculée par le signal d'intérêt soit préservée dans*

le processus, tandis que le reste des propriétés du signal reste inaltéré – p.ex., bande passante et durée d'impulsion – et sans introduire de bruit ou de distorsion externes.

0.2.2 Solution proposée

La solution proposée consiste en la formulation d'une généralisation de l'effet Talbot, de sorte que la période d'un signal répétitif puisse être arbitrairement ajustée exclusivement par des manipulations des distributions de phase temporelle et spectrale du signal – préservant intrinsèquement l'énergie.

0.2.3 Considérations supplémentaires

Bien que la méthode proposée pour le contrôle arbitraire de période soit universelle dans sa formulation (elle s'applique aux ondes périodiques dans tout domaine de représentation, en particulier le temps, la fréquence, la position, et le moment transverse), cette thèse accorde une attention particulière à la manipulation arbitraire de spectres optiques par des moyens qui conservent l'énergie, visant à développer des techniques qui peuvent être utiles pour le traitement et la génération de peignes de fréquence optique.

De plus, la méthode produit des résultats intéressants lorsqu'elle est appliquée à des signaux apériodiques, par exemple, à des impulsions isolées ou à des séquences d'impulsions modulées (qui ont des spectres continus).

0.3 Description universelle de l'effet Talbot

L'effet Talbot – ou auto-imagerie – est au cœur des développements rapportés dans cette thèse.

0.4 Vue d'ensemble des effets Talbot

Les effets Talbot se manifestent lorsqu'une onde présentant une périodicité sur l'un de ses domaines de représentation – espace, moment transverse, temps ou fréquence – est affectée par un propagateur imposant un profil de phase quadratique spécifique à travers l'espace réciproque (de Fourier) de ce domaine. La définition mathématique de ces profils de phase est connue sous le nom de «condition de Talbot». Cela donne lieu à des images parfaites de l'onde (auto-imagerie entière) ou à des sous-images où la période initiale est divisée par un nombre naturel (auto-imagerie fractionnaire). Bien que l'effet ait été initialement observé et expliqué dans le contexte de la diffraction de Fresnel des ondes spatialement périodiques, sa description a été étendue au domaine temporel par l'application de la dualité spatio-temporelle bien connue, et plus récemment aux domaines des fréquences, et des moments transverses (observée sous la forme de spectre angulaire). Les réalisations temporelles et spectrales de ce phénomène sont à la base de la méthode rapportée pour le contrôle périodique des signaux optiques; cependant, il convient de mentionner que tous les résultats présentés dans ce travail sont immédiatement applicables aux domaines spatial et du moment transverse, grâce à l'application directe de la dualité espace-temps.

0.4.1 Effet Talbot temporel

L'effet Talbot temporel est observé lorsqu'un train périodique d'impulsions optiques, avec la période t_r, se propage à travers un milieu transparent présentant une certaine quantité de dispersion de vitesse de groupe (GVD, pour 'group velocity dispersion' en anglais). Ce processus peut être décrit comme un filtre de phase unitaire, avec une fonction de transfert spectral, $\mathcal{H}_{\mathrm{GVD}}(\omega)$, donnée par,

$$\mathcal{H}_{\mathrm{GVD}}(\omega) = e^{-i\frac{1}{2}\beta_2 z\omega^2} \tag{1}$$

où i est l'unité imaginaire, β_2 est le coefficient de dispersion de second ordre du milieu (GVD par unité de longueur, mesurée à la fréquence centrale de l'onde), z est la longueur de propagation, et $\omega = 2\pi\nu$. Notez la variation de phase quadratique en fonction de la variable de domaine de Fourier, ω, comme prévu ci-dessus.

L'hypothèse principale ici est que l'impulsion sur chaque période de la séquence est identique à la suivante. Aucune restriction particulière n'est imposée à l'enveloppe d'amplitude complexe de l'impulsion. La condition temporelle de Talbot fournit la quantité de GVD nécessaire pour obtenir une image de Talbot spécifique,

$$2\pi\left|\beta_2\right| z = \frac{p}{q} t_r^2 \tag{2}$$

où p et q sont deux nombres naturels co-premiers. Le train d'impulsions obtenu à la sortie du milieu dispersif a une période d'impulsions $q^{-1}t_r$, tandis que le FSR de son spectre de peigne reste inchangé. Puisque le processus implique uniquement une manipulation de la phase spectrale, l'énergie d'entrée totale est redistribuée dans un train d'impulsions avec un taux de répétition plus élevé. L'énergie de sortie par impulsion est ensuite divisée par q.

En raison de la nature discrète de la représentation du train en peigne dans le domaine spectral, la condition temporelle de Talbot a une représentation discrète comme suit,

$$\phi_{k;p,q} = \sigma\pi\frac{p}{q}k^2 \tag{3}$$

où σ est le signe du coefficient de dispersion de second ordre, c.-à-d. $\sigma = 1$ si $\beta_2 > 0$ et $\sigma = -1$ si $\beta_2 < 0$. Le coefficient $\phi_{k;p,q}$ représente la quantité requise de déphasage spectral à appliquer à la k-ème ligne du peigne de fréquence correspondant pour satisfaire la condition de l'image de Talbot marquée par $\{p, q\}$.

Une caractéristique clé de cet effet est que le train d'impulsions à période divisée obtenu acquiert un profil de phase temporelle déterministe d'impulsion à impulsion. En négligeant un facteur constant, ces phases s'écrivent comme suit,

$$\varphi_{n;s,q} = -\sigma\pi\frac{s}{q}n^2 \tag{4}$$

où s et q sont deux nombres naturels co-premiers.

0.4.2 Effet Talbot spectral

Une version spectrale de l'effet Talbot peut être observée dans le domaine fréquentiel. En particulier, lorsque le déphasage temporel, $\varphi_{n;s,q}$, (voir Eq. 4) est introduit à la n -ème impulsion d'un train, à l'origine sans variations de phase d'impulsion à impulsion, le FSR de son spectre de fréquences est divisé par le facteur entier q. De façon similaire à l'effet Talbot temporel, le peigne de sortie à FSR divisé acquiert un profil de phase spectrale ligne-à-ligne, $\phi_{k;p,q}$, donné par Eq. 3.

0.5 Dualité de Fourier de l'effet Talbot

L'expression des phases temporelles de Talbot donnée par Eq. 4 satisfait une condition de Talbot, c'est-à-dire que son expression est isomorphe à la phase spectrale de Talbot, donnée par Eq. 3, nécessaire pour produire un effet temporel de Talbot. Cette symétrie mathématique est appelée la dualité temps-fréquence (plus généralement, la dualité de Fourier) de l'effet Talbot.

Le coefficient $\varphi_{n;s,q}$ représente le déphasage acquis par la n-ème impulsion de la séquence, après propagation à travers un milieu à GVD satisfaisant l'équation. 2. Les valeurs de s ne dépendent que de p et q et sont déterminées par la parité du produit pq. En particulier, si $\mathbb{E}$ dénote l'ensemble des nombres naturels pairs et $\mathbb{O}$ dénote l'ensemble des nombres naturels impairs, le paramètre s prend les valeurs suivantes,

$$s = \begin{cases} p\left(\left[\frac{1}{p}\right]_q\right)^2 & \forall\, pq \in \mathbb{E} \\ 8p\left[\frac{1}{2}\right]_q\left(\left[\frac{1}{2p}\right]_q\right)^2 & \forall\, pq \in \mathbb{O} \end{cases} \tag{5}$$

où $[1/x]_q$ est l'inverse multiplicatif modulaire de x modulo q, c.à.d l'entier positif (unique) inférieur à q vérifiant $x[1/x]_q = 1 \pmod q$. Cette relation peut être écrite de manière plus compacte,

$$sp = 1 + q\epsilon_q \pmod{2q} \tag{6}$$

où ϵ_q est la parité de q, c.-à-d. $\epsilon_q = 0\,\forall\, q \in \mathbb{E}$ et $\epsilon_q = 1\,\forall\, q \in \mathbb{O}$.

0.6 Effets Talbot contrôlés par la phase

Les formes fonctionnelles des phases Talbot temporelles et spectrales (Eqs. 4 et 3, respectivement), et leur relation (Eq. 6), fournissent la clé pour réaliser un contrôle arbitraire de la période de répétition d'un train d'impulsions ou d'un peigne de fréquence. Pour ce faire, il faut simplement trouver et appliquer la bonne recette de phases de Talbot. Deux méthodes différentes, bien qu'équivalentes, peuvent être conçues pour fixer arbitrairement la période de répétition du train/peigne d'intérêt. Ces deux méthodes diffèrent selon l'ordre dans lequel les phases spécifiques de Talbot sont appliquées. Ils sont nommés respectivement *méthode de Talbot temporelle contrôlé par la phase* (PCTTM, pour 'phase-controlled temporal Talbot method' en anglais) et *méthode de Talbot spectrale contrôlé par la phase* (PCSTM, pour 'phase-controlled spectral Talbot method' en anglais).

0.6.1 Méthode de Talbot temporelle contrôlé par la phase

Ce processus peut être compris comme une généralisation de l'effet Talbot temporel, c'est-à-dire une méthode pour transformer un train d'impulsions optiques de période t_r en un nouveau train de période rt_r, où le facteur de multiplication de la période de répétition r peut être n'importe quelle fraction irréductible, c'est-à-dire $r \in \mathbb{Q}$. En général, r est un nombre rationnel, tel que $r = q_2^{-1} q_1 \; \forall \; \{q_1, q_2\} \in \mathbb{N}$ est une paire des nombres co-premiers. Si la transformation est entièrement achevée, dans le domaine fréquentiel, cela se traduit par une division du FSR du peigne de fréquence correspondant par le facteur r, c'est-à-dire de $\nu_r = t_r^{-1}$ à $r^{-1}\nu_r$. Différentes combinaisons de phases de Talbot temporelles et spectrales pourraient être conçues pour atteindre le même facteur de multiplication; c'est-à-dire des valeurs différentes des paramètres p, q et s dans les équations 3 et 4. La solution générale, représentée sur la figure 0.4, comprend les quatre étapes suivantes.

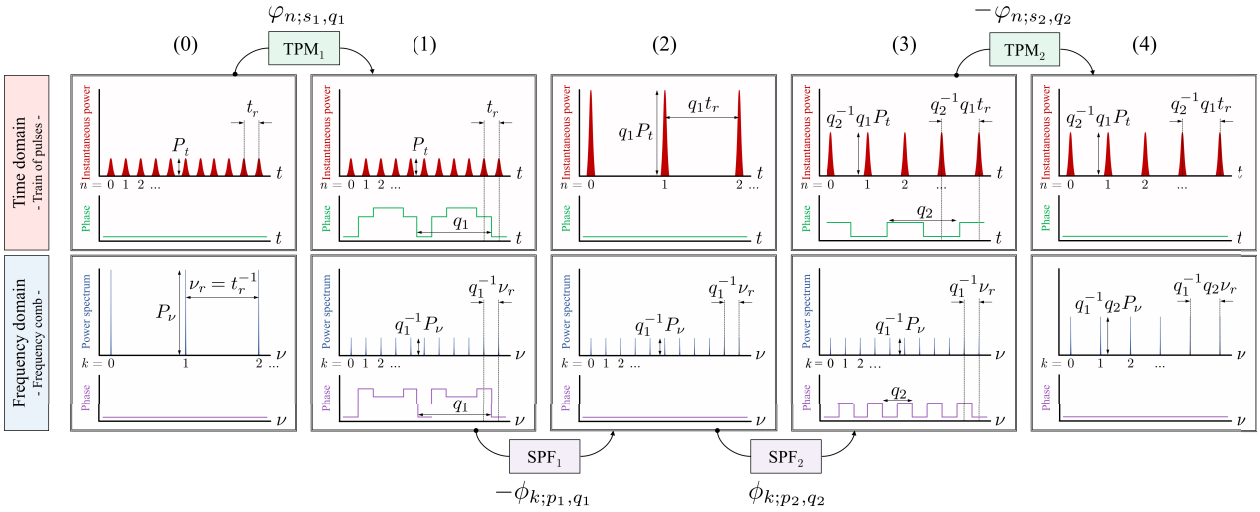

Figure 0.4 – Méthode de Talbot temporelle contrôlé par la phase. Étapes pour transformer un train d'impulsions avec une période t_r en un nouveau train avec une période rt_r, avec $r = q_2^{-1}q_1$, à travers l'application des phases de Talbot. Dans le domaine fréquentiel, la représentation du train en peigne de fréquence correspondant avec FSR ν_r est transformée en un nouveau peigne avec FSR $r^{-1}\nu_r$. Dans l'exemple illustré, $r = 5/2$.

0. **Entrée**. Le point de départ est un train d'impulsions optiques de période t_r, correspondant à un peigne de fréquence avec FSR $\nu_r = t_r^{-1}$ (Fig. 0.4(0)). L'objectif est de réaliser un train d'impulsions avec une période rt_r, avec $r \in \mathbb{Q}$, c.-à-d., $r = q_2^{-1}q_1 \; \forall \; \{q_1, q_2\} \in \mathbb{N}$.

1. **TPM$_1$** (modulation de phase temporelle 1). Le train d'entrée est modulé temporellement avec la séquence $\varphi_{n;s_1,q_1}$, correspondant à une condition spectrale de Talbot s_1/q_1 (voir Eq. 4). Le peigne de fréquence résultant a un FSR $q_1^{-1}\nu_r$, alors que la période d'impulsion reste égale à t_r (Fig. 0.4(1)).

2. **SPF$_1$** (filtrage de phase spectrale 1). À la suite de TPM$_1$, le peigne avec FSR divisé acquiert une phase spectrale $\phi_{k;p_1,q_1}$ (Fig. 0.4(1)), où p_1 est donné par Eq. 6 (avec $s \leftarrow p_1$, $p \leftarrow s_1$ et $q \leftarrow q_1$).). Cette phase est annulée par un filtre de fréquence passe-tout avec le profil de phase opposé, $-\phi_{k;p_1,q_1}$, résultant en un train d'impulsions avec une période de répétition $q_1 t_r$ (Fig. 0.4(2)). À ce stade, le train d'impulsions initial, avec la période t_r, a été transformé en un autre train d'impulsions avec une période $q_1 t_r$ sans variations de phase entre impulsions. Si le facteur de multiplication de période temporelle désirée est entier, cette étape est la dernière.

3. **SPF$_2$** (filtrage de phase spectrale 2). L'application d'une seconde phase spectrale $\phi_{k;p_2,q_2}$ (correspondant à une condition temporelle de Talbot p_2/q_2) divise la période de répétition temporelle du train obtenue après SPF$_1$ par le facteur q_2. Si q_1 et q_2 sont des nombres naturels co-premiers, l'effet global est la multiplication de la période d'impulsion d'entrée par la fraction $r = q_2^{-1}q_1$ (Fig. 0.4(3). Notez que, selon les valeurs calculées de q_1 et q_2, ce facteur peut être supérieur ou inférieur à 1.

4. **TPM$_2$** (modulation de phase temporelle 2). Enfin, puisque le train d'impulsions obtenu après SPF$_2$ (Fig. 0.4(3)) est une sous-image de Talbot du train obtenue après SPF$_1$ (Fig. 0.4(2)), il y aura des variations de phase temporelle d'impulsions à impulsions non compensées. Ces phases peuvent être annulées par une étape supplémentaire de modulation de phase temporelle avec la séquence $-\varphi_{n;s_2,q_2}$, où s_2 est donné par Eq. 6 (avec $s \leftarrow s_2$, $p \leftarrow p_2$ et $q \leftarrow q_2$). L'inverse du facteur de multiplication de la période temporelle affecte alors le FSR du peigne de sortie obtenu, devenant $r^{-1}\nu_r$ (Fig. 0.4(4)).

0.6.2 Méthode de Talbot spectrale contrôlé par la phase

Ce processus peut être compris comme une généralisation de l'effet Talbot spectral, c'est-à-dire une méthode pour transformer un peigne de fréquence avec FSR ν_r en un nouveau peigne avec FSR $r^{-1}\nu_r$, où le facteur de multiplication de la période spectrale, r^{-1}, peut être n'importe quelle fraction irréductible, c'est-à-dire $r \in \mathbb{Q}$. De manière similaire au PCTTM, en général, $r = q_2^{-1}q_1 \; \forall \; \{q_1, q_2\} \in \mathbb{N}$ et $\{q_1, q_2\}$ sont des nombres co-premiers, et si la transformation est entièrement terminée, dans le domaine temporel, cela se traduit par une multiplication de la période de répétition des impulsions correspondante par le facteur r, c'est-à-dire de $t_r = \nu_r^{-1}$ à rt_r Notez que, pour une comparaison pratique, nous considérons ici l'inverse du facteur de multiplication de période d'impulsion, afin de garder la définition du paramètre r cohérente avec celle donnée dans le modèle du PCTTM. Différentes combinaisons de phases de Talbot temporelles et spectrales pourraient être conçues pour atteindre le même facteur de multiplication; c'est-à-dire des valeurs différentes des paramètres p, q et s dans les équations 3 et4. La solution générale, représentée sur la figure. 0.5, comprend les quatre étapes suivantes.

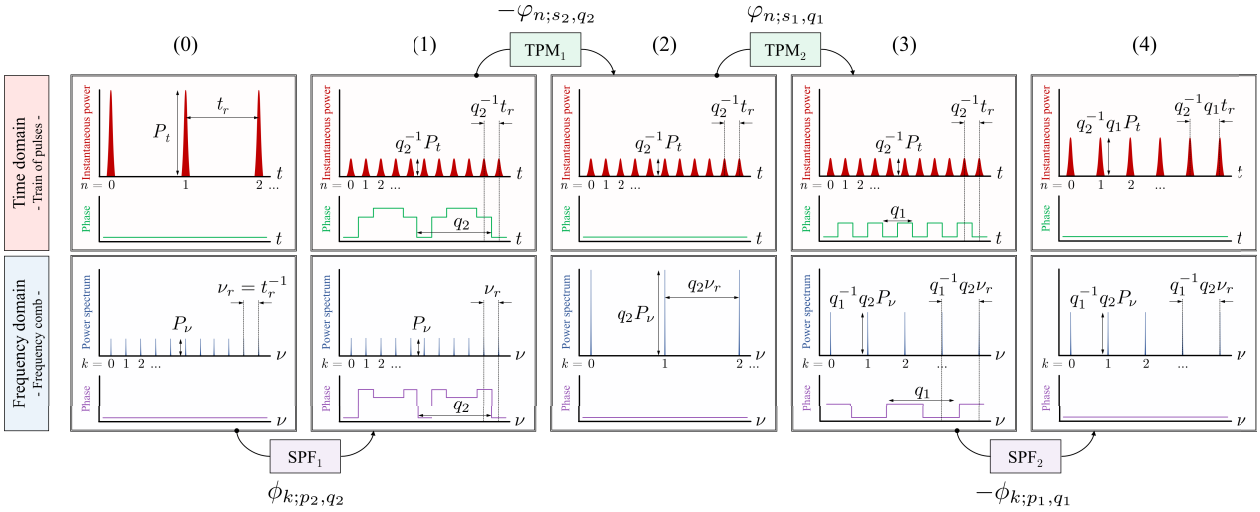

Figure 0.5 – Méthode de Talbot spectrale contrôlée par la phase. Étapes pour transformer un peigne de fréquence avec FSR ν_r en un nouveau peigne avec période $r^{-1}\nu_r$, avec $r = q_2^{-1}q_1$, à travers l'application des phases de Talbot. Dans le domaine temporel, la représentation du peigne en un train d'impulsions correspondant, avec une période d'impulsion t_r, est transformée en un nouveau train avec une période rt_r. Dans l'exemple illustré, $r = 5/2$.

0. **Entrée**. Le point de départ de la méthode est un peigne de fréquence avec un FSR ν_r, correspondant à un train d'impulsions optiques de période $t_r = \nu_r^1$ (Fig. 0.5(0)).

1. **SPF$_1$** (filtrage de phase spectrale 1). Le peigne d'entrée est filtré en phase avec la séquence $\phi_{k;p_2,q_2}$. Le train d'impulsions résultant a une période $q_2^{-1}t_r$, alors que le FSR du peigne reste égal à ν_r (Fig. 0.5(1)).

2. **TPM$_1$** (modulation de phase temporelle 1). La phase temporelle acquise est annulée par une modulation de phase additionnelle avec le profil de phase opposé, $-\varphi_{n;s_2,q_2}$. Le résultat est un peigne à phase plate avec FSR $q_2\nu_r$ (Fig. 0.5(2)). Si le facteur de multiplication du FSR souhaité est entier, il s'agit de l'étape finale. Le paramètre s_2 est donné par Eq. 6 (avec $s \leftarrow s_2$, $p \leftarrow p_2$ and $q \leftarrow q_2$).

3. **TPM$_2$** (modulation de phase temporelle 2). Une seconde modulation de phase temporelle $\varphi_{k;s_1,q_1}$ divise le FSR par q_1. Si q_2 et q_1 sont des nombres naturels co-premiers, l'effet global est la division du FSR d'entrée par le facteur rationnel $r = q_2^{-1}q_1$, aboutissant à $r^{-1}\nu_r$ (Fig. 0.5(3)). Encore une fois, ce facteur peut être supérieur ou inférieur à 1.

4. **SPF$_2$** (filtrage de phase spectral 2). Les phases spectrales résiduelles, acquises grâce à l'application de TPM$_2$, peuvent être annulées par l'application d'une étape supplémentaire de filtrage passe-tout, correspondant à $-\phi_{k;p_1,q_1}$, où p_1 est donné par Eq. 6 (avec $s \leftarrow p_1$, $p \leftarrow s_1$ et $q \leftarrow q_1$). La période d'impulsion obtenue sera alors égale à rt_r.

0.6.3 Considérations sur la conservation de l'énergie et sur le bruit

Le PCTTM et le PCSTM décrivent les opérations nécessaires pour manipuler arbitrairement les périodes de répétition des trains d'impulsions et des peignes de fréquence. De telles opérations sont des manipulations des distributions de phase temporelle et spectrale du signal d'intérêt. En tant que tel, idéalement, toute l'énergie transportée par le signal est préservée dans le processus. C'est l'un des principaux avantages de la méthodologie rapportée. Pour les facteurs de multiplication de période d'impulsions (FSR) supérieurs à 1, les impulsions obtenues (lignes de peigne) en sortie ont une énergie par période accrue, produisant ainsi un effet *d'amplification passive d'énergie* des impulsions (lignes de peigne) de sortie. La méthode ne modifie toutefois pas le bruit additif porté par le signal, car il s'agit de fluctuations aléatoires incohérentes qui ne satisfont pas aux conditions de Talbot nécessaires au contrôle de la période. De plus, les implémentations pratiques des manipulations de phase décrites – filtrage de phase spectrale et modulation de phase temporelle – n'introduisent pas de bruit externe supplémentaire dans le processus. Il est alors possible d'obtenir des formes d'onde de sortie à plus faible bruit, par rapport aux formes d'onde d'entrée, grâce à l'application d'effets Talbot contrôlés par la phase. Il convient de noter que la puissance moyenne du signal reste inchangée après l'application de la méthode. Ceci est dû au fait que les transformations décrites redistribuent simplement l'énergie totale transportée par le signal dans un ensemble différent de périodes de sortie.

0.7 Contrôle arbitraire de période des trains d'impulsions

La méthode PCTTM transforme un train d'impulsions de période t_r en un nouveau train de période rt_r, où $r = q_2^{-1}q_1$. Par exemple, si $q_1 > q_2$, le train de sortie a une période d'impulsion plus élevée que le train d'entrée (c'est-à-dire un taux de répétition inférieur) et si $q_2 > 1$, le facteur de multiplication de période est un nombre fractionnaire. Notez que, si l'on ne s'intéresse qu'à manipuler la période du train d'impulsion, et non le FSR de son spectre de peigne de fréquence correspondant, la dernière étape de la méthode peut être omise.

0.7.1 Manipulations de phase impliquées

Les manipulations de phase nécessaires pour la division fractionnaire du taux de répétition d'un train d'impulsions sont implémentées ici comme modulation de phase temporelle directe du train d'impulsions et propagation du train à travers un milieu optique présentant une dispersion de vitesse de groupe du second ordre.

0.7.1.1 Modulation de phase temporelle

La première étape de la méthode consiste à appliquer une phase temporelle $\varphi_{n;s,q_1}$ à la n-ème impulsion du train d'intérêt. Dans les expériences rapportées ici, $s = q_1 - 1$, de sorte que la phase appliquée,

$$\varphi_{n;q_1-1,q_1} = -\pi \frac{q_1 - 1}{q_1} n^2 \tag{7}$$

0.7.1.2 Dispersion de la vitesse du groupe

Les deuxième et troisième étapes de la méthode, ici combinées en une seule, consistent en l'application des phases spectrales $-\phi_{k;p_1,q_1}$ et $\phi_{k;p_2,q_2}$ à la k-ème ligne de la représentation en peigne de fréquence du train d'intérêt. Ces phases sont appliquées en séquence à un peigne de fréquence avec le même FSR (voir les étapes 2 et 3 de la Fig. 0.4). Dans les expériences rapportées ici, $p_1 = p_2 = 1$, de sorte que la phase globale appliquée,

$$\phi_{k;1,q_2} - \phi_{k;1,q_1} = \pi \left(\frac{1}{q_2} - \frac{1}{q_1} \right) n^2 \tag{8}$$

Selon l'équation 2, la quantité requise de GVD,

$$2\pi\beta_2 z = \left(\frac{1}{q_2} - \frac{1}{q_1} \right) (q_1 t_r)^2 \tag{9}$$

0.7.2 Démonstration expérimentale

La technique de division fractionnaire du taux de répétition proposée est démontrée sur un train d'impulsions optiques dans le proche infrarouge dans la bande C des télécommunications optiques, et avec un taux de répétition dans le régime GHz. Ces caractéristiques constituent une preuve de concept pratique, facile à mettre en œuvre avec un équipement de télécommunication standard.

0.7.2.1 Configuration expérimentale

Fig. 0.6 montre un schéma simplifié de la configuration expérimentale utilisée pour valider le concept de division fractionnaire du taux de répétition.

Un laser à verrouillage de modes actif (MLL, pour 'Mode-locked laser' en anglais) génère le train d'impulsions d'entrée. Un synthétiseur radiofréquence pilote le laser au taux de répétition d'entrée souhaité. Le laser délivre des impulsions optiques de type Gaussien limitées par transformée de Fourier, avec une

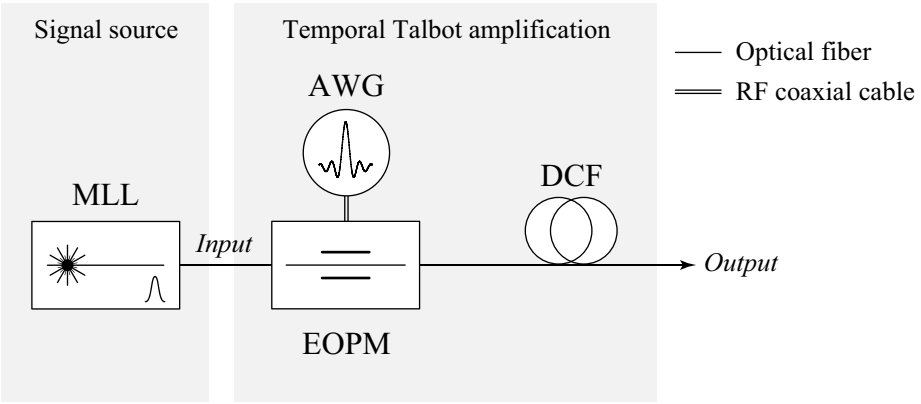

Figure 0.6 – Multiplication fractionnaire de taux de répétition, configuration expérimentale. MLL, laser à verrouillage de modes; AWG, générateur de forme d'onde arbitraire; EOPM, modulateur de phase électro-optique; DCF, fibre à compensation de dispersion.

largeur d'impulsion à mi-hauteur d'environ 6 ps, à une longueur d'onde centrale de 1550 nm (environ 193.55 THz). Le spectre correspondant est un peigne de fréquence optique cohérent avec un FSR dicté par le taux de répétition du laser.

Le profil de modulation de phase temporel prescrit est chargé dans la mémoire d'un générateur de formes d'ondes arbitraires (AWG, pour 'arbitrary waveform generator' en anglais) capable de délivrer 24 Gs/s avec une bande passante analogique de 7 GHz. L'AWG génère un signal de tension électrique analogique suivant les niveaux de phase requis par Eq. 7 pour une valeur donnée de q_1, et correspondant au taux de répétition des impulsions optiques générées. Ce signal de tension est amplifié et transmis à un modulateur de phase électro-optique (EOPM, pour 'Electro-optical phase modulator' en anglais), avec une bande passante RF de 40 GHz, qui module la phase de chaque impulsion en conséquence.

Enfin, le train modulé en phase se propage sur un tronçon de fibre compensatrice de dispersion (DCF, pour 'dispersion-compensating fiber' en anglais). Cette fibre optique a une dispersion normale ($\beta_2 > 0$) à la longueur d'onde de travail, et sa longueur est choisie pour correspondre à la condition requise, définie par Eq. 9.

0.7.2.2 Résultats expérimentaux

La table 0.1 liste les paramètres des signaux d'entrée testés, l'ensemble des configurations expérimentales pour la division fractionnaire du taux de répétition, et les résultats obtenus.

Fig. 0.7 montre un ensemble de mesures correspondant aux conditions expérimentales et aux résultats listés dans le tableau 0.1.

L'AWG génère les signaux de tension représentés sur la Fig. 0.7(a). Ces signaux de tension pilotent l'EOPM modulant la phase du train d'impulsions optiques d'entrée. Ceci produit des images spectrales de Talbot, résultant en une division du FSR par le paramètre q_1 (Fig. 0.7(b)). Les spectres de puissance optique montrés sont mesurés par un analyseur de spectre optique.

La propagation des trains modulés en phase a travers la DCF présentant la quantité de GVD requise (voir le tableau 0.1) produit la division du taux de répétition par le facteur fractionnaire anticipé, et l'amplification passive associée par le même facteur, r (Fig. 0.7(c)). Les traces temporelles montrées sont mesurées par

Table 0.1 – Multiplication fractionnaire du taux de répétition, conditions expérimentales et résultats. Liste des périodes d'impulsions d'entrée et de sortie et des paramètres de configuration de la PCTTM pour un ensemble de 7 expériences conduites.

	Période d'impulsion		**Paramètres de PCTTM**			
	t_r [a]	rt_r [b]	q_1 [c]	q_2 [d]	r [e]	$\beta_2 z$ [f]
(1)	126.139	168.185	4	3	$1.\overline{3}$	3376.415
(2)	84.092	126.139	3	2	1.5	1688.207
(3)	79.777	132.962	5	3	$1.\overline{6}$	3376.415
(4)	63.568	111.244	7	4	1.75	3376.415
(5)	53.185	132.962	5	2	2.5	3376.415
(6)	63.069	168.185	8	3	$2.\overline{6}$	8441.038
(7)	62.902	220.157	7	2	3.5	11020.156

[a] Période d'impulsion d'entrée (ps).
[b] Période d'impulsion de sortie (ps).
[c] Numérateur.
[d] Dénominateur.
[e] Facteur de multiplication de la période d'impulsion.
[f] Dispersion du second ordre (ps^2/rad).

un oscilloscope à échantillonnage optique avec une bande passante d'acquisition équivalente de 500 GHz. Il est à noter que la perte totale d'insertion dans le chemin du signal optique est de $\sim 13,5$ dB pour la démonstration expérimentale rapportée. Les traces temporelles montrées sont normalisées à la valeur de puissance crête temporelle du signal d'entrée.

Enfin, la figure 0.7(d) montre les spectres radiofréquence des trains d'impulsions d'entrée et de sortie, mesurés par un analyseur de spectre radiofréquence équipé d'une photodiode à bande passante de 45 GHz. Les harmoniques mesurées dans les spectres de puissance RF vérifient la division fractionnaire correcte du taux de répétition.

0.8 Contrôle arbitraire du FSR des peignes de fréquence

La MTSCP transforme un peigne de fréquence avec un FSR ν_r en un nouveau peigne avec FSR $r^{-1}\nu_r$, où $r = q_2^{-1}q_1$. Notez que, si l'on veut seulement manipuler le FSR du peigne, et non la période d'impulsion du train d'impulsions correspondant, la dernière étape de la méthode peut être omise.

0.8.1 Manipulations de phase impliquées

Les manipulations de phase requises pour le contrôle arbitraire du FSR d'un peigne de fréquence sont réalisées ici par une propagation à travers un milieu optique présentant une dispersion de vitesse de groupe (GVD) et une modulation de phase temporelle directe du train d'impulsions résultant.

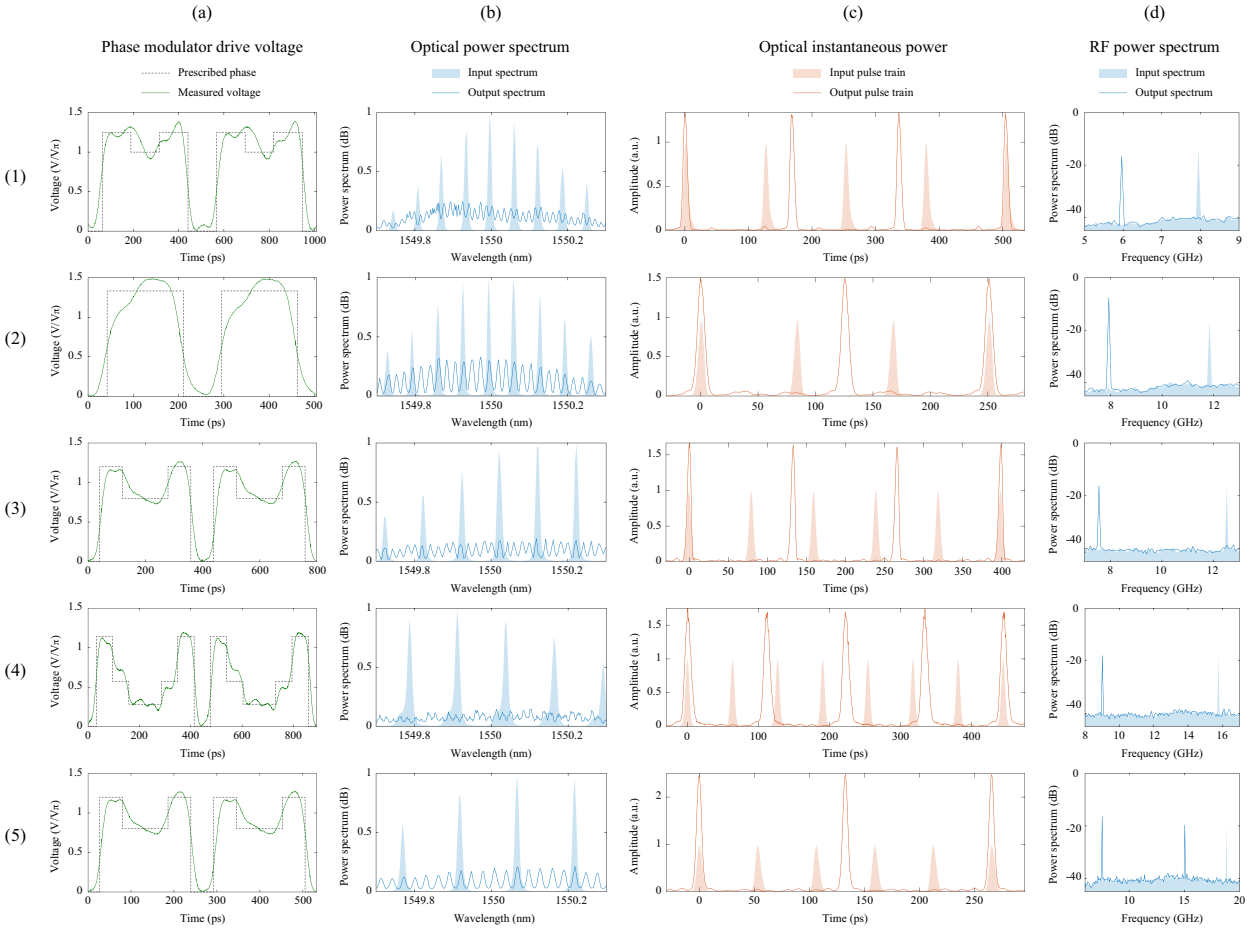

Figure 0.7 – Multiplication fractionnaire du taux de répétition, résultats expérimentaux. Ensemble de mesures correspondant aux conditions expérimentales et aux résultats listés sur le Tableau 0.1, et suivant la même numérotation (1) - (5). a) Séquences de modulation de phase temporelle prescrites et tensions de commande appliquées au modulateur EOPM, où V_π désigne la tension demi-onde de l'EOPM (c'est-à-dire le niveau de tension requis pour appliquer un déphasage de π rad au signal optique); (b) spectres de puissance optique de la représentation en peigne de fréquence d'entrée et de sortie du train d'impulsions traité, normalisé à la puissance de crête du peigne d'entrée (l'effet d'auto-imagerie spectrale anticipée est observé, conduisant à la division du FSR par le facteur q_1); (c) mesures de puissance instantanée des trains d'impulsions d'entrée et de sortie, normalisées à la puissance de crête temporelle du train d'entrée (on observe la multiplication fractionnaire anticipée de la période d'impulsion, ainsi que l'effet correspondant d'amplification passive par redistribution d'énergie); (d) les spectres de puissance radiofréquence des trains d'impulsions d'entrée et de sortie, vérifiant l'effet attendu de division fractionnaire du taux de répétition.

0.8.1.1 Dispersion de la vitesse de groupe

La première étape de la méthode consiste à appliquer une phase spectrale $\phi_{k;p_2,q_2}$ à la k-ème ligne du peigne d'intérêt. Dans les expériences rapportées, la valeur $p_2 = 1$ est choisie pour minimiser la quantité totale de GVD requise, cependant, toute valeur entière peut être conçue, à condition que p_2 et q_2 soient co-premiers. De cette façon, la séquence de phase appliquée s'écrit,

$$\phi_{k;1,q_2} = \pi \frac{1}{q_2} k^2 \tag{10}$$

Selon l'équation. 2, la quantité requise de GVD,

$$2\pi\beta_2 z = \frac{1}{q_2\nu_r^2} \tag{11}$$

0.8.1.2 Modulation de phase temporelle

Les deuxième et troisième étapes de la méthode, ici combinées en une seule, consistent en l'application des phases temporelles $-\varphi_{k;s_2,q_2}$ et $\varphi_{k;s_1,q_1}$ à la n-ème impulsion de la représentation temporelle du peigne d'intérêt. Ces phases sont appliquées en séquence à un train d'impulsions avec la même période (voir les étapes 2 et 3 de la Fig. 0.5). Dans les expériences rapportées, $s_2 = q_2 - 1$ et $s_1 = q_1 - 1$, de sorte que la phase globale appliquée soit donnée comme suit,

$$\varphi_{n;q_1-1,q_1} - \varphi_{n;q_2-1,q_2} = -\pi\frac{q_1 - q_2}{q_1 q_2}n^2 \tag{12}$$

0.8.2 Démonstration expérimentale

La technique proposée pour le contrôle arbitraire du FSR des peignes de fréquence est démontrée sur un peigne cohérent correspondant à un train d'impulsions optiques dans le proche infrarouge, plus précisément dans la bande C de télécommunications optiques, et avec un taux de répétition dans le régime GHz. Ces caractéristiques constituent une preuve de concept pratique, facile à mettre en œuvre avec un équipement de télécommunication standard.

0.8.2.1 Configuration expérimentale

La figure 0.8 montre un schéma simplifié de la configuration expérimentale utilisée pour valider le concept de contrôle arbitraire du FSR.

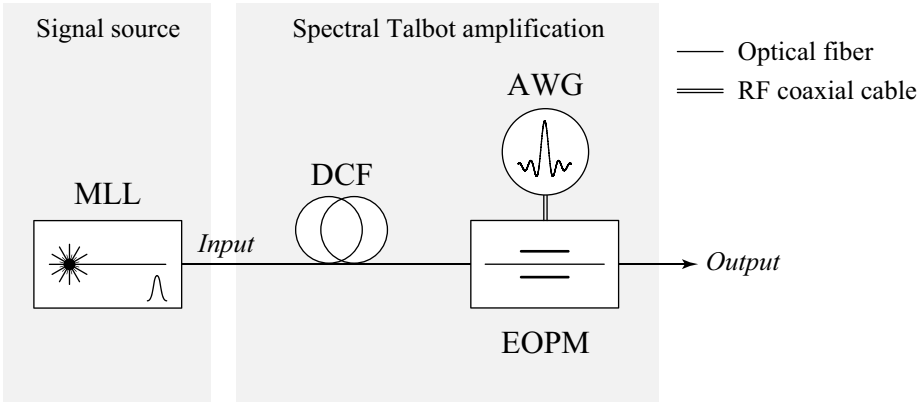

Figure 0.8 – Contrôle arbitraire du FSR des peignes de fréquence, configuration expérimentale. MLL, laser à verrouillage de modes; DCF, fibre de compensation de dispersion; AWG, générateur de forme d'onde arbitraire; EOPM, modulateur de phase électro-optique.

Un laser à verrouillage de modes actif (MLL) génère le peigne de fréquence d'entrée. Un synthétiseur radiofréquence pilote le laser sur le FSR d'entrée ν_r désiré. Le laser délivre des impulsions optiques de

type Gaussien limitées par transformée de Fourier, avec une largeur d'impulsion à mi-hauteur (FWHM) d'environ 3 ps, à une longueur d'onde centrale de 1554.4 nm (environ 193 THz) et une période de répétition des impulsions, t_r, dictée par le FSR.

Le train d'impulsions d'entrée se propage sur un tronçon de fibre de compensation de dispersion (DCF). Cette fibre optique a une dispersion normale ($\beta_2 > 0$) à la longueur d'onde de travail, et sa longueur est choisie pour correspondre à la condition définie par Eq. 11. Le train d'impulsions de sortie correspond à une sous-image temporelle de Talbot avec une période d'impulsion $q_1^{-1}t_r$, tandis que le FSR du peigne correspondant reste inchangé.

Enfin, le profil de modulation de phase temporel prescrit (donné par Eq. 12) est chargé dans la mémoire d'un générateur de forme d'onde arbitraire (AWG) capable de délivrer 50 Gs/ s avec une bande passante analogique de 14GHz. L'AWG génère un signal de tension analogique suivant les niveaux de phase requis par Eq. 12, avec un taux de répétition qui correspond à celui des impulsions à la sortie du milieu dispersif (GVD). Ce signal de tension est amplifié et délivré à un modulateur de phase électro-optique (EOPM), avec une bande passante RF de 40 GHz, qui module la phase de chaque impulsion (une ligne à retard optique accordable est utilisée pour aligner le signal optique sur le signal de tension qui pilote le modulateur, et un contrôleur de polarisation est utilisé pour maximiser l'efficacité de la modulation).

0.8.2.2 Résultats expérimentaux

Le tableau 0.2 liste les paramètres des signaux d'entrée testés, l'ensemble des configurations expérimentales pour le contrôle arbitraire du FSR, et les résultats obtenus.

Table 0.2 – Contrôle arbitraire du FSR, conditions expérimentales et résultats. Liste des valeurs du FSR d'entrée et de sortie et des paramètres de configuration de la MTSCP pour un ensemble de 5 expériences conduites.

	FSR		**Paramètres de MTSCP**				
	ν_r [a]	$r^{-1}\nu_r$ [b]	q_2 [c]	q_1 [d]	r^{-1} [e]	$10\log_{10}(r^{-1})$ [f]	$\beta_2 z$ [g]
(1)	9.451	18.902	2	1	2	3	891.527
(2)	9.463	28.391	3	1	3	4.7	592.369
(3)	9.451	37.804	4	1	4	6	445.455
(4)	7.717	11.575	3	2	1.5	1.7	890.911
(5)	9.451	3.781	2	5	0.4	-4	890.911

[a] FSR d'entrée (GHz).
[b] FSR de Sortie (GHz).
[c] Numérateur.
[d] Dénominateur.
[e] Facteur de multiplication du FSR, échelle linéaire.
[f] Facteur de multiplication du FSR, échelle logarithmique (dB).
[g] Dispersion de second ordre (ps^2/rad).

Fig 0.9 montre un ensemble de mesures correspondant aux conditions expérimentales et aux résultats listés sur le Tableau 0.2.

Le peigne de fréquence d'entrée se propage d'abord sur une longueur de DCF présentant la quantité de GVD requise (voir le Tableau 0.2). Le train d'impulsions obtenu à la sortie de DCF est une sous-image temporelle de Talbot du train d'entrée (division d'impulsions par le facteur q_2), tandis que le spectre de puissance du peigne à la sortie de DCF reste inchangé.

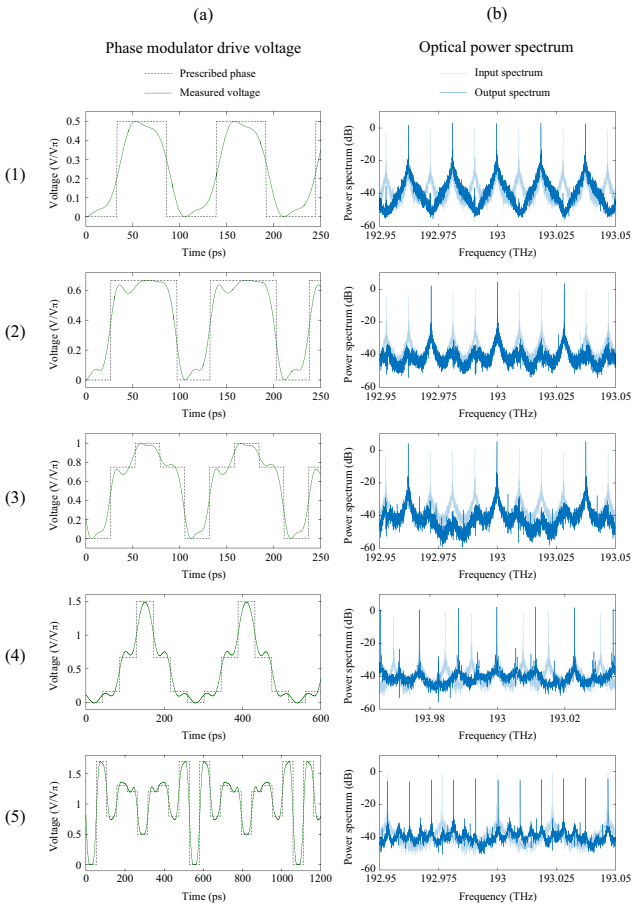

Figure 0.9 – Contrôle arbitraire du FSR, résultats expérimentaux. Ensemble de mesures correspondant aux conditions expérimentales et résultats listés sur le Tableau 0.2, et suivant la même numérotation (1) - (5). a) Séquences de modulation de phase temporelle et tensions de commande appliquées au modulateur EOPM, où V_π désigne la tension demi-onde de l'EOPM (c'est-à-dire le niveau de tension requis pour appliquer un déphasage de π rad au signal optique); (b) spectres de puissance optique des peignes de fréquence d'entrée et de sortie, normalisés à la puissance de crête du peigne d'entrée (la multiplication du FSR anticipée par le facteur r^{-1} est observée, ainsi que l'effet d'amplification passive des lignes spectrales par redistribution d'énergie).

L'AWG génère les signaux de tension représentés sur la Fig. 0.9(a). Ces signaux de tension pilotent l'EOPM modulant la phase du train d'impulsions à la sortie du DCF. Ceci produit la modification du FSR attendue (multiplication du FSR d'entrée par le facteur r^{-1}), et l'amplification passive des lignes spectrales du peigne associé. Fig. 0.9(b) montre les spectres de puissance d'entrée et de sortie, mesurés avec un analyseur de spectre optique avec une résolution de 5 MHz, et normalisés à la puissance spectrale de crête du peigne d'entrée.

0.9 Traitement des ondes apériodiques grâce à l'effet Talbot spectral généralisé

Les transformations d'ondes de la MTSCP, appliquées aux signaux apériodiques, produisent des effets intéressants dans leurs spectres. Deux exemples d'application de la MTSCP aux signaux temporels apériodiques sont rapportés et discutés: (i) une méthode pour transformer de façon réversible le spectre d'énergie d'une onde large bande, afin d'éviter l'interaction entre l'onde et un objet dans le but de dissimuler l'objet, et (ii) une technique pour comprimer le spectre d'une séquence d'impulsions courtes modulées, par exemple un signal de télécommunication, sans modifier la forme temporelle – y compris la durée – des impulsions individuelles de la séquence.

0.9.1 Invisibilité par dissimulation spectrale

L'invisibilité peut être obtenue en manipulant les manières dont les ondes voyagent dans l'espace. En général, un observateur est capable de détecter et d'étudier un objet en analysant l'interaction entre cet objet et une onde de sonde, provenant d'une source d'éclairage connue. Une telle interaction imprime une signature sur l'onde d'illumination, permettant à l'observateur de détecter et, dans une certaine mesure, d'étudier les propriétés de l'objet cible. Un dispositif de cape d'invisibilité spatiale redirige l'onde d'illumination autour d'une zone prescrite. De cette façon, les objets situés dans la région masquée évitent toute interaction avec l'onde. L'observateur est alors incapable de détecter la présence de l'objet. De même, les événements temporels, qui sont détectés par la variation transitoire - signature temporelle - qu'ils impriment sur un signal de sonde, peuvent être cachés de la détection à travers une cape d'invisibilité temporelle. Un tel dispositif ralentit de manière appropriée la vitesse de propagation de l'onde avant que l'événement cible ait lieu, et l'accélère après la fin de l'événement, créant ainsi une période de temps durant laquelle l'onde ne transporte pas d'énergie.

Les premières démonstrations d'invisibilité par dissimulation optique présentaient des conceptions de métamatériaux basées sur des éléments d'optiques dans lesquelles une transformation de coordonnées conforme est appliquée aux équations de Maxwell, obtenant l'ensemble des paramètres électromagnétiques requis pour atteindre les chemins de propagation d'onde désirés. La principale limitation de ces conceptions était le fait que l'invisibilité n'était atteinte qu'à une seule longueur d'onde. Les avancées récentes dans ce domaine ont donné lieu à des capes d'invisibilité comportant de larges bandes passantes d'opération, reposant généralement sur une ingénierie précise de la réponse électromagnétique d'un matériau exotique ou d'un système optique complexe. Cependant, des études récentes et approfondies, utilisant une analyse électromagnétique complète, ont prédit que les capes spatiales traditionnelles induisent une distorsion dans le spectre d'énergie des ondes d'éclairage à large bande. Pour qu'un objet soit entièrement caché, un dispositif d'invisibilité doit être capable de restituer les variations exactes d'amplitude et de phase de l'onde d'illumination, à la fois spatialement et temporellement (c'est-à-dire le champ complet), à sa sortie. C'est en effet l'un des principaux défis fondamentaux dans le domaine de l'invisibilité par dissimulation otique actuellement.

Par des principes de conception fondamentaux, les stratégies de dissimulation actuelles modifient nécessairement les variations de phase parmi les différentes composantes de fréquence d'une onde d'illumination à large bande. Ceci est dû au fait qu'une couche d'invisibilité force différentes composantes de fréquence de l'onde d'illumination à se propager à travers différents chemins optiques, subissant ainsi des retards différents. Une telle distorsion de phase altère inévitablement le profil temporel d'éclairage. Par conséquent, les approches de dissimulation actuelles sont vulnérables à la détection par des méthodes d'observation simples. Par exemple, une impulsion courte cohérente en phase – correspondant à un spectre de fréquence large bande continue – incident dans le dispositif de dissimulation sera sévèrement déformée. Un observateur équipé d'instruments communs de détection de phase ou de détection temporelle pourrait facilement détecter une telle distorsion, révélant ainsi la présence du dispositif d'invisibilité. Il a été avancé que des concepts fondamentalement nouveaux, au-delà des solutions d'invisibilité classiques proposées à ce jour, devenaient nécessaires pour la réalisation d'une dissimulation à large bande préservant la phase.

Atteindre l'invisibilité dans la représentation fréquentielle de l'onde d'illumination pourrait fournir une solution à ce problème. La figure 0.10 illustre schématiquement le processus d'observation d'un objet à travers la signature distincte qu'il imprime sur le spectre de fréquence continu d'une onde d'illumination à large bande.

Le concept proposé ici repose sur la redistribution de l'énergie de l'onde entrante vers des régions de fréquences qui ne seront pas affectées par l'interaction avec l'objet à dissimuler, grâce à des transformations

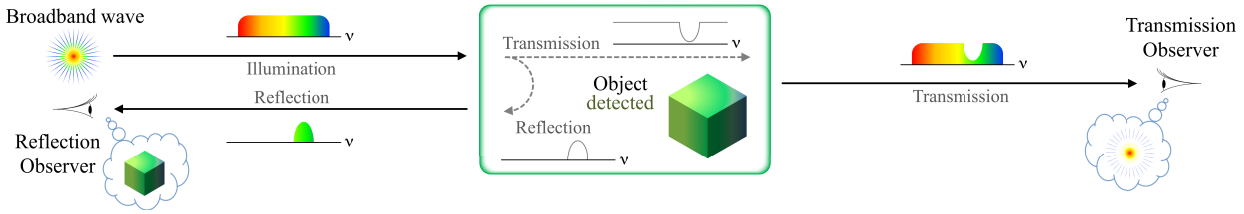

Figure 0.10 – Détection d'un objet à travers sa signature fréquentielle sur une onde d'illumination à large bande. Pour la simplicité de l'illustration, seule la diffusion de l'onde par la cible est représentée.

préservant l'énergie. Ces transformations sont conçues pour créer, de manière réversible, une «ouverture» (c.à.d. une bande de fréquence vide) à travers la (les) région (s) désirée (s) du spectre d'illumination. L'onde se propage alors à travers l'objet sans interagir avec lui, et l'application subséquente des transformations opposées rétablit le spectre d'onde à son état original exact - tant en amplitude qu'en phase - lorsque l'onde a dépassé l'objet. Cela garantit que la cible et le dispositif de dissimulation restent invisibles pour tout observateur, y compris par une détection temporelle à large bande, ou sensible à la phase. Fig. 0.11 illustre le principe d'invisibilité discuté ici.

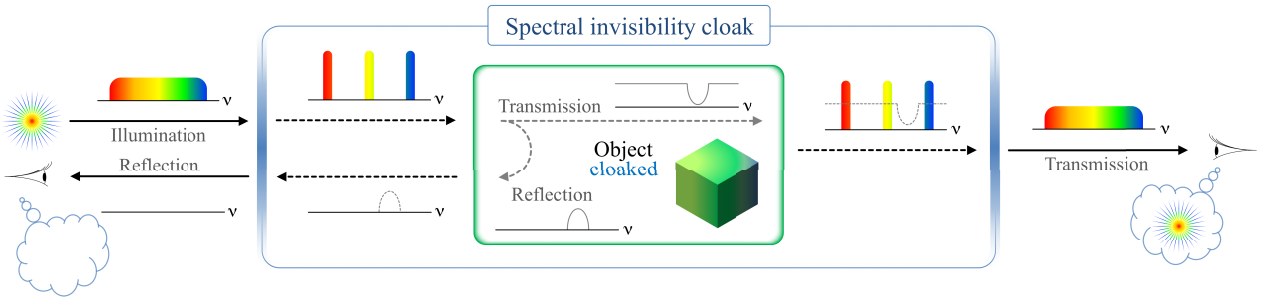

Figure 0.11 – Invisibilité spectrale par dissimulation de la signature fréquentielle d'un objet. Une ouverture de fréquence est générée dans le spectre de l'onde d'illumination grâce à des transformations d'ondes réversibles et préservant l'énergie. La réponse spectrale de l'objet, située dans une telle ouverture, n'interagit pas avec l'onde d'illumination, ainsi, la signature n'est pas imprimée. Une fois que l'onde a traversé l'objet, les transformations d'onde opposées restaurent le spectre d'illumination (à la fois en amplitude et en phase) à son état d'origine exact.

0.9.1.1 Principe de fonctionnement

Pour simplifier l'explication, considérons d'abord un train d'impulsions avec une période de répétition t_r comme onde d'illumination. Cela correspond à un peigne de fréquence avec un FSR $\nu_r = t_r^{-1}$. Dans cette situation, la MTSCP peut être utilisée pour multiplier le FSR du peigne par un facteur entier, $r^{-1} = q_2$. Rappelons que, selon les dérivations de la MTSCP, d'abord, un déphasage spectral $\phi_{k;p_2,q_2}$ doit être appliqué à la k-ème ligne du peigne. Dans les expériences rapportées, la valeur $p_2 = 1$ est choisie pour minimiser la quantité totale de GVD requise. De cette façon, la séquence de phase appliquée s'écrit,

$$\phi_{k;1,q_2} = \sigma\pi\frac{1}{q_2}k^2 \tag{13}$$

Cela se traduit par une GVD nécessaire,

$$2\pi|\beta_2|z = \frac{1}{q_2\nu_r^2} \tag{14}$$

L'onde obtenue est un train d'impulsions avec une période de répétition $q_2^{-1}t_r$. Ensuite, un déphasage temporel $-\varphi_{n;s_2,q_2}$, (où s_2 est obtenu à partir de l'équation. 6, pour les valeurs données de q_2 et p_2) est appliqué à la n-ème impulsion du train résultant. Dans les expériences rapportées, $s_2 = q_2 - 1$, de sorte que,

$$-\varphi_{n;q_2-1,q_2} = \sigma\pi\frac{q_2-1}{q_2}n^2 \tag{15}$$

Le facteur de multiplication du FSR obtenu dans cette configuration du MTSCP est $r^{-1} = q_2$, ce qui donne un peigne avec un FSR,

$$\nu_c = r^{-1}\nu_r \tag{16}$$

En raison de la préservation de l'énergie intrinsèque de la transformation, le peigne avec FSR multiplié peut être rétabli dans son état d'origine en appliquant les manipulations de phase opposées.

Remarquablement, lorsque les transformations décrites sont appliquées à une onde d'éclairage cohérente à large bande avec un spectre de fréquence purement continu (par exemple, une seule impulsion temporelle courte), un ensemble périodique de larges ouvertures est généré dans le spectre de l'onde. Les transformations de phase requises dans cette situation sont les mêmes que celles décrites ci-dessus pour un train d'impulsions périodique. Cependant, les valeurs de r et ν_r peuvent maintenant être choisies arbitrairement pour obtenir la largeur désirée de ces bandes. Cette largeur est fixée par,

$$\Delta\nu_g = (r^{-1} - 1)\nu_r \tag{17}$$

Ceci rend le fonctionnement du dispositif d'invisibilité indépendant des propriétés de l'onde d'illumination (par exemple, le taux de répétition). Comme discuté ci-dessus, l'onde d'illumination peut ensuite être restaurée à son état d'origine exact en appliquant les transformations de phase opposées.

0.9.1.2 Configuration expérimentale

La figure 0.12 montre un schéma simplifié de la configuration expérimentale utilisée pour valider le concept d'invisibilité par dissimulation spectrale.

La source d'illumination utilisée est un laser à verrouillage de modes avec une fréquence de répétition de 250 MHz et un filtre optique utilisé pour sélectionner une bande passante de 4 nm autour d'une longueur d'onde centrale de $1554.$ nm (correspondant à une bande passante de 3 dB) $\sim$500 GHz autour de 192.85 THz). Le spectre de fréquences à large bande cohérent en phase qui en résulte correspond à une impulsion temporelle ~ 1.4 picoseconde.

Le dispositif de dissimulation se compose de deux tronçons de fibre optique – pour la mise en œuvre des milieux à GVD d'entrée et de sortie – avec une amplitude de dispersion égale et des signes opposés, et deux modulateurs de phase électro-optiques pilotés par un synthétiseur radiofréquence.

Une bobine de fibre monomode standard (SMF) de 10 km a été utilisée comme section dispersive d'entrée du dispositif de dissimulation, avec une dispersion du second ordre totale de 173 ps/nm (correspondant à -222.6 ps^2/rad). La section dispersive de sortie est appariée à l'entrée en concaténant une bobine de fibre de compensation de dispersion, conçue pour compenser la dispersion de 20 km de fibre SMF à la longueur d'onde de travail, avec une bobine SMF supplémentaire de 10 km. Ces valeurs de dispersion satisfont

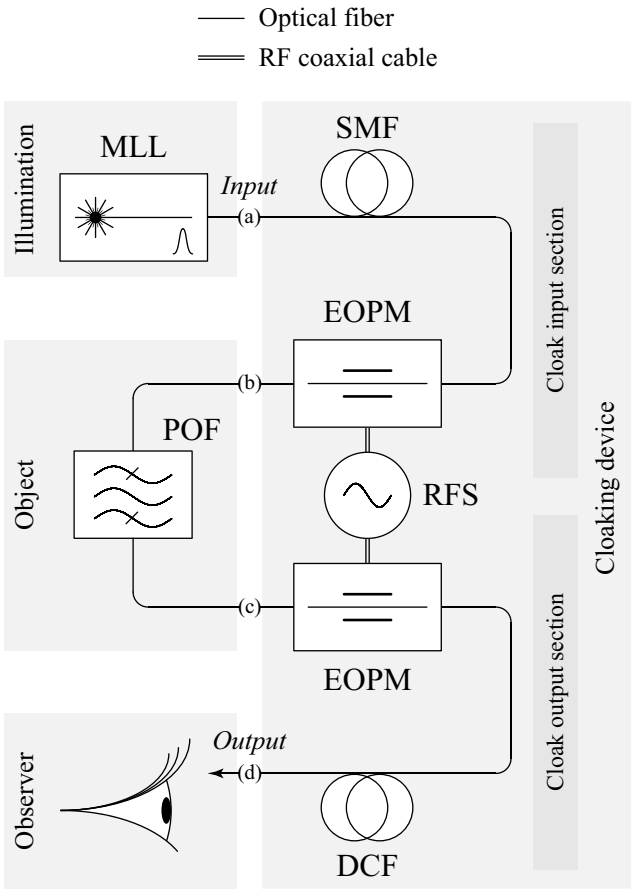

Figure 0.12 – Dissimulation par invisibilité spectrale, configuration expérimentale. MLL, laser à verrouillage de modes; SMF, fibre monomode; EOPM, modulateur de phase électro-optique; RFS, synthétiseur radiofréquence; POF, filtre optique programmable; DCF, fibre à compensation de dispersion.

la condition de Talbot souhaitée pour $\nu_r = 19$ GHz et $r^{-1} = 2$ (voir Eq. 14). Notez que cette valeur de ν_r est 76 fois plus élevée que le taux de répétition du laser d'illumination; en tant que tel, le taux de répétition d'illumination ne satisfait manifestement pas la condition de Talbot pour la dispersion fournie par le dispositif de dissimulation. De plus, cette quantité de dispersion est insuffisante pour induire une interférence entre deux impulsions consécutives quelconques, assurant ainsi l'absence d'interaction entre les impulsions entrantes dans le système.

Les deux modulateurs de phase électro-optiques sont pilotés par une sinusoïde à 19 GHz générée par le synthétiseur radiofréquence. La tension de pilotage générée correspond à une approximation de premier ordre de la séquence de phase de Talbot $r^{-1} = 2$. L'alignement du signal de tension de pilotage sur le signal optique est réalisé par une ligne à retard optique accordable. Des contrôleurs de polarisation sont utilisés à l'entrée de chaque modulateur afin de maximiser l'efficacité de la modulation. Deux amplificateurs radiofréquences sont utilisés pour amplifier la sortie du synthétiseur avant chaque étage de modulation, afin d'adapter le signal radiofréquence à la tension demi-onde des modulateurs de phase. La figure 0.13 montre une mesure de la tension de pilotage de modulation de phase, avec la mesure de l'impulsion dispersée à laquelle elle est appliquée dans le dispositif de dissimulation.

L'objet à dissimuler (caractérisation du domaine fréquentiel représenté sur Fig. 0.14) est un filtre optique programmable, programmé pour avoir une réponse en fréquence linéaire consistant en un ensemble de résonances espacées de 38 GHz, chacune avec une largeur à 3 dB de 17.5 GHz.

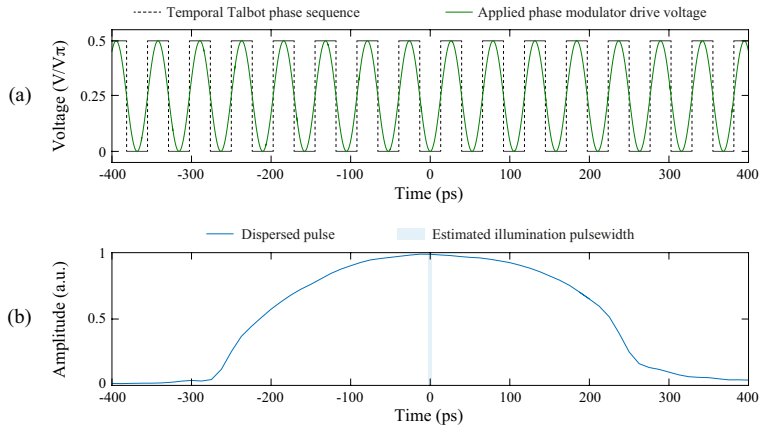

Figure 0.13 – Modulation de phase et propagation de l'impulsion à travers le dispositif d'invisibilité spectrale. (a) Profil périodique de la phase de Talbot temporel associé à une condition de Talbot avec $r^{-1} = 2$. V_π représente la tension demi-onde du modulateur de phase électro-optique. (ligne pointillée) Phase prescrite obtenue à partir de la théorie de l'effet Talbot. (ligne continue) Tension (mesurée) de commande du modulateur de phase utilisée dans les expériences, se rapprochant de la phase de Talbot en utilisant une composante à une seule fréquence. (b) Trace d'amplitude temporelle photo-détectée de l'impulsion dispersée, représentée par rapport à la durée estimée de 1.4 ps de l'impulsion d'illumination d'origine, mesurée par un oscilloscope en temps réel avec 28 Gsa/s équipé d'une photodiode de 43 GHz.

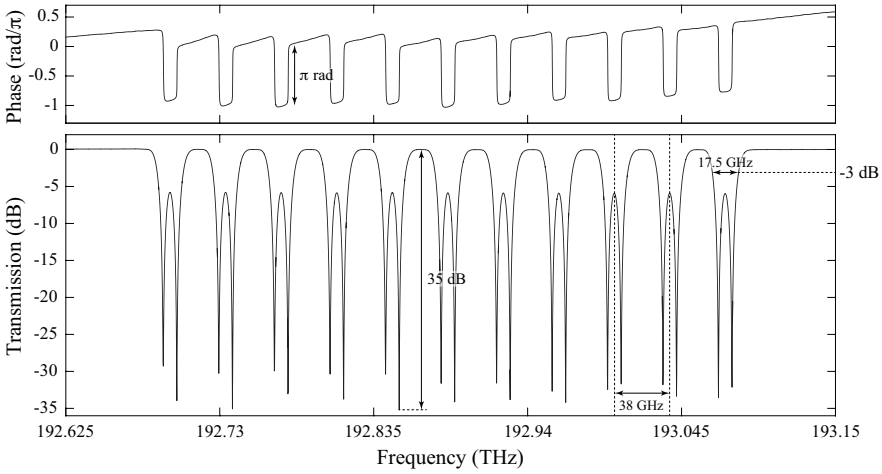

Figure 0.14 – L'Objet de test utilisé dans la démonstration expérimentale d'invisibilité par dissimulation spectrale. Phase (en haut) et amplitude en échelle logarithmique des profils spectraux de transmission (en bas) du filtre optique linéaire, utilisé comme objet à dissimuler dans la démonstration expérimentale d'invisibilité par dissimulation spectrale. Les mesures sont effectuées avec un analyseur de vecteur optique avec une résolution en fréquence de 200 MHz.

0.9.1.3 Résultats expérimentaux

Fig. 0.15 montre un ensemble de mesures spectrales des ondes impliquées dans le processus de dissimulation spectrale. Ces mesures ont été effectuées par un analyseur de spectre optique avec une résolution de 2 GHz.

Fig. 0.15(a) montre le spectre de l'onde d'illumination à large bande cohérente. La signature d'amplitude spectrale de l'objet est clairement observée sur Fig. 0.15(b), lorsque les modulateurs de phase ne sont pas pilotés (dissimulation désactivée). Lorsque la dissimulation est activée, cette configuration produit l'ensemble attendu d'ouvertures dans le spectre d'illumination. Ces bandes ont une largeur de $\Delta\nu_g = 19$ GHz, et une période spectrale $\nu_c = 38$ GHz (Fig. 0.15(c)). On notera qu'une augmentation de 3 dB de l'intensité de crête – correspondant à un facteur linéaire de $\sim$2 – est observée dans le spectre, en accord avec la conservation d'énergie attendue, à partir du paramètre r^{-1}.

La présence des ouvertures dans le spectre d'illumination permet à l'onde de se propager à travers le filtre (Fig. 0.15(d)) sans interagir avec lui. Dans cette situation, un observateur surveillant le spectre de sortie détectera l'onde d'illumination originale exacte, comme si l'objet n'était pas présent (Figs. 0.15(e) et (f)).

Figure 0.15 – Invisibilité par dissimulation spectrale, résultats expérimentaux, domaine fréquentiel. Spectres de puissance optique mesurés des ondes impliquées, normalisés au maximum de l'intensité spectrale d'illumination, illustrant les transformations mises en œuvre pour la génération et l'inversion des ouvertures de fréquence. Le spectre de transmission de l'objet à dissimuler (caractérisation complète sur Fig. 0.14)) est montré à titre de référence. Les points de mesure, comme marqués sur Fig. 0.12, sont indiqués. (a) Spectre d'illumination (Fig. 0.12(a)). (b) Signature d'amplitude spectrale de l'objet, détectée sur l'onde d'illumination lorsque les transformations ne sont pas appliquées (Fig. 0.12(d)). (c) Les ouvertures de fréquence induites dans l'onde d'illumination lorsque les transformations sont appliquées (Fig. 0.12(b)). (d) Réponse spectrale de l'objet inséré dans les ouvertures de fréquence (Fig. 0.12(c)). (e) Effet de la dissimulation spectrale sur le spectre d'illumination de sortie en l'absence de l'objet (Fig. 0.12(d)). (f) Spectre de sortie mesuré lorsque l'objet est présent et que la dissimulation est activée, montrant la prévention de l'interaction onde-objet, et la dissimulation résultante de l'objet (Fig. 0.12(d)). Les ondulations résiduelles sur le spectre restauré sont attribuées au fait que les résonances de l'objet sont légèrement plus larges que les ouvertures de fréquence générés.

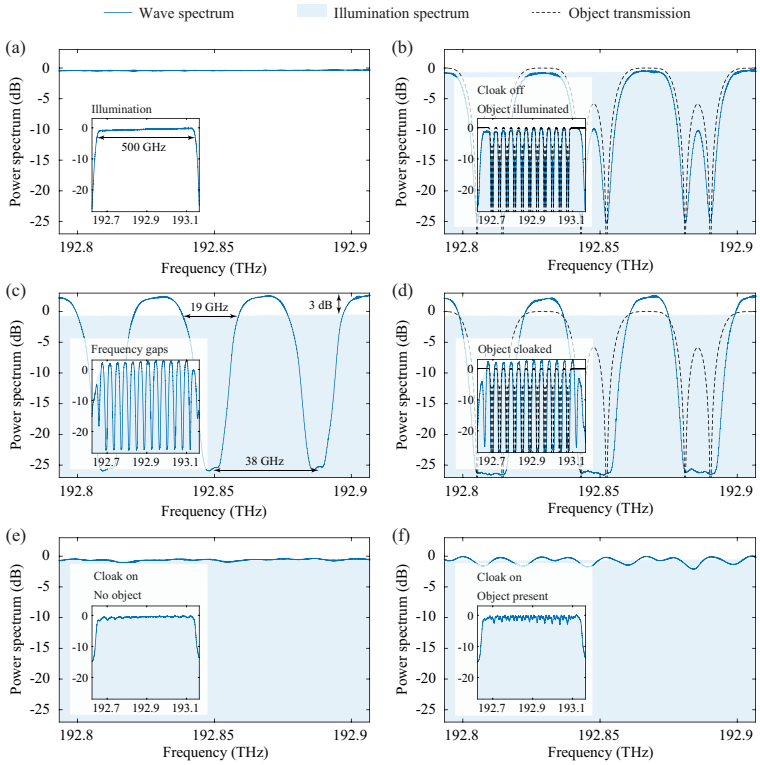

Afin de démontrer que le dispositif de dissimulation spectrale préserve l'onde d'illumination originale exacte, en amplitude et en phase, des mesures temporelles de l'onde de propagation à l'entrée et à la sortie du dispositif sont effectuées (Fig. 0.16).

Figure 0.16 – Invisibilité par dissimulation spectrale, résultats expérimentaux, autocorrélation temporelle. Traces d'autocorrélation temporelle mesurées des ondes impliquées. Les points de mesure, comme marqués sur Fig. 0.12, sont indiqués. (a) Trace d'autocorrélation de l'onde d'illumination (Fig. 0.12(a)), et interpolation numérique de la trace attendue pour une impulsion limitée par la transformée de Fourier (c'est-à-dire avec un profil de phase spectral constant). (b) Signature temporelle de l'objet lorsque la dissimulation est désactivée (Fig. 0.12 (d)). (c) Trace d'autocorrélation de l'onde à la sortie quand l'objet est absent (Fig. 0.12 (d)). (d) Trace d'autocorrélation lorsque l'objet est présent et que la dissimulation est activée (Fig. 0.12(d)), montrant une dissimulation réussie de l'objet.

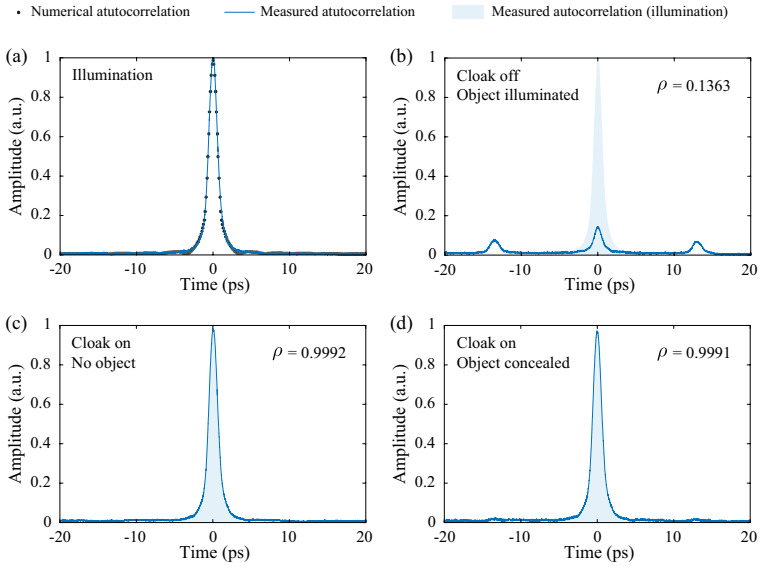

Fig. 0.16(a) montre l'autocorrélation mesurée de l'impulsion d'illumination. Cette courbe est comparée à l'autocorrélation attendue, calculée à partir du spectre d'illumination mesuré, en supposant un profil de phase spectrale uniforme. Le bon accord entre les deux courbes suggère que l'impulsion d'illumination est limitée par transformée de Fourier [2]

Lorsque la dissimulation est désactivée, l'autocorrélation de sortie mesurée est significativement déformée, révélant la signature de l'objet dans le domaine temporel (Fig. 0.16(b)). En revanche, l'onde se propage sans distorsion observable lorsque la dissimulation est activée, que l'objet soit présent ou non (Figs. 0.16(c) et (d)).

Pour quantifier la similarité entre les courbes d'autocorrélation mesurées des ondes d'illumination et de sortie, on calcule leur coefficient d'inter-corrélation, ρ. Le coefficient d'inter-corrélation obtenu entre l'onde d'illumination et les ondes à la sortie du dispositif de dissimulation est supérieur à $0,999$, indépendamment de la présence de l'objet (Figs. 0.16(c) et (d)).

0.9.2 Compression spectrale préservant la forme d'onde des signaux de données pulsés

Les concepts de redistribution d'énergie spectrale proposés - en particulier, les transformations d'onde du MTSCP - peuvent être exploités pour comprimer le spectre d'une séquence d'impulsions courtes arbitraires (par exemple, aléatoires) modulées en données, sans altérer la forme temporelle – y compris la durée temporelle – de ses impulsions constitutives. Comme les opérations agissent seulement sur la phase des signaux impliquées, un tel processus serait entièrement réversible, de sorte que le signal original pourrait être récupéré sans aucune perte d'information (y compris la récupération complète de la forme d'onde de données pulsée).

Une telle méthode de compression spectrale des signaux de données, avec préservation d'énergie, pourrait trouver une application immédiate dans le multiplexage des signaux dans le domaine fréquentiel, tout en conservant de courtes impulsions temporelles combinant ainsi l'efficacité spectrale et le bon fonctionnement des systèmes de multiplexage par répartition en fréquence avec les avantages de la transmission de données à impulsions courtes, notamment, la performance, la robustesse, et la polyvalence, typique des systèmes de multiplexage par répartition dans le temps.

0.9.2.1 Principe de fonctionnement

Le processus de compression spectrale avec préservation de la forme d'onde proposé dans cette thèse est similaire au concept d'invisibilité par dissimulation spectrale expliqué précédemment, avec la particularité que la fréquence du signal d'entrée, dans ce cas, satisfait à la condition de Talbot, comme dans la formulation originale du MTSCP appliquée aux peignes de fréquence. Dans cette situation, l'apériodicité temporelle introduite par la séquence de modulation – données – produit un spectre continu où des écarts de fréquence peuvent être générés, suivant une méthodologie identique à celle introduite dans la Section 0.9.1.1 pour la mise en œuvre de l'invisibilité spectrale. De manière similaire à l'implémentation de la dissimulation spectrale, l'inversion des transformations MTSCP restaure complètement le signal d'entrée d'origine. Fig. 0.17 illustre le concept.

Le cas considéré ici est celui d'une séquence d'impulsions de durée Δt modulée par des données. Ces séquences sont obtenues par modulation temporelle en amplitude et / ou en phase d'un train d'impulsions

[2] Une impulsion limitée par transformée de Fourier a des distributions de phase temporelle et spectrale linéaires et donc sa durée temporelle est la plus courte possible, compte tenu de sa bande passante.

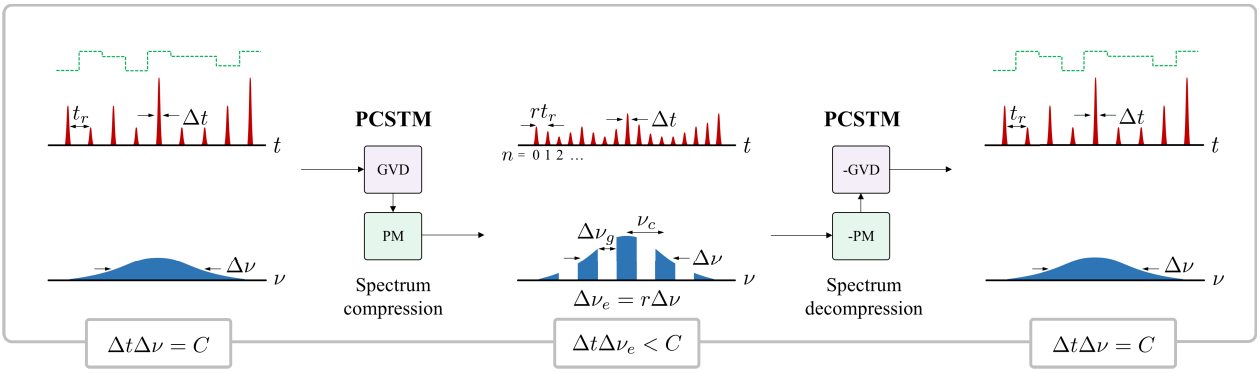

Figure 0.17 – Compression spectrale préservant la forme d'onde des séquences d'impulsions modulées Illustration du concept proposé pour surmonter la contrainte d'étalement du spectre d'une séquence d'impulsions arbitrairement modulée par les données (avec un produit temps-bande passante donné par C) grâce à des transformations linéaires réversibles en phase uniquement (dans l'exemple représenté, GVD: dispersion de vitesse de groupe de second ordre, PM: modulation de phase temporelle quadratique). De telles transformations de phase agissent sur la totalité de la séquence d'impulsions, plutôt que sur des impulsions individuelles. Le résultat est la compression souhaitée de la bande passante totale occupée, tout en conservant la forme d'impulsion individuelle originale: la largeur spectrale globale reste inchangée, mais des ouvertures fréquentiels périodiques sont introduites dans le spectre, réduisant la bande passante occupée effective (et atteignant un produit effectif temps-bande passante inférieur à celui du signal pulsé d'origine, sans modifier la largeur d'impulsion d'origine). La forme d'onde du signal de données original peut être entièrement récupérée par application des transformations de phase linéaire inversée (-GVD, -PM).

périodique, par des données choisies arbitrairement. Le taux de symbole, ν_r, est défini par la période d'impulsion de la séquence, $t_r = \nu_r^{-1}$. Dans le domaine fréquentiel, suite à un tel processus de modulation, la séquence de données résultante présente un spectre d'énergie continu sur toute la largeur de bande de fréquence, $\Delta\nu$, des impulsions courtes dans la séquence. En supposant des impulsions limitées par transformée de Fourier, la relation entre la durée d'impulsion temporelle et la bande passante en fréquence est donnée par le produit temps-bande passante (TBP), $\Delta t\Delta\nu = C$, pour une constante C dépendant de l'enveloppe temporelle des impulsions.

Le processus de compression spectrale consiste en l'application des transformations de phase spectrale et temporelle définies par la MTSCP (avec une valeur entière de $r^{-1} = q_2$) à la séquence d'impulsions modulées en entrée. Ces transformations sont identiques à celles données dans Eqs. 14 et 15, où, dans ce cas, t_r n'est plus une constante arbitraire, mais plutôt fixé par le débit de symbole du signal d'intérêt, de manière similaire à la formulation originale de la MTSCP pour les peignes de fréquence. Le signal obtenu après propagation à travers le milieu à GVD, tel que défini dans Eq. 14, est un train d'impulsions avec une période de répétition $q_2^{-1}t_r$, où les impulsions individuelles conservent leur profil temporel d'origine, y compris la largeur d'impulsion Δt. L'application ultérieure de la séquence de modulation de phase temporelle définie dans Eq. 15 entraîne la génération d'un ensemble périodique d'ouvertures dans le spectre de fréquence continu du signal, avec une période spectrale ν_c et une bande passante $\Delta\nu_g$, donné par, Eqs. 16 et 17, respectivement. Ceci produit une compression de la gamme de fréquence globale occupée par la séquence d'impulsions modulée, réduisant la bande passante effective de la séquence à,

$$\Delta\nu_e = r\Delta\nu \tag{18}$$

tandis que l'enveloppe spectrale conserve sa forme et sa largeur d'origine, $\Delta\nu$.

En conséquence, la TBP effective de la séquence de sortie est réduite par rapport à l'entrée, et plus précisément, la relation d'incertitude pour la bande passante occupée effective s'écrit,

$$\Delta t \Delta \nu_e = rC \tag{19}$$

Enfin, l'application des transformations de phase opposées (-PM et -GVD) restaure la séquence d'impulsions de données à son état d'origine exact dans les domaines temporel et fréquentiel.

0.9.2.2 Configuration expérimentale

Fig. 0.18 montre un schéma simplifié de la configuration expérimentale utilisée pour valider le concept de compression spectrale avec préservation de la forme d'onde.

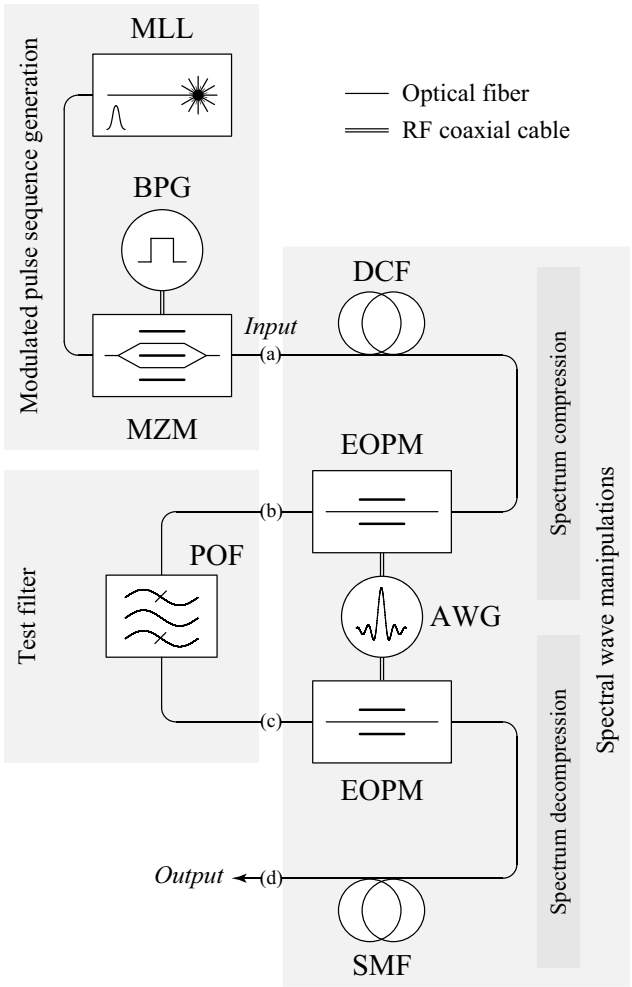

Figure 0.18 – Compression spectrale préservant la forme d'onde, configuration expérimentale. MLL, laser à verrouillage de modes; BPG, générateur de trames binaires; MZM, modulateur Mach-Zehnder; DCF, fibre de compensation de dispersion; EOPM, modulateur de phase électro-optique; AWG, générateur de forme d'onde arbitraire; POF, filtre optique programmable; SMF, fibre optique monomode.

Un laser à verrouillage de modes génère des impulsions optiques à un taux de répétition de $\nu_r = 9.45$ GHz (période de répétition des impulsions $t_r = 105.82$ ps), à une fréquence centrale de 193.4 THz (correspondant à une longueur d'onde centrale de 1551.2 nm). Ces impulsions ont une largeur temporelle à mi-hauteur de $\Delta t = 2.58$ ps. Le spectre associé est un peigne de fréquence avec un FSR ν_r, et une largeur spectrale à 3 dB $\Delta\nu = 126.2$ GHz. Le TBP estimé est $\sim$0.326, proche de la valeur attendue de $C \simeq 0.315$ pour les impulsions sech^2 limitées par transformée de Fourier.

Un modulateur Mach-Zehnder électro-optique est utilisé pour moduler en amplitude le train d'impulsions avec une séquence binaire (0/1) pseudo-aléatoire (PRBS, pour 'pseudo-random bit sequence' en anglais) $2^7 - 1$, générée par un générateur de trames à 12 Gb/s. Cette modulation génère un signal de données RZ.

Le milieu dispersif d'entrée du compresseur spectral est un tronçon de fibre compensatrice de dispersion, fournissant une dispersion totale du second ordre de -349.5 ps/nm à la longueur d'onde de travail. Cela correspond à une valeur de $\beta_2 z = 446.5$ ps^2/rad, satisfaisant la condition temporelle de Talbot requise pour les valeurs de ν_r GHz et $r^{-1} = 4$ (voir Eq. 14). À la longueur d'onde de travail, cela correspond à la dispersion opposée d'environ 20 km de fibre mono-mode standard, qui est utilisée comme milieu dispersif de sortie du décompresseur spectral.

Deux modulateurs de phase électro-optiques à 40 GHz de bande passante sont utilisés pour introduire les phases temporelles de Talbot requises aux signaux optiques dispersés. Un générateur de forme d'onde arbitraire de 50 Gsa/s avec une bande passante analogique de 14 GHz génère un signal de tension avec le profil temporel requis, représenté sur Fig. 0.19.

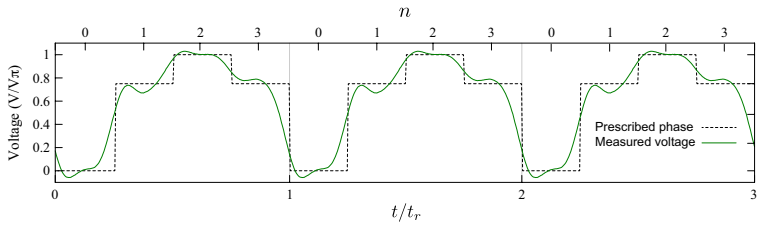

Figure 0.19 – Fonction de modulation de phase pour la compression spectrale préservant la forme d'onde. Profil périodique de phase de Talbot temporel associé à une condition de Talbot avec $r^{-1} = 4$. V_π représente la tension demi-onde du modulateur de phase électro-optique. (ligne pointillée) Phase prescrite obtenue à partir de la théorie d'effet Talbot. (ligne continue) Tension de commande (mesurée) du modulateur de phase utilisée dans les expériences.

Un filtre optique programmable est utilisé pour vérifier que les intervalles de fréquence générés ne contiennent pas d'énergie significative.

0.9.2.3 Résultats expérimentaux

Fig. 0.20 compile les résultats d'une expérience où le concept de compression spectrale préservant la forme d'onde est validé.

Fig. 0.20(a.1) montre les spectres du peigne de fréquence initial et du signal de données RZ modulé, ainsi que l'enveloppe de son spectre de puissance. Comme prévu, le spectre du signal modulé est un continuum sur toute la largeur de bande de fréquence des impulsions individuelles, avec des composantes d'horloge discrètes aux fréquences des lignes de peigne d'origine. La représentation correspondante du domaine temporel est montrée dans Fig. 0.20(a.2), y compris le train d'impulsions modulé, son diagramme de l'oeil [3], et le détail d'une impulsion unique de la séquence. Comme prévu, le spectre et le profil de puissance instantané correspondent à une forme d'impulsion sech^2 limitée par transformée de Fourier, en bon accord avec la valeur du TBP estimée ci-dessus.

La figure 0.20(b.1) montre le spectre résultant du processus de génération d'ouvertures (c'est-à-dire, après GVD et PM). Comme prévu, la période entre ouvertures de fréquence obtenue est $\nu_c = 37.8$ GHz, ce qui correspond à la suppression de 3 sur 4 composantes d'horloge (lignes de peigne d'origine), en accord avec la valeur de $r^{-1} = 4$. Fig. 0.20(b.2) montre que la séquence d'impulsions d'origine est répartie en

[3] Le diagramme de l'oeil d'un signal de données numériques est une superposition des intervalles de symboles – périodes – de la séquence, enregistrés sur une période de temps suffisamment longue. Cette représentation est un outil puissant pour l'évaluation des effets combinés du bruit et des interférences inter-symbols, puisqu'elle contient une combinaison de toutes les réalisations possibles de la séquence de modulation numérique.

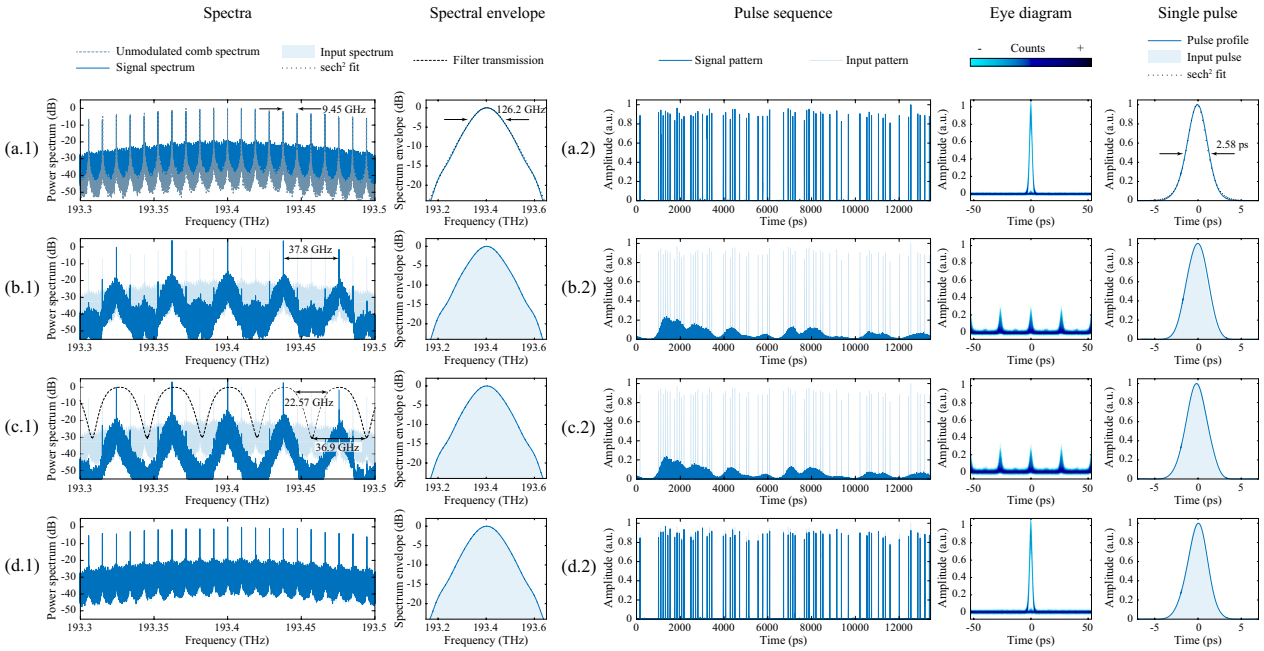

Figure 0.20 – Compression spectrale préservant la forme d'onde, résultats expérimentaux. Génération d'ouvertures de fréquence dans une séquence d'impulsions optiques courtes avec modulation d'intensité binaire (on-off-keying, OOK). Les points de mesure, comme marqués sur la figure 0.18, sont indiqués. (a.1) Spectre de la séquence d'origine, obtenu par modulation d'amplitude directe d'un train d'impulsions optiques répétitif ou d'un peigne de fréquence optique périodique (illustré à titre de référence) avec un PRBS binaire $2^7 - 1$ (Fig. 0.18(a)). (a.2) Profil temporel, diagramme de l'œil, et détail d'une seule impulsion de la séquence originale (Fig. 0.18(a)). (b.1) Spectre, et (b.2) profil temporel, diagramme de l'œil, et détail d'impulsion unique de la séquence après l'application du processus de compression spectrale (Fig. 0.18(b)). L'enveloppe spectrale globale et la forme d'impulsion temporelle – y compris la durée – restent inchangées, tandis que des ouvertures périodiques de fréquence sont induits dans la séquence. (c.1), (c.2) Un filtre périodique coupe-bande est introduit dans les intervalles de fréquence à des fins de test (Fig. 0.18(c)). En raison du mécanisme de redistribution de l'énergie donnant lieu aux ouvertures de fréquence, la séquence temporelle n'est pas affectée par le filtre, un résultat qui confirme que les espaces créés ne contiennent aucune information. (d.1), (d.2) Séquence de sortie après l'application des transformations de phase inverse, fermant les ouvertures de fréquence et ramenant la séquence de données temporelle modulée à son état d'origine exact (Fig. 0.18(c)).

un plus grand nombre d'impulsions courtes, avec un taux de répétition équivalent augmenté 4-fois par rapport à l'entrée (voir diagramme de l'œil sur Fig. 0.20(b.2)). Les impulsions obtenues conservent la largeur temporelle et la forme globale (voir le détail d'une impulsion unique sur Fig. 0.20(b.2)).

Afin de confirmer la capacité de compression spectrale du procédé, un filtre optique linéaire de test est introduit. Sa réponse en fréquence consiste en un ensemble de bandes coupées, avec une période spectrale $\nu_T = 36.9$ GHz (proche de ν_c), qui se chevauchent avec les ouvertures de fréquence générés (voir les spectres mesurés dans Fig. 0.20(c.1)). La bande passante à 3 dB de chacune des bandes coupées est $\Delta\nu_T = 22.57$ GHz. En raison de la présence des ouvertures de fréquence, le signal se propage à travers le filtre sans interagir avec lui, et la forme d'onde temporelle reste entièrement inchangée (voir mesures dans le domaine temporel dans Fig. 0.20(c.2)). Ceci démontre que la bande passante effective du signal modulé a été compressée, au moins, par un facteur $\nu_T^{-1}\Delta\nu_T = 0.612$; en d'autres termes, plus de 60% du spectre de fréquences occupé par le signal de données d'entrée a été libéré, tout en maintenant la forme temporelle originale des impulsions dans la séquence. Il est à noter que, idéalement, pour la valeur calculée de $r^{-1} = 4$, la compression spectrale attendue devrait atteindre 75%; cependant, des imperfections pratiques dans la mise en œuvre de la modulation de phase (limitée par la bande passante électronique disponible) et de la dispersion (associées à de faibles écarts de longueur de fibre par rapport à l'idéal) conduisent à une suppression impar-

faite de l'énergie du signal dans les ouvertures spectrales, jusqu'à $\sim$20 dB dans les expériences rapportées ici.

Enfin, l'application du profil de modulation de phase temporelle inverse et la propagation à travers une fibre optique avec une valeur de GVD inverse restituent le signal de données à son état original exact (y compris le profil de modulation de données original), à la fois dans les domaines fréquentiels et temporels (voir Figs. 0.20(d.1) et (d.2), respectivement).

0.10 Conclusion

L'effet Talbot – ou auto-imagerie – est observé lorsqu'un objet ou une onde périodique est affecté par un propagateur imposant une variation de phase à travers sa représentation dans le domaine de Fourier (par exemple, le spectre discret de fréquence d'un signal temporel périodique) avec une dépendance quadratique spécifique avec la variable correspondante dans le domaine de Fourier. Le phénomène, rapporté initialement dans le régime de diffraction de Fresnel des ondes optiques paraxiales, a été observé indépendamment dans les domaines temporel, spectral, et angulaire de l'optique ondulatoire, ainsi qu'à travers différents systèmes d'ondes tels que les ondes de matière et les fonctions quantiques.

Dans cette thèse de doctorat, une description générale de l'effet Talbot a été rapportée, unifiant toutes les manifestations du phénomène dans un cadre mathématique unique. Un tel formalisme décrit le phénomène en termes de distributions de phase des ondes impliquées dans n'importe quelle paire de variables de Fourier-conjuguées, avec une indépendance du domaine d'observation (par exemple, temps / fréquence, position / moment, etc.). La possibilité de calculer des phases de Talbot dans des domaines réciproques de Fourier a permis la formulation d'une méthode de transformation d'onde générale pour transformer une onde périodique originale en une nouvelle onde, où la nouvelle période peut être fixée arbitrairement. De plus, comme la méthode n'implique que des transformations des distributions de la phase de l'onde, tout son contenu énergétique est préservé dans le processus.

Des cas particulièrement intéressants de formes d'onde périodiques sont des trains d'impulsions optiques et leur contrepartie spectrale, des peignes de fréquence optique. Ces signaux trouvent une application étendue dans une multitude de domaines de la science et de l'ingénierie, dans certains cas, devenant le facteur essentiel permettant de progrès technologiques importants. La période de répétition de tels signaux est un facteur clé pour leur utilisation dans différentes applications. La méthodologie de contrôle universelle de périodicité rapportée est une solution de traitement de signal attrayante à la manipulation arbitraire de signaux périodiques, offrant une grande flexibilité dans la conception de la période de sortie désirée, en plus de la caractéristique intéressante de préserver potentiellement l'énergie du signal à traiter. Ceci est en fort contraste avec les méthodes conventionnelles basées sur la modulation d'amplitude directe et le filtrage d'amplitude, où une grande quantité d'énergie est délibérément rejetée dans le processus, affectant négativement les caractéristiques de bruit du signal. En outre, dans ces méthodes, seule la multiplication/division par des facteurs entiers est accessible.

De plus, des phénomènes intéressants apparaissent dans les spectres des ondes temporelles apériodiques (p. ex, impulsions optiques isolées et séquences d'impulsions modulées par les données) lorsqu'ils sont traités par les mêmes méthodes de transformation d'ondes que celles décrites dans cette thèse, avec des applications potentielles à l'invisibilité par dissimulation optique et à la compression spectrale préservant la forme d'onde des signaux de données pulsés.

En conclusion générale, compte tenu de la large gamme d'applications de signaux optiques périodiques temporels et spectraux (trains d'impulsions et peignes de fréquence), l'intérêt pour les méthodes présentées

dans cette thèse peut être prévu, grâce à leur grande flexibilité et leur efficacité énergétique. En outre, ce projet pourrait inspirer le développement de nouvelles applications qui tireraient profit des stratégies de redistribution de l'énergie pour concevoir des systèmes et des techniques de traitement du signal. Par exemple, des méthodes d'atténuation du bruit de signaux arbitraires – non nécessairement périodiques –, basées sur la redistribution de l'énergie, pourraient être envisagées. Enfin, la généralité des transformations d'ondes rapportées rend les méthodes proposées attractives pour l'application aux ondes électromagnétiques sur tout le spectre d'énergie, et même pour des plateformes d'ondes fondamentalement différentes, telles que les ondes de matière, les ondes quantiques, les ondes acoustiques, et les ondes thermiques.

Contents

List of figures

List of tables and code listings

Nomenclature

Accronyms and abbreviations

A

ASE	Amplified spontaneous emission
AWG	Arbitrary waveform generator
AWGN	Additive white Gaussian noise

B

B2B	Back-to-back
BER	Bit error rate
BPG	Bit pattern generator

C

CEO	Carrier-envelope offset
CW	Continuous-wave

D

D	Diffraction
DCF	Dispersion-compensating fiber
DCPS	Direct-current power supply
DEMUX	Demultiplexing

E

EDFA	Erbium-doped fiber amplifier
EOPM	Electro-optical phase modulator
EPA	Error pattern analyzer
ESO	Electrical sampling oscilloscope

F

FDM	Frequency-division multiplexing
FSFL	Frequency-shifted feedback loop
FSR	Free spectral range
FWHM	Full width at half maximum

G

GVD	Group velocity dispersion

L

Laser	Light amplification by stimulated emission of radiation
Lidar	Light detection and ranging
LSI	Linear and shift-invariant
LTI	Linear and time-invariant

M

MIMO Multiple-input multiple-output

MLL Mode-locked laser

MUX Multiplexing

MZM Mach-Zehnder modulator

N

NLSE Nonlinear Schrödinger equation

NRZ Nonreturn-to-zero

O

OAC Optical autocorrelator

OSA Optical spectrum analyzer

OSNR Optical signal-to-noise ratio

OSO Optical sampling oscilloscope

OTDL Optical tunable delay line

OTDM Optical time-division multiplexing

P

PC Polarization controller

PCSTM Phase-controlled spectral Talbot method

PCTTM Phase-controlled temporal Talbot method

PD Photodiode

PM Phase modulation

POF Programmable optical filter

PRBS Pseudo-random binary sequence

PROUD Phase reconstruction through optical ultrafast differentiation

PUT Process under test

Q

QAM Quadrature amplitude modulation

R

Radar Radio detection and ranging

RF Radio-frequency

RFA Radio-frequency amplifier

RFa Radio-frequency attenuator

RFPD Radio-frequency power divider

RFS Radio-frequency synthesizer

RFSA Radio-frequency spectrum analyzer

RZ Return-to-zero

S

S-PROUD Spectral phase reconstruction through optical ultrafast differentiation

S-TAI Spectral Talbot array illuminator

SM Spatial modulator

SMF Single-mode fiber

SNR Signal-to-noise ratio

SPF Spectral phase filtering

SSI Spectral self-imaging

SUT Signal under test

T

T-TAI Temporal Talbot array illuminator

TAI Talbot array illuminator

TBP Time-bandwidth product

TDM Time-division multiplexing

TM Temporal modulation

TPM Temporal phase modulation

TSI Temporal self-imaging

V

VOA Variable optical attenuator

W

WDM Wavelength-division multiplexing

Y

YC Y-coupler

Symbols

Units are specified in brackets where applicable (see system of units below).

Wave representation domains

u Real space

U Fourier space (Fourier conjugate of u)

$x\ y\ z$ Space (m)

$\hat{\mathbf{x}}\ \hat{\mathbf{y}}\ \hat{\mathbf{z}}$ Space base

$k_x\ k_y\ k_z$ Momentum (m^{-1}rad)

$\theta_x\ \theta_y\ \theta_z$ Angular spectrum (rad)

t Time (s)

ω Radial frequency (s^{-1}rad)

ν Linear frequency (Hz)

λ Wavelength (m)

Wave parameters

c Speed of light ($\mathrm{s}^{-1}\mathrm{m}$)

c_0 Speed of light in the vacuum ($\mathrm{s}^{-1}\mathrm{m}$)

n Refractive index

$\mathbf{r}$ Position vector (m)

$\mathbf{k}$ Wavevector (m^{-1}rad)

$\hbar$ Wavenumber (m^{-1}rad)

α Attenuation coefficient (m^{-1})

β Propagation constant (m^{-1})

β_l l-th order dispersion coefficient ($\mathrm{m}^{-1}\mathrm{rad}^{-1}\mathrm{s}^{l}$)

γ Nonlinear parameter ($\mathrm{W}^{-1}\mathrm{m}^{-1}$)

L_D Dispersion length (m)

t_g Group delay (s)

v_g Group velocity ($\mathrm{s}^{-1}\mathrm{m}$)

$\hbar(t)$ Time-domain wave operator

$\mathscr{H}(\omega)$ Radial frequency-domain wave operator

$\mathscr{H}(\nu)$ Linear frequency-domain wave operator

σ_t Full temporal width at height e^{-1} (s)

σ_ω Full spectral width at height e^{-1} (s^{-1}rad)

Δt Full width at half-maximum pulse duration (s)

$\Delta\nu$ 3-dB linear frequency bandwidth (Hz)

C Transform-limited time-bandwidth product

P_t Time-domain peak power (W)

P_ν Frequency-domain peak power (W)

Periodic signal parameters

u_r Real space period (arbitrary domain)

U_r Fourier space period (arbitrary domain)

$x_r\ y_r$ Transverse spatial period (m)

t_r Temporal period (s)

ω_r Radial frequency spectral period (s^{-1}rad)

ν_r Linear frequency spectral (Hz)

n Pulse number in a pulse train

k Line number in a frequency comb

c_k Fourier series coefficient (k-th harmonic)

η Comb line visibility

τ_c Duty cycle

E_p Energy per pulse (J)

P_{avg} Average power (W)

Experimental parameters

V_π Modulator half-wave voltage (V)

β_2 Second-order dispersion in ω ($\text{rad}^{-1}\text{ps}^2$)

D Second-order dispersion in λ (m^{-2}s)

ν_T Test filter spectral period (Hz)

$\Delta\nu_T$ Test filter 3-dB bandwidth (Hz)

Q Eye diagram quality factor

ν_c S-TAI spectral period (Hz)

$\Delta\nu_g$ Frequency gap 3-dB bandwidth (Hz)

ν_0 FSFL seed frequency (Hz)

L_c FSFL cavity length (m)

t_c FSFL cavity round-trip time (s)

ν_c FSFL cavity round-trip frequency (Hz)

ν_s FSFL shifting frequency (Hz)

Talbot effect parameters

z_{T} Talbot length (m)

θ Talbot condition parameter

ς Sign of the Talbot condition parameter

p Real-space Talbot condition numerator

q Real-space Talbot condition denominator

s Fourier-space Talbot condition numerator

m Fourier-space Talbot condition denominator

c Fourier-space Talbot condition constant

r Real-space period multiplication factor

r^{-1} Fourier-space period multiplication factor

$\phi_{k;p,q}$ Fourier-space Talbot phase sequence (rad)

$\varphi_{n;s,m,c}$ Real-space Talbot phase sequence (rad)

$G_{n;p,q}$ Generalized quadratic Gauss sum

Number sets

$\mathbb{N}$ Natural numbers

$\mathbb{E}$ Even natural numbers

$\mathbb{O}$ Odd natural numbers

$\mathbb{Z}$ Integer numbers

$\mathbb{Q}$ Rational numbers

$\mathbb{R}$ Real numbers

$\mathbb{C}$ Complex numbers

Relation symbols

$=$ Equal to

$\neq$ Not equal to

$:=$ Defined as

$\equiv$ Equivalent to

$\approx$ Approximately equal to

$\in$ Contained in

$\notin$ Not contained in

$\sim$ On the order of

$>$ Greater than

$\gg$ Much greater than

$\geq$ Greater than or equal to

$<$ Less than

$\ll$ Much less than

$\leq$ Less than or equal to

$\Longrightarrow$ Implies

$\Longleftrightarrow$ If and only if

$\pm$ Plus or minus

$\rightarrow$ Function domain

$\leftarrow$ Variable exchange

Statistics

$\mathrm{E}\{\cdot\}$ Expected value

$\mathrm{Var}\{\cdot\}$ Variance

$\mathrm{Cov}\{\cdot,\cdot\}$ Covariance

$\mathrm{CV}\{\cdot\}$ Coefficient of variation

Functions, operations and other symbols

i Imaginary unit

$\cdot^*$ Complex conjugate

$|\cdot|$ Absolute value

$\mathscr{F}\{\cdot\}$ Fourier transform

$\mathscr{F}^{-1}\{\cdot\}$ Inverse Fourier transform

$\cdot * \cdot$ Convolution integral

$\mathrm{d}\cdot$ Differential

$\frac{\mathrm{d}}{\mathrm{d}\cdot}\cdot$ Derivative

$\frac{\partial}{\partial\cdot}\cdot$ Partial derivative

$\int_{\cdot}^{\cdot} \mathrm{d}\cdot$ Integral

$\sum_{\cdot}^{\cdot}$ Summation

$\prod_{\cdot}^{\cdot}$ Product

$\delta(\cdot)$ Dirac's delta

$\nabla^2\cdot$ Laplacian

$\tilde{\nabla}^2\cdot$ Transverse Laplacian

$(\mathrm{mod}\ \cdot)$ Modulo

$\mathrm{sgn}\{\cdot\}$ Sign

$\epsilon_{\cdot}$ Parity

$\left[\frac{1}{\cdot}\right]_{\cdot}$ Modular multiplicative inverse

$\left(\frac{\cdot}{\cdot}\right)$ Jacobi symbol

$\max_{\cdot}\{\cdot\}$ Maximum value

$\min_{\cdot}\{\cdot\}$ Minimum value

$\lfloor\cdot\rfloor$ Floor

ρ Cross-correlation coefficient

System of units

This dissertation uses the international system of units (SI, short for Système International) for mathematical and physical developments, as well as for presentation of numerical and experimental results. The SI is built around seven base units; the most relevant four in this dissertation are the meter (m, unit of length), the second (s, unit of time), the kilogram (kg, equivalent to 1000 grams, g, unit of mass), and the ampere (A, unit of electric current). Other units are defined based upon these fundamental ones, such as the radian (rad, unit of angle, corresponding to $\mathrm{m}\cdot\mathrm{m}^{-1}$), the hertz (Hz, unit of linear frequency, corresponding to s^{-1}), or the volt

(V, unit of voltage or electrical potential, corresponding to $\mathrm{kg{\cdot}m^2{\cdot}s^{-3}{\cdot}A^{-1}}$). A specific prefix can be added to any of such units to change its magnitude by a multiple of 10 factor (so that, for instance, a gigahertz, GHz, corresponds to 10^9 Hz), as follows,

	Prefix name		deca	hecto	kilo	mega	giga	tera	peta	exa	zetta	yotta
Multiples	Prefix symbol		da	h	k	M	G	T	P	E	Z	Y
	Magnitude factor	10^0	10^1	10^2	10^3	10^6	10^9	10^{12}	10^{15}	10^{18}	10^{21}	10^{24}
	Prefix name		deci	centi	milli	micro	nano	pico	femto	atto	zepto	yocto
Submultiples	Prefix symbol		d	c	m	μ	n	p	f	a	z	y
	Magnitude factor	10^0	10^{-1}	10^{-2}	10^{-3}	10^{-6}	10^{-9}	10^{-12}	10^{-15}	10^{-18}	10^{-21}	10^{-24}

Certain magnitudes are characterized by units expressed in relative terms. Relative units can be presented in linear scale, representing the ratio of two magnitudes; e.g., the ratio of the magnitudes A and B, measured in units of a and b, respectively writes,

$$C = \frac{A}{B} \tag{20}$$

where the units of C are $b^{-1}a$. It is often convenient to present such units in logarithmic scale. The base used for logarithmic scale in this representation in this representation is 10, so that,

$$\log_{10}(C) = \log_{10}(A) - \log_{10}(B) \tag{21}$$

If A and B have the same units (i.e., C is adimensional), the magnitude $10\log_{10}(C)$ is measured in decibels (dB).

Absolute units can also be represented in logarithmic scale, referenced to a fixed value. A common example is the dBm, i.e., the amount of power, P (in watts, W, corresponding to $\mathrm{kg{\cdot}m^2{\cdot}s^{-3}}$), relative to 1 mW, represented in base-10 logarithmic scale,

$$P_{\mathrm{dBm}} = 10\log_{10}\left(\frac{P}{1\ \mathrm{mW}}\right) \tag{22}$$

Constants

The following table lists some mathematical and physical constants used throughout this dissertation.

Name	Pi	Euler's number	Speed of light in the vacuum
Symbol	π	e	c_0
SI units			m/s
Definition/Value	$\displaystyle\int_{-1}^{1} \frac{1}{\sqrt{1-\chi^2}}\,\mathrm{d}\chi$	$\displaystyle\lim_{\chi\to\infty}\left(1+\frac{1}{\chi}\right)^{\chi}$	299792458
Approximation	$\sim$3.14159265	$\sim$2.71828183	

Objectives and organization of the thesis

Original contributions

The central point of this Ph.D. dissertation is the unification of the different manifestations of the Talbot effect under a universal mathematical framework. For this purpose, a generalization of the conditions necessary for observation of the Talbot effect in representation domains related by a Fourier transform is introduced (*objective 1*). In particular, the relationship between the spectral and temporal phase functions describing the manifestation of Talbot effects in the domains of time and frequency in periodic signals is established. This will be referred to as the *time-frequency duality* of the Talbot effect. Such mathematical duality provides a powerful tool for calculation of Talbot phases in Fourier-conjugate domains, and it is the foundation of all signal processing methods and phenomena presented in this dissertation.

Based on the proposed time-frequency duality, a general method for tailoring the period of repetitive signals is presented (*objective 2*). This method involves manipulations of the phase profiles of the signal of interest in both its real and Fourier domains. Such a methodology has the following characteristics:

- **It applies to periodic signals in any domain of representation**. It is compatible with any wave platform where basic filtering and modulation operations can be implemented, e.g., for optical waves in the time, frequency, space or transverse momentum domains. This dissertation focuses on the time/frequency picture, particularly, for the technologically relevant case of manipulating the free spectral range (FSR) of optical frequency combs.
- **It allows for arbitrary transformations of the input period**. In particular, the output period is any desired integer or fractional multiple of the input period, that can be either higher or lower than 1.
- **It preserves the entire energy of the input signal**, simply redistributing it to achieve the desired period transformation. This can lead to an effect of amplification of individual signal features without the need for an external energy supply.
- **It does not introduce noise or distortion to the input signal**. This, combined with the previously mentioned passive amplification effect, allows for the de-noising, and even sub-noise detection of signals.

The experimental contributions of this dissertation rely on application of the aforementioned periodicity control model to optical signals in the time and frequency domains, with the purpose of studying interesting

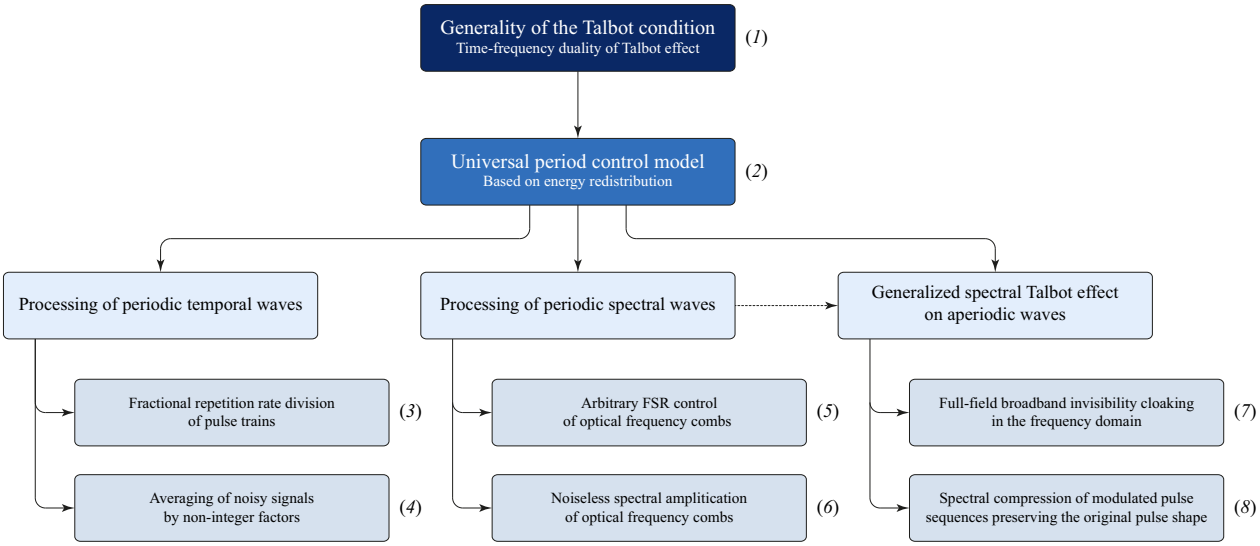

Objectives and original contributions. The numbers next to each box in the diagram correspond to the numbering of the objectives described in the text.

phenomena and proposing practical applications. The method is first showcased in the demonstration of fractional repetition rate division of a train of optical pulses, i.e., the multiplication of its pulse period by a fractional factor higher than 1 (*objective 3*). In this scenario, the properties of the noise in the obtained rate-divided signal are studied (*objective 4*), resulting in a noise reduction by a fractional factor, equivalent to the averaging of a non-integer number of realizations of the process. This interesting result is simply not allowed by the fundamental mathematical definition of statistical averaging of multiple events, essentially involving the sum of a discrete (integer) number of realizations of the process under analysis.

The main focus of the experimental part of this thesis is on the application of the periodicity control model to optical signals in the frequency domain. Arbitrary tailoring of the FSR of a frequency comb is demonstrated (*objective 5*), with potential important implications in the myriad of scientific and applied fields where frequency combs are the enabling technological factor; e.g., high-resolution spectroscopy, high-precision frequency metrology and calibration, waveform shaping, optical communications, etc. Additionally, the impact of the method on the noise content of the combs is studied (*objective 6*), achieving, under certain conditions, output frequency combs with lower noise floor levels than their input counterparts, even allowing for the sub-noise detection of signals in the frequency domain.

Finally, the proposed period control method is applied to aperiodic signals, in order to study its effects on their frequency spectra. It is demonstrated that, under certain conditions, the method has the capability of introducing gaps in the continuous spectrum of an aperiodic signal. This effect is exploited to demonstrate a scheme for invisibility cloaking that preserves the full-field (both amplitude and phase variations) of a broadband wave (*objective 7*). Additionally, when applied to a modulated data signal (e.g., from an optical telecommunications system), the method achieves compression of the signal's spectrum, while preserving the duration and overall shape of its temporal pulses (*objective 8*). This can be understood as a way of globally overcoming the time-bandwidth product limit, imposed by the uncertainty principle of the Fourier transform in data-modulated sequences of pulses (recall that a consequence of the Fourier uncertainty principle states that the product of the temporal and spectral spreads of a signal has a fixed lower bound).

Methodology

The listed objectives are approached with the following strategy:

- *Objectives 1 and 2*: The generality of the Talbot condition, as well as the universal period control model resulting from its formulation, are mathematically developed and numerically validated.
- *Objectives 3 to 8*: The different studied phenomena are mathematically modeled, numerically validated and experimentally demonstrated. In all cases, simplified circuit diagrams of the used experimental setups are provided, with more detailed, complete circuit diagrams in Appendix D.

All numerical simulations are carried out using MATLAB® R2015b.

Layout of the thesis

This Ph.D. thesis is organized in 7 chapters, covering the following topics:

Chapter 1. Introduction and motivation

This chapter introduces the problem addressed in this thesis, as well as the proposed solution. The relevance and importance of periodic signals and objects in the current scientific and technological world is discussed. Special attention is directed towards the particularly interesting case of periodic trains of pulses and frequency combs in the realm of optical waves. The critical importance of controlling and generating periodic temporal and spectral signals is discussed, as well as the limitations and shortcomings of current solutions that address this problem, with special attention to their impact on the noise and overall energy of the signal of interest. The chapter then addresses the general motivation of this dissertation, namely the proposal and demonstration of a universal method for noiseless periodicity control of repetitive waves based on redistributing the energy already carried by the signal of interest. This methodology is aimed at overcoming the drawbacks of the state-of-the-art solutions discussed in the chapter. Special attention is directed towards arbitrary control of spectrally-periodic optical signals, an area of increasing interest due to the high impact of the optical frequency comb in current science and engineering applications.

Chapter 2. Review of linear wave propagation and the Talbot effect

This chapter provides the basic mathematical and physical background used in the developments and discussions along this dissertation. Fundamental concepts of optical wave propagation and basic wave operations are revised, with particular emphasis on the mathematical formalism describing the temporal evolution of optical waves. A brief overview of the theory of Talbot effect is presented, enunciated in the framework of Fourier analysis and signal processing. This interesting phenomenon is at the core of the methods and techniques proposed in this thesis.

Chapter 3. Generalized Talbot effect

This chapter presents a generalization of the Talbot effect, as well as the relationships between its different realizations in all domains of representation of waves. A general definition of the condition leading to observation of the Talbot phenomena is presented. Additionally, the mathematical basis of the universal periodicity control method – central point of this dissertation – is presented. The problem is addressed in the framework of the time/frequency representation of optical signals, corresponding to the experimental demonstrations presented in following chapters. Two equivalent realizations of the method are introduced, discussed and compared. This chapter deals with *objectives 1* and *2*.

Chapter 4. Processing of periodic temporal waves

In this chapter, the universal period control method proposed in chapter 3 is applied to a periodic temporal signal. In particular, energy-preserving division of the repetition rate of a train of optical pulses by fractional factors is demonstrated. Considerations on noise mitigation are described, where the process produces a counter-intuitive effect of noise averaging, equivalent to calculating the mean of a non-integer number of noise contributions. This chapter deals with *objectives 3* and *4*.

Chapter 5. Processing of periodic spectral waves

In this chapter, the universal period control method proposed in chapter 3 is applied to periodic spectral signals – frequency combs – to demonstrate arbitrary, energy-preserving control of their frequency spacing. This feat is relevant to many areas of application of frequency combs. The impact of the method on the noise characteristics of the comb is studied, and results showing noiseless spectral amplification of the comb signal are reported. This chapter deals with *objectives 5* and *6*.

Chapter 6. Generalized spectral Talbot effect on aperiodic waves

The effects of the universal period control method on aperiodic signals are studied in this chapter. The method has the capability to introduce free spectral regions – frequency gaps – to the continuous spectra of aperiodic waves. Two applications are discussed; (i) a method for full-field invisibility cloaking in the frequency domain and, (ii) a method for compressing the spectrum of sequences of modulated pulses (e.g., telecommunication data signals) while preserving the original pulse duration and overall temporal shape. The latter is additionally used as a robust, energy-efficient technique for format conversion of modulated pulse sequences. This chapter deals with *objectives 7* and *8*.

Chapter 7. Conclusion and perspectives

This chapter summarizes the work presented in this dissertation and discusses its potential prospects, as well as tentative paths of future work.

Additional information is provided in 5 appendices, listed A to E:

Appendix A. Review of continuous-variable Fourier analysis

This Appendix provides a brief review of basic concepts of the Fourier transform for functions of continuous independent variables.

Appendix B. Review of Fourier optics and the space-time duality

This Appendix provides a brief summary of the Fourier optics formalism for modeling the paraxial propagation of waves, as well as the space-time duality, a mathematical symmetry between the equations describing paraxial wave propagation and temporal wave evolution.

Appendix C. MATLAB code listings

This Appendix contains the MATLAB code used in the calculation of Fourier-dual Talbot phase profiles.

Appendix D. Detailed circuit schematics

This Appendix contains detailed schematics of the electro-optical circuits used in the experimental demonstration of the systems, techniques and phenomena reported in this dissertation.

Appendix E. Generation of frequency combs with user-defined FSR

This Appendix reports the theoretical foundations and experimental demonstration of a technique for frequency comb generation with user-defined line frequency spacing, based on a realization of phase-controlled Talbot phenomena on a CW-seeded frequency-shifted feedback loop cavity.

Publications by the candidate

Associated publications

The following list includes publications containing the work presented in this dissertation.

Associated publications in peer-reviewed journals

[APj1] L. Romero Cortés, R. Maram, and J. Azaña, "Fractional averaging of repetitive waveforms induced by self-imaging effects," *Phys. Rev. A*, **92**, 041 804(R) (2015).

[APj2] L. Romero Cortés, H. Guillet de Chatellus, and J. Azaña, "On the generality of the Talbot condition for inducing self-imaging effects on periodic objects," *Opt. Lett.*, **41**, 340–343 (2016).

[APj3] L. Romero Cortés, H. Guillet de Chatellus, and J. Azaña, "On the generality of the Talbot condition for inducing self-imaging effects on periodic objects: erratum," *Opt. Lett.*, **41**, 5784–5784 (2016).

[APj4] R. Maram, L. Romero Cortés, J. van Howe, and J. Azaña, "Energy-preserving arbitrary repetition-rate control of periodic pulse trains using temporal Talbot effects," *J. Lightwave Technol.*, **35**, 658–668 (2017). **Invited**.

[APj5] L. Romero Cortés, R. Maram, H. Guillet de Chatellus, and J. Azaña, "Subnoise detection and passive amplification of frequency combs through customized coherent spectral energy redistribution," *Phys. Rev. Applied*, **9**, 064 017 (2018).

[APj6] L. Romero Cortés, M. Seghilani, R. Maram, and J. Azaña, "Full-field broadband invisibility through reversible wave frequency-spectrum control," *Optica*, **5**, 779–786 (2018). **Selected for OSA news release**.

[APj7] H. Guillet de Chatellus, L. Romero Cortés, and J. Azaña, "Arbitrary energy-preserving control of the line spacing of an optical frequency comb over six orders of magnitude through self-imaging," *Opt. Express*, **26**, 21 069–21 085 (2018).

Associated contributions to international conferences

[APc1] L. Romero Cortés, R. Maram, and J. Azaña "Real-time averaging of repetitive optical waveforms by non-integer factors based on temporal self-imaging," in *Conference on Lasers and Electro-Optics (CLEO),* San Jose (CA), USA (2015), paper **STu4N.7**.

[APc2] L. Romero Cortés, R. Maram, and J. Azaña "Spectral compression of complex-modulated signals without loss of information by joint temporal-spectral self-imaging," in *European Conference on Optical Communications (ECOC),* Valencia, Spain (2015), paper **301**.

[APc3] L. Romero Cortés, R. Maram, L. Lei, and J. Azaña "Robust RZ to NRZ format converter based on linear joint temporal-spectral self-imaging and band-pass filtering," in *European Conference on Optical Communications (ECOC),* Valencia, Spain (2015), paper **249**.

[APc4] H. Guillet de Chatellus, L. Romero Cortés, and J. Azaña "Lossless arbitrary FSR control of optical frequency combs using joint time-frequency self-imaging," in *Conference on Lasers and Electro-Optics (CLEO),* San Jose (CA), USA (2016), paper **SM2I.6**.

[APc5] L. Romero Cortés, R. Maram, and J. Azaña "Energy-preserving arbitrary repetition rate control of waveform trains," in *International Conference on Optical, Optoelectronic and Photonic Materials and Applications (ICOOPMA),* Montreal, Canada (2016), paper **Mo-C1-I1**. **Invited**.

[APc6] L. Romero Cortés, R. Maram, H. Guillet de Chatellus, and J. Azaña "Arbitrary control of the free spectral range of periodic optical frequency combs through linear energy-preserving time-frequency Talbot effects," in *IEEE Photonics Conference (IPC),* Waikoloa (HI), USA (2016), paper **MF2.2**.

[APc7] L. Romero Cortés, R. Maram, and J. Azaña "Full-field broadband invisibility cloaking," in *IEEE Photonics Conference (IPC),* Waikoloa (HI), USA (2016), paper **MF3.5**.

[APc8] L. Romero Cortés, R. Maram, H. Guillet de Chatellus, and J. Azaña "Phase controlled spectral Talbot effect," in *IEEE-OSA Montreal Networking Event & Poster Competition,* Montreal, Canada (2017), poster **5**. **Best poster award**.

[APc9] L. Romero Cortés, R. Maram, H. Guillet de Chatellus, and J. Azaña "Noiseless spectral amplification of optical frequency combs," in *Conference on Lasers and Electro-Optics (CLEO),* San Jose (CA), USA (2017), paper **STu4I.3**.

[APc10] L. Romero Cortés, M. Seghilani, R. Maram, and J. Azaña "Frequency domain invisibility enables phase-preserving broadband cloaking," in *Conference on Lasers and Electro-Optics (CLEO),* San Jose (CA), USA (2017), paper **SM4I.7**.

[APc11] L. Romero Cortés, R. Maram, and J. Azaña "Arbitrary period control and noise mitigation in periodic waveforms through coherent energy redistribution," in *Pacific Rim Conference on Lasers and Electro-Optics (CLEO-PR),* Singapore (2017), paper **3-2k-5**. **Invited**.

[APc12] B. Crockett, L. Romero Cortés, and J. Azaña "On-the-fly recovery of arbitrary waveforms from in-band noise by linear coherent spectral energy re-distribution," in *Conference on Lasers and Electro-Optics (CLEO),* San Jose (CA), USA (2018), paper **SF3N.7**.

[APc13] L. Romero Cortés, R. Maram, and J. Azaña "Noiseless control and amplification of periodic waveforms through Talbot self-imaging," in *Union of Radio Science Atlantic Radio Science Meeting (URSI AT-RASC),* Gran Canaria, Spain (2018), paper **D01-07**. **Invited**.

[APc14] L. Romero Cortés, R. Maram, H. Guillet de Chatellus, and J. Azaña "Energy-preserving frequency comb signal processing techniques: arbitrary FSR control and noise mitigation," in *Photonics North Conference,* Montreal, Canada (2018). **Invited**.

Other publications

The following list contains other work reported by, or in collaboration with the candidate, published in the course of the candidate's Ph.D. before the time this dissertation was submitted.

Other publications in peer-reviewed journals

[OPj1] M. Burla, L. Romero Cortés, M. Li, X. Wang, L. Chrostowski, and J. Azaña, "Integrated waveguide Bragg gratings for microwave photonics signal processing," *Opt. Express*, **21**, 25 120–25 147 (2013). Featured issue: *Microwave Photonics*. **Invited**.

[OPj2] M. Burla, L. Romero Cortés, M. Li, X. Wang, L. Chrostowski, and J. Azaña, "On-chip programmable ultra-wideband microwave photonic phase shifter and true time delay unit," *Opt. Lett.*, **39**, 6181–6184 (2014).

[OPj3] M. Burla, M. Li, L. Romero Cortés, X. Wang, M. R. Fernández-Ruiz, L. Chrostowski, and J. Azaña, "Terahertz-bandwidth photonic fractional Hilbert transformer based on a phase-shifted waveguide Bragg grating on silicon," *Opt. Lett.*, **39**, 6241–6244 (2014).

[OPj4] R. Maram, L. Romero Cortés, and J. Azaña, "Sub-harmonic periodic pulse train recovery from aperiodic optical pulse sequences through dispersion-induced temporal self-imaging," *Opt. Express*, **23**, 3602–3613 (2015).

[OPj5] R. Ashrafi, M. R. Dizaji, L. Romero Cortés, J. Zhang, J. Yao, J. Azaña, and L. R. Chen, "Time-delay to intensity mapping based on a second-order optical integrator: application to optical arbitrary waveform generation," *Opt. Express*, **23**, 16 209–16 223 (2015).

[OPj6] H. F. Martins, J. Pastor-Graells, L. Romero Cortés, D. Piote, S. Martin-Lopez, J. Azaña, and M. Gonzalez-Herraez, "PROUD-based method for simple real-time in-line characterization of propagation-induced distorsions in NRZ data signals," *Opt. Lett.*, **40**, 4356–4359 (2015).

[OPj7] L. Lei, J. Huh, L. Romero Cortés, R. Maram, B. Wetzel, D. Duchesne, R. Morandotti, and J. Azaña, "Observation of spectral self-imaging by nonlinear parabolic cross-phase modulation," *Opt. Lett.*, **40**, 5403–5406 (2015).

[OPj8] R. Maram, L. Romero Cortés, , and J. Azaña, "Programmable fiber-optics pulse repetition-rate multiplier," *J. Lightwave Technol.*, **34**, 448–455 (2015). Featured issue: *Selected Papers from OFC 2015*. **Invited**.

[OPj9] H. Guillet de Chatellus, L. Romero Cortés, and J. Azaña, "Optical real-time Fourier transformation with kilohertz resolutions," *Optica*, **3**, 1–8 (2015).

[OPj10] H. Guillet de Chatellus, L. Romero Cortés, and J. Azaña, "Real-time Fourier transformation with kHz resolution," *Optics and Photonics News* (2016).

[OPj11] H. Guillet de Chatellus, L. Romero Cortés, A. Deville, M. Seghilani, and J. Azaña, "Diffraction-induced bidimensional Talbot self-imaging with full independent period control," *Phys. Rev. Lett.*, **118**, 133 903 (2017).

[OPj12] J. Pastor-Graells, L. Romero Cortés, H. F. Martins, M. R. Fernández-Ruiz, J. Azaña, S. Martin-Lopez, and M. Gonzalez-Herraez, "SNR enhancement in high-resolution phase-OTDR systems using chirped pulse amplification concepts," *Opt. Lett.*, **42**, 1728–1731 (2017).

[OPj13] M. Kues, C. Reimer, P. Roztocki, L. Romero Cortés, S. Sciara, B. Wetzel, Y. Zhang, A. Cino, S. T. Chu, B. E. Little, D. J. Moss, L. Caspani, J. Azaña, and R. Morandotti, "On-chip generation of high-dimensional entangled quantum states and their coherent control," *Nature*, **546**, 622–626 (2017).

[OPj14] R. Maram, M. Seghilania, J. Jeon, X.-Z. Li, L. Romero Cortés, J. van Howe, and J. Azaña, "Demonstration of input-to-output gain and temporal noise mitigation in a Talbot amplifier," arXiv:1710.00033 (2017).

[OPj15] M. Kues, C. Reimer, P. Roztocki, L. Romero Cortés, S. Sciara, J. Azaña, Y. Zhang, and R. Morandotti, "Scaling on-chip entangled photon States to higher dimensions," *Optics and Photonics News* (2017).

[OPj16] R. Maram, M. Seghilania, J. Jeon, X.-Z. Li, L. Romero Cortés, J. van Howe, and J. Azaña, "Demonstration of input-to-output gain and temporal noise mitigation in a Talbot amplifier," *IEEE Photon. Technol. Lett.*, **30**, 665–668 (2018).

[OPj17] B. MacLellan, P. Roztocki, M. Kues, C. Reimer, L. Romero Cortés, Y. Zhang, S. Sciara, B. Wetzel, A. Cino, S. T. Chu, B. E. Little, D. J. Moss, L. Caspani, J. Azaña, and R. Morandotti, "Generation and coherent control of pulsed quantum frequency combs," *J. Vis. Exp.*, **136**, e57 517 (2018).

[OPj18] H. Guillet de Chatellus, L. Romero Cortés, C. Schnébelin, M. Burla, and J. Azaña, "Reconfigurable photonic generation of broadband chirped waveforms using a single CW laser and low-frequency electronic," *Nat. Commun.*, **9:2438** (2018).

[OPj19] P. Roztocki, S. Sciara, C. Reimer, L. Romero Cortés, Y. Zhang, B. Wetzel, M. Islam, B. Fischer, A. Cino, S. T. Chu, B. E. Little, D. J. Moss, L. Caspani, J. Azaña, M. Kues, and R. Morandotti, "Complex quantum state generation and coherent control based on integrated frequency combs," *J. Lightwave Technol.* (In press). **Invited**.

[OPj20] C. Reimer, Y. Zhang, P. Roztocki, S. Sciara, Romero Cortés, M. Islam, B. Fischer, B. Wetzel, A. C. Cino, S. T. Chu, B. Little, D. Moss, L. Caspani, J. Azaña, M. Kues, and R. Morandotti, "On-chip frequency combs and telecommunications signal processing meet quantum optics," *Front. Optoelectron.*, **11**, 134–147 (2018). **Review Article Invited Paper. Special Issue – Photonics Research in Canada**.

Other contributions to international conferences

[OPc1] M. Burla, M. Li, L. Romero Cortés, X. Wang, L. Chrostowski, and J. Azaña "2.5 THz bandwidth on-chip photonic fractional Hilbert transformer based on a phase-shifted waveguide Bragg grating," in *IEEE Photonics Conference (IPC),* San Diego (CA), USA (2013), paper **WD2.2**.

[OPc2] L. Romero Cortés, M. Burla, and J. Azaña "Self-referenced non-interferometric complete optical signal characterization from intensity-only measurements," in *IEEE Photonics Conference (IPC),* San Diego (CA), USA (2013), paper **TuG1.6**.

[OPc3] M. Burla, L. Romero Cortés, M. Li, X. Wang, L. Chrostowski, and J. Azaña "On-chip ultra-wideband microwave photonic phase shifter and true time delay line based on a single phase-shifted waveguide Bragg grating," in *IEEE International Topical Meeting on Microwave Photonics (MWP),* Beijing, China (2013), paper **39**.

[OPc4] M. Burla, L. Romero Cortés, M. Li, X. Wang, L. Chrostowski, and J. Azaña "On-chip quasi-THz bandwidth microwave photonic phase shifter based on a waveguide Bragg grating on silicon," in *Conference on Lasers and Electro-Optics (CLEO),* San Jose (CA), USA (2013), paper **STu2G.3**.

[OPc5] R. Maram, L. Romero Cortés, and J. Azaña "Reconfigurable optical sub-harmonic clock recovery based on inverse temporal self-imaging," in *Conference on Lasers and Electro-Optics (CLEO),* San Jose (CA), USA (2013), paper **SW3J.3**.

[OPc6] L. Romero Cortés, R. Maram, and J. Azaña "Photonic integrator based on a distributed feedback semiconductor optical amplifier," in *Advanced Photonics Meeting. Bragg Gratings, Photosensitivity and Poling in Glass Waveguides (BGPP),* Barcelona, Spain (2013), paper **BW3D.5**.

[OPc7] L. Romero Cortés and J. Azaña "All-optical reconfigurable regenerative RZ to NRZ format converter based on a Mach-Zehnder interferometer and a temporal photonic integrator," in *IEEE Photonics Conference (IPC),* San Diego (CA), USA (2014), paper **TuG3.4**.

[OPc8] R. Maram, L. Romero Cortés, and J. Azaña "Electrically-Tunable Fiber-Optics Pulse Repetition-Rate Multiplier," in *Optical Fiber Communications Conference (OFC),* Los Angeles (CA), USA (2015), paper **W1K.5**. **Top score**.

[OPc9] R. Maram, L. Romero Cortés, and J. Azaña "Programmable fibre-optics pulse repetition rate multiplier for high-speed optical communication systems," in *European Conference on Optical Communications (ECOC),* Valencia, Spain (2015), paper **745**.

[OPc10] R. Maram, L. Romero Cortés, and J. Azaña "Versatile fiber-optics pulse repetition-rate multipliers based on temporal self-Imaging," in *Optical Fiber Communications Conference (OFC),* Anaheim (CA), USA (2016), paper **W3E.4**. **Invited**.

[OPc11] H. Guillet de Chatellus, L. Romero Cortés, and J. Azaña "Passive amplification of periodic 2D images through self-imaging," in *Imaging and Applied Optics Congress,* Heidelberg, Germany (2016), paper **MW1G.2**.

[OPc12] J. Pastor-Graells, L. Romero Cortés, H. F. Martins, M. R. Fernández-Ruiz, J. Azaña, S. Martin-Lopez, and M. Gonzalez-Herraez "20 dB SNR enhancement in phase-sensitive OTDR using pulse stretching and recompression," in *Optical Fiber Sensors (OFS),* Jeju, South Korea (2017), paper **OFS100-375**.

[OPc13] H. Guillet de Chatellus, L. Romero Cortés, M. Burla, C. Schnébelin, and J. Azaña "Agile photonic generation of arbitrary RF chirped waveforms," in *Conference on Lasers and Electro-Optics (CLEO),* San Jose (CA), USA (2017), paper **SF2L.3**.

[OPc14] C. Reimer, M. Kues, P. Roztocki, L. Romero Cortés, S. Sciara, B. Wetzel, Y. Zhang, A. Cino, S. T. Chu, B. E. Little, D. J. Moss, L. Caspani, J. Azaña, and R. Morandotti "High-dimensional frequency-bin entanglement in on-chip optical frequency combs," in *Photonics North,* Ottawa, Canada (2017), paper **XuNF-35**.

[OPc15] H. Guillet de Chatellus, C. Schnébelin, L. Romero Cortés, M. Burla, and J. Azaña "Agile photonic generation of arbitrary RF chirped waveforms based on a single CW laser," in *European Conference on Lasers and Electro-Optics (CLEO-Europe),* Munich, Germany (2017), paper **CI-P.16**.

[OPc16] H. Guillet de Chatellus, L. Romero Cortés, A. Deville, M. Seghilani, , and J. Azaña "Arbitrary and independent period control of bidimensional periodic wavefronts by generalized self-imaging," in *Imaging and Applied Optics Congress,* San Francisco (CA), USA (2017), paper **IW4E.1**.

[OPc17] L. Romero Cortés, A. Deville, M. Seghilani, I. Hamam, H. Guillet de Chatellus, and J. Azaña "Enhanced restoration of faulty images by Talbot amplification," in *Imaging and Applied Optics Congress,* San Francisco (CA), USA (2017), paper **IW4E.2**.

[OPc18] H. Guillet de Chatellus, C. Schnebelin, L. Romero Cortés, M. Burla, and J. Azaña "Génération photonique de signaux chirpés à partir d'un laser continu," in *Journées Nationales d'Optique Guidée (JNOG),* Limognes, France (2017), paper **207**.

[OPc19] J. Pastor-Graells, L. Romero Cortés, H. F. Martins, M. R. Fernández-Ruiz, J. Azaña, S. Martin-Lopez, and M. Gonzalez-Herraez "OTDR sensible a la fase con resolución espacial milimétrica," in *Reunión Española de Optoelectrónica (OPTOEL),* Santiago de Compostela, Spain (2017), paper **11**.

[OPc20] C. Reimer, M. Kues, P. Roztocki, L. Romero Cortés, S. Sciara, B. Wetzel, Y. Zhang, A. Cino, S. Chu, B. Little, D. Moss, L. Caspani, J. Azaña, and R. Morandotti "Integrated generation of high-dimensional entangled photon states and their coherent control," in *Frontiers in Optics (FiO),* Washington, D.C., USA (2017), paper **FTh3E.2**.

[OPc21] M. Seghilani, R. Maram, L. Romero Cortés, and J. Azaña "Dual repetition-rate harmonically mode-locked fiber laser using intracavity temporal Talbot effect," in *IEEE Photonics Conference (IPC),* Orlando (FL), USA (2017).

[OPc22] M. Seghilani, R. Maram, L. Romero Cortés, and J. Azaña "Generation of a 128-GHz optical pulse train from a 250-MHz frequency comb using temporal self-imaging," in *IEEE Photonics Conference (IPC),* Orlando (FL), USA (2017).

[OPc23] H. Guillet de Chatellus, C. Schnébelin, M. Burla, L. Romero Cortés, and J. Azaña "Reconfigurable photonic generation of arbitrary RF chirped waveforms based on a single CW laser," in *IEEE International Topical Meeting on Microwave Photonics (MWP),* Beijing, China (2017), paper **1570378717**.

[OPc24] P. Roztocki, M. Kues, C. Reimer, L. Romero Cortés, S. Sciara, B. Wetzel, Y. Zhang, A. Cino, S. T. Chu, B. E. Little, D. J. Moss, L. Caspani, J. Azaña, and R. Morandotti "Integrated generation of complex optical quantum states and their coherent control," in *SPIE NanoPhotonics Australasia,* Melbourne, Australia (2017), paper **10456-104561A**. **Invited**.

[OPc25] C. Reimer, M. Kues, P. Roztocki, S. Sciara, L. R. Cortés, B. Wetzel, Y. Zhang, A. Cino, S. Chu, B. Little, D. J. Moss, L. Caspani, J. Azaña, and R. Morandotti "On-chip quantum optical frequency comb sources," in *Optical Fiber Communications Conference (OFC),* San Diego (CA), USA (2018), paper **M4G.4**.

[OPc26] M. Seghilani, X.-Z. Li, L. Romero Cortés, R. Maram, and J. Azaña "Dual repetition-rate laser based on in-cavity fractional temporal self-imaging for low-noise RF signal generation," in *Optical Fiber Communications Conference (OFC),* San Diego (CA), USA (2018), paper **M2J.2**.

[OPc27] M. Kues, C. Reimer, S. Sciara, P. Roztocki, L. Romero Cortés, B. Wetzel, Y. Zhang, A. C. Cino, S. T. Chu, B. E. Little, D. J. Moss, L. Caspani, J. Azaña, and R. Morandotti "Integrated frequency combs for on-chip generation of high-dimensional entangled photon states and their coherent control," in *SPIE Photonics Europe,* Strasbourg, France (2018), paper **10672-29**. **Invited**.

[OPc28] P. Roztocki, M. Kues, C. Reimer, L. Romero Cortés, S. Sciara, B. Wetzel, Y. Zhang, A. Cino, S. T. Chu, B. E. Little, D. J. Moss, L. Caspani, J. Azaña, and R. Morandotti "Scalable on-chip generation and coherent control of complex optical quantum states," in *Conference on Lasers and Electro-Optics (CLEO),* San Jose (CA), USA (2018), paper **JTh4C.2**.

[OPc29] M. Kues, C. Reimer, P. Roztocki, L. Romero Cortés, S. Sciara, B. Wetzel, Y. Zhang, A. Cino, S. T. Chu, B. E. Little, D. J. Moss, L. Caspani, J. Azaña, and R. Morandotti "On-chip entangled D-level photon states–scalable generation and coherent processing," in *Conference on Lasers and Electro-Optics (CLEO),* San Jose (CA), USA (2018), paper **FW4F.2**.

[OPc30] M. Seghilani, X.-Z. Li, R. Maram, L. Romero Cortés, and J. Azaña "Generation of a CEO-stabilized optical frequency comb with programmable sub-MHz FSR using spectral self-imaging," in *Conference on Lasers and Electro-Optics (CLEO),* San Jose (CA), USA (2018), paper **JTh2A.157**.

[OPc31] P. Roztocki, M. Kues, C. Reimer, L. Romero Cortés, S. Sciara, B. Wetzel, Y. Zhang, A. Cino, S. T. Chu, B. E. Little, D. J. Moss, L. Caspani, J. Azaña, and R. Morandotti "On-chip generation and coherent control of complex optical quantum states," in *Union of Radio Science Atlantic Radio Science Meeting (URSI AT-RASC),* Gran Canaria, Spain (2018), paper **S-D13-03**. **Invited**.

[OPc32] M. Seghilani, R. Maram, L. Romero Cortés, and J. Azaña "Self-action mitigation for high repetition rate ultrashort pulses using fractional temporal self-imaging," in *Pacific Rim Conference on Lasers and Electro-Optics (CLEO-PR),* Hong Kong (2018). **Invited**.

[OPc33] B. Crockett, L. Romero Cortés, and J. Azaña "Denoising Amplification of Arbitrary Optical Waveforms by Linear Coherent Energy Redistribution," in *Advanced Photonics Congress,* Zurich, Switzerland (2018), paper **SpW2G.3**.

[OPc34] R. Maram, M. Seghilani, J. Jeon, X.-Z. Li, L. Romero Cortés, J. Van Howe, and J. Azaña "Temporal noise mitigation in a Talbot amplifier," in *IEEE Photonics Conference (IPC),* Reston (VA), USA (2018).

CHAPTER 1

Introduction and motivation

This chapter introduces the problem addressed in this thesis, as well as the proposed solution. The relevance and importance of periodic signals and objects in the current scientific and technological world is discussed. Special attention is directed towards the particularly interesting case of periodic trains of pulses and frequency combs in the realm of optical waves. The critical importance of controlling and generating periodic temporal and spectral signals is discussed, as well as the limitations and shortcomings of current solutions that address this problem, with special attention to their impact on the noise and overall energy of the signal of interest. The chapter then addresses the general motivation of this dissertation, namely the proposal and demonstration of a universal method for noiseless periodicity control of repetitive waves based on redistributing the energy already carried by the signal of interest. This methodology is aimed at overcoming the drawbacks of the state-of-the-art solutions discussed in the chapter. Special attention is directed towards arbitrary control of spectrally-periodic optical signals, an area of increasing interest due to the high impact of the optical frequency comb in current science and engineering applications.

1.1 Periodic objects in science and engineering

Inasmuch as the central points of this dissertation deal with, and profoundly rely on the concept of *periodicity*, it seems only natural to begin this document by looking at the impact of periodic objects in the current scientific and technological state of the world.

A periodic object is one whose properties repeat at multiples of a defined interval – the fundamental period – in some observation domain. Note that I use the term *object* in a very loose sense here. For instance, we could say that the clock signal of a digital system is a periodic object in time, or a temporally-periodic object, in the same way that a material with a crystalline structure is a periodic object in space, or a spatially-periodic object. In general, a function, $\psi : \mathbb{R} \to \mathbb{C}$, is periodic in the representation domain u if $\psi(u \pm N u_r) = \psi(u)\ \forall\ N \in \mathbb{N}$, where $u_r > 0$ is the fundamental period.

Not only periodic structures are of interest to science, but many of the technological advances we have witnessed over the years rely on spatially-periodic objects. In the context of materials science, for instance, crystalline structures diffract X-rays, electrons and neutrons, producing patterns with sharp Bragg reflection spots, due to their periodic nature [1, 2]. This facilitates the study of solids through the analysis of the diffracted periodic waves. Indeed, the diffraction of waves from periodic structures finds technological application in many areas of engineering. Diffraction gratings are the enabling component of a myriad of photonic devices and techniques, key to modern optical experimentation [3]. These include lasers, spectrometers, telescopes, signal processing devices, photolitographic instruments, etc. These gratings are not necessarily static objects, as they can also be generated dynamically by means of acousto-optic interaction of light and sound waves [4]. Furthermore, advances in the field of metamaterials – specially-engineered periodic structures – have brought to life effects and applications seemingly out of science fiction, through the use of transformation optics [5], including the negative refraction of light [6], flat lenses [7], lenses with focusing power beyond the diffraction limit [8], fast and slow light propagation [9], and even devices capable of rendering objects invisible [10].

On the other hand, many natural phenomena exhibit temporal periodicity. Pulsar neutron stars rotate with extremely precise periods, some of them even rivaling the timekeeping accuracy of modern atomic clocks [11]. Additionally, temporally- and/or spectrally-periodic signals (the latter referring to signals exhibiting periodicity along their frequency-domain representation) play a pivotal role in the current scientific and technological landscape. Pulsed radar and lidar systems are prime examples [12, 13]. Moreover, the advent of digital signal processing systems revolutionized the fields of information and communications theory, ultimately giving birth to the modern internet and computing era. Such systems intrinsically rely on periodic signals and processes for basic processing operations and timing [14].

In this context, periodic optical signals have a prominent position, especially since the development and maturity of the mode-locked laser [15]. The main focus of this dissertation deals with the problem of controlling the period of repetitive optical waves, in particular, for optical signals in the time and frequency domains of representation.

1.2 Periodic optical signals in the time and frequency domains

A handful of technological wonders, such as the airplane and the radio, have revolutionized the world through history in ways we could have never imagined. The laser is certainly one of them. The development of the laser has been a turning point in the history of scientific discovery. In 1917, Albert Einstein developed his theory of stimulated emission [16]. It took over three decades for it to be put to practical use. Since then, the

impact of the laser on the technological world has been such that nowadays we could not conceive our lives without it. Fig. 1.1 shows a summarized timeline of the events leading to the development of modern laser sources.

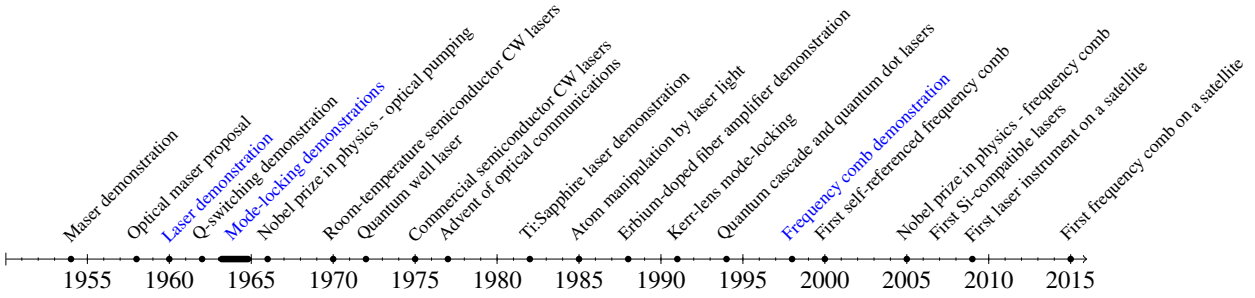

Figure 1.1 – History of the laser. Compilation of relevant events leading from the original conception of the laser to current developments of laser technology.

The laser – light amplification by stimulated emission of radiation – is a coherent optical oscillator. In general terms, laser radiation is emitted when an optical gain medium, enclosed within a resonant cavity, is excited by an energy pump mechanism [16]. Continuous-wave (CW) lasers emit a monochromatic light wave, itself a periodic optical signal (see Fig. 1.2(a)). However, multitude of practical applications require pulsed laser signals, consisting of a periodic temporal envelope oscillating at the optical laser frequency. Such waves are no longer monochromatic, as their spectra is made out of a certain number of frequency components (see Fig. 1.2(b)). These signals can be achieved through several means. For instance, the pump current of a CW laser can be electrically switched to directly turn its emission on and off, thus obtaining a pulsed optical signal [17]. This method, however, is generally inefficient, as the transient times associated with the population inversion process in the laser gain medium do not generally allow for the production of short pulses at high repetition rates [16]. Nowadays, it is common to use electro-optical devices, known as amplitude modulators, to achieve optical pulses from CW lasers with repetition rates on the order of tens of GHz [18].

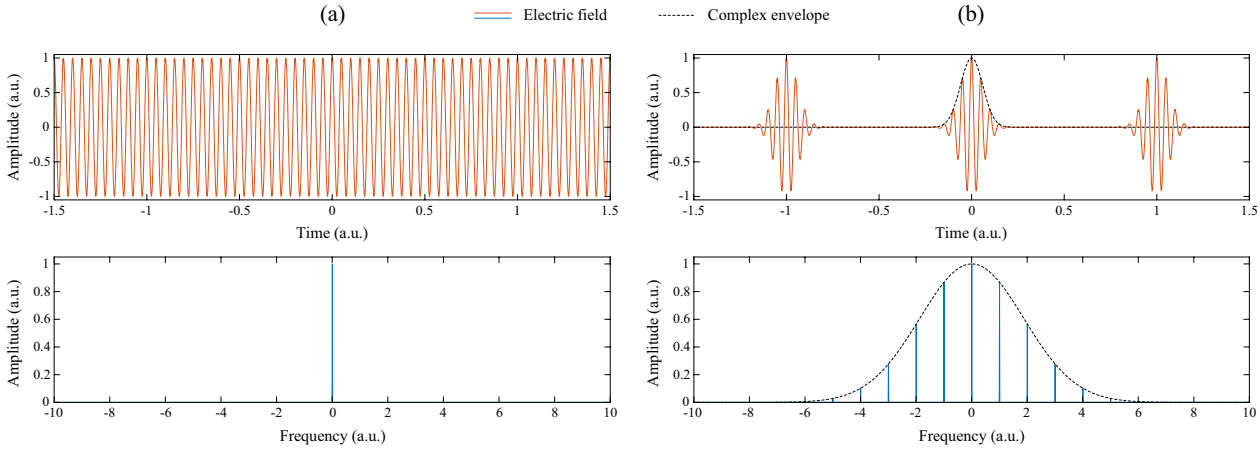

Figure 1.2 – Comparison between continuous and pulsed light waves. Numerical simulation showing the electric field amplitude (top) and its spectrum (bottom) of (a) a continuous wave, and (b) a periodic pulsed wave with the same central frequency. The frequency spectrum of the continuous optical wave corresponds to a single frequency component, while the spectrum of the pulsed optical wave is a collection of equally-spaced frequency components (where the frequency separation is the reciprocal of the pulse period). Note that the shown frequency values in the bottom plots are represented relative to the central frequency of the wave.

There are two problems, however, associated with electro-optical techniques in the generation of periodic waveforms. First, the extinction ratio of amplitude modulators is limited by the precision of current fabrication methods [19]. This results in a background of unsuppressed light superimposed to the generated pulses. Second, the obtained pulses have a minimum temporal duration that is limited by the electrical bandwidth of the modulator and by the speed of the available electronics. Nowadays, typical electronic waveform generators and amplifiers can produce radio-frequencies in the order of tens of GHz. Moreover, electro-optical modulation has only been demonstrated with radio-frequency bandwidths slightly over 100 GHz [20]. Achieving optical pulses with temporal widths below a few tens of ps – and associated broad optical bandwidths – becomes extremely challenging, if at all possible, by electro-optical means alone.

A myriad of scientific and technological applications require precisely-timed, periodic trains of short optical pulses. A second kind of lasers achieve such requirements through a process known to as mode-locking.

1.2.1 Mode-locked lasers

Mode-locking is the process by which the different longitudinal modes oscillating in a laser cavity are strongly locked in phase, resulting in a well-defined phase distribution along the emission spectrum of the laser (see Fig. 1.3) [15, 21]. Interference between these modes causes the formation of a short optical pulse circulating within the cavity, which gives rise to radiation of pulsed laser light. This way, the stimulated photons leaving the laser cavity are concentrated over a short period of time, achieving higher values of peak optical power than their CW counterparts (for a given value of average optical power). State-of-the-art mode-locked lasers routinely produce periodic trains of optical pulses, with pulse durations in the picosecond (10^{-12} s), femtosecond (10^{-15} s), and more recently, attosecond (10^{-18} s) regimes [22].

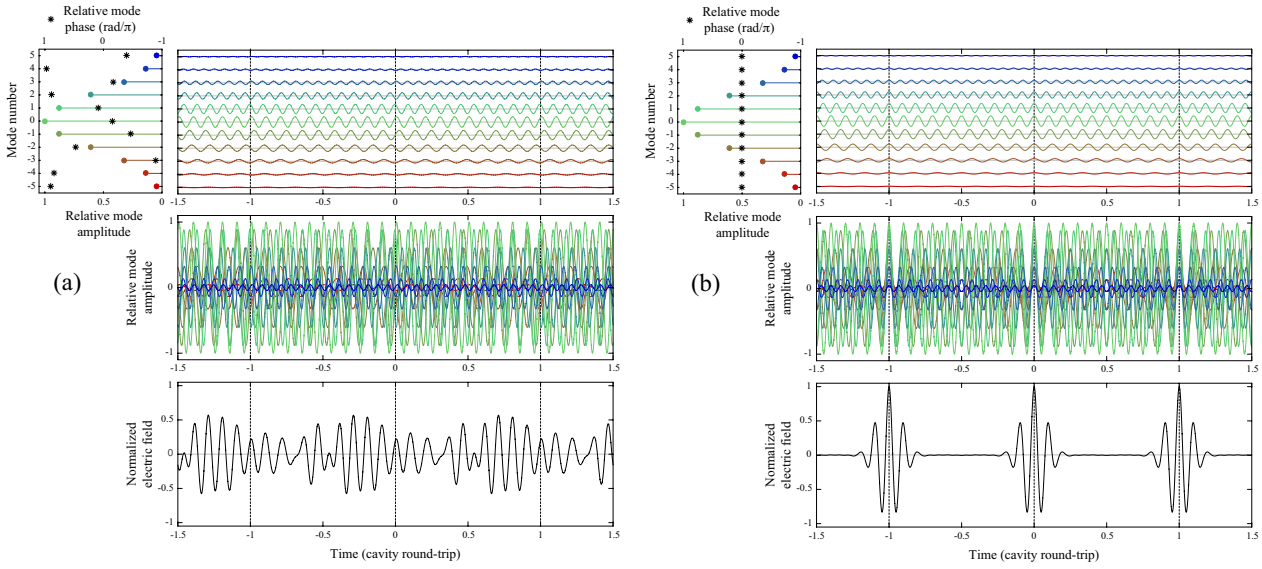

Figure 1.3 – Principle of mode-locking. Numerical simulation illustrating the coherent interference of monochromatic waves. An optical cavity supports a number of longitudinal modes, oscillating at optical frequencies. (a) When the relative phases between cavity modes are not deterministically defined, the laser emits an electric field with fluctuating amplitude. (b) When all cavity modes are locked in phase, the laser emits a train of optical pulses, with a repetition rate given by the reciprocal of the round-trip time of a photon in the cavity. The temporal duration of the pulses is determined by the number of supported cavity modes, through a Fourier-reciprocity relationship.

Generally speaking, there are two main methods to achieve mode-locking. Passive mode-locking relies on a nonlinear passive element – a saturable absorber – that modulates the losses of the resonator [15, 23]. Very short pulse durations and high pulse energies can be attained through this method [24]; however, the repetition rate of the resulting pulse train is typically low (in the range of tens to a few hundreds of MHz) and fixed. Additionally, in some situations, a pulse circulating through a passively mode-locked laser cavity may break up into two or more closely spaced replicas, leading to the emission of pulse bunches [23]. Passively mode-locked lasers are the usual light source of choice for applications such as spectroscopy [25], and laser surgery [26], among others. Furthermore, recent studies propose this technology as a promising candidate for clean nuclear fusion energy [27].

Another group of applications, including telecommunications [28, 29], radio-frequency generation [30], and waveform shaping [31, 32], usually require significantly higher repetition rates. These disciplines do not rely on ultra-high peak power pulses, that can in fact be damaging to photonic components and systems. Active mode-locking is generally better suited for applications in this framework. Such lasers can achieve pulses in the ps regime at repetition rates in the GHz regime, by periodically modulating the laser cavity loss through an active element, e.g., an optical modulator [15, 23]. This method has the additional advantage of offering some – although limited – capability of controlling the repetition rate by adjusting the modulation frequency. On the other hand, these lasers usually suffer from higher level of noise than their passive counterparts.

Some laser structures, particularly mode-locked diode lasers, can be operated in a combination of passive and active mode-locking. Hybrid mode-locked lasers can generate fairly short pulses with some degree of repetition rate control. However, these systems are extremely difficult to optimize, and imperfections in the design usually lead to poor pulse quality, pulse replicas, chirped pulses, and strong variations of the temporal pulse emission period, due to the low attainable pulse energies [23].

1.2.2 The optical frequency comb

A common feature of all mode-locked lasers is that their emission spectra is discrete. A periodic train of optical pulses, provided a coherent phase relation between pulses of the train, can always be described in the frequency domain as a collection of equally-spaced frequency components. Such discrete periodic spectra are referred to as *optical frequency combs*[1] [33, 34], and the spectral components are commonly called the comb lines or teeth.

In a frequency comb, the frequency of the k-th comb line is determined by two parameters, the free spectral range (FSR), ν_r, and the offset frequency, ν_0, following Eq. 1.1.

$$\nu_k = \nu_0 + k\nu_r \tag{1.1}$$

The FSR of the comb sets the repetition rate of the corresponding temporal pulse train, where the pulse period is the reciprocal of the FSR [33]. If the offset frequency is nonzero, the temporal envelope of the pulse train experiences a phase deviation, $\Delta\phi$ (known as the carrier-envelope offset, CEO), with respect to

[1] It is worth noting that the definition of frequency comb varies from author to author. For instance, for certain scientific disciplines – particularly involving high precision metrology – a discrete line spectrum only qualifies as a frequency comb if both the repetition rate and the absolute frequency offset are stabilized to a frequency reference with a high degree of precision, and with a very low level of phase noise. In the context of this dissertation, any optical signal with a discrete spectrum consisting on a collection of frequency components with an equal, well-defined separation, and deterministic line-by-line phase relationships (i.e., phase-coherent) qualifies as a frequency comb.

the underlying optical carrier, so that, $\Delta\phi\nu_r = 2\pi\nu_0$ [35]. Fig. 1.4 illustrates the parameters of a frequency comb in the time and frequency domains of representation.

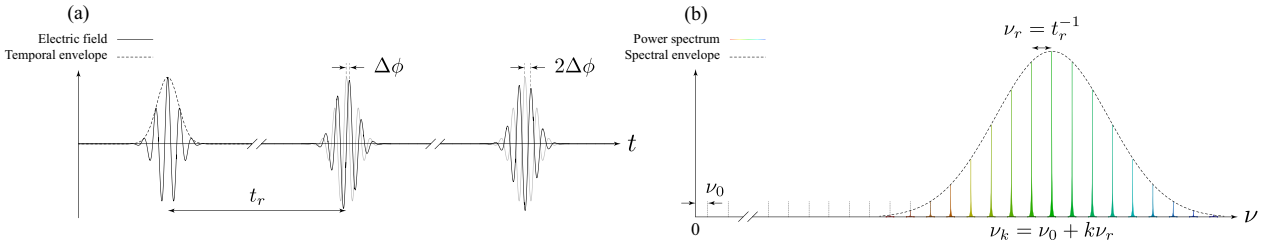

Figure 1.4 – Parameters of a frequency comb in the time and frequency domains. The parameters of (a) a train of pulses and (b) its frequency comb representation are related by the Fourier transform, where the comb spectral envelope is given by the Fourier transform of the temporal envelope of one pulse. The comb FSR is the reciprocal of the temporal pulse period. The symbols t and ν represent the time and frequency variables, respectively.

The first hints of frequency combs in the literature date from the late 1970's, in the experiments of Nobel Prize laureate Theodor Wolfgang Hänsch in high-resolution spectroscopy using short optical pulses [36]. However, it was not until 20 years later that the development of the frequency comb achieved maturity. Nowadays, combs are used in a myriad of scientific and applied disciplines, and they are the key enabling factor of many technological fields [33, 37], ranging from high-resolution spectroscopy of molecules and atoms [25], to the astronomical search for exo-planets [38–40].

1.2.3 Technological considerations of periodic optical signals

Periodic trains of optical pulses and their frequency comb spectra are fundamental to a myriad of scientific and applied disciplines, impossible to realize otherwise. Some examples include high-precision frequency metrology [41], high-resolution atomic and molecular spectroscopy [25,42], high-accuracy spectrograph calibration (e.g., as used in astronomical telescopes) [38–40], ultrafast optical and microwave signal processing and generation [30–32], optical communications and computing [18, 28, 29], sensing [OPj12], nonlinear and quantum optics [43] [OPj13], etc.

One of the key parameters of these signals is their period of repetition, i.e., the pulse period of the train, and the corresponding FSR of the comb (see Fig. 1.4). Most applications require that these parameters are fixed with precision. For instance, the rate at which information is transmitted in a telecommunication system, and processed in a computing system, is strongly related to the pulse period of the clock signal [14, 18]. Moreover, distinct applications require fundamentally different orders of magnitude. As an example, typical atomic and molecular spectroscopy applications require frequency combs with FSR values in the MHz regime, while astronomical spectrographic measurements, as well as applications aimed at arbitrary waveform generation and processing, are performed with combs in the GHz regime [33]. Table 1.1 summarizes some of the applications of periodic pulse trains and frequency combs, depending on the repetition rate regime.

Another fundamental factor of periodic signals for their practical use is the energy per pulse of a pulse train, and the peak line power in a frequency comb. Applications of pulse trains such as nonlinear microscopy [44], laser micromachining [45], and realization of relativistic optical processes [46], require pulses with high peak power levels. Additionally, this is related to the signal-to-noise ratio (SNR), a key parameter for every discipline relying on signal detection, ranging from spectroscopy to optical communications [14, 39, 42].

Table 1.1 – Applications of pulse trains and frequency combs. Different applications typically require different regimes of the repetition rate of the train – the comb FSR.

FSR regime	Application examples
kHz	High-energy physics
	Laser micromachining
	Laser pumping
	Biomedial imaging
	Laser surgery
	Mass spectrometry
MHz	Optical frequency metrology
	High-precision spectroscopy
	Optical time transfer
	Coherent light detection and ranging
	Laser microscopy
	Sensor interrogation
GHz	High-speed communications
	High-speed computing
	Microwave photonics
	Radio-frequency generation
	Optical waveform shaping
	High-precision spectrograph calibration

1.3 Controlling the period of periodic optical signals

Methods aimed at manipulating the period of repetitive waveforms can be categorized in two groups: Techniques that affect the signal generation mechanism to obtain the desired period, and techniques that manipulate the already generated signal and transform its period.

1.3.1 Control of the generation mechanism

These techniques involve altering, either the signal source itself, or its generation process, to target a desired pulse repetition rate.

1.3.1.1 Cavity miniaturization

Miniaturizing a laser cavity effectively reduces the round-trip time of the photons in the resonator. Mode-locking of such short cavities can generate trains of pulses with very high repetition rates.

Miniature bulk solid-state laser diodes have achieved repetition rates in the GHz regime, and even exceeding the THz [47]. However, the spectral emission bandwidth of such structures is typically low, and harmonic mode-locking (explained in the following Section) is necessary for high repetition rates.

Additionally, optical micro-resonators have attracted a great deal of attention lately as integrated sources of optical frequency combs. These integrated combs are generated through nonlinear interaction of a continuous-wave pump laser, coupled to one of the resonances, with the cavity [48]. High bandwidths (even reaching an octave) and repetition rates (from tens to hundreds of GHz) have been achieved with micro-resonator combs. However, FSR tunability is very limited (if at all possible), the generated comb suffers from intensity nonuniformity, and frequency noise in the comb modes (associated to processes such as thermo-refractive and thermo-elastic noise) is enhanced in micro-resonator cavities [23].

1.3.1.2 Harmonic mode-locking

The repetition rate of pulse trains generated by mode-locked lasers can be increased by the harmonic mode-locking technique, where several pulses are simultaneously sustained by the resonant cavity (see Fig. 1.5) [23]. This method is interesting for laser architectures where the cavity length cannot be made short enough to achieve the targeted repetition rate with a single pulse (e.g., for fiber lasers operating in the GHz regime) [49]. This technique is mainly used in actively mode-locked lasers, although passive harmonic mode-locking is also possible.

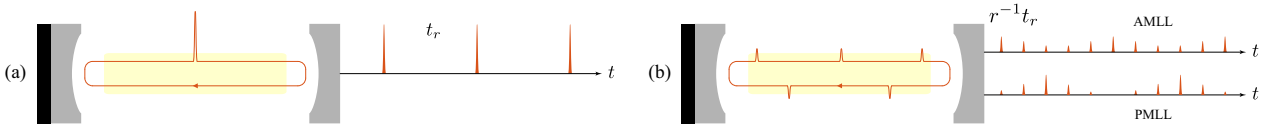

Figure 1.5 – Fundamental and harmonic mode-locking. In the fundamental mode-locking technique (a), a single pulse circulates trough the laser cavity. In the harmonic mode-locking technique (b), r pulses ($r = 5$ in the shown example) circulate in the cavity with equal temporal separation, thus multiplying the repetition rate of the laser by the factor r. In actively mode-locked lasers (AMLL), harmonic mode-locking does not ensure equal energy per pulse or phase coherent between consecutive pulses. In passively mode-locked lasers (PMLL), harmonic mode-locking may lead to burst emission.

A carefully stabilized laser cavity can exhibit lower phase noise and timing jitter[2] when exploited in a harmonic mode-locking configuration than in the fundamental mode-locking scheme. This is due to the lower interaction time between the intra-cavity generated noise and each pulse circulating through the resonator. However, this technique faces important performance and implementation shortcomings, not the least of which is a typically poor long-term stability, as the laser can switch oscillation between different sets of modes or even oscillate on different sets of modes simultaneously [23].

In actively mode-locked lasers, multiple pulses can coexist in the cavity if the modulator is driven with a harmonic of the fundamental resonant frequency. However, this does not guarantee that the pulses will be generated with equal energies. Some pulses might not be generated at all (a phenomenon known as pulse dropout). Furthermore, the mutual phase coherence between pulses of the train is not guaranteed [23]. In such situations, a frequency comb spectrum is not formed.

Passively mode-locked lasers operating under harmonic mode-locking also face the problem of nonuniform pulse-to-pulse intensity distribution. Moreover, achieving a constant pulse period is often challenging, and pulses might be emitted in bursts rather than periodically [23].

[2] See Section 1.4 for clarifications.

A number of sophisticated techniques have been developed in order to solve these problems. Some include the use of spectral filters (e.g., resonant subcavities) inserted into the resonator. Electronic feedback stabilization is often required, as well as external amplitude equalizers, typically reducing the output signal energy. The complexity of the system is thus increased, and lasers operating under harmonic mode-locking conditions typically suffer from poor long-term stability [23, 50].

Finally, arbitrary-numerator rational harmonic mode-locking, where the fundamental repetition rate is multiplied by the fraction of two arbitrary integers, has been demonstrated [51]. However, the mentioned problems of stability and nonuniform pulse-to-pulse intensity distributions are accentuated in this technique.

1.3.2 Period manipulation through signal processing

The period of a repetitive signal can be modified through signal processing operations. These are performed on the optical signal itself, outside the laser cavity, and therefore, they tend to be more versatile than the previously explained methods, as virtually any signal can be targeted, independently of its source. Such operations involve manipulation of the signal in the time domain – temporal modulation – and/or manipulation of its frequency spectrum – spectral filtering. Depending on the nature of said manipulations, signal processing methods can be categorized in two groups: methods that manipulate the energy content of the signal directly, and methods that manipulate the phase distributions of the signal.

1.3.2.1 Methods based on direct energy manipulation

Traditional, well-established approaches for periodicity control through manipulation of pulse trains and frequency combs include spectral amplitude filtering and temporal pulse picking (or time gating), sketched in Fig. 1.6.

A spectral amplitude filter is a straightforward way of directly multiplying the FSR of a frequency, simply by eliminating $r-1$ out of each r consecutive comb lines. This effectively produces an r-fold increase of the FSR [39, 40], and an associated r-fold reduction of the pulse period of the train [52].

The dual operation is also possible, in the form of pulse picking [53], where a temporal amplitude gate – on/off amplitude modulation – selects one pulse out of each r consecutive pulses and throws away the remaining $r-1$. The repetition period is then directly increased by r, and the associated FSR of the corresponding comb spectrum is reduced by the same factor.

The main drawback of these approaches is their low energy efficiency. Both methods involve the deliberate discarding of a fraction $1-r^{-1}$ of the original signal energy, resulting in an energy loss that increases with the factor r. Amplification may then become necessary, thus incurring in the associated SNR degradation, unavoidable in classical active processes [16].

Additionally, these methods suffer from practical implementation shortcomings. The amplitude filtering method needs high-finesse filters, with tight design and operational requirements (e.g., precise spectral alignment between the filter and the comb, sustainable over long periods of time), in order to achieve signals with high temporal and spectral quality. Unsuppressed comb lines will result in residual pulse-to-pulse amplitude fluctuations in the time domain (see Fig. 1.6(a)) [54]. Similarly, the imperfect suppression of undesired pulses in pulse picking techniques results in spectral line-to-line amplitude fluctuations of the obtained comb (see Fig. 1.6(b)). The relatively low extinction ratio of current electro-optic intensity modulators often forces to use optical gates based on nonlinear effects (incurring in even higher energy inefficiency), or optical switches based on semiconductor optical amplifiers and acousto-optic modulators (with typically low

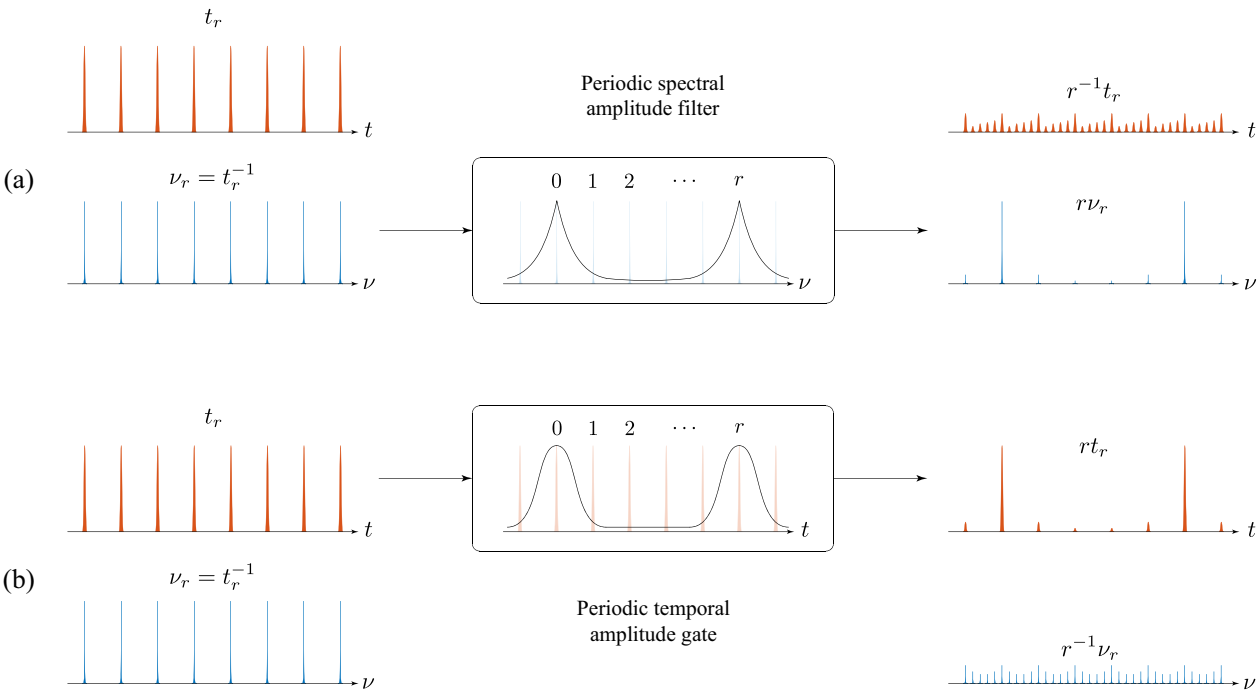

Figure 1.6 – Signal processing methods for period control through direct energy manipulation. Traditional periodicity control methods for trains of optical pulses and optical frequency combs: (a) spectral amplitude filtering and (b) pulse picking by temporal amplitude gating (shown example for a period multiplication factor $r = 5$).

operation speeds). Moreover, a precise timing between the pulse train and the pulse picking gate becomes a critical factor for a correct pulse suppression.

Approaches aimed at mitigating the problem of energy loss in pulse picking methods, such as coherent addition of pulses in optical cavities, have also been demonstrated. However, these require stringent operation conditions, difficult to achieve and maintain, including precise matching between the cavity round-trip and the pulse period, as well as the need for offset frequency stabilization [55].

Last, but not least, the very nature of these techniques forces the factor r to be necessary integer. This is due to the fact that one can only suppress an integer number of pulses/lines. Fractional period multiplication/division could be achieved through combinations of amplitude filtering and pulse picking techniques, suffering from the critical aforementioned drawbacks associated to both methodologies.

Versatile methods to control the pulse period of optical trains and the FSR of frequency combs with high energy efficiency and low signal degradation based on passive, linear processes are highly desired.

1.3.2.2 Methods based on phase manipulation

Signal processing solutions to the periodicity control problem based on phase-only manipulations – temporal phase modulation and/or spectral phase filtering – are particularly attractive (see Fig. 1.7). Phase transformations recycle the total energy carried by the target signal into an output signal that satisfies the required specifications. Additionally, such solutions offer an increased tolerance to practical implementation errors, greatly relaxing the design requirements of methods involving direct amplitude manipulations.

Considering all these important advantages, several techniques for periodicity manipulation through phase-controlled energy redistribution have been proposed. In particular, an important set of these techniques

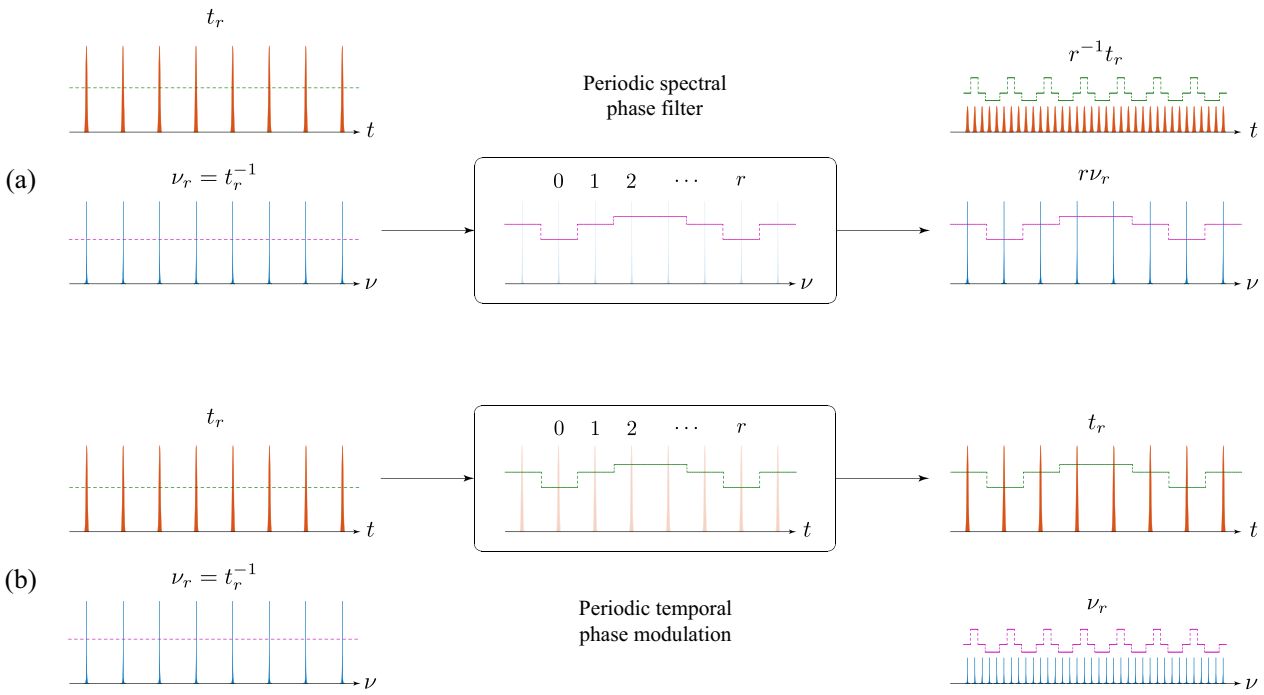

Figure 1.7 – Signal processing methods for period control through phase-only manipulation. Examples of (a) pulse period division (repetition rate multiplication) through periodic spectral phase filtering, and (b) FSR division through periodic temporal phase modulation (both temporal and spectral phase profiles are shown in dashed line). The period of repetition is, in both cases, divided by an integer number ($r = 5$ in the shown example), and phase variations remain in both time and frequency domains in both situations.

relies on periodic phase transformations based on the theory of Talbot self-imaging[3]. Such methods have been developed to achieve multiplication and/or division of the repetition period of pulse trains by arbitrary (integer or fractional) factors [56–58] [APj1, APj4]. Likewise, Talbot-based methods have been also reported to achieve multiplication and/or division of the FSR of frequency combs by arbitrary (integer or fractional) factors [59–61] [APj5]. Some of these methods are, in fact, proposals reported in this dissertation.

Due to their inherent phase-only nature, these approaches ideally preserve the total energy of the signal of interest, where the desired output signal is obtained from a coherent redistribution of the energy of the input signal. As such, methods based exclusively on phase transfomations have the potential to reduce the impact of noise by focusing the energy of a periodic signal on a lower number of output periods [57] [APj1, APj4, APj5]. Such methods offer an attractive signal processing solution to the periodicity control problem. However, all proposed solutions only implement the targeted period transformation in one representation domain. The schemes defined for pulse repetition rate control involve a combination of temporal phase modulation and spectral phase filtering (e.g., dispersive propagation) [56–58], and generally, they do not implement the counterpart FSR control in the related frequency comb spectrum. Moreover, designs aimed at frequency comb periodicity control proposed prior to the realization of the work reported in this dissertation have only achieved FSR division by integer factors, and they also do not implement the counterpart repetition rate control on the corresponding pulse train [59–61]. In both situations, residual phase variations remain uncompensated on the dual domain (see Fig. 1.7). Establishing the nature and characteristics of such residual phase variations remains an unsolved problem.

[3]For a review of Talbot self-imaging, consult Section 2.4, and for detailed analysis, consult Chapter 3.

1.4 Mitigation of noise in periodic optical signals

Our ability to detect signals or events and to extract information contained therein is ultimately limited by the strength of said signal and that of every other unwanted event detected simultaneously. Such unwanted events conform the noise content of the measurement and, although it arises in the form of many different manifestations, noise is ubiquitous, and its origin mechanisms are often random and difficult to control.

Random noise is a fundamental limiting factor in the detection of any physical event [62]. In particular, the problem of noise mitigation in periodic signals is intrinsic to scientific disciplines like spectroscopy [42, 63], and radio-astronomy [39, 64], to name a few. Additionally, technological fields such as sensing [OPj12], telecommunications [14, 28], and data processing [65], face similar challenges when dealing with the inherent noise present alongside the signals of interest.

Periodic signals experience different kinds of noise. These include random fluctuations of the amplitude of the signal period-to-period, random fluctuations of the phase of the signal period-to-period, random fluctuations of the instantaneous phase distribution within each individual pulse, random additive noise (including amplitude and phase fluctuations) with a specific spectral content (e.g., white Gaussian noise, as generated by optical amplifiers), and random fluctuations of the period duration (known as timing jitter). Fig. 1.8 illustrates these noise mechanisms in periodic signals.

The problem of noise mitigation has been treated in depth for signals in their *real domain* of representation, i.e., the domains of time (for temporal signals) or space (for spatial images). It should be noted, however, that the problem becomes particularly challenging when the information of interest is available along the *Fourier domain* representation of the processed signal, e.g., the frequency domain for temporal waves. Frequency combs are a good example of such situations [66], as the measurement, detection and study of physical systems and processes is often performed in the frequency domain, e.g., through the vast family of comb-based spectroscopy techniques [25, 42]. Furthermore, the presence of random noise fluctuations across the comb frequency spectrum has a critical impact on its performance quality, e.g., degrading the SNR of comb-based telecommunication systems [28, 29], deteriorating the quality of spectroscopic measurements [42], or limiting the accuracy of astronomical spectrometry [67]. Nonetheless, suchlike any problem involving measurements directly in the Fourier domain of frequencies, reducing the noise floor of a frequency comb poses significant challenges.

Similarly to the problem of periodicity control, techniques to mitigate the noise of periodic optical signals can be classified as methods that affect the generation process and methods that affect the generated signal.

1.4.1 Control of the generation mechanism

Based on their point of origin, noise mechanisms in mode-locked lasers fall into one of two categories: noise generated within the laser cavity, and noise generated outside the laser cavity [68].

Intracavity noise arises from fluctuations of the pump power, environmental perturbations of the cavity length and amplified spontaneous emission (ASE) photons generated within the laser cavity. This results in the broadening of the individual comb lines, that acquire a finite linewidth, as opposed to the ideal case of an infinitely-narrow frequency component. Linewidth broadening results in fluctuations of the repetition rate over time – timing jitter – and pulse-to-pulse amplitude and phase variations. These mechanisms produce a noise content that is generally well-behaved and easy to model. As a result, its contribution can, in general, be suppressed through feedback in order to stabilize the generation process [68].

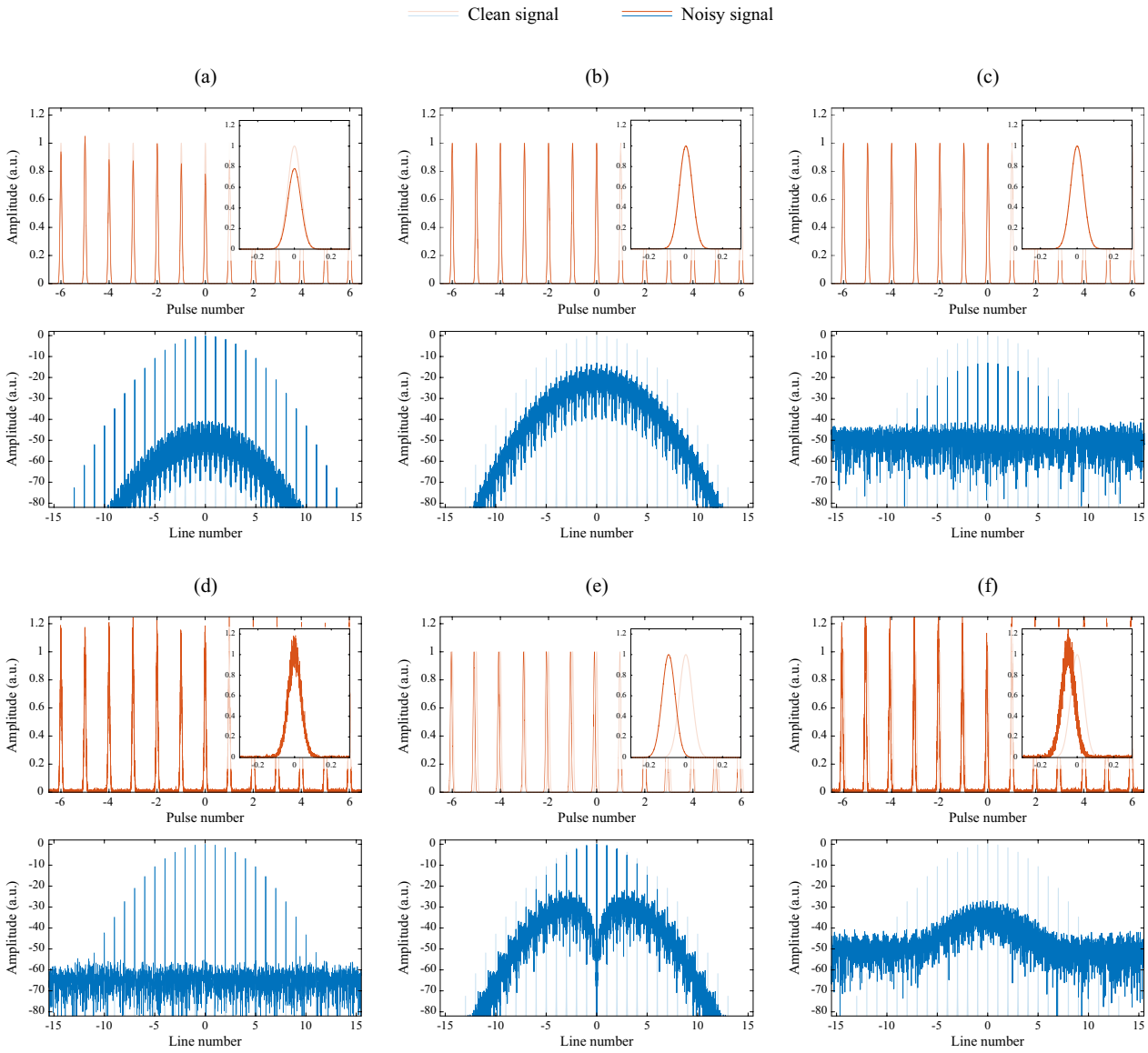

Figure 1.8 – Noise mechanisms in periodic signals. Numerical simulation showing different forms of noise on periodic signals; power distributions shown in the time (top) and frequency (bottom) domains: (a) pulse-to-pulse amplitude fluctuations, (b) pulse-to-pulse phase fluctuations, (c) intra-pulse phase fluctuations, (d) additive white Gaussian noise, (e) timing jitter, and (f) a combination of all of them.

Extracavity noise sources are mainly associated to shot noise and ASE resulting from amplification processes outside of the laser cavity, typically required to induce spectral broadening of the comb, fundamental for operations such as the stabilization of the offset frequency through f-$2f$ interferometry [33, 68]. Such noise contributions can, in most cases, be modeled as additive white Gaussian noise, provided that their power spectral density is mostly uniform throughout the majority of the signal's spectrum (which is a reasonable assumption as long as the signal of interest fits within the gain bandwidth of the amplifier responsible for injecting the noise). Extracavity noise mechanisms cannot be suppressed in a deterministic way, as the fluctuations introduced across the comb frequency spectrum are independent of the signal source. The result is a noise floor that reduces the visibility of the comb lines (see Fig. 1.8) [68].

Mitigating the impact of the uncorrelated spectral noise floor in periodic optical signals is an interesting problem, generally difficult to approach, but of great importance for achieving an adequate practical performance quality of the signal of interest.

1.4.2 Noise mitigation by signal processing

Signal processing solutions can help mitigating the extra-cavity noise contribution. Amplitude filtering is perhaps the most straightforward method for noise mitigation of arbitrary signals. A band pass filter rejects the power spectral density of noise at frequencies outside the bandwidth of the signal of interest, so-called out-of-band noise [69]. This method, however, cannot remove the noise located in-band with the signal of interest.

In the case of optical frequency combs, a periodic optical filter, aligned with the comb lines, could, in principle, be used for mitigation of the in-band noise spectral components (sharing the bandwidth occupied by the signal). But this would require extremely precise design, fine-tuning and alignment of the filter [67], including accurate a priori knowledge of the absolute frequencies of the comb lines.

Alternatively, for periodic signals, both in-band and out-of-band noise contributions can be mitigated by directly averaging the value of the signal of interest over several consecutive periods [70]. This method mitigates both in-band and out-of-band noise contributions, however, it requires the detection of many consecutive realizations of the signal, followed by a numerical post-processing step.

As mentioned in Section 1.3.2.2, it was recently shown that techniques based on redistributing the energy of the periodic signal of interest into a lower number of periods prior to detection effectively implements a coherent addition of the repetitive waveform only (not the incoherently-related noise), thus enabling effective noise mitigation in a deterministic way. Such a mechanism can be practically realized by use of generalized Talbot self-imaging phenomena in temporally-dispersive media; a process that has been referred to as *passive Talbot amplification* [57]. Noise mitigation through this process can outperform classical averaging, e.g., achieving higher levels of extinction ratio in a single measurement [57], and even enabling the access to fractional averaging factors (a feat not allowed by conventional statistics, as shown in Chapter 4) [APj1], as well as the detection of signals originally buried completely under incoherent noise [APj5].

1.5 Motivation

1.5.1 Definition of the project

The main objective of this dissertation is *to propose and demonstrate a universal method to control the period of repetitive optical signals, in such a way that the energy carried by the signal of interest is preserved in the process, while the rest of its properties remain unaltered* (e.g., bandwidth and temporal duration), *and without introducing any external noise or distortion*.

1.5.2 Proposed solution

The proposed solution involves *the formulation of a generalization of the Talbot effect, so that the period of a repetitive signal can be arbitrarily tailored exclusively through manipulations of the temporal and spectral phase distributions of the signal* – inherently energy-preserving.

1.5.3 Additional considerations

Although the method for arbitrary period control (proposed and explained in chapter 3, and experimentally demonstrated in chapters 4 and 5) is universal in its formulation (it applies to periodic waves in any domain of representation, in particular, time, frequency, position and transverse momentum, and in any regime, e.g., radio, microwaves, optics, etc, potentially even extending to other platforms, such as acoustics, matter waves, thermal waves, etc), this dissertation focuses on the arbitrary manipulation of optical spectra by energy-preserving means, aimed at developing techniques that can be of use for the processing and generation of optical frequency combs (discussed in chapter 5).

Additionally, the method produces interesting results when applied to aperiodic signals, e.g., to isolated pulses or to modulated sequences of pulses (e.g., telecommunication data signals), which have continuous spectra. These results, as well as potential practical applications, are discussed in chapter 6.

CHAPTER 2

Review of linear wave propagation and the Talbot effect

This chapter provides the basic mathematical and physical background used in the developments and discussions along this dissertation. Fundamental concepts of optical wave propagation and basic wave operations are revised, with particular emphasis on the mathematical formalism describing the temporal evolution of optical waves. A brief overview of the theory of Talbot effect is presented, enunciated in the framework of Fourier analysis and signal processing. This interesting phenomenon is at the core of the methods and techniques proposed in this thesis.

2.1 Mathematical modeling of the evolution of waves

A proper understanding of the properties of optical waves and the mechanisms governing their interactions with matter requires the electromagnetic theory of light. Furthermore, light is emitted and absorbed in wavepackets called photons, which exhibit properties of both waves and particles simultaneously. Phenomena such as the photo-electric effect and the nature of non-classical light are explained by the photon theory of light, and studied in the field of quantum optics. However, phenomena such as diffraction and interference can be accurately described by the wave theory of light. The formalism of wave optics models the interaction of optical waves with objects and systems whose dimensions are comparable to the wavelength. This approximation, together with the fundamentals of Fourier analysis, is a sufficient theoretical basis for the derivations and findings reported in this dissertation.

This Chapter provides a brief review of said topics. Section 2.2 briefly presents the mathematical formulation of the wavefunction (i.e., the analytical construction used to model the evolution of waves). Section 2.3 summarizes the basic concepts of temporal wave propagation (i.e., the mathematical modeling of the temporal evolution of waves along their interaction with systems), with special attention to the operator formulation of linear wave dynamics in the domains of time and frequency. Such a formulation is strongly based on the discipline of Fourier analysis and the principle of harmonic decomposition; a review covering these topics is provided in Appendix A. Finally, Section 2.4 introduces the Talbot effect, a phenomenon upon which the entirety of this dissertation is based.

2.2 Wave theory of light

This section introduces the basic concepts and definitions necessary to model light as scalar waves propagating through free space and dielectric media. The contents of this Section are a summary of concepts, compiled from the following sources: [16, 71].

2.2.1 Speed of light and refractive index

A wave is a dynamic perturbation of a medium that either stores or propagates energy through it. Wave optics describes the propagation of light as electromagnetic waves that travel through a medium with velocity c, so that,

$$c = \frac{c_0}{n} \tag{2.1}$$

where $c_0 = 299792458$ m/s is the speed of light in the vacuum, and $n \geq 1$ is a constant[1] known as the refractive index of the medium[2].

[1] In general, n is a function of position, $\mathbf{r}$, so that for a given trajectory, S, within the propagation medium, the optical path length, δs (which is proportional to the time taken by the wave to traverse the trajectory S) is,

$$\delta s = \int_S n(\mathbf{r})\,\mathrm{d}s \tag{2.2}$$

where $\mathrm{d}s$ is a differential element of length along the path S.

[2] It should be noted that under certain conditions, plasmas and X-rays may exhibit a refractive index below unity [72].

2.2.2 The wave equation

Mathematically, a wave is described by a real scalar function, $\Upsilon : (\mathbb{R}^3, \mathbb{R}) \to \mathbb{R}$, of position, $\mathbf{r} = x\hat{\mathbf{x}}+y\hat{\mathbf{y}}+z\hat{\mathbf{z}}$, and time, t, known as the wavefunction. Wavefunctions are solutions of the wave equation,

$$\left(\nabla^2 - \frac{1}{c^2}\frac{\partial^2}{\partial t^2}\right)\Upsilon(\mathbf{r}, t) = 0 \tag{2.3}$$

where ∇^2 is the Laplacian operator,

$$\nabla^2 := \frac{\partial^2}{\partial^2 x} + \frac{\partial^2}{\partial^2 y} + \frac{\partial^2}{\partial^2 z} \tag{2.4}$$

Note that Eq. 2.3 is linear, and thus, the principle of superposition holds: the sum of wavefunctions is itself a wavefunction.

It will be convenient to write the real wavefunction, $\Upsilon(\mathbf{r}, t)$ as the real part of a complex function, $\psi : (\mathbb{R}^3, \mathbb{R}) \to \mathbb{C}$, so that, $\Upsilon(\mathbf{r}, t) = \mathcal{R}e\{\psi(\mathbf{r}, t)\}$.

2.2.2.1 Monochromatic waves

If the wave of interest is represented by a wavefunction with harmonic time dependence, it is said to be monochromatic[3]. The complex wavefunction writes then,

$$\psi(\mathbf{r}, t) = \psi(\mathbf{r})e^{i\omega t} \tag{2.5}$$

where ω is the radial frequency of the wave, measured in rad/s. From a practical viewpoint, it is often convenient to measure the linear frequency[4] (or simply, frequency), ν, in Hz, so that,

$$\omega = 2\pi\nu \tag{2.6}$$

This definition is convenient because it immediately relates to the temporal period of the monochromatic wave, $t_0 = \nu^{-1}$, i.e., the time (in seconds) that the wave takes to complete a cycle. Fig. 2.1 shows a representation of the wavefunction of a monochromatic wave.

The complex wavefunction necessarily satisfies the wave equation. Using Eq. 2.5 in Eq. 2.3,

$$\left(\nabla^2 + \text{ƙ}^2\right)\psi(\mathbf{r}) = 0 \tag{2.7}$$

[3] Practically, in the context of visible light propagation, monochromatic waves are those that carry only one color.

[4] Optical waves are most commonly classified as those whose frequency ranges from ∼300 GHz to ∼3 PHz, i.e., from the far infrared to the near ultraviolet (including the visible spectrum, roughly ranging from ∼430 THz to ∼750 THz). However, the postulates of wave optics still apply to all regions of the electromagnetic spectrum (including radio-frequency, microwaves, etc).

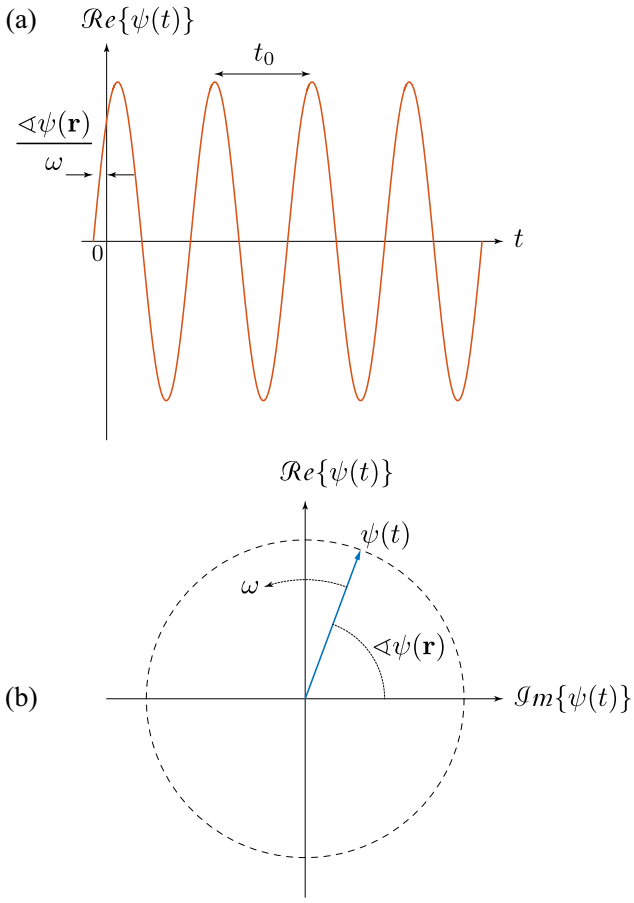

Figure 2.1 – Monochromatic wave. Representation of a monochromatic wave at a fixed position in space. (a) The wavefunction is harmonic in time, and it oscillates at a fixed frequency, ω. (b) The complex wavefunction is a phasor of fixed length that rotates with angular velocity ω.

Eq. 2.7 is known as the Helmholtz equation, and $\hbar$ is the wavenumber,

$$\hbar = \frac{\omega}{c} \tag{2.8}$$

The spatial phase of the wave, $\sphericalangle\psi(\mathbf{r})$, defines the wavefronts, as equiphase surfaces, i.e., surfaces satisfying $\sphericalangle\psi(\mathbf{r}) = 2l\pi \;\forall\; l \in \mathbb{Z}$.

2.2.2.2 Plane waves

The most basic solution of the wave equation is the plane wave, defined by a complex amplitude,

$$\psi(\mathbf{r}) = \psi_0 e^{-i\mathbf{k}\cdot\mathbf{r}} \tag{2.9}$$

where ψ_0 is a generally complex constant, and $\mathbf{k} = \hbar_x\hat{\mathbf{x}} + \hbar_y\hat{\mathbf{y}} + \hbar_z\hat{\mathbf{z}}$ is the vector that defines the propagation direction of the plane wave, known as the wavevector (see Fig. 2.2). Note that $\hbar_x^2 + \hbar_y^2 + \hbar_z^2 = \hbar^2$, so that $|\mathbf{k}| = \hbar$.

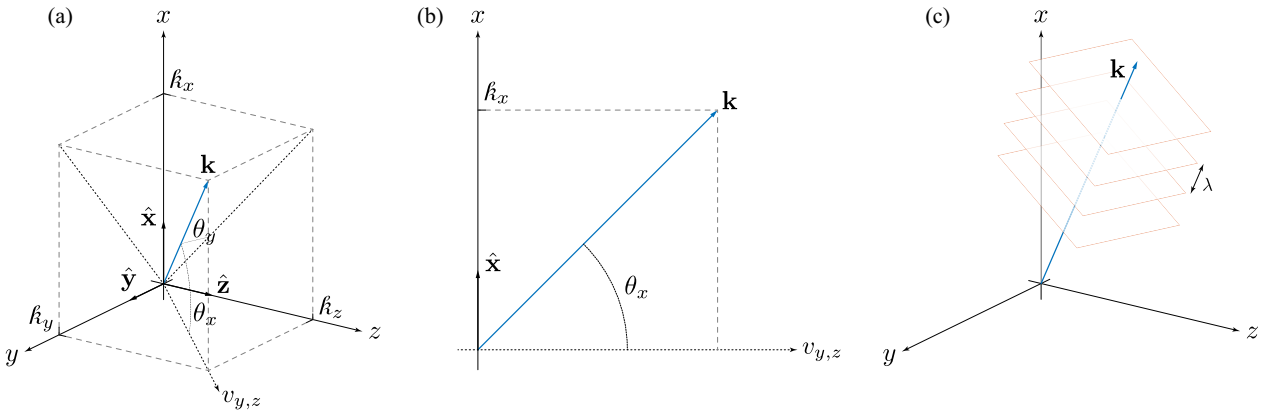

Figure 2.2 – The wavevector. The wavevector, $\mathbf{k} = \hbar_x\hat{\mathbf{x}} + \hbar_y\hat{\mathbf{y}} + \hbar_z\hat{\mathbf{z}}$, unambiguously describes a plane wave with wavenumber $\hbar = |\mathbf{k}|$, propagating in the direction of $\mathbf{k}$. (a) Components of the wavevector in Cartesian coordinates; $v_{y,z}$ denotes the direction of the projection of the vector $\mathbf{k}$ onto the plane $\{y, z\}$. (b) Detail of the wavevector components in the plane that contains the vector $\mathbf{k}$ and its projection onto the plane $\{y, z\}$. (c) Wavefronts of a plane wave (note that the equiphase surfaces of a plane wave are boundless planes, here depicted as squares for illustration purposes).

The spatial phase of the plane wave writes, $\sphericalangle\psi(\mathbf{r}) = \sphericalangle\psi_0 - \mathbf{k}\cdot\mathbf{r}$. Since $\sphericalangle\psi_0$ is a real constant, the wavefronts satisfy the equation of parallel planes, perpendicular to $\mathbf{k}$ (see Fig. 2.2(c)),

$$\hbar_x x + \hbar_y y + \hbar_z z = \sphericalangle\psi_0 + 2l\pi \;\forall\; l \in \mathbb{Z} \tag{2.10}$$

The separation between wavefronts is $\hbar^{-1}2\pi$. This quantity is known as the wavelength, λ, so that,

$$\lambda = \frac{c}{\nu} \tag{2.11}$$

It should be noted that, as a wave travels through a medium, its phase velocity[5] (and consequently, its wavelength), is reduced by the refractive index, n; its frequency, however, remains unaltered.

Taking z as the reference dimension, the wavevector makes angles θ_x and θ_y with the planes $\{y, z\}$ and $\{x, z\}$, respectively (as shown in Fig. 2.2(a)), so that,

$$\hbar\sin(\theta_x) = \hbar_x \tag{2.12}$$
$$\hbar\sin(\theta_y) = \hbar_y \tag{2.13}$$

These angles are related to the concept of *spatial frequency*, which arises from the principle of plane wave decomposition. In general, an arbitrary spatial wavefront can be expressed as a sum of plane waves with different wavevectors through application of the Fourier transform. This is the basis of the discipline of *Fourier optics* [16, 71], and it is mathematically equivalent to the principle of harmonic decomposition in the Fourier analysis formalism of signals and systems[6] [73, 74].

[5]The phase velocity of a wave is the rate at which its phase propagates in space. This is the velocity at which the phase of any one frequency component of the wave travels.

[6]For further details about Fourier analysis and the signals and systems formalism, consult Appendix A.

2.3 Temporal evolution of waves

Many physical phenomena manifest as variations of the properties of waves with time. For instance, pulsar stars are precisely studied thanks to the highly accurate timing of the fluctuations in the light waves they emit. Furthermore, the measurement and control of temporal variations in propagating waves is the cornerstone of areas of technology, such as signal processing, telecommunications and computing, ubiquitous in modern-day society.

The contents of this Section are a summary of concepts, compiled from the following sources: [16, 75].

2.3.1 Propagation of light through dielectric media

Consider a monochromatic plane wave propagating through a dielectric medium, along the z axis,

$$\psi(\mathbf{r}, t) = \psi_0 e^{i(\omega t - \hbar z)} \tag{2.14}$$

The medium will reduce the propagation speed of the wave with respect to c_0 by its refractive index (see Eq. 2.1). Additionally, it will absorb a fraction of the energy carried by the wave. This is represented by a complex-valued wavenumber, of the form,

$$\hbar := \beta - i\frac{\alpha}{2} \tag{2.15}$$

where $\beta = \hbar n \in \mathbb{R}$ is the propagation constant of the wave in the medium (the rate at which the phase changes with z), and $\alpha \in \mathbb{R}$ is the attenuation coefficient (the rate at which the amplitude decreases[7] with z). Note that the propagation constant can be either positive or negative.

A plane wave with an arbitrary temporal amplitude can be written as,

$$\psi(\mathbf{r}, t) = \psi(t) e^{-i\hbar z} \tag{2.16}$$

As a consequence of the principle of harmonic decomposition[8], an arbitrary temporal amplitude can be expanded as a superposition of monochromatic waves oscillating at different radial frequencies, through application of the Fourier transform.

$$\Psi(\omega) = \int_{-\infty}^{\infty} \psi(t) e^{-i\omega t}\, \mathrm{d}t \tag{2.17}$$

$$2\pi\psi(t) = \int_{-\infty}^{\infty} \Psi(\omega) e^{i\omega t}\, \mathrm{d}\omega \tag{2.18}$$

where $\Psi(\omega)$ is the frequency spectrum of the wave.

[7] It should be noted that in active propagation media, such as in optical amplifiers, α will actually contribute to increase the wave amplitude. Here, however, only passive propagation media is considered.

[8] For further details on the principle of harmonic decomposition and its relationship to Fourier analysis, consult Appendix A.

Both the real and imaginary parts of the wavenumber, β and α, are frequency-dependent real functions. The propagation constant can be expressed as a Taylor series expansion around the central frequency of the wave, ω_0, often referred to as the carrier frequency,

$$\beta(\omega) = \sum_{l=1}^{\infty} \frac{\beta_l}{l!}(\omega - \omega_0)^l \tag{2.19}$$

where,

$$\beta_l = \left. \frac{\partial^l}{\partial \omega^l} \beta(\omega) \right|_{\omega=\omega_0} \tag{2.20}$$

2.3.1.1 Complex envelope and the narrow-band approximation

A large set of interesting physical phenomena manifest in the form of waves whose spectra consists of a certain range of frequency components, centered around a specific frequency value, ω_0. These include the paradigm of optical pulsed waveforms, particularly relevant in the context of this dissertation.

In such situations, it is usually convenient to write the temporal amplitude in terms of a complex temporal envelope, $\tilde{\psi}(t)$, and an oscillatory term at ω_0, representing the central – carrier – frequency,

$$\psi(t) = \tilde{\psi}(t) e^{i\omega_0 t} \tag{2.21}$$

In this formulation, the complex envelope $\tilde{\psi}(t)$ is known as the equivalent base-band signal. This allows for a convenient representation of the frequency spectrum around a normalized central frequency, through the change of variables $\omega \leftarrow \omega - \omega_0$.

If $\tilde{\psi}(t)$ varies slowly with time, the wave is considered narrow-band. This results on a localized frequency spectrum, that does not extend far from the central component, ω_0. In this situation, it becomes reasonable to expect the high-order derivatives of $\beta(\omega)$ to approach 0 at frequencies close to ω_0. Neglecting high-order terms in the Taylor series expansion of $\beta(\omega)$ (typically $l > 2$ in Eq. 2.19) is known as the narrow-band approximation.

2.3.1.2 The nonlinear Schrödinger equation

The nonlinear Schrödinger equation (NLSE) models the propagation of optical waves through dielectric media. This equation takes into consideration both linear and nonlinear phenomena. For the temporal envelope of a wave propagating through a dielectric with propagation constant β and attenuation α, along the z direction, the NLSE writes,

$$\left(\frac{\partial}{\partial z} - \beta_0 + i \sum_{l=1}^{\infty} \frac{\beta_l}{i^l l!} \frac{\partial^l}{\partial t^l} + \frac{\alpha}{2} + i\gamma |\tilde{\psi}(z,t)|^2 \right) \tilde{\psi}(z,t) = 0 \tag{2.22}$$

where γ is the nonlinear parameter of the medium, responsible for the occurrence of a nonlinear temporal phase-shift, proportional to the power distribution of the wave, along its propagation through the medium. Note that, as per Eq. 2.16, for a plane wave propagating in the z direction, $\tilde{\psi}(z,t) = \tilde{\psi}(t)e^{-i\hbar z}$.

A case of particular interest in the context of this dissertation is the linear propagation of waves through transparent, second-order dispersive media, characterized by $\alpha = 0$, $\gamma = 0$, and $\beta_l = 0 \; \forall \; l \neq 2$. The resulting NLSE (now a linear equation) writes,

$$\left(\frac{\partial}{\partial z} - i\frac{\beta_2}{2}\frac{\partial^2}{\partial t^2} \right) \tilde{\psi}(z,t) = 0 \tag{2.23}$$

2.3.2 Temporal wave propagators

The temporal evolution of scalar electromagnetic waves along their propagation through optical media can be described by the formalism of signals and systems theory[9]. The effect of an optical system on a impinging wave is characterized by a linear operator, known as a wave propagator. The propagator can be expressed both in the time domain, $\hbar(t)$, and in the frequency domain, $\mathcal{H}(\omega)$. If the system implements an operation that is linear (i.e., it satisfies the principle of superposition for any number of input waves) and invariant to displacements in t (i.e., it remains equal for input waves affected by different temporal delays), $\hbar(t)$ is said to be the temporal impulse response of the system, and $\mathcal{H}(\omega)$, its spectral transfer function, forming a Fourier transform pair. The system described by such an operator is then said to be linear and time-invariant (LTI).

In the following, two important examples of temporal wave transformations – temporal modulation and chromatic dispersion – are discussed.

2.3.2.1 Temporal modulation

Temporal modulation is the process by which an optical system introduces a time-dependent change to the complex amplitude of a wave. The process is described by the multiplication of the complex amplitude of the impinging wave in the time domain, $\psi(0,t)$, by the temporal modulation function, $\hbar_{\text{TM}}(t)$, so that,

$$\psi(z,t) = \hbar_{\text{TM}}(t)\psi(0,t) \tag{2.24}$$

where here it is assumed that the wave enters the system at $z = 0$, and then travels through it along the propagation axis, z.

In the Fourier domain, the operation is described by the convolution integral between the frequency spectrum of the wave, $\Psi(0,\omega)$, and the Fourier transform of the temporal modulation function, $\mathcal{H}_{\text{TM}}(\omega)$,

$$\Psi(z,\omega) = \frac{1}{2\pi}\int_{-\infty}^{\infty} \mathcal{H}_{\text{TM}}(\Omega)\Psi(0,\omega-\Omega)\,\mathrm{d}\Omega \tag{2.25}$$

Fig. 2.3 schematically depicts the operation.

[9] For a review of basic concepts of signals and systems theory, consult Appendix A.

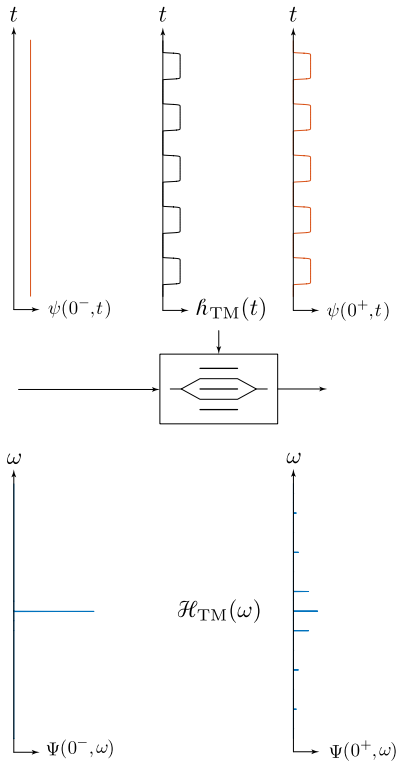

Figure 2.3 – Temporal modulation. Operator model of the temporal modulation process. The shown example consist on a periodic, real modulation function. The modulator – the optical system used to carry out the modulation process – is considered infinitesimally thin, making the process spatially localized; the notation $z = 0^+$ and $z = 0^-$ refer to the planes immediately before and after the modulator, respectively. (top) Real space. (bottom) Fourier space.

The temporal modulation function can be purely real, in which case the process is referred to as amplitude modulation, a complex function with uniform magnitude, in which case the process is referred to as phase modulation, or a combination of both, in which case the process is referred to as complex, or I/Q modulation.

If $\psi(0,t)$ is a monochromatic wave (i.e., a wave with a spectrum consisting of a single frequency component), the temporal modulation process will generate an output frequency spectrum, $\Psi(z,\omega)$, with additional frequency components. Temporal modulation transforms monochromatic waves into polychromatic waves.

In practice, this process is achieved through nonlinear interaction between two waves, e.g., a radio-frequency voltage wave and an optical wave in an electro-optical modulator, or two optical waves in a nonlinear medium. However the process is in any case described by an operator that satisfies the principle of superposition[10]; the transformation is, thus, linear. On the other hand, the operator is not time-invariant. This is immediately verified as the transformations suffered by the wave of interest are directly proportional to the temporal variations of the modulation function. This time-dependence is the mechanism responsible for the generation of new frequency components in the spectrum of the wave of interest.

2.3.2.2 Chromatic dispersion

Chromatic dispersion is the process by which different frequency components of a light wave traverse an optical medium at different propagation velocities. This is the consequence of a propagation constant with a nonlinear dependence with frequency.

[10]For further clarification, consult Appendix A.

Neglecting the losses of the medium – the medium is then said to be transparent – and assuming linear propagation ($\alpha = 0$ and $\gamma = 0$ in Eq. 2.22), the chromatic dispersion operator is a complex, unitary transfer function,

$$\mathscr{H}_{\text{GVD}}(\omega) = e^{-i\beta(\omega)z} \tag{2.26}$$

This way, the output spectrum writes,

$$\Psi(z,\omega) = \mathscr{H}_{\text{GVD}}(\omega)\Psi(0,\omega) \tag{2.27}$$

This operation is LTI, as it satisfies the principle of superposition, and it applies equally to any time-delayed copy of the same input wave.

As previously mentioned, in the narrow-band approximation, the high-order terms of the propagation constant ($l > 2$ in Eq. 2.19) are neglected. The spectral phase factor in Eq. 2.26 writes then,

$$\beta(\omega)z \approx \beta_0 z + \beta_1 z\omega + \frac{1}{2}\beta_2 z\omega^2 \tag{2.28}$$

The transit of the wave through the medium has an associated propagation delay. This delay is, in general, different for each constituent frequency component of the wave, due to the effect of dispersion. The group delay, $t_g(\omega)$, is the time it takes the complex envelope to traverse the medium,

$$t_g(\omega) := -\frac{\partial}{\partial\omega}\beta(\omega)z \tag{2.29}$$

and the group velocity – the speed at which the complex envelope propagates through the medium – is then,

$$v_g(\omega) = \frac{z}{t_g(\omega)} \tag{2.30}$$

It follows then that if the group delay experienced by the wave in the medium is a linear function of frequency, the wave obtained at the output of the medium is simply a delayed copy of the input one. Using Eq. 2.28 in 2.29, the group delay associated to the propagation of the wave through the medium in the narrow-band approximation writes,

$$t_g(\omega) \approx -\beta_1 z - \beta_2 z\omega \tag{2.31}$$

The term $\beta_0 z$ in Eq. 2.28 introduces a constant phase-shift to the frequency spectrum, equal for all frequency components of the wave. This translates into a constant phase term along the time-domain representation of the signal, and, as per Eq. 2.31, it has no effect on the group delay distribution. The term $\beta_1 z\omega$ in Eq. 2.28 introduces a spectral phase-shift, linear with the frequency variable; this, as per Eq. 2.31, translates into a constant delay for all frequency components of the wave. This term can be neglected by choosing a reference frame that moves with the wave, at speed β_1^{-1}, i.e., by applying the change of variables $t \leftarrow t + \beta_1 z$.

The terms with $l \geq 2$ in the $\beta(\omega)$ decomposition are known as the chromatic dispersion coefficients. In particular, the term $\beta_2 z$ in Eq. 2.28 introduces a phase-shift to the spectrum of the wave, with a quadratic

dependence with frequency. As per Eq. 2.31, this term translates into a linear variation of the group delay frequency distribution, resulting in different frequency components traveling through the medium at different speeds. The product $\beta_2 z$ is, thus, commonly known as group velocity dispersion (GVD).

Considering only the second-order dispersion coefficient, β_2 (GVD per unit length, measured at the central frequency of the wave), the dispersion transfer function writes,

$$\mathcal{H}_{\mathrm{GVD}}(\omega) = e^{-i\frac{1}{2}\beta_2 z\omega^2} \tag{2.32}$$

The inverse Fourier transform of Eq. 2.32 gives the impulse response of the second-order dispersion process in the medium,

$$h_{\mathrm{GVD}}(t) = e^{i\frac{1}{2\beta_2 z}t^2} \tag{2.33}$$

and the associated time-domain input/output relationship is defined as a convolution integral,

$$\psi(z,t) = \int_{-\infty}^{\infty} h_{\mathrm{GVD}}(\tau)\psi(0,t-\tau)\,\mathrm{d}\tau \tag{2.34}$$

The dispersion process is then modeled as a linear all-pass filter – a spectral transfer function with unitary amplitude – with a phase distribution exhibiting a quadratic dependence with frequency. Fig. 2.4 schematically depicts the operation.

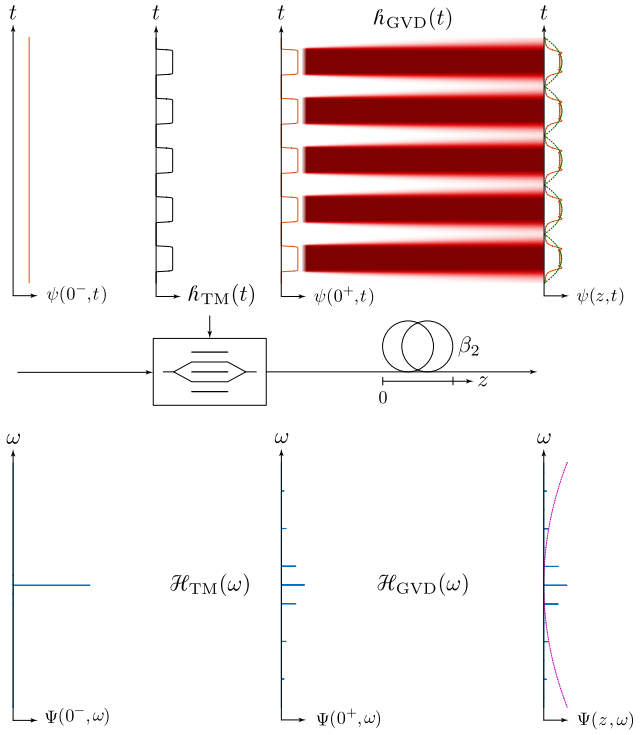

Figure 2.4 – Chromatic dispersion. Operator model of the group velocity dispersion process. In the shown example, the wave obtained after the temporal modulation process shown in Fig. 2.3 propagates a distance L away from the modulator through a GVD medium. (top) Real space. (bottom) Fourier space.

From a practical viewpoint, chromatic dispersion is particularly relevant in the problem of propagation of optical pulses through transparent media. For a practical example, consider a complex temporal envelope defined by a Gaussian function of time with unitary amplitude, and its Fourier transform

$$\tilde{\psi}(0,t) = e^{-\frac{t^2}{2\sigma_t^2}} \tag{2.35}$$

$$\tilde{\Psi}(0,\omega) = \frac{\sqrt{2\pi}}{\sigma_\omega} e^{-\frac{\omega^2}{2\sigma_\omega^2}} \tag{2.36}$$

where σ_t and σ_ω are the half-widths at height e^{-1} of the functions $\tilde{\psi}(0,t)$ and $\tilde{\Psi}(0,\omega)$, in the time and frequency domains respectively, satisfying $\sigma_\omega = \sigma_t^{-1}$.

Eq. 2.27 (with Eq. 2.32) gives the expression of the output spectrum.

$$\tilde{\Psi}(z,\omega) = \frac{\sqrt{2\pi}}{\sigma_\omega} e^{-\frac{1}{2}\left(\frac{1}{2\sigma_\omega^2} + i\beta_2 z\right)\omega^2} \tag{2.37}$$

Calculation of the inverse Fourier transform[11] of Eq. 2.37 gives, after some rearranging, the expression of the output temporal envelope,

$$\tilde{\psi}(z,t) = \frac{\sigma_t}{\sqrt[4]{\sigma_t^4 + (\beta_2 z)^2}} e^{-\frac{1}{2}\left(\frac{\sigma_t^2 t^2}{\sigma_t^4 + (\beta_2 z)^2} + i\left(\frac{\beta_2 z t^2}{\sigma_t^4 + (\beta_2 z)^2} - \tan^{-1}\left(\frac{\beta_2 z}{\sigma_t^2}\right)\right)\right)} \tag{2.38}$$

The output signal is a Gaussian pulse with an acquired temporal phase profile and modified amplitude and width. The temporal width of the pulse at the output of the dispersive medium is,

$$\sigma_t' = \sigma_t \sqrt{1 + \left(\frac{z}{L_\mathrm{D}}\right)^2} \tag{2.39}$$

where $\sigma_t' > \sigma_t$ and L_D is the dispersion length of the pulse in the medium,

$$L_\mathrm{D} = \frac{\sigma_t^2}{|\beta_2|} \tag{2.40}$$

The dispersive medium causes the pulse to broaden in time. As anticipated, this is due to different frequency components propagating at different speeds. For instance, if $\beta_2 > 0$, the higher frequency components of the pulse travel with higher speed than the lower ones, thus moving towards the leading edge of the pulse; similarly, the lower end of the spectrum moves towards the trailing edge of the pulse, due to lower propagation speeds. Not only this causes the pulse to stretch, but such a redistribution of frequencies results on a quadratic temporal phase along the pulse envelope,

$$\sphericalangle\tilde{\psi}(z,t) = \frac{1}{2}\left(\frac{\beta_2 z t^2}{(\sigma_t^4 + (\beta_2 z)^2} - \tan^{-1}\left(\frac{\beta_2 z}{\sigma_t^2}\right)\right) \tag{2.41}$$

[11] For the Fourier transform pair of a Gaussian function, as well as a list of properties of the Fourier transform, useful in this calculation, consult Appendix A.

Differentiating the temporal phase with respect to time gives the instantaneous frequency of the pulse.

$$\frac{\mathrm{d}}{\mathrm{d}t}\sphericalangle\tilde{\psi}(z,t) = \frac{\beta_2 z}{\sigma_t^4 + (\beta_2 z)^2}t \tag{2.42}$$

In the equivalent base-band representation, the instantaneous frequency is a measurement of the deviation of the frequency occurring at each time instant from the carrier. As shown in Eq. 2.42, second-order GVD produces a linear instantaneous frequency distribution, or chirp. Fig. 2.5 illustrates the effect of second-order dispersion on a Gaussian pulse.

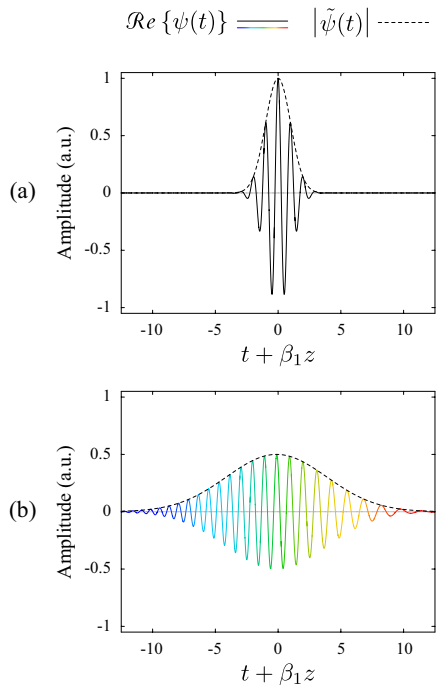

Figure 2.5 – Gaussian pulse stretching due to second-order GVD. Numerical simulation showing the the effect of propagation through second-order group velocity dispersive media of a Gaussian pulse. The input pulse (a) has unitary amplitude and $\sigma_t = 1$. The carrier frequency is $\omega_0 = 2\pi$. The total simulated second-order dispersion is chosen to produce a multiplication of the input pulse duration by a factor 4; with the chosen pulse parameters this value corresponds to $\beta_2 z = \sqrt{3}$. The pulse obtained at the output of the medium (b) has reduced its amplitude by $\sqrt{4}$, as a result of the pulse broadening effect (losses are neglected). The output waveform shows the anticipated chirp of the underlying carrier frequency, with higher frequencies (shorter wavelengths represented in blue color) moving towards the leading edge of the pulse (faster), and lower frequencies (longer wavelengths represented in red color) moving towards the trailing edge (slower).

The parameter β_2 has units of ps^2/rad/km. It is sometimes convenient to define the second-order dispersion coefficient with respect to wavelength, instead of radial frequency,

$$D = -\frac{2\pi c}{\lambda^2}\beta_2 \tag{2.43}$$

where D is measured in ps/nm/km.

As per the definition of the propagation constant, the dispersion coefficient is a real magnitude (i.e., with sign). A medium characterized by a positive β_2 parameter ($D < 0$) is said to exhibit normal dispersion. For instance, this is the case of standard single-mode optical fibers for wavelengths shorter than $\sim$1310 nm. On the other hand, a medium characterized by a negative β_2 parameter ($D > 0$) is said to exhibit anomalous dispersion, as encountered in standard single-mode optical fibers for wavelengths longer than $\sim$1310 nm. Fig. 2.6 shows the second-order dispersion characteristic of the Corning® SMF-28 standard single-mode optical fiber [76].

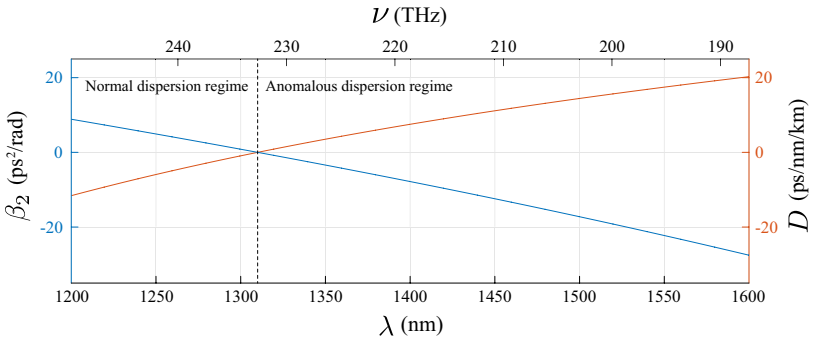

Figure 2.6 – Second-order dispersion characteristic of SMF-28. Spectral distribution of the parameters β_2 and D, for the Corning® SMF-28 standard single-mode optical fiber, with a zero-dispersion wavelength of 1310 nm ($\sim$228.8492 THz).

2.4 The Talbot effect

The Talbot effect – or self-imaging – is at the heart of the developments reported in this dissertation.

2.4.1 Brief history

Talbot effect was first observed by the British scientist William Henry Fox Talbot, in the context of his pioneering works in photography. Talbot noticed that, when illuminated with a monochromatic wave, a coarsely-ruled diffraction grating – an object with a periodic amplitude transmittance – would produce images, faithful to the grating pattern and perfectly in focus. Such images would reappear periodically at integer multiples of a particular distance, that would later come to be known as the *Talbot length*. Talbot published his findings on the subject in 1836 [77], but immediately abandoned it as a mere curiosity, in order to pursue his work on photography, thus leaving behind the phenomenon that, decades later, would carry his name.

It took 45 years for the effect to be revisited by British physicist and Nobel Prize laureate John William Strutt, 3rd Baron Rayleigh. Rayleigh explained Talbot effect as a natural consequence of near-field – Fresnel – diffraction on its 1881 letter to the *Philosophical Magazine* [78]. Furthermore, he found the analytic expression of the Talbot length,

$$z_{\mathrm{T}} = \frac{x_r^2}{\lambda} \tag{2.44}$$

where x_r is the spatial repetition period of the complex amplitude transmittance of the object (assuming a one-dimensional object, periodic along the x dimension) illuminated by a monochromatic wave, with wavelength λ.

Rayleigh already anticipated the practical usefulness of the phenomenon, proposing that it could be used to accurately reproduce a diffraction grating by exposing photographic film to one of the focused images that form at integer multiples of the Talbot length. Since then, extensive work has been devoted to the study of the phenomenon and its practical applications [79, 80], which nowadays are found in diverse areas of science and technology, including holography [81, 82], image processing [83, 84], lithography [85], electron interferometry [86], plasmonics [87] matter wave physics [88, 89], quantum optics [90], etc.

2.4.2 Temporal Talbot effect

A dual phenomenon to the spatial Talbot effect, first postulated by Tomasz Jannson and Joanna Jannson in 1981 [91], can be observed in the paradigm of second-order group-velocity dispersion of time-periodic waveform trains. Temporal Talbot effect has been used as an extremely simple and efficient method for multiplying the repetition rate of pulse trains [56], and it finds extensive application in several areas of laser physics, [92], signal processing [93, 94], telecommunications [95], etc.

Consider a t_r-periodic temporal wave of interest. Its frequency-domain representation corresponds to a frequency comb with linear frequency line spacing $\nu_r = t_r^{-1}$. Temporal Talbot effect occurs when such a spectrum is affected by a frequency-domain wave propagator of the form,

$$\mathcal{H}_{\text{TSI}}(\omega) := e^{i\frac{1}{2}\theta\omega^2} \tag{2.45}$$

where TSI stands for 'temporal self-imaging'.

The condition for the parameter θ, necessary for the observation of temporal Talbot effect is [56],

$$2\pi|\theta| = \frac{p}{q}t_r^2 \tag{2.46}$$

where p and q are two mutually-prime natural numbers (i.e., $q^{-1}p$ is an irreducible fraction).

Note that Eq. 2.45 has the form of the transfer function of a dispersive medium in the narrow-band approximation, given in Eq. 2.32, with the parameter θ playing the role of the total second-order dispersion of the medium, $\beta_2 z$. In this context, it is possible to define a Talbot length – the required propagation distance through the GVD medium to achieve the first temporal Talbot image – as,

$$z_{\text{T}} = \frac{t_r^2}{2\pi|\beta_2|} \tag{2.47}$$

where the second-order dispersion coefficient plays the role of the wavelength in Eq. 2.44.

Solutions of Eq. 2.46 yielding dispersion values with $q = 1$ result in output pulse trains corresponding to perfect reconstructions of the input pulse train, i.e., as if the original train never underwent dispersive propagation. This is the time-domain dual of the phenomenon originally observed by Talbot in the Fresnel diffraction of periodic images. Indeed, the well-known space-time duality[12] – a relationship between spatial and temporal wave phenomena arising from a mathematical isomorphism in the equations describing wave propagation – accounts for this relationship [96]. On the other hand, solutions of Eq. 2.46 yielding dispersion values with $q > 1$ produce output pulse trains where the individual pulses are reconstructed without distortion, but with a reduced pulse period, $q^{-1}t_r$. The effect is that of a repetition-rate multiplication of the input pulse train, achieved purely through dispersive propagation of the input pulse train.

The dispersive medium, when satisfying the temporal Talbot condition in Eq. 2.46, and assuming transparency (i.e., neglecting insertion losses), effectively redistributes the entirety of the energy carried by the input pulse train into either an equal number of output periods ($q = 1$), or into a higher one (q output periods per input period, with $q > 1$). The first case is known as integer temporal Talbot effect, and the obtained output trains are referred to as integer temporal Talbot images. The second case is known as fractional

[12] For a review of the space-time duality, consult Appendix B.

temporal Talbot effect, and the obtained – higher-pulse-rate – output trains are referred to as temporal Talbot sub-images. Due to the fact that the entire energy of the input wave is, ideally, preserved through the process, the resulting output pulses have their energy content reduced (divided) by the factor q. Fig. 2.7 illustrates the process.

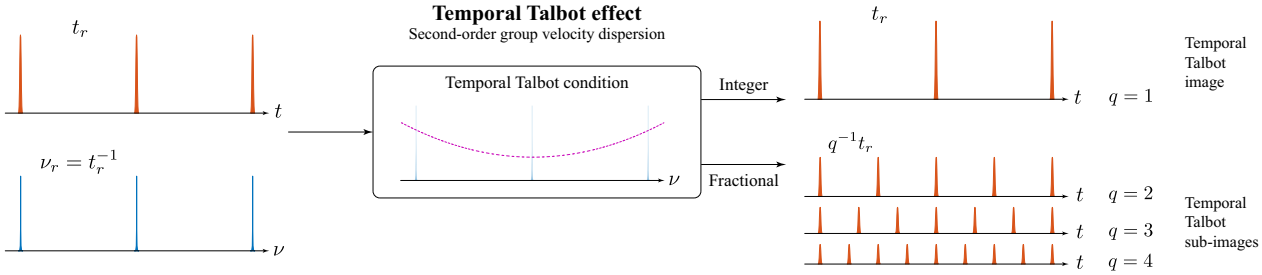

Figure 2.7 – Temporal Talbot effect. Schematic depiction of the formation of temporal Talbot images ($q = 1$) and sub-images ($q > 1$), in the dispersive propagation of a periodic train of pulses. The transformation leading to observation of temporal Talbot effect is the application of a quadratic spectral phase (here shown in linear frequency, ν).

Fig. 2.8 shows a numerical simulation illustrating the formation of the $\{p = 1, q = 2\}$ temporal Talbot sub-image.

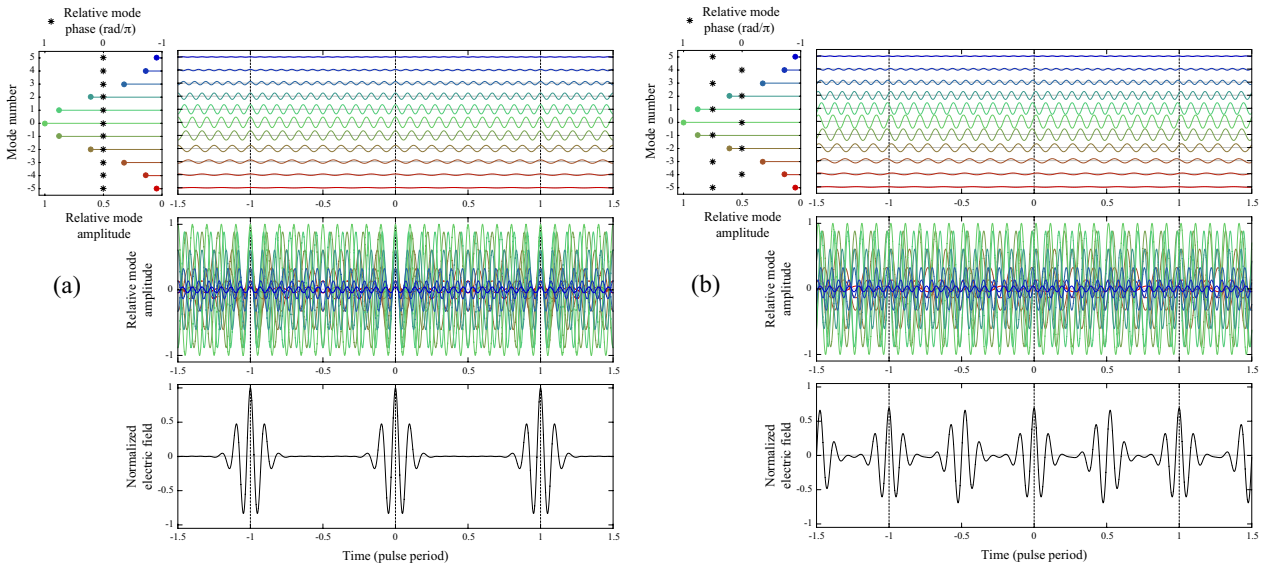

Figure 2.8 – Formation of temporal Talbot sub-images. Numerical simulation illustrating the coherent interference between spectral modes of a periodic pulse train affected by a spectral phase distribution corresponding to a temporal Talbot sub-image. (a) Input pulse train (with uniform spectral mode phase distribution), and (b) output pulse train corresponding to the $\{p = 1, q = 2\}$ temporal Talbot sub-image (see Eq. 2.46).

Note that, while the temporal Talbot sub-images are rate-multiplied replicas of the input pulse train, their power spectra is identical to that of the input train. This is so because the involved transformation is simply a modification of the input phase distribution along the frequency domain (see Eq. 2.45). It follows then, that each temporal Talbot sub-image has an associated temporal phase variation, acquired due to the temporal energy redistribution process (see pulse-to-pulse instantaneous phase variation of the output pulse train in Fig. 2.8(b)). These phase variations have been shown to exhibit mathematical forms that follow the solutions of generalized quadratic Gauss sums [97–99]. The properties of such phase variations are of key importance for the developments reported in this dissertation, and are studied in depth in Chapter 3.

2.4.3 Spectral Talbot effect

If one exchanges the domains of time and frequency in the previous scenario, a frequency-domain counterpart of the temporal Talbot effect can be observed in the power spectrum of a frequency comb. Heuristically, this arises as a consequence of the symmetry property of the Fourier transform[13]. Spectral Talbot effect was first postulated by José Azaña in 2005 [59], and it has since been proposed as a versatile, energy-efficient method for controlling the FSR of frequency combs [61].

Consider again a t_r-periodic pulse train, corresponding to a frequency comb with FSR $\nu_r = t_r^{-1}$. The mechanism responsible for spectral Talbot effect is described by a temporal phase modulation operator of the form,

$$\hbar_{\mathrm{SSI}}(t) := e^{i\frac{1}{2}\theta t^2} \tag{2.48}$$

where SSI stands for 'spectral self-imaging', and in this case, θ defines the spectral Talbot condition as [100],

$$2\pi|\theta| = \frac{s}{m}\omega_r^2 \tag{2.49}$$

where s and m are, again, two mutually-prime natural numbers (i.e., $m^{-1}s$ is an irreducible fraction), and $\omega_r = 2\pi\nu_r$.

In this situation, the spectral Talbot images ($m = 1$) and sub-images ($m > 1$) correspond to the spectra of the output pulse train (obtained after temporal phase modulation), resulting in perfect reconstructions of the input comb (integer spectral Talbot effect) or reconstructions with a reduced FSR, $m^{-1}\nu_r$ (fractional spectral Talbot effect), respectively. Similarly to the temporal Talbot scenario described above, energy conservation ensures that the output comb lines have an energy content reduced (divided) by the factor m. Fig. 2.9 illustrates the process.

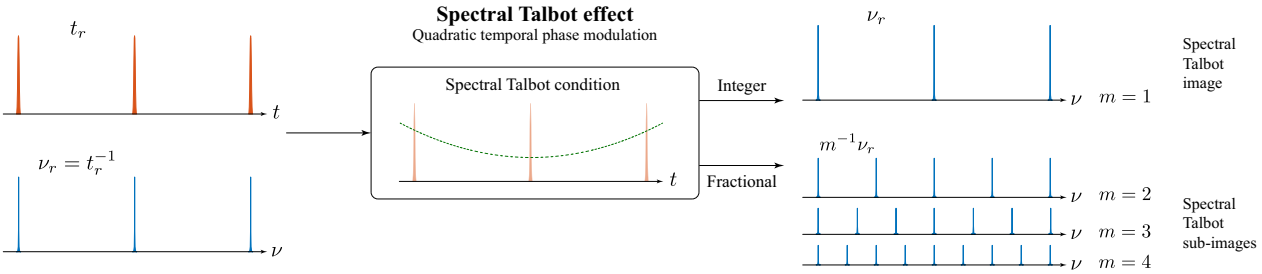

Figure 2.9 – Spectral Talbot effect. Schematic depiction of the formation of spectral Talbot images ($m = 1$) and sub-images ($m > 1$), in the temporal phase modulation of a periodic train of pulses. The transformation leading to observation of spectral Talbot effect is the application of a quadratic temporal phase.

It should be noted that the temporal phase profile of the operator in Eq. 2.48 is continuous, and follows a quadratic variation with time. As shown in Fig. 2.9, this continuous variation results in nonuniform phase fluctuations within the pulses in the time domain. If the temporal duration of the pulses is sufficiently short (approaching deltas in the limit of infinite bandwidth), these variations can be considered flat. However, for long pulses, or exceedingly sharp temporal phase variations of the spectral Talbot operator, uncompensated phase fluctuations within the duration of different pulses will introduce distortion in the spectrum of the train. This situation does not occur in the temporal Talbot effect scenario, as the spectral phase variations

[13]For details on the properties of the Fourier transform, consult Appendix A.

induced by the temporal Talbot propagator are applied to a frequency comb, where the individual frequency components are expected to be sufficiently narrow. A more general formulation of the temporal and spectral Talbot conditions involves the use of discrete phase sequences, defining the phase level to be applied to each comb line or temporal pulse. This formulation will be developed in Chapter 3.

Regarding the phase distributions of the waves in the time and frequency domains, a similar situation to that of the previously described temporal Talbot effect arises here. While the spectral Talbot sub-images are FSR-divided replicas of the input frequency comb, their instantaneous power distribution is identical to that of the input train. This is so because the involved transformation is simply a modification of the input phase distribution along the time domain (see temporal phase modulation function in Eq. 2.48). It follows then, that each spectral Talbot sub-image has an associated spectral phase variation, acquired due to the spectral energy redistribution process. It is unclear, however, whether such residual phases are equivalent to those described by Eq. 2.46, i.e., whether or not the phases acquired by temporal and spectral Talbot sub-images satisfy the corresponding Talbot condition in their observation domain. Chapter 3 formulates the relationship between temporal and spectral Talbot phases, hereinafter referred to as the time-frequency duality of the Talbot effect, which is the cornerstone upon which all the developments reported in this dissertation are based.

CHAPTER 3

Generalized Talbot effect

This chapter presents a generalization of the Talbot effect, as well as the relationships between its different realizations in all domains of representation of waves. A general definition of the condition leading to observation of the Talbot phenomena is presented. Additionally, the mathematical basis of the universal periodicity control method – central point of this dissertation – is presented. The problem is addressed in the framework of the time/frequency representation of optical signals, corresponding to the experimental demonstrations presented in following chapters. Two equivalent realizations of the method are introduced, discussed and compared. The work presented in this Chapter was reported in [APj2, APj3, APj4] [APc5, APc8, APc11, APc13, APc14].

3.1 Generality of the Talbot condition

As introduced in Section 2.4, temporal Talbot effect is observed when a periodic train of pulses is affected by a specific quadratic phase profile across its frequency domain representation, giving rise to perfect images of the train (integer temporal self-imaging), or to sub-images where the initial temporal period is divided by a natural number (fractional temporal self-imaging), as shown in Fig. 3.1(a). Similarly, spectral Talbot effect is observed when a periodic spectral waveform, e.g., a frequency comb, is affected by a specific quadratic phase profile across its time domain representation, giving rise to perfect images of the comb (integer spectral self-imaging), or to sub-images where the initial spectral period is divided by a natural number (fractional spectral self-imaging), as shown in Fig. 3.1(b). These quadratic phase profiles are determined by the well-known *Talbot condition* [56, 100].

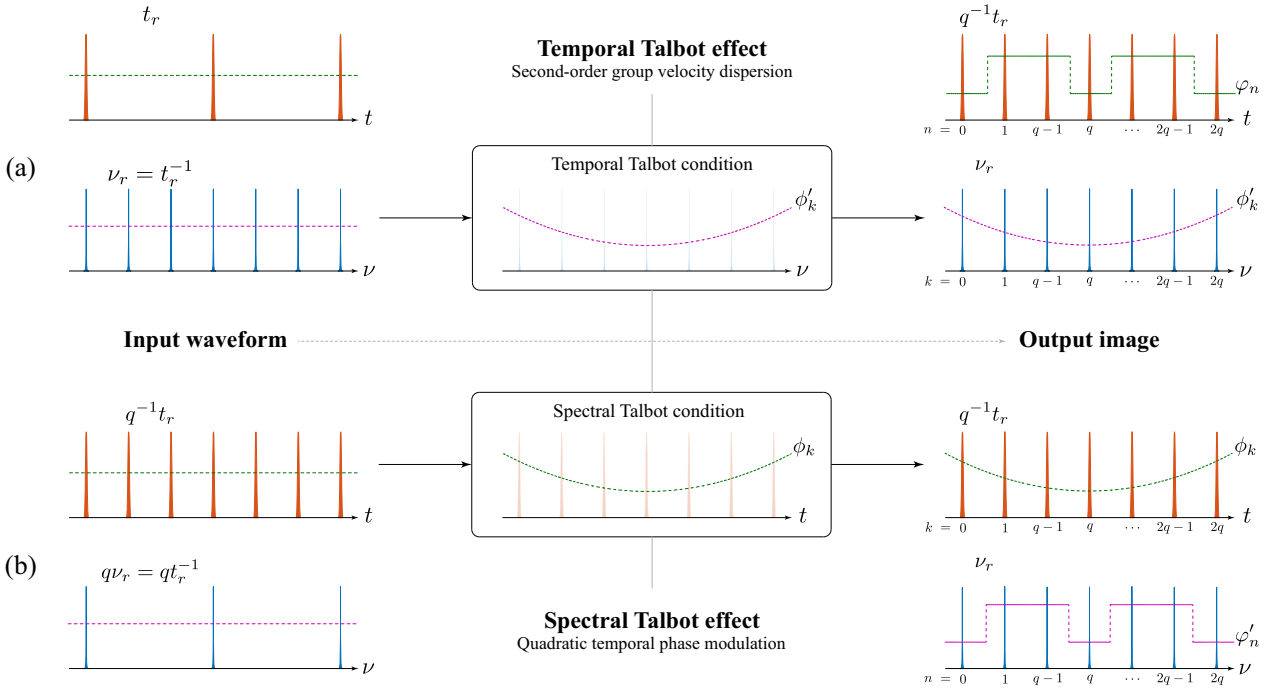

Figure 3.1 – Time-frequency duality of the Talbot effect. Comparison of (a) temporal and (b) spectral Talbot effect applied to obtain sub-images of (a) a train of pulses and (b) a frequency comb. The periods of the input object are selected to generate output images with equal period in both time and frequency domains. The obtained temporal and spectral phase profiles are sketched for comparison (dashed lines). In this representation, the amplitudes of all temporal pulses and spectral lines are kept equal for convenience of interpretation (not considering the effects of energy redistribution associated to self-imaging). Additionally, the pulsewidth is considered short enough to neglect the effects of non-uniform phase variations within the duration of a pulse.

The problem under consideration here is the Fourier relationship between temporal and spectral Talbot effects. Fig. 3.1 compares the results of a q-factor fractional temporal Talbot effect [56] (Fig. 3.1(a)), and a fractional spectral Talbot effect [100] by the same factor (Fig. 3.1(b)). The temporal Talbot effect in Fig. 3.1(a) is induced through quadratic spectral phase filtering of a phase-locked pulse train, where the applied phase satisfies the corresponding temporal Talbot condition [56] (e.g., through second order group-velocity dispersion [75]). The resulting output temporal sub-image exhibits a temporal period equal to the input one divided by q. Particularly important here is the fact the output temporal train acquires a pulse-to-pulse phase variation that results from computing the phase of a quadratic Gauss sum [97–99]. On the other hand, the spectral Talbot effect in Fig. 3.1(b) can be induced through quadratic temporal phase modulation of a phase-locked frequency comb, where the applied phase now satisfies the corresponding spectral Talbot

condition [100] (e.g., through a time lens [60]). Similarly to the temporal Talbot effect, the resulting output spectral sub-image exhibits a spectral period equal to the input one divided by q, as well as a line-to-line phase variation.

Notice that the temporal pulse period of the signal in Fig. 3.1(b) is chosen to be q times shorter than the one of the signal in Fig. 3.1(a), so that the two processes render identical temporal and spectral repetition periods. However, as illustrated in Fig. 3.1, the temporal phase profiles of the two output signals are, in principle, different. In particular, whereas the temporal phase profile applied to the input train in order to obtain a spectral Talbot sub-image satisfies the Talbot condition (ϕ_k in Fig. 3.1(b)), the temporal phase variation acquired by the temporal Talbot sub-image in the temporal self-imaging scenario is dictated by a Gauss sum (φ_n in Fig. 3.1(a)). A similar relationship occurs between the phases ϕ'_k in Fig. 3.1(a) and φ'_n in Fig. 3.1(b). The question being asked here is whether the phase variations acquired by a Talbot sub-image in their observation domain satisfy the Talbot condition, in a similar way that the phases introduced in the corresponding Fourier-dual domain, in order to trigger the effect, do. In other words, this section aims to establish a relationship between the solutions of quadratic Gauss sums and the Talbot condition, in order to determine whether there exists a duality between manifestations of the Talbot effect in the time and frequency domains. In particular, if some of the resulting Gauss sums lead to phase profiles that do not follow the general Talbot condition, it would follow that self-imaging effects could be achieved through the use of an additional set of phase profiles other than those given by the Talbot condition.

In anticipation, this is, in fact, not the case, as the solutions of quadratic Gauss sums do satisfy the Talbot condition, which suggests that the Talbot condition may encompass all possible quadratic phase patterns for inducing self-imaging effects.

3.1.1 The time-frequency duality of the Talbot effect

The mathematical derivations in this Section establish the precise relationship between the two phase profiles leading to Talbot effect in the observation domains of time and frequency (related by the Fourier transform). Some of these derivations follow the steps of John Hannay and Sir Michael Victor Berry in [97], Sir Michael Victor Berry and Susanne Klein in [98], and Shigeki Matsutani and Yoshihiro Ônishi in [99], with some modifications and needed corrections. These authors studied the phases associated to spatial Talbot images, obtained from a periodic grating[1]. Concepts of modular arithmetic and number theory [101], as well as Fourier analysis [73], are used in the following calculations.

Let us consider a generic, one-dimensional waveform, periodic along the time domain, represented by the variable t. As shown in Eqs. 3.1 and 3.2, such a wave can be analytically modeled by a – generally complex – periodic function of t, $\psi : \mathbb{R} \to \mathbb{C}$, and its Fourier transform in the radial frequency domain $\Psi : \mathbb{R} \to \mathbb{C}$, represented by the variable ω, so that $\Psi(\omega) = \mathscr{F}\{\psi(t)\}$. Note that, as per the properties of the Fourier transforms of periodic functions, $\Psi(\omega)$ is a Dirac comb[2],

$$\psi(t) := \sum_{n=-\infty}^{\infty} \hat{\psi}\left(t - nt_r\right) \tag{3.1}$$

$$\Psi(\omega) := \sum_{k=-\infty}^{\infty} c_k \delta\left(\omega - k\omega_r\right) \tag{3.2}$$

[1] While these derivations were originally formulated in the paradigm of spatial Talbot effect, the time-domain formulation used here for studying the phases associated to temporal Talbot effect is mathematically analogous.

[2] For further details on the Fourier transforms of periodic functions and Dirac combs, consult appendix A.

where,

t_r	is the temporal period of $\psi(t)$,
$\omega_r = 2\pi t_r^{-1}$	is the period of $\Psi(\omega)$ along the radial frequency domain[3],
$\hat{\psi} : \mathbb{R} \to \mathbb{C}$	is the complex amplitude of a single period of $\psi(t)$, so that $\hat{\psi}(t) = 0 \; \forall \; \lvert t \rvert > t_r/2$,
δ	is the unitary Dirac delta function,
$c_k = \omega_r \hat{\Psi}(k\omega_r)$	is the complex weight of the k-th delta of $\Psi(\omega)$, with $\hat{\Psi}(\omega) = \mathscr{F}\{\hat{\psi}(t)\}$.

It should be noted that $\psi(t)$ is here written in the equivalent base-band representation (corresponding to $\tilde{\psi}(t)$ in the notation used in Chapter 2).

The temporal representation of the wave can be expressed in terms of the convolution integral of $\hat{\psi}(t)$ and a Dirac comb with period t_r,

$$\begin{aligned} \psi(t) &= \hat{\psi}(t) * \sum_{n=-\infty}^{\infty} \delta\left(t - nt_r\right) \\ &= \int_{-\infty}^{\infty} \left(\hat{\psi}(t-\tau) \sum_{n=-\infty}^{\infty} \delta\left(\tau - nt_r\right) \right) \mathrm{d}\tau \end{aligned} \tag{3.3}$$

The periodicity of $\psi(t)$ is set by the Dirac comb in Eq. 3.3, independently of the value of $\hat{\psi}(t)$. For mathematical convenience, and without loss of generality, this term can be dropped from the analysis, so that $\hat{\psi}(t) = \delta(t) \iff c_k = \omega_r \; \forall \; k$.

$$\psi(t) = \sum_{n=-\infty}^{\infty} \delta\left(t - nt_r\right) \tag{3.4}$$

$$\Psi(\omega) = \omega_r \sum_{k=-\infty}^{\infty} \delta\left(\omega - k\omega_r\right) \tag{3.5}$$

This definition of the periodic wave of interest, $\psi(t)$, is convenient; since $\delta(t)$ has an infinitesimally narrow extent in t, any Talbot sub-image, involving division of the period t_r by any natural factor, can be represented, and therefore studied on the basis of this formalism. Furthermore, since Talbot effect is the result of a linear operator, the principle of superposition holds, and the effects of a finite extent in t of $\hat{\psi}(t)$ can always be incorporated a posteriori.

[3] A similar expression could be formulated in linear frequency, ν, noting that $\omega_r = 2\pi\nu_r$, where ν_r is the spectral period in the linear frequency domain (with units of Hz).

3.1.1.1 Frequency spectra of temporal Talbot (sub-)images

Temporal Talbot effect, as described in Section 2.4.2, arises from the action of a spectral wave propagator applying a phase variation to the frequency spectrum of the time-periodic wave of interest, with a quadratic dependence with frequency,

$$\mathscr{H}_{\text{TSI}}(\omega) := e^{i\frac{1}{2}\theta\omega^2} \tag{3.6}$$

where the condition for the parameter θ, necessary for the observation of temporal Talbot effect is,

$$2\pi|\theta| = \frac{p}{q}t_r^2 \tag{3.7}$$

where p and q are two mutually-prime natural numbers (i.e., $q^{-1}p$ is an irreducible fraction).

Recall that, as described in Section 2.4.2, such a transformation is inherent in second-order GVD media, although any phase filtering operation of the form described by Eq. 3.6 that satisfies the condition given in Eq. 3.7 will produce temporal Talbot effect.

The spectrum of the temporal Talbot (sub-)image, $\Psi'(\omega)$, resulting from the action of the operator $\mathscr{H}_{\text{TSI}}(\omega)$ on the spectrum of the wave of interest, $\Psi(\omega)$ is,

$$\begin{aligned}\Psi'(\omega) &= \mathscr{H}_{\text{TSI}}(\omega)\Psi(\omega) \\ &= \omega_r \sum_{k=-\infty}^{\infty} \delta\left(\omega - k\omega_r\right) e^{i\frac{1}{2}\theta\omega^2}\end{aligned} \tag{3.8}$$

Applying the sampling property of the Dirac delta function[4] and substituting θ (Eq. 3.7) in Eq. 3.8, gives the phase shift applied to each frequency component of the comb.

$$\begin{aligned}\Psi'(\omega) &= \omega_r \sum_{k=-\infty}^{\infty} \delta\left(\omega - k\omega_r\right) e^{i\frac{1}{2}\theta(k\omega_r)^2} \\ &= \omega_r \sum_{k=-\infty}^{\infty} \delta\left(\omega - k\omega_r\right) e^{i\pi\frac{p}{q}k^2}\end{aligned} \tag{3.9}$$

[4]The sampling property of the Dirac delta function states that,

$$\psi(u)\delta(u-u_0) = \psi(u_0)\delta(u-u_0)$$

This property was implicitly used in Eq. 3.3 to remove the envelope $\hat{\psi}(t)$. For additional details, consult Appendix A.

This way, the temporal Talbot condition can be rewritten as a discrete function of k (the index running over ω in steps of ω_r). This represents the line-to-line phase shift required in the Fourier-dual (frequency) domain, ω, to observe any desired Talbot (sub-)image in the representation (time) domain, t,

$$\phi'_{k;p,q} := \pi \frac{p}{q} k^2 \tag{3.10}$$

3.1.1.2 Time-domain representation of temporal Talbot (sub-)images

The expression for the (sub-)image $\psi'(t)$ is given by the inverse Fourier transform of $\Psi'(\omega)$,

$$\begin{aligned}
\psi'(t) &= \mathscr{F}^{-1}\left\{\Psi'(\omega)\right\} \\
&= \frac{1}{2\pi}\int_{-\infty}^{\infty} \Psi'(\omega) e^{i\omega t}\,\mathrm{d}\omega \\
&= \frac{\omega_r}{2\pi}\int_{-\infty}^{\infty} \left(\sum_{k=-\infty}^{\infty} \delta\left(\omega - k\omega_r\right) e^{i\pi\frac{p}{q}k^2}\right) e^{i\omega t}\,\mathrm{d}\omega \\
&= \frac{\omega_r}{2\pi}\sum_{k=-\infty}^{\infty} e^{ik\omega_r t} e^{i\pi\frac{p}{q}k^2} \\
&= \frac{\omega_r}{2\pi}\sum_{k=-\infty}^{\infty} e^{i2\pi\left(\frac{t}{t_r}k + \frac{p}{2q}k^2\right)}
\end{aligned} \tag{3.11}$$

Defining, $k := nq + l$, with $\{n \in \mathbb{Z} \mid -\infty < n < \infty\}$ and $\{l \in \mathbb{N} \mid 0 < l < q-1\}$, the argument of the complex exponential in the last step of Eq. 3.11 writes,

$$\frac{t}{t_r}k + \frac{p}{2q}k^2 = \frac{t}{t_r}nq + \frac{t}{t_r}l + \frac{1}{2}pqn^2 + \frac{p}{2q}l^2 + pnl \tag{3.12}$$

and the last sum in Eq. 3.11 can be split into groups of q terms,

$$\psi'(t) = \frac{\omega_r}{2\pi}\sum_{l=0}^{q-1} e^{i2\pi\left(\frac{t}{t_r}l + \frac{p}{2q}l^2\right)} \sum_{n=-\infty}^{\infty} e^{i2\pi\left(\frac{t}{t_r}qn + \frac{1}{2}pqn^2 + pnl\right)} \tag{3.13}$$

At this point, one must note that,

$$\begin{aligned}
e^{i\pi pqn^2} &= (-1)^{pqn^2} \\
&\equiv (-1)^{pqn} \\
&= e^{i\pi pqn}
\end{aligned} \tag{3.14}$$

and that $e^{i2\pi pnl} \equiv e^{i2\pi} = 1 \;\forall\; \{p, n, l\} \in \mathbb{Z}$.

This way,

$$\psi'(t) = \frac{\omega_r}{2\pi} \sum_{l=0}^{q-1} e^{i2\pi\left(\frac{t}{t_r}l + \frac{p}{2q}l^2\right)} \sum_{n=-\infty}^{\infty} e^{i2\pi\left(\frac{t}{t_r}qn + \frac{1}{2}pqn\right)} \tag{3.15}$$

As stated by Berry and Klein in [98], the observation in Eq. 3.14 is the mathematical heart of the Talbot effect, because it renders the argument of the second exponential in Eq. 3.15 linear in n, so that the Poisson summation formula[5] gives, after some rearranging, the expression of the output image, $\psi'(t)$ as a Dirac comb,

$$\psi'(t) = \frac{1}{q} \sum_{n=-\infty}^{\infty} \delta\left(t - n\frac{t_r}{q} + p\frac{t_r}{2}\right) \sum_{l=0}^{q-1} e^{i2\pi\left(\frac{t}{t_r}l + \frac{p}{2q}l^2\right)} \tag{3.16}$$

and the sampling property gives,

$$\psi'(t) = \frac{1}{q} \sum_{n=-\infty}^{\infty} \delta\left(t - n\frac{t_r}{q} + p\frac{t_r}{2}\right) \sum_{l=0}^{q-1} e^{i\frac{\pi}{q}\left(pl^2 + (2n-pq)l\right)} \tag{3.17}$$

From Eq. 3.17, it immediately holds that the period of the output image in the observation – time – domain is $q^{-1}t_r$, as expected for a periodic waveform satisfying the temporal Talbot condition in Eq. 3.10.

3.1.1.3 The time-frequency duality of the Talbot condition

The second sum in Eq. 3.17 has the form of a generalized quadratic Gauss sum.

$$G_{n;p,q} := \sum_{l=0}^{q-1} e^{i\frac{\pi}{q}\left(pl^2 + (2n-pq)l\right)} \tag{3.18}$$

It can be demonstrated that the solution of this sum is a complex number with magnitude $\sqrt{q}$, and a phase that depends on the numbers p and q [97–99].

The magnitude of the sum ensures the conservation of energy between the input waveform $\psi(t)$ (with period t_r) and the output (sub-)image $\psi'(t)$ (with period $q^{-1}t_r$). Additionally, if the phase profile along the time domain of $\psi'(t)$ satisfies a Talbot condition, $G_{n;p,q}$ must necessarily yield an exponent of the form,

$$\varphi_{n;s,m,c} := -\pi\frac{s}{m}n^2 - \pi c \tag{3.19}$$

where s and m are two mutually-prime natural numbers that must depend on p and q only, and c is a real constant, also dependent on p and q. Note that this expression is isomorphic to the phase sequence responsible for the observation of the effect, i.e., the phase of the (sub-)image in the Fourier-dual domain U, $\Psi'(\omega)$ (given by the Talbot condition in Eq. 3.10), except for the constant c (that does not alter the nature of the Talbot image since it simply represents an equal phase shift for all the components of the comb) and the

[5] For further details on the Poisson summation formula, consult Appendix A.

opposite sign (that indicates complex conjugation, due to the application of the Fourier transform). If this hypothesis holds, the output image should write,

$$\psi'(t) = \frac{e^{-i\pi c}}{\sqrt{q}} \sum_{n=-\infty}^{\infty} \delta\left(t - n\frac{t_r}{q} + p\frac{t_r}{2}\right) e^{-i\pi\frac{s}{m}n^2} \tag{3.20}$$

The goal here is to solve the Gauss sum in Eq. 3.18 and compare the form of its solutions with Eq. 3.19. Hannay and Berry provided a general solution to these sums in [97]. Following the steps of their derivations, three sets of solutions are found, depending on the parity of p and q. Denoting the set of even natural numbers by $\mathbb{E}$, and the set of odd natural number by $\mathbb{O}$,

$$G_{n;p,q} = \begin{cases} \sqrt{q}e^{-i\pi\left(\frac{q-1}{4}+\frac{p}{q}\left(\left[\frac{1}{p}\right]_q\right)^2 n^2+\frac{1}{2}\left(1-\left(\frac{p}{q}\right)\right)\right)} & \forall\,\{p\in\mathbb{E},\ q\in\mathbb{O}\} \quad (3.21a) \\ \sqrt{q}e^{-i\pi\left(\frac{q-1}{4}+\frac{2p}{q}\left[\frac{1}{2}\right]_q\left(\left[\frac{1}{2p}\right]_q\right)^2 (2n+q)^2+\frac{1}{2}\left(1-\left(\frac{p}{q}\right)\right)\right)} & \forall\,\{p\in\mathbb{O},\ q\in\mathbb{O}\} \quad (3.21b) \\ \sqrt{q}e^{i\pi\left(\frac{p}{4}-\frac{p}{q}\left(\left[\frac{1}{p}\right]_q\right)^2 n^2+\frac{1}{2}\left(1-\left(\frac{q}{p}\right)\right)\right)} & \forall\,\{p\in\mathbb{O},\ q\in\mathbb{E}\} \quad (3.21c) \end{cases}$$

where $\left[\frac{1}{a}\right]_b$ is the modular multiplicative inverse of a modulo b, i.e. the (unique) positive integer smaller than b satisfying Eq. 3.22,

$$a\left[\frac{1}{a}\right]_b = 1 \pmod b \tag{3.22}$$

and $\left(\frac{a}{b}\right)$ is the Jacobi symbol, equal in this case to the Legendre symbol since, as per Eqs. 3.21a, 3.21b and 3.21c, the lower argument is always an odd prime number, such that,

$$\left(\frac{a}{b}\right) := \begin{cases} 0 & \iff a \equiv 0 \\ +1 & \iff a \not\equiv 0,\ \{\exists\, n\in\mathbb{Z} \mid n^2 \equiv a \pmod b\} \\ -1 & \iff a \not\equiv 0,\ \{\nexists\, n\in\mathbb{Z} \mid n^2 \equiv a \pmod b\} \end{cases} \tag{3.23}$$

Table 3.2 lists some values of the modular multiplicative inverse, $\left[\frac{1}{a}\right]_b$, and the Jacobi symbol, $\left(\frac{a}{b}\right)$, respectively.

Rearranging terms in the arguments of the complex exponentials on Eqs. 3.21a, 3.21b and 3.21c, and dropping all the factors that contribute a net phase of 2π,

Table 3.2 – Modular multiplicative inverse and Jacobi symbol. (left) Values of the modular multiplicative inverse, $\left[\frac{1}{a}\right]_b$, for $\{a \in \mathbb{N} \mid 1 \leq a \leq 10\}$ and $\{b \in \mathbb{N} \mid 2 \leq b \leq 11\}$. (right) Values of the Jacobi symbol, $\left(\frac{a}{b}\right)$, for $\{a \in \mathbb{N} \mid 1 \leq a \leq 10\}$ and $\{b \in \mathbb{O} \mid 1 \leq b \leq 19\}$.

		a									
		1	2	3	4	5	6	7	8	9	10
b	2	1		1		1		1		1	
	3	1	2		1	2		1	2		1
	4	1	1	3		1	1	3		1	1
	5	1	3	2	4		1	3	2	4	
	6	1	1	1	5	5		1	1	1	5
	7	1	4	5	2	3	6		1	4	5
	8	1	1	3	1	5	7	7		1	1
	9	1	5	1	7	2	8	4	8		1
	10	1	1	7	8	1	2	3	9	9	
	11	1	6	4	3	9	2	8	7	5	10

		a									
		1	2	3	4	5	6	7	8	9	10
b	1	+1	+1	+1	+1	+1	+1	+1	+1	+1	+1
	3	+1	−1		+1	−1		+1	−1		+1
	5	+1	−1	−1	+1		+1	−1	−1	+1	
	7	+1	+1	−1	+1	−1	−1		+1	+1	−1
	9	+1	+1		+1	+1		+1	+1		+1
	11	+1	−1	+1	+1	+1	−1	−1	−1	+1	−1
	13	+1	−1	+1	+1	−1	−1	−1	−1	+1	+1
	15	+1	+1		+1			−1	+1		
	17	+1	+1	−1	+1	−1	−1	−1	+1	+1	−1
	19	+1	−1	−1	+1	+1	+1	+1	−1	+1	−1

$$G_{n;p,q} = \begin{cases} \sqrt{q} e^{-i\pi \frac{p\left(\left[\frac{1}{p}\right]_q\right)^2}{q} n^2 - i\pi\left(\frac{q-1}{4} + \frac{1-\left(\frac{p}{q}\right)}{2}\right)} & \forall \{p \in \mathbb{E},\ q \in \mathbb{O}\} \quad (3.24a) \\ \sqrt{q} e^{-i\pi \frac{8p\left[\frac{1}{2}\right]_q\left(\left[\frac{1}{2p}\right]_q\right)^2}{q} n^2 - i\pi\left(\frac{q-1}{4} + \frac{1-\left(\frac{p}{q}\right)}{2}\right)} & \forall \{p \in \mathbb{O},\ q \in \mathbb{O}\} \quad (3.24b) \\ \sqrt{q} e^{-i\pi \frac{p\left(\left[\frac{1}{p}\right]_q\right)^2}{q} n^2 + i\pi\left(\frac{p}{4} + \frac{1-\left(\frac{q}{p}\right)}{2}\right)} & \forall \{p \in \mathbb{O},\ q \in \mathbb{E}\} \quad (3.24c) \end{cases}$$

Identifying terms in Eqs. 3.24a, 3.24b and 3.24c gives the phases of the Talbot images in the form of Eq. 3.19, where the parameters s, m and c are functions of p and q. Table 3.3 shows the values of these parameters. Eq. 3.18 can thus be rewritten,

$$G_{n;p,q} = \sqrt{q} e^{i\varphi_{n;s,m}} \quad (3.25)$$

As shown in Table 3.3, $m = q \,\forall\, \{p, q\} \in \mathbb{N}$; on the other hand, in general $s \neq p$, depending on the parity of p and q. In most practical situations, a constant phase factor does not contribute to any observable or, in any case, relevant effect on a wave of interest. It is convenient then to write only the relationship between the parameter s and the coefficients p and q,

$$s = \begin{cases} p\left(\left[\frac{1}{p}\right]_q\right)^2 & \forall \quad pq \in \mathbb{E} \\ 8p\left[\frac{1}{2}\right]_q\left(\left[\frac{1}{2p}\right]_q\right)^2 & \forall \quad pq \in \mathbb{O} \end{cases} \quad (3.26)$$

Table 3.3 – Coefficients of the Talbot phases in Fourier-dual domains. Relationship between the parameters s, m and c of the Talbot phase in an observation domain (Eq. 3.19) and the parameters p and q of the Talbot phase in its Fourier-dual domain (Eq. 3.10).

Fourier-dual domain	**Observation domain**		
Parity of $\{p, q\}$	s	m	c
$p \in \mathbb{E}$ $q \in \mathbb{O}$	$p\left(\left[\frac{1}{p}\right]_q\right)^2$	q	$\frac{q-1}{4} + \frac{1-\left(\frac{p}{q}\right)}{2}$
$p \in \mathbb{O}$ $q \in \mathbb{O}$	$8p\left[\frac{1}{2}\right]_q\left(\left[\frac{1}{2p}\right]_q\right)^2$	q	$\frac{q-1}{4} + \frac{1-\left(\frac{p}{q}\right)}{2}$
$p \in \mathbb{O}$ $q \in \mathbb{E}$	$p\left(\left[\frac{1}{p}\right]_q\right)^2$	q	$-\frac{p}{4} - \frac{1-\left(\frac{q}{p}\right)}{2}$

In a later work, motivated by the findings reported here [APj2, APj3], and published shortly thereafter [102], Carlos Rodríguez Fernández-Pousa found an elegant, more compact formulation of the parameter s,

$$sp = 1 + q\epsilon_q \pmod{2q} \tag{3.27}$$

where ϵ_q is the parity of q, so that,

$$\epsilon_a := \begin{cases} 0 & \forall \quad a \in \mathbb{E} \\ 1 & \forall \quad a \in \mathbb{O} \end{cases} \tag{3.28}$$

If the phases acquired by the Talbot sub-images, $\varphi_{n;s,m,c}$, satisfy a Talbot condition, s and m must be mutually prime. This character is established by demonstrating that q does not divide s in any case. To verify this, it suffices to note that $\left[\frac{1}{a}\right]_q$ and q are, by definition, mutually-prime for any q and a mutually-prime. This proves that, as anticipated, the Talbot condition is satisfied by both sets of phases, $\phi'_{k;p,q}$ in ω, and $\varphi_{n;s,m,c}$ in t, and so the time-frequency duality of the Talbot effect is established.

The findings compiled on this Section can be summarized in the Fourier transform pair $\psi'(t) \overset{\mathscr{F}}{\longleftrightarrow} \Psi'(\omega)$ (Eqs. 3.29 and 3.30, together with Table 3.3).

$$\psi'(t) = \frac{e^{-i\pi c}}{\sqrt{q}} \sum_{n=-\infty}^{\infty} \delta\left(t - n\frac{t_r}{q} + p\frac{t_r}{2}\right) e^{-i\pi\frac{s}{m}n^2} \tag{3.29}$$

$$\Psi'(\omega) = \frac{2\pi}{t_r} \sum_{k=-\infty}^{\infty} \delta\left(\omega - k\frac{2\pi}{t_r}\right) e^{i\pi\frac{p}{q}k^2} \tag{3.30}$$

It should be noted that, from a practical perspective, the definitions used here are generally insufficient to accurately model realistic signals. Important considerations such as the time-bandwidth product must be taken into account in a practical context. As such, the effects of a finite value of $\hat{\psi}(t)$ should be considered.

These can be easily introduced to the derivation by simply solving the convolution integral in Eq. 3.3 and calculating the values of the coefficients c_k in Eq. 3.2.

3.1.2 Universal Fourier duality of the Talbot effect

The results reported in Section 3.1.1 demonstrate that the residual phases acquired by temporal Talbot sub-images along the time domain satisfy the general expression of the Talbot condition, in the same way that the spectral Talbot phases, responsible for observation of the phenomenon, do. An identical mathematical development, starting from application of a temporal Talbot phase to a periodic pulse train (inducing spectral Talbot effect) would demonstrate that the same relationship applies to the frequency-domain phase variations induced to the resulting spectral Talbot sub-images. More generally, such a relationship applies to any pair of Fourier-conjugate variables (e.g., to the position/momentum picture) in both directions. Application of a phase profile, satisfying the general Talbot condition, to a periodic function defined along a certain observation domain, will result on a Talbot sub-image represented along the corresponding Fourier-dual domain, with an associated phase profile that also satisfies the general Talbot condition.

Indeed, realizations of Talbot phenomena have been reported across several observation domains. In particular, all representation domains of spatial and temporal waves support realization of a Talbot effect. These include position (space) [77], transverse momentum (typically observed in the form of angular spectrum) [103], time [91], and frequency [59]. Fig. 3.2 illustrates the relationships between different domains where a form of Talbot effect can be observed. The different representations of waves in these domains are mathematically related by two analytical constructions. Wave phenomena represented in domains separated horizontally in Fig. 3.2 are related by the space-time duality[6], a well-known mathematical isomorphism between the equations describing spatial and temporal propagation of waves [96]. For instance, this is the case for the formal duality between paraxial diffraction and second-order chromatic dispersion (relating spatial and temporal Talbot effects), and spatial and temporal lenses (relating angular and spectral Talbot effects). On the other hand, wave phenomena represented in domains separated vertically in Fig. 3.2 are related by the Fourier transform[7].

Let us consider two adimensional variables, u and U, denoting to the observation domain, along which Talbot images occur, and its Fourier-dual domain, respectively. An u_r-periodic wave under analysis can be represented in such domains as follows,

$$\psi(u) = \sum_{n=-\infty}^{\infty} \delta\left(u - n u_r\right) \tag{3.31}$$

$$\Psi(U) = U_r \sum_{k=-\infty}^{\infty} \delta\left(U - k U_r\right) \tag{3.32}$$

where $U_r = 2\pi u_r^{-1}$, and the wave is assumed to be a Dirac comb, so as to facilitate the analysis of the periodic component and associated phase profiles.

[6] For a review of the space-time duality, consult Appendix B.

[7] For a review of Fourier analysis, consult Appendix A.

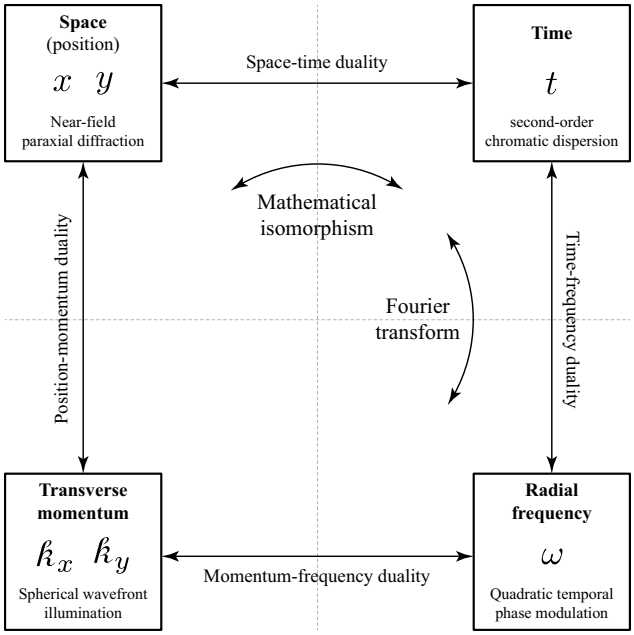

Figure 3.2 – Relationship between representation domains of waves. Each box contains the name of an observation domain of waves, its commonly-used representation symbol, and the mechanism that leads to observation of Talbot effect in such domain.

Talbot effect, observed in the domain u, results from the action of a unitary operator on the Fourier-domain representation of the wave under analysis, $\Psi(U)$,

$$\mathscr{H}_{\phi}(U) := e^{i\phi'(U)} \tag{3.33}$$

where the phase profile has a quadratic dependence with the variable U,

$$\phi'(U) := \frac{1}{2}\theta U^2 \tag{3.34}$$

The solutions for θ that produce all possible fractional and integer Talbot (sub-)images in the domain u are of the form,

$$2\pi|\theta| = \frac{p}{q}u_r^2 \tag{3.35}$$

where p and q are two mutually-prime natural numbers.

The parameter θ is related to the mechanism responsible for producing a particular manifestation of the Talbot effect. If u represents the transversal position of a spatially-periodic wavefront – a periodic image – with wavelength λ, propagating a length z in free space, then $2\pi\theta = \lambda z$ [78]; if u represents the time stamp of a temporally-periodic train of pulses traveling through a dispersive medium of length z and second-order dispersion coefficient β_2, then $\theta = \beta_2 z$ [56]; if u represents the frequency axis of a coherent optical frequency comb, then θ is the chirp parameter of a quadratic temporal phase modulation profile (e.g., for a phase modulator with half-wave voltage V_π, driven by a voltage signal $V(t) = Vt^2$, $\theta = 2\pi V_\pi^{-1} V$) [61]; if u represents the transverse momentum distribution of a wave (linearly proportional to its spatial distribution of diffraction angles under the paraxial approximation), then θ is the chirp parameter of a spatial light phase modulation profile (e.g., for a spatially-periodic wavefront with wavelength λ, propagating through a thin lens with focal length f, $\theta = 2\pi(\lambda f)^{-1}$) [103]. Table 3.4 summarizes the formulation of the Fourier-dual

representations of periodic structures susceptible of experience Talbot effects, as well as the associated values of the parameter θ in Eq. 3.35.

Table 3.4 – Representation domains supporting a Fourier duality of the Talbot effect. Summary of the relations between the four representation domains where Talbot effects are observed and their Fourier-dual domains. Examples of Talbot propagators are given (parameter θ in Eq. 3.34), as discussed in the text. In domains supporting two dimensions – space and transverse momentum – the expression of a 1D object is given as an example.

Observation domain				**Propagator**		**Fourier-dual domain**			
Domain	u	u_r	$\psi(u)$	Mechanism	θ	Domain	U	U_r	$\Psi(U)$
Space (position)	x	x_r	$\sum_{n=-\infty}^{\infty} \delta(x - nx_r)$	Paraxial diffraction	$\frac{\lambda z}{2\pi}$	Transverse momentum	k_x	$\frac{2\pi}{x_r}$	$\frac{2\pi}{x_r} \sum_{k=-\infty}^{\infty} \delta\left(k_x - k\frac{2\pi}{x_r}\right)$
Transverse momentum	k_x	k_r	$\sum_{n=-\infty}^{\infty} \delta(k_x - nk_r)$	Thin lens	$\frac{2\pi}{\lambda f}$	Space (position)	x	$\frac{2\pi}{k_r}$	$\frac{2\pi}{k_r} \sum_{k=-\infty}^{\infty} \delta\left(x - k\frac{2\pi}{k_r}\right)$
Time	t	t_r	$\sum_{n=-\infty}^{\infty} \delta(t - nt_r)$	2nd-order dispersion	$\beta_2 z$	Radial frequency	ω	$\frac{2\pi}{t_r}$	$\frac{2\pi}{t_r} \sum_{k=-\infty}^{\infty} \delta\left(\omega - k\frac{2\pi}{t_r}\right)$
Radial frequency	ω	ω_r	$\sum_{n=-\infty}^{\infty} \delta(\omega - n\omega_r)$	Quadratic phase modulation	$2\pi\frac{V}{V_\pi}$	Time	t	$\frac{2\pi}{\omega_r}$	$\frac{2\pi}{\omega_r} \sum_{k=-\infty}^{\infty} \delta\left(t - k\frac{2\pi}{\omega_r}\right)$

An identical mathematical development to that used in Section 3.1.1 for the case of temporal Talbot effect, starting from the general definitions above, results in the following Fourier transform pair for the output wave, $\psi'(u) \overset{\mathscr{F}}{\longleftrightarrow} \Psi'(U)$,

$$\psi'(u) = \frac{e^{-i\pi c}}{\sqrt{q}} \sum_{n=-\infty}^{\infty} \delta\left(u - n\frac{u_r}{q} + p\frac{u_r}{2}\right) e^{-i\pi\frac{s}{m}n^2} \tag{3.36}$$

$$\Psi'(U) = \frac{2\pi}{u_r} \sum_{k=-\infty}^{\infty} \delta\left(U - k\frac{2\pi}{u_r}\right) e^{i\pi\frac{p}{q}k^2} \tag{3.37}$$

where u represents any observation domain, and U is its Fourier-dual (e.g., any of the Fourier-conjugate pairs of Table 3.4).

The results summarized in the Fourier pair in Eqs. 3.36 and 3.37 and Table 3.3 can be enunciated as a fundamental property of the Fourier transform of Dirac combs. This solution is, then, general, and, in particular, it applies to any of the pairs of Fourier-conjugate variables listed in Table 3.4. As such, the reported formulation of the Fourier duality, along with the space-time duality [96], provides a complete picture of Talbot effect, relating its manifestations in all observation domains[8].

3.1.3 The Talbot carpet

Eqs. 3.36 and 3.37, together with Table 3.3 are sufficient to describe all images and sub-images of a periodic wave arising through Talbot effect in any observation domain. The ordered representation of the entire set

[8]It should be noted that, while in the reported derivations a single dimension of the observation domain is considered (sufficient in general for the time/frequency picture), multidimensional objects, such as 2D spatial images, can be studied under the presented mathematical analysis, simply by extending the definition of $\psi(u)$ and the Talbot phases to extra dimensions.

of such images and sub-images is referred to as the *Talbot carpet*. Fig. 3.3 shows a representation of this structure.

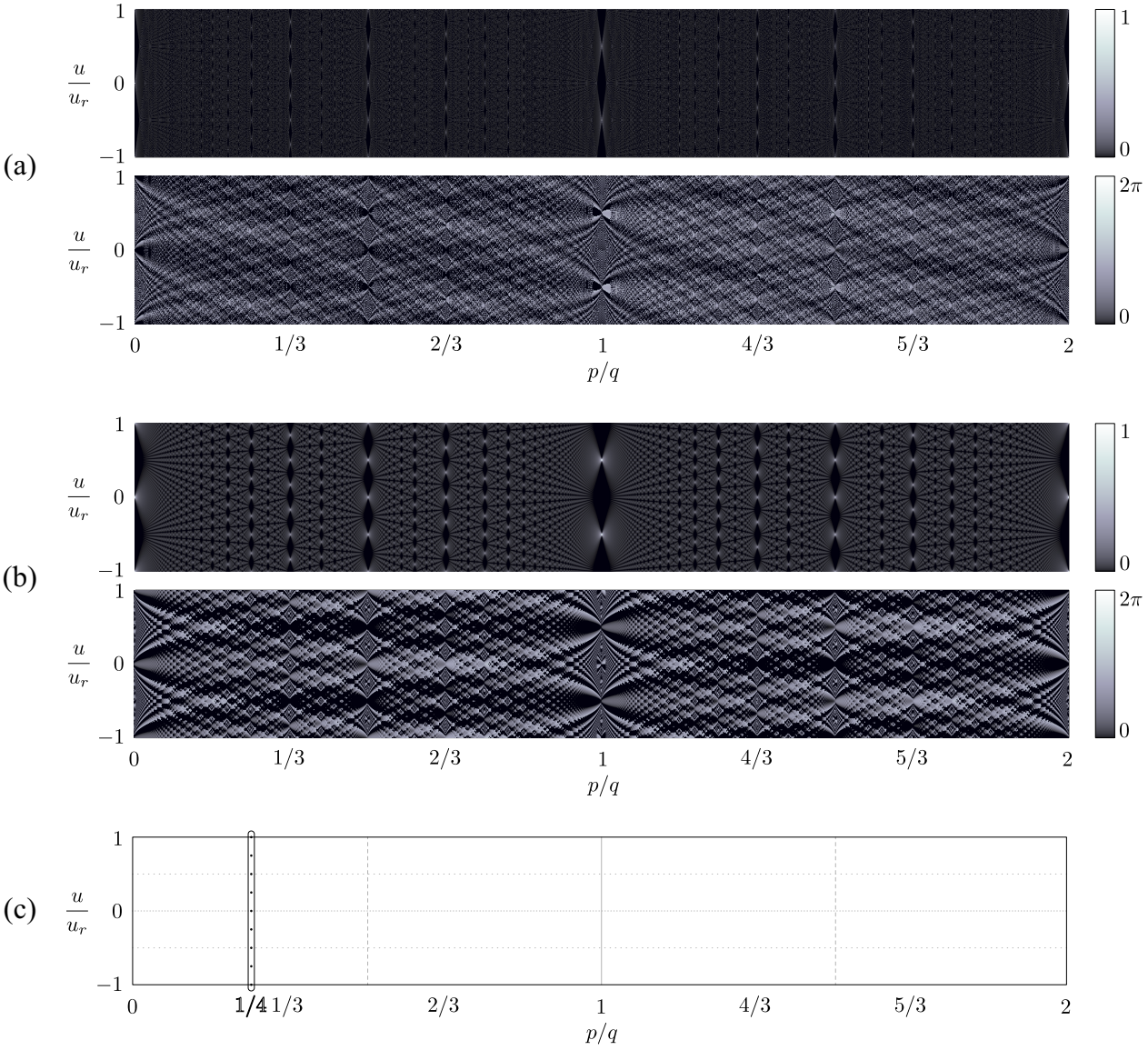

Figure 3.3 – Talbot carpet. Representation of amplitude and phase Talbot carpets in the observation domain, u; (a) amplitude (top) and phase (bottom) carpets for a periodic Dirac comb; (b) amplitude (top) and phase (bottom) carpets for a periodic Gaussian train with full-width at half maximum $u_r/50$; (c) schematic representation of the carpet, highlighting the image $p = 1$, $q = 4$.

The illustrations in Fig. 3.3(a) are the amplitude and phase Talbot carpets in the observation domain, u, for a periodic Dirac comb (Eq. 3.36). Each value of the fraction $q^{-1}p$ corresponding to a Talbot condition renders a Talbot (sub-)image. Irrational values of the fraction produce diffused images of the object $\psi(u)$, where the individual features of each period of $\psi(u)$ are not reconstructed in $\psi'(u)$, but they are rather distorted by the application of the propagator. For instance, this situation corresponds to a temporal sub-image where the amount of group velocity dispersion does not correspond to the value prescribed by the Talbot condition. Fig. 3.3(b) shows the amplitude and phase Talbot carpets of a periodic waveform with a Gaussian envelope function ($\hat{\psi}$ in Eq. 3.1), with a full-width at half maximum equal to a 50-th of u_r, obtaining smoother features.

This representation of Talbot effect has practical interest beyond its aesthetic appeal. In the following Sections the Talbot carpet will be useful to represent transformations between different Talbot (sub-)images, a methodology that will allow to formulate a universal method for controlling the period of repetitive waveforms in any domain of observation. Fig. 3.3(c) depicts a schematic representation of the carpet that will be used in the following Sections.

3.1.4 Properties of the Talbot condition

The fact that both sets of Talbot phases $\phi'_{k;p,q}$ and $\varphi_{n;s,m,c}$ satisfy the Talbot condition is relevant from an application perspective. Following the notation used throughout this Section, let us consider a periodic waveform $\psi(u)$ with period u_r. If a Talbot phase $\phi'_{k;p,q}$ is applied to its U_r-periodic spectrum, $\Psi(U)$, the resulting image in u-space, $\psi'(u)$ becomes $(q^{-1}u_r)$-periodic, and it acquires the phase $\varphi_{n;s,m=q,c}$. This situation is equivalent to the direct application of the phase $\varphi_{n;s,m}$ to an object $\psi'(u)$, periodic in u with period $q^{-1}u_r$, and originally phase-free. Such an object would have a periodic spectrum $\Psi'(U)$ with period qU_r. This operation could then be understood as emulating a *virtual* Talbot effect transforming a *virtual* object $\Psi'(U)$ into the image $\Psi(U)$, U_r-periodic. Dual Talbot effects can then be used in both time and frequency domains to construct images from virtual waveforms with arbitrarily-defined repetition periods. This property is the basis for the universal period control method, proposed and detailed in Section 3.2.

In the following paragraphs, some properties of the Talbot phases of mathematical interest are discussed.

3.1.4.1 Solution set of the Talbot condition

It is interesting to note a few properties of the discrete set of allowed solutions of the Talbot propagator, identified by the rational values of the fraction $q^{-1}p$ in Eqs. 3.35 and 3.10.

Fig. 3.4(a) illustrates the 866 possible combinations of p and q that give rise to a valid integer ($q = 1$) or fractional ($q > 1$) Talbot condition in the interval $\{q \in \mathbb{N},\ p \in \mathbb{N} \mid 1 \leq q \leq 55\ \ 1 \leq p \leq 25\}$.

Fig. 3.4(b) shows the (unique) allowed value of q for any given value of $q^{-1}p \in \mathbb{Q}$, in the interval $\{q^{-1}p \in \mathbb{Q} \mid 0 < q^{-1}p \leq 2\}$. The 2-periodicity of this solution set in $q^{-1}p$ is consistent with the periodicity of the Talbot carpet, as the fraction $q^{-1}p$ represents the normalized argument of the Talbot propagator.

Fig. 3.4(c) lists the amount of allowed values of p (i.e, the number of valid Talbot conditions) for a given q, when $q^{-1}p$ lays in its fundamental period. This, in turn, corresponds to the number of possible solutions to achieve a period division factor q in the fundamental period of the Talbot carpet[9]. It is easy to verify from Fig. 3.4(c) that, for odd values of q, exactly half of the allowed solutions for p are odd, giving rise to odd values of pq. These solutions correspond to Talbot sub-images with a lateral shift of half a period (see Eqs. 3.29 and 3.30). Fig. 3.5 shows some pairs of Talbot phases in Fourier-dual domains, where the mentioned effects can be assessed[10].

From the structure of the dual Talbot phase sequence (Eq. 3.19), it is easy to demonstrate that $\varphi_{n;s,q}$ and $\varphi_{n;s+2Nq,q}$ are congruent modulo 2π, for any $N \in \mathbb{Z}$,

[9]Note that, in general, multiple values of $q^{-1}p$ may achieve a given period division factor q; e.g., $q = 3$ allows for $p = \{1, 2, 4, 5\}$ in the fundamental period of the Talbot carpet.

[10]The phase sequences shown in Fig. 3.5 are generated from the analytic expressions developed in this chapter, as well as by numerically solving the associated Gauss sums (see MATLAB source code in Appendix C).

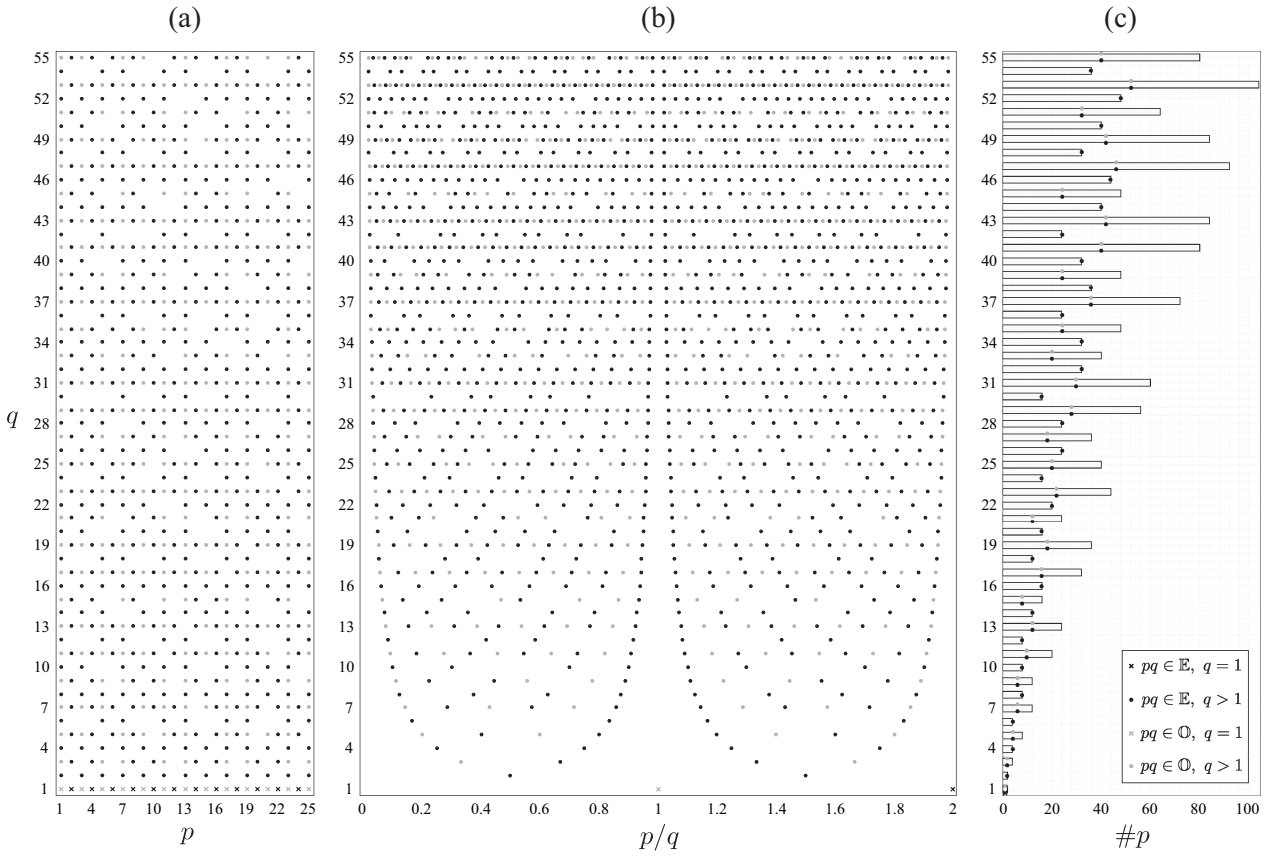

Figure 3.4 – Solution set of the Talbot condition. The Talbot propagator only exists for values of p and q satisfying $q^{-1}p \in \mathbb{Q}$. (a) Snapshot of the set of Talbot conditions for $\{q \in \mathbb{N},\ p \in \mathbb{N} \mid 1 \leq q \leq 55\ 1 \leq p \leq 25\}$. (b) Value of q associated to each value of $q^{-1}p$, in the interval $\{q^{-1}p \in \mathbb{Q} \mid 0 < q^{-1}p \leq 2\}$. (c) Number of allowed values of p for each value of q. Black marks correspond to even values of pq, while light grey marks correspond to odd values of pq.

$$\begin{aligned} \varphi_{n;s+2Nq,q,c} &= -\pi\frac{s}{q}n^2 - 2N\pi n^2 - \pi c \\ &\equiv -\pi\frac{s}{q}n^2 - \pi c \\ &= \varphi_{n;s,q,c} \end{aligned} \tag{3.38}$$

where it should be noted that, $e^{-i2N\pi n^2} \equiv e^{i2\pi} = 1\ \forall\ \{n, N\} \in \mathbb{Z}$.

This is consistent with the fact that the Talbot carpet is $2q$-periodic in its longitudinal dimension, evidenced also by Fig. 3.4(b). As such, the solutions for the parameter s are not unique; they are in fact, periodic, with the fundamental range $\{s \in \mathbb{N} \mid 1 \leq s \leq 2q - 1\}$. Equivalently, when choosing a particular Talbot phase in the dual domain U, values of p separated by an arbitrary multiple of $2q$ will result on congruent values of $s \pmod{2q}$, within the fundamental range. Table 3.5 lists the fundamental values of the parameter s for some combinations of p and q.

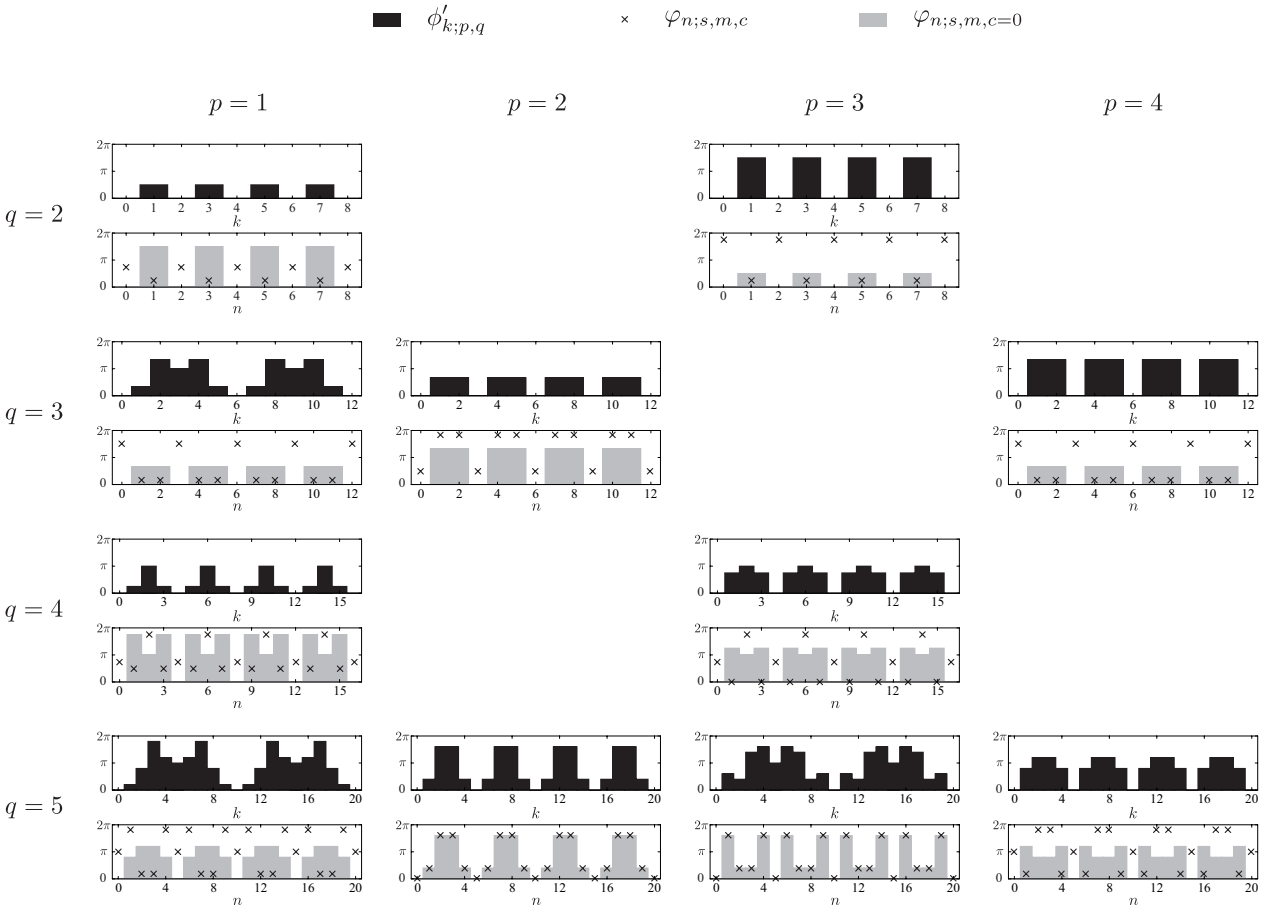

Figure 3.5 – Talbot phases in Fourier-dual domains. Values of $\phi'_{k;p,q} \pmod{2\pi}$ and $\varphi_{n;s,m,c} \pmod{2\pi}$ are shown in the ranges $\{k \in \mathbb{Z} \mid 0 \leq k \leq 4q\}$ and $\{n \in \mathbb{Z} \mid 0 \leq n \leq 4m\}$, respectively, for each allowed pair $\{p, q \mid q^{-1}p \in \mathbb{Q}\}$. Results for $\varphi_{n;s,m,c} \pmod{2\pi}$ are included for the case $c = 0$.

3.1.4.2 Similarity

A particularly interesting Talbot self-image is the one corresponding to the condition $p = q \pm 1$. It can be shown that in this situation, $s = p$ (see main diagonal in Table 3.5), which implies that, if the constant c is neglected (recall that, from a practical viewpoint, this parameter does not contribute significantly to the structure of the image $\psi'(u)$), the discrete phase profiles along the two Fourier-related domains have identical expressions (except for the opposite sign). That is,

$$\phi'_{k;q\pm1,q} \equiv -\varphi_{k;s,q,c=0} \; \forall \, \{q \in \mathbb{N} \mid q > 1\} \tag{3.39}$$

where the variable change $n \leftarrow k$ is only necessary to compare the structure of both sequences on equal grounds.

3.1.4.3 Periodicity along Fourier-dual representation domains

From the self-imaging theory, the Talbot phases are expected to be q-periodic in both k and n [100]. In order to verify this, it suffices to evaluate the sequences in $k \leftarrow k + q$ and $n \leftarrow n + q$. For the sequence in k,

Table 3.5 – Values of the coefficients of the Talbot phases in Fourier-dual domains. Values of $s \pmod{2q}$ for different values of p and q.

		p									
		1	2	3	4	5	6	7	8	9	10
q	2	1		3		1		3		1	
	3	4	2		4	2		4	2		4
	4	1		3		5		7		1	
	5	6	8	2	4		6	8	2	4	
	6	1				5		7			
	7	8	4	12	2	10	6		8	4	12
	8	1		11		13		7		9	
	9	10	14		16	2		4	8		10
	10	1		7				3		9	
	11	12	6	4	14	20	2	8	18	16	10

$$\begin{aligned} \phi'_{k+q;p,q} &= \pi\frac{p}{q}(k+q)^2 \\ &= \pi\frac{p}{q}k^2 + 2\pi pk + \pi pq \\ &\equiv \pi\frac{p}{q}k^2 + \pi pq \\ &= \phi'_{k;p,q} + \pi pq \end{aligned} \tag{3.40}$$

where, once more, Euler's identity implies $e^{i2\pi pk} \equiv e^{i2\pi} = 1 \,\forall\, \{k \in \mathbb{Z}, p \in \mathbb{N}\}$; and, similarly, the sequence in n,

$$\varphi_{n+q;s,q,c} \equiv \varphi_{n;s,q,c} + \pi sq \tag{3.41}$$

The periods of the Talbot phases in U and u depend on the parity of the products pq and sq respectively. For the phase sequence in U, the hypothesis of q-periodicity holds only when $pq \in \mathbb{E}$. If $pq \in \mathbb{O}$, the period of the sequence $\phi'_{k;p,q}$ is equal to $2q$. This discrepancy is explained by the fact that the extra net π factor in $\phi'_{k;p,q}$ when $pq \in \mathbb{O}$ introduces a shift in the u domain by half of the input period (represented in Eq. 3.29 by of the factor $2^{-1}pu_r$), a phenomenon that has been referred to as 'inverted' Talbot effect[11] [56].

For the phase sequence in the u domain, it should be noted that, from Table 3.3, $q \in \mathbb{O} \implies s \in \mathbb{E}$, necessarily. This implies that all of the Talbot images in u verify $sq \in \mathbb{E}$, and the sequence $\varphi_{n;s,q,c}$ is always q-periodic. This is consistent with the fact that the comb in the U domain is not expected to undergo any additional shift by the application of the Talbot propagator.

[11] Note that, although this lateral shift is observed when $pq \in \mathbb{O}$, a shift of half an input period when $q \in \mathbb{E}$, even if $p \in \mathbb{O}$, does not introduce any shift at all to an infinitely-periodic object (for any value of p). This is because the input period, u_r, is an even multiple of the output one $q^{-1}u_r$. The factor $2^{-1}pu_r$ in Eq. 3.29, including only the parameter p, is sufficient to model this effect, although, if it serves to facilitate interpretation, it can also be written as $2^{-1}pqu_r$, or $\epsilon_p 2^{-1}u_r$, where ϵ_p is the parity of p (see Eq. 3.28).

These findings on the periodicity of the Talbot phases can be easily assessed from Fig. 3.5.

3.2 Universal periodicity control model

The results reported in the previous Section, in particular, the expressions of Talbot phase sequences in domains related by a Fourier transform, provides a starting point for a general method to arbitrarily tailor the period of any repetitive waveform. Periodic trains of pulses and frequency combs (their frequency-domain counterpart) are particularly interesting examples of periodic signals, with intrinsic relevance and deep implications in a myriad of scientific and technological disciplines[12].

The goal here is to obtain an output pulse train (frequency comb) with a pulse repetition period (FSR) multiplied (divided) by a factor $r \in \mathbb{Q}$, defined by the interplay of Talbot conditions, where r can, in principle, be any rational factor lower or higher than 1.

This Section presents a step-by-step description of a universal method to arbitrarily set the period of any periodic waveform, observable in a wave representation domain where the Fourier transform is defined (see Table 3.4). The method is formulated in the time/frequency picture, in the context of periodic trains of pulses and frequency combs, although direct application of the space-time duality[13] suffices for an equivalent formulation in the space/momentum picture of spatial images and angular spectra [96].

3.2.1 Signal definitions

Similarly to the development in Section 3.1.1, the definitions of the original signal of interest and its Fourier transform are,

$$\psi(t) := \sum_{n=-\infty}^{\infty} \hat{\psi}\left(t - nt_r\right) \tag{3.42}$$

$$\Psi(\nu) := \sum_{k=-\infty}^{\infty} c_k \delta\left(\nu - k\nu_r\right) \tag{3.43}$$

where,

t_r is the pulse repetition period of the train,
$\nu_r = t_r^{-1}$ is the free spectral range (FSR) of the comb,
$\hat{\psi} : \mathbb{R} \to \mathbb{C}$ is the complex amplitude of a single pulse, so that $\hat{\psi}(t) = 0 \; \forall \; |t| > t_r/2$,
$c_k = \nu_r \hat{\Psi}(k\nu_r)$ is the complex weight of the k-th delta of the comb, with $\hat{\Psi}(\nu) = \mathscr{F}\{\hat{\psi}(t)\}$.

Note that in this case, the Fourier transform is done in linear frequency, ν, instead of radial frequency, $\omega = 2\pi\nu$. This choice of variables is simply a matter of convenience, as it is common when working with frequency combs and pulse trains to define quantities such as the FSR and the repetition rate in Hz, rather than in rad/s, while the use of the radial frequency variable in Section 3.1.1 allowed for simpler expressions of the Fourier transforms obtained through the mathematical developments.

[12] Consult chapter 1 for a detailed review on the applications of temporally- and spectrally-periodic signals.
[13] For a review of the space-time duality, consult Appendix B.

Fig. 3.6 illustrates the relationship between a periodic train of pulses (Eq. 3.42, Fig. 3.6(a)) and its frequency comb representation (Eq. 3.43, Fig. 3.6(b)).

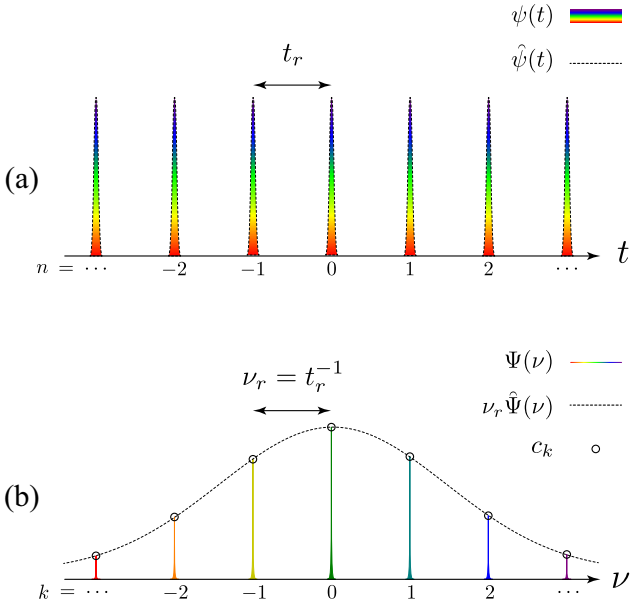

Figure 3.6 – Relationship between a train of pulses and its frequency comb representation. A periodic train of pulses (a) with pulse repetition period t_r has a spectrum in the form of a coherent frequency comb (b) with FSR $\nu_r = t_r^{-1}$. The relation between the different parameters of Eqs. 3.42 and 3.43 is illustrated. The shown representation deals with the complex envelope of the involved signals; the underlying carrier frequency is not shown for simplicity of representation.

3.2.1.1 Power distributions

It will be useful in the following, to introduce some definitions relative to the power distributions of $\psi(t)$ and $\Psi(\nu)$. In particular, the instantaneous power of $\psi(t)$ – the energy per unit time[14] carried by the train – is defined as $\psi^*(t)\psi(t)$. For a single pulse, the instantaneous power is $\hat{\psi}^*(t)\hat{\psi}(t)$, where the maximum is referred to as the peak power, $P_t := \max_{t\in\mathbb{R}}\{\psi^*(t)\psi(t)\} = \max_{t\in\mathbb{R}}\{\hat{\psi}^*(t)\hat{\psi}(t)\}$. On the other hand, $\Psi^*(\nu)\Psi(\nu)$ gives the power per unit frequency, i.e., the amount of energy per time delivered by each frequency component of $\psi(t)$, and it is referred to as its power spectrum. Similarly, a measure of peak spectral power of the comb can be defined in the frequency domain as $P_\nu := \max_{\nu\in\mathbb{R}}\{\Psi^*(\nu)\Psi(\nu)\} = \max_{k\in\mathbb{Z}}\{c_k^* c_k\}$. Note that, in the limit case, $\hat{\psi}(t) = \delta(t) \implies P_\nu = \nu_r^2 P_t$. As a remark, since $\psi(t)$ and $\Psi(\nu)$ are Fourier conjugates, Parseval's theorem holds, and the energy per pulse can be calculated either from the complex envelope[15] $\hat{\psi}(t)$, or from the complex coefficients of $\Psi(\nu)$, $c_k = \nu_r\hat{\Psi}(k\nu_r)$,

$$\frac{1}{t_r}\int_{-\infty}^{\infty}\hat{\psi}^*(t)\hat{\psi}(t)\,\mathrm{d}t = \sum_{k=-\infty}^{\infty} c_k^* c_k \tag{3.44}$$

[14] Not to be confused with intensity, which is power per unit area. Here, all the energy is assumed to be coupled to a single spatial mode.

[15] Note that, as per the definition of $\hat{\psi}(t)$,

$$\int_{-\infty}^{\infty}\hat{\psi}^*(t)\hat{\psi}(t)\,\mathrm{d}t = \int_{t_0}^{t_0+t_r}\psi^*(t)\psi(t)\,\mathrm{d}t$$

where t_0 is an arbitrary point in the domain of definition of $\psi(t)$.

For periodic trains of pulses, it is convenient to also define the average power, P_{avg} as the mean rate of energy flow per pulse period. Given a pulse train with repetition period t_r, and pulse duration Δt, in the first approximation – for a pulse with a rectangular shape – the average power writes,

$$P_{\text{avg}} = \frac{\Delta t}{t_r} P_t \tag{3.45}$$

Fig. 3.7 illustrates the relationship between the mentioned parameters for a periodic train of rectangular pulses.

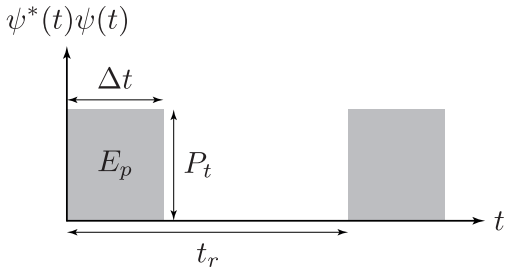

Figure 3.7 – Relation between power and time parameters on periodic signals. Relationship between pulse duration (Δt), repetition period (t_r), energy per pulse (E_p) and pulse peak power (P_t), for a periodic sequence of rectangular pulses.

Note that the peak power can then be written as the energy per pulse, E_p, per unit time,

$$P_t = \frac{E_p}{\Delta t} \tag{3.46}$$

and the fraction of time occupied by the pulse, known as *duty cycle*, τ_c, can be defined as,

$$\begin{aligned} \tau_c &:= \frac{\Delta t}{t_r} \\ &= \frac{P_{\text{avg}}}{P_t} \end{aligned} \tag{3.47}$$

3.2.2 Talbot propagators for periodic trains of pulses and frequency combs

The temporal and spectral Talbot propagators, as described in Eqs. 2.45 and 2.48, respectively, involve modifications of the spectral and temporal phase profiles of the periodic signal of interest, that follow quadratic variations with the frequency and time variables, respectively. It is convenient, however, to define discrete Talbot propagators for periodic signals, providing the constant phase level to be applied to each individual comb line or pulse of the train. This is possible by using the definitions of the spectral and temporal Talbot phases, $\phi_{k;p,q}$ and $\phi_{k;s,m,c}$, given in Eqs. 3.10 and 3.19, respectively. These are the basic building blocks of the periodicity control method proposed in this section.

3.2.2.1 The discrete temporal Talbot propagator

From Eq. 3.10, the phase level to be applied to the k-th line of a frequency comb to observe any temporal Talbot (sub-)image is[16],

[16]The notation of the Talbot phase sequence in k is simplified here for convenience.

$$\begin{aligned} \phi_{k;p,q} &:= \varsigma\phi'_{k;p,q} \\ &= \varsigma\pi\frac{p}{q}k^2 \end{aligned} \tag{3.48}$$

where $\varsigma = \pm 1$. In particular, if the effect is achieved through propagation of the periodic signal of interest through a second-order dispersive medium of length z and second-order dispersion coefficient β_2, then $\varsigma = \text{sgn}\{\beta_2\}$, where $\text{sgn}\{\cdot\}$ is an operator that returns the sign of its argument, so that,

$$\text{sgn}\{a\} := \begin{cases} -1 & \iff a < 0 \\ 0 & \iff a = 0 \\ +1 & \iff a > 0 \end{cases} \tag{3.49}$$

In this situation (as stated in Section 2.4.2), the total amount of second-order dispersion satisfies the temporal Talbot condition,

$$2\pi|\beta_2|z = \frac{p}{q}t_r^2 \tag{3.50}$$

The discrete operator responsible for temporal Talbot effect writes, then,

$$\{\mathcal{H}_{\text{TSI}}\}_{k;p,q} := e^{i\phi_{k;p,q}} \tag{3.51}$$

Application of this propagator to the frequency comb spectrum of a t_r-periodic train of pulses, produces a new pulse train with period $q^{-1}t_r$, affected by the pulse-to-pulse phase profile described in Eq. 3.19 (where s is calculated from Eq. 3.27).

This operation is a quadratic spectral phase filtering (SPF) transformation. For optical waves, as stated above, the operation can be achieved through GVD propagation [56], or through a specially-designed multi-level optical phase filter, following the values of the sequence $\phi_{k;p,q}$ at k-multiples of ν_r [100].

3.2.2.2 The discrete spectral Talbot propagator

Since, as demonstrated in Section 3.1, the phase sequence $\varphi_{n;s,q,c}$ (Eq. 3.19) satisfies the general Talbot condition. As such, neglecting a constant phase term (constant c in Eq. 3.29), the phase level to be applied to the n-th pulse of a pulse train to observe any spectral Talbot (sub-)image is[17],

$$\begin{aligned} \varphi_{n;s,q} &:= \varsigma\varphi_{n;s,m=q,c=0} \\ &= -\varsigma\pi\frac{s}{q}n^2 \end{aligned} \tag{3.52}$$

[17] The notation of the Talbot phase sequence in n is simplified here for convenience.

The discrete operator responsible for spectral Talbot effect writes, then,

$$\{\mathcal{H}_{\text{SSI}}\}_{n;s,q} := e^{i\varphi_{n;s,q}} \tag{3.53}$$

Application of this propagator to the pulse train representation of a ν_r-periodic frequency comb, produces a new comb with period $q^{-1}\nu_r$, affected by the line-to-line phase profile described in Eq. 3.10 (where p is calculated from Eq. 3.27).

For optical waves, this operator can be practically implemented as electro-optical temporal phase modulation (TPM) of the input signal with a multilevel voltage driving signal following the values of the sequence $\varphi_{n;s,q}$ at n-multiples of t_r. Additionally, for pulses with sufficiently short temporal durations, the sequence $\varphi_{n;s,q}$ can be approximated by a continuous function of time, provided that the phase variations within a single pulse are slow enough to be considered constant. Nonlinear cross-phase modulation with parabolic-shaped pump pulses has been demonstrated as a successful candidate of this operation with ps-wide optical pulses [OPj7].

3.2.2.3 The Talbot propagator as a transformation on the Talbot carpet

The application of a specific Talbot phase can be interpreted as a displacement from one point in the Talbot carpet to a different one. This visual way of interpreting the effect is particularly useful to picture the transformations involved in the model for periodicity control reported in the following.

To illustrate this, let us consider a train of pulses with period t_r, to which we apply a temporal Talbot phase $\varphi_{n;s,m}$ (from Equation 3.52), satisfying a spectral Talbot condition for the pair $\{s, q\} \in \mathbb{N}$, and $q^{-1}s \in \mathbb{Q}$.

Fig. 3.8 shows the effect of such a phase transformation along the spectral and temporal amplitude Talbot carpets.

The applied temporal phase *transports* the plane 0 to the plane $q^{-1}s$ in the spectral carpet, dividing the input FSR by q (as shown in the bottom plot of Fig. 3.8).

The outcome of this temporal phase modulation is then a spectral Talbot effect. The input pulse period remains unaltered, but the applied temporal phase emulates the effect of dispersive propagation of a *virtual* pulse train with original period qt_r, to the temporal sub-image $q^{-1}p$ (as shown in the top plot of Fig. 3.8). This corresponds to a spectral phase $\phi_{k;p,m}$ (from Eq. 3.48), acquired by the FSR-divided comb.

The applied temporal phase has then the effect of selecting a sub-image, $q^{-1}p$, in a *virtual* temporal carpet where the period of the virtual pulse train at the input – plane 0 – is q times the period of the real pulse train under analysis (see Fig. 3.8, top).

Equivalently, this corresponds to a displacement on the spectral carpet to a, generally different, sub-image $q^{-1}s$. Note that while the denominator, q, is the same in both domains, in general, $p \neq s$.

The dual situation, i.e., temporal Talbot effect, would be produced by the spectral phase filtering of a frequency comb with a Talbot phase sequence $\phi_{k;p,q}$. In such case, the resulting transformations would be the selection of the sub-image $q^{-1}s$ in a virtual spectral Talbot carpet with an input FSR q times larger than that of the real comb under analysis; and a displacement on the temporal carpet to the sub-image $q^{-1}p$, where generally, $s \neq p$.

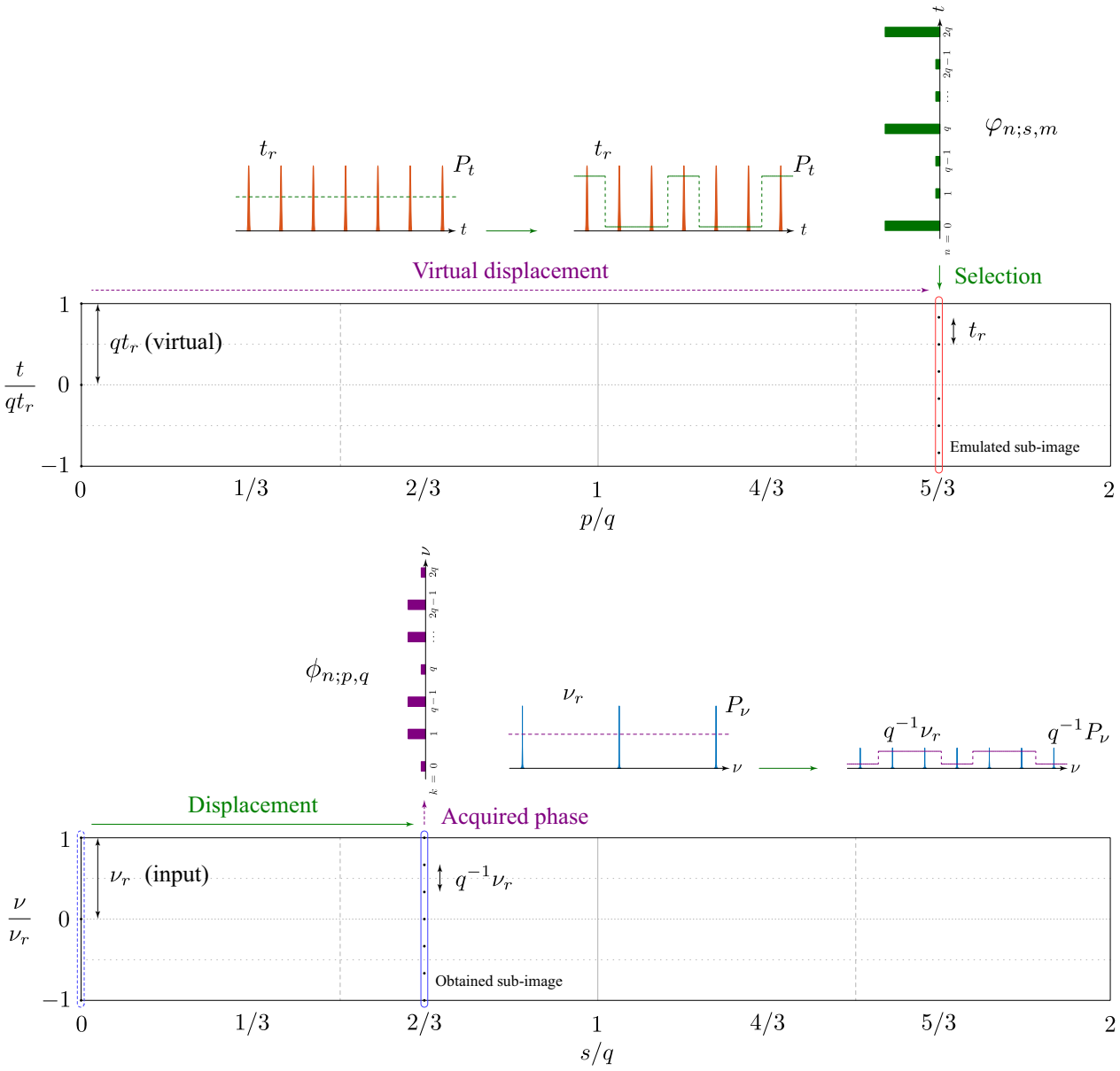

Figure 3.8 – The Talbot propagator as a transformation in the Talbot carpet. The temporal phase $\varphi_{n;s,m}$, applied to a train of pulses with period t_r (top), produces the sub-image $q^{-1}s$ of a fractional spectral Talbot effect (bottom). Moreover, the output train behaves as the sub-image $q^{-1}p$ of a virtual temporal Talbot carpet with fundamental period qt_r (as illustrated in the top figure). As such, the output $q^{-1}\nu_r$-periodic comb acquires the spectral phase $\phi_{n;p,q}$. Note that, in general, $p \neq s$; in the given example, $s = 2$ and $q = 3$, resulting in $p = 5$ (see Table 3.5).

3.2.3 Phase-controlled Talbot effects

The time-frequency duality of the Talbot effect is the key to achieve an arbitrary control of the repetition period of a pulse train or a frequency comb. For this purpose, one simply must find and apply the right recipe of Talbot phases to transform a pulse train (frequency comb) into a new one with an arbitrary, user-defined pulse period (FSR).

The method can be intuitively understood from Fig. 3.8, where one could design a combination of Talbot phases to select a specific Talbot (sub-)image, and then induce a displacement to a different Talbot

(sub-)image with different period in the same carpet. The transformations required to achieve such arbitrary control of periodicity are detailed in this Section.

Two different, though equivalent, methods can be designed for this purpose. These two methods differ by the order on which the specific Talbot phases are applied. Here the are referred to as *phase-controlled temporal Talbot method* (PCTTM) and *phase-controlled spectral Talbot method* (PCSTM).

3.2.3.1 Phase-controlled temporal Talbot method

This Section describes a method to transform a train of optical pulses with period t_r into a new train with period rt_r, where the multiplication factor of the repetition period, r, can be any irreducible fraction of the form $r = q_2^{-1}q_1 \; \forall \; \{q_1 \in \mathbb{N}, q_2 \in \mathbb{N} \mid q_2^{-1}q_1 \in \mathbb{Q}\}$, i.e., r is the ratio of two co-prime natural numbers.

If the transformation is entirely completed, in the frequency domain, this translates into a division of the corresponding frequency comb FSR by the factor r, i.e., from $\nu_r = t_r^{-1}$ to $r^{-1}\nu_r$.

Different combinations of temporal and spectral Talbot phases could be designed to achieve the same multiplication factor; i.e., different values of the parameters p, q, s and m in Eqs. 3.48 and 3.52. This Section describes the general solution of the problem and then provides guidelines to achieve particular solutions that minimize the displacement on the temporal Talbot carpet (corresponding to the case of minimum required dispersion in a practical implementation).

General solution

The general phase-controlled temporal Talbot method is summarized in Figure 3.9. Recall that the goal here is to transform a train of pulses with period t_r into a new train with period rt_r, where $r = q_2^{-1}q_1$.

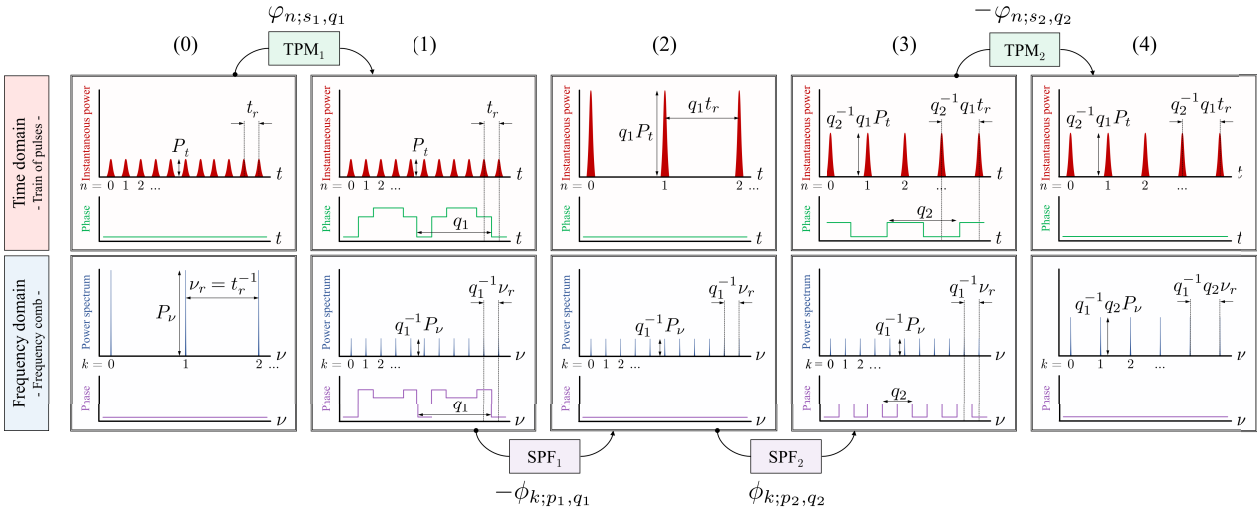

Figure 3.9 – Phase-controlled temporal Talbot method. Steps to transform a train of pulses with period t_r into a new train with period rt_r, with $r = q_2^{-1}q_1$, through the application of Talbot phases. In the frequency domain, the corresponding frequency comb representation of the train, with FSR ν_r is transformed into a new comb with FSR $r^{-1}\nu_r$. In the illustrated example, $r = 5/2$.

As such, the method consists of the following four steps.

0. **Input**. The starting point is a train of pulses with period t_r, corresponding to a frequency comb with FSR $\nu_r = t_r^{-1}$ (Fig. 3.9(0)). From Eqs. 3.42 and 3.43,

$$\psi_0(t) := \sum_{n=-\infty}^{\infty} \hat{\psi}\left(t - nt_r\right) \tag{3.54}$$

$$\Psi_0(\nu) := \sum_{k=-\infty}^{\infty} c_k \delta\left(\nu - k\nu_r\right) \tag{3.55}$$

The power distributions (see Section 3.2.1.1),

$$\psi_0^*(t)\psi_0(t) = \sum_{n=-\infty}^{\infty} \left|\hat{\psi}\left(t - nt_r\right)\right|^2 \tag{3.56}$$

$$\Psi_0^*(\nu)\Psi_0(\nu) = \sum_{k=-\infty}^{\infty} \left|c_k\right|^2 \delta\left(\nu - k\nu_r\right) \tag{3.57}$$

and thus, the values of peak power in time and frequency are,

$$P_t = \max_{t\in\mathbb{R}}\{\psi_0^*(t)\psi_0(t)\} \tag{3.58}$$

$$P_\nu = \max_{k\in\mathbb{Z}}\{c_k^* c_k\} \tag{3.59}$$

1. **TPM$_1$** (temporal phase modulation 1). A spectral Talbot propagator of the form $\{\mathcal{H}_{\text{SSI}}\}_{n;s_1,q_1}$ (Eq. 3.53) is applied to $\psi_0(t)$, inducing a spectral Talbot effect described by the Talbot condition $\{s_1, q_1\}$. This corresponds to a temporal phase modulation with the sequence $\varphi_{n;s_1,q_1}$ (Eq. 3.52).

Choosing $\varsigma = 1$,

$$\psi_1(t) = \sum_{n=-\infty}^{\infty} \hat{\psi}\left(t - nt_r\right) e^{-i\pi\frac{s_1}{q_1}n^2} \tag{3.60}$$

$$\Psi_1(\nu) = \frac{e^{i\pi c_1}}{\sqrt{q_1}} \sum_{k=-\infty}^{\infty} c_k \delta\left(\nu - k\frac{\nu_r}{q_1} + s_1\frac{\nu_r}{2}\right) e^{i\pi\frac{p_1}{q_1}k^2} \tag{3.61}$$

where c_1 is the constant phase term in the frequency domain, associated to the application of the Talbot phase $\varphi_{n;s_1,q_1}$.

The power distributions,

$$\psi_1^*(t)\psi_1(t) = \sum_{n=-\infty}^{\infty} \left|\hat{\psi}\left(t - nt_r\right)\right|^2 \tag{3.62}$$

$$\Psi_1^*(\nu)\Psi_1(\nu) = \frac{1}{q_1}\sum_{k=-\infty}^{\infty} |c_k|^2\, \delta\left(\nu - k\frac{\nu_r}{q_1} + s_1\frac{\nu_r}{2}\right) \tag{3.63}$$

TPM_1 does not alter the instantaneous power of the train, as it simply involves the application of a temporal phase profile. The associated power spectrum, however, is affected by this operation, as different frequency components of the comb are shifted due to the effect of the spectral Talbot propagator. The FSR of the resulting comb is $q_1^{-1}\nu_r$, while the pulse period remains equal to t_r (Fig. 3.9(1)). Similarly, the resulting peak powers of the train and the comb are P_t and $q_1^{-1}P_\nu$, respectively.

2. **SPF_1** (spectral phase filtering 1). As a result of TPM_1, $\Psi_1(\nu)$ acquired a line-to-line spectral phase profile, $\phi_{k;p_1,q_1}$, associated to the Talbot condition $\{p_1, q_1\}$ (Eq. 3.48). As anticipated in Section 3.2.2.3, this result is equivalent to the action of a temporal Talbot propagator of the form $\{\mathcal{H}_{\text{TSI}}\}_{k;p_1,q_1}$ on a virtual comb with FSR $q_1^{-1}\nu_r$. In the time domain, $\psi_1(t)$ resembles a Talbot sub-image, obtained from a virtual train with period $q_1 t_r$.

Application of the propagator $\{\mathcal{H}_{\text{TSI}}\}^*_{k;p_1,q_1}$ (spectral phase profile $-\phi_{k;p_1,q_1}$) to $\Psi_1(\nu)$, cancels the residual spectral line-to-line phases induced by TPM_1.

$$\psi_2(t) = \sqrt{q_1}e^{i\pi c_1}\sum_{n=-\infty}^{\infty}(-1)^{nq_1s_1}\hat{\psi}\left(t - nq_1t_r\right) \tag{3.64}$$

$$\Psi_2(\nu) = \frac{e^{i\pi c_1}}{\sqrt{q_1}}\sum_{k=-\infty}^{\infty} c_k\delta\left(\nu - k\frac{\nu_r}{q_1} + s_1\frac{\nu_r}{2}\right) \tag{3.65}$$

where the term $(-1)^{nq_1s_1}$ introduces an additional phase factor associated to the lateral shift experienced by the comb when $s_1q_1 \in \mathbb{O}$. This term arises from the frequency shift property of the Fourier transform, which introduces a term $e^{i2\pi s_1\frac{\nu_r}{2}t}$ to $\psi_2(t)$, and, due to the sampling property of Dirac deltas, results in $(-1)^{nq_1s_1}$.

The power distributions,

$$\psi_2^*(t)\psi_2(t) = q_1\sum_{n=-\infty}^{\infty}\left|\hat{\psi}\left(t - nq_1t_r\right)\right|^2 \tag{3.66}$$

$$\Psi_2^*(\nu)\Psi_2(\nu) = \frac{1}{q_1}\sum_{k=-\infty}^{\infty}|c_k|^2\,\delta\left(\nu - k\frac{\nu_r}{q_1} + s_1\frac{\nu_r}{2}\right) \tag{3.67}$$

The power spectrum is not altered by SPF_1. The pulse period of the train, however, is multiplied by q_1 due to the cancellation of spectral phases, becoming q_1t_r (Fig. 3.9(2)). Conservation of energy ensures that the peak power values in time and frequency are q_1P_t and q_1P_ν, respectively. The energy of the original train is redistributed into a train with a larger pulse spacing. Since no additional power was added nor was any subtracted from the train, the average power must remain unchanged. The energy per pulse must, in turn,

increase, thus resulting in the obtained peak power enhancement by q_1. This effect has been referred to as *passive Talbot amplification* [57].

Note that this process can be implemented as linear dispersive propagation, and the required amount of GVD, $\beta_2 z$, can be calculated by substituting $p \leftarrow p_1$, $q \leftarrow q_1$ and $t_r \leftarrow q_1 t_r$ in Equation 3.50.

If the desired temporal period multiplication factor is integer, this is the final step, and $r = q_1$.

3. **SPF$_2$** (spectral phase filtering 2). At this point, $\Psi_2(\nu)$ is free of line-to-line phase variations, but its FSR is $q_1^{-1}\nu_r$. As such, application of a new temporal Talbot propagator of the form $\{\mathcal{H}_{\text{TSI}}\}_{k;p_2,q_2}$ (spectral phase profile $\phi_{k;p_2,q_2}$) to $\Phi_2(\nu)$ produces a temporal self-image, satisfying the Talbot condition $\{p_2, q_2\}$ for an input period $q_1 t_r$.

$$\psi_3(t) = \sqrt{\frac{q_1}{q_2}} e^{i\pi(c_1+c_2)} \sum_{n=-\infty}^{\infty} (-1)^{n q_1 s_1} \hat{\psi}\left(t - n\frac{q_1}{q_2}t_r + p_2 q_1 \frac{t_r}{2}\right) e^{-i\pi\frac{s_2}{q_2}n^2} \tag{3.68}$$

$$\Psi_3(\nu) = \frac{e^{i\pi c_1}}{\sqrt{q_1}} \sum_{k=-\infty}^{\infty} c_k \delta\left(\nu - k\frac{\nu_r}{q_1} + s_1\frac{\nu_r}{2}\right) e^{i\pi\frac{p_2}{q_2}k^2} \tag{3.69}$$

where c_2 is the constant phase term in the time domain, associated to the application of the Talbot phase $\phi_{n;p_2,q_2}$.

The power distributions,

$$\psi_3^*(t)\psi_3(t) = \frac{q_1}{q_2} \sum_{n=-\infty}^{\infty} \left|\hat{\psi}\left(t - n\frac{q_1}{q_2}t_r + p_2 q_1 \frac{t_r}{2}\right)\right|^2 \tag{3.70}$$

$$\Psi_3^*(\nu)\Psi_3(\nu) = \frac{1}{q_1} \sum_{k=-\infty}^{\infty} |c_k|^2 \, \delta\left(\nu - k\frac{\nu_r}{q_1} + s_1\frac{\nu_r}{2}\right) \tag{3.71}$$

The application of a second spectral phase $\phi_{k;p_2,q_2}$ divides the temporal repetition period of the train obtained after SPF$_1$ by the factor q_2. If q_1 and q_2 are mutually-prime natural numbers, the overall effect is the multiplication of the input pulse period by the fraction $r = q_2^{-1}q_1$ (Fig. 3.9(3)). Note that, depending of the designed values of q_1 and q_2 this factor can be either higher or lower than 1. Similarly, the resulting peak powers of the train and the comb are $q_2^{-1}q_1 P_t$ and $q_1^{-1}P_\nu$, respectively.

If the desired outcome is the multiplication of the pulse period of $\psi_0(t)$ by the factor r, regardless of the value of the corresponding frequency comb, no further steps are necessary.

As a note on implementation, since the application of the temporal Talbot propagator does not alter the FSR of the comb in the frequency domain, the two consecutive spectral phase filtering steps, SPF$_1$ and SPF$_2$, can be combined into a single operation,

$$\begin{aligned} \phi_{k;p_2,q_2} - \phi_{k;p_1,q_1} &\equiv \phi_{k;p_2q_1-p_1q_2,q_1q_2} \\ &= \pi\frac{p_2q_1 - p_1q_2}{q_1q_2}k^2 \end{aligned} \tag{3.72}$$

If this process is implemented as GVD propagation, the total amount of dispersion can always be designed to be smaller than the sum of the magnitudes of both dispersive propagation steps taken independently. This is due to the fact that the sign of $\phi_{k;p_2,q_2}$ can be chosen arbitrarily, and the sign of $\phi_{k;p_1,q_1}$ is determined by the sign of $\varphi_{n;s_1,q_1}$, which can be set arbitrarily as well.

4. **TPM$_2$** (temporal phase modulation 2). Finally, $\psi_3(t)$ has uncompensated pulse-to-pulse phase variations, of the form $\varphi_{n;s_2,q_2}$. This is due to the fact that $\psi_3(t)$, is a temporal Talbot sub-image of $\psi_2(t)$. Application of a new spectral Talbot propagator of the form $\{\mathcal{H}_{\text{SSI}}\}^*_{n;s_2,q_2}$ (spectral phase profile $-\varphi_{n;s_2,q_2}$) to $\psi_3(t)$, compensates for the mentioned phase variations.

$$\psi_4(t) = \sqrt{\frac{q_1}{q_2}} e^{i\pi(c_1+c_2)} \sum_{n=-\infty}^{\infty} (-1)^{nq_1s_1} \hat{\psi}\left(t - n\frac{q_1}{q_2}t_r + p_2q_1\frac{t_r}{2}\right) \tag{3.73}$$

$$\Psi_4(\nu) = \sqrt{\frac{q_2}{q_1}} e^{i\pi(c_1+c_2)} \sum_{k=-\infty}^{\infty} (-1)^{nq_2p_2} c_k \delta\left(\nu - k\frac{q_2}{q_1}\nu_r + s_1\frac{\nu_r}{2}\right) \tag{3.74}$$

The power distributions,

$$\psi_3^*(t)\psi_3(t) = \frac{q_1}{q_2} \sum_{n=-\infty}^{\infty} \left|\hat{\psi}\left(t - n\frac{q_1}{q_2}t_r + p_2q_1\frac{t_r}{2}\right)\right|^2 \tag{3.75}$$

$$\Psi_3^*(\nu)\Psi_3(\nu) = \frac{q_2}{q_1} \sum_{k=-\infty}^{\infty} |c_k|^2 \delta\left(\nu - k\frac{q_2}{q_1}\nu_r + s_1\frac{\nu_r}{2}\right) \tag{3.76}$$

Application the variable changes $t' \leftarrow t + p_2q_1t_r/2$ and $\nu' \leftarrow \nu + s_1\nu_r/2$, results in the power distributions,

$$\psi_4^*(t')\psi_4(t') = r \sum_{n=-\infty}^{\infty} \left|\hat{\psi}\left(t' - nrt_r\right)\right|^2 \tag{3.77}$$

$$\Psi_4^*(\nu')\Psi_4(\nu') = \frac{1}{r} \sum_{k=-\infty}^{\infty} |c_k|^2 \delta\left(\nu' - k\frac{\nu_r}{r}\right) \tag{3.78}$$

The global outcome of the method is, as anticipated, the transformation of a pulse train (frequency comb) with pulse period t_r (FSR ν_r) into a new train (comb) with period rt_r (FSR $r^{-1}\nu_r$), where $r = q_2^{-1}q_1$. Consequent transformations of the peak powers of the train and comb to rP_t and $r^{-1}P_\nu$, respectively, are also achieved.

Table 3.7 summarizes the general solution of the PCTTM, and Fig. 3.10 shows the involved transformations on the temporal Talbot carpet for a particular example with $r = 5/2$.

Fig. 3.11 shows a step-by-step numerical simulation example, illustrating the results of the application of the PCTTM to multiply the repetition period of a pulse train by the factor $r = 5/2 = 2.5$ (and the FSR of its corresponding frequency comb representation by $r^{-1} = 2/5 = 0.4$).

Table 3.7 – Phase-controlled temporal Talbot method, general solution. Summary of parameters and outcomes of each step of the phase-controlled temporal Talbot method with pulse period multiplication factor $r = q_2^{-1}q_1$ (and corresponding FSR multiplication factor $r^{-1} = q_1^{-1}q_2$). The listed values ensure an output signal free of temporal and/or spectral Talbot phase variations.

	0. **Input**	1. **TPM$_1$**	2. **SPF$_1$**	3. **SPF$_2$**	4. **TPM$_2$**
Applied Talbot phase		$\varphi_{n;s_1,q_1}$ [a]	$-\phi_{k;p_1,q_1}$ [b]	$\phi_{k;p_2,q_2}$ [c]	$-\varphi_{n;s_2,q_2}$ [d]
Pulse repetition period Time domain	t_r	t_r	$q_1 t_r$	$q_2^{-1}q_1 t_r$	$q_2^{-1}q_1 t_r$
Free spectral range Frequency domain	ν_r	$q_1^{-1}\nu_r$	$q_1^{-1}\nu_r$	$q_1^{-1}\nu_r$	$q_1^{-1}q_2\nu_r$

[a] s_1 is a free parameter.
[b] p_1 is obtained from Eq. 3.27 with $\{s \leftarrow s_1, q \leftarrow q_1\}$.
[c] p_2 is a free parameter.
[d] s_2 is obtained from Eq. 3.27 with $\{p \leftarrow p_2, q \leftarrow q_2\}$.

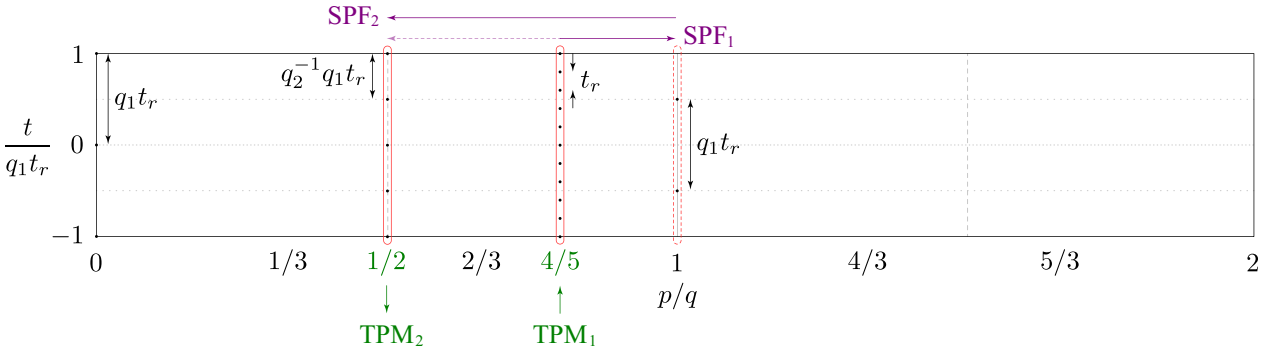

Figure 3.10 – Phase-controlled temporal Talbot method, temporal Talbot carpet. Phase transformations of the PCTTM shown as movements in the temporal Talbot carpet. Shown example for $r = 5/2$.

Note that the problem reduces to the calculation of four Talbot conditions. Since there are, in general, several allowed values of p (or s) for each value of q, many configurations of the method are possible to achieve a desired value of r. The parameters s_1 and p_2 can be set freely[18]. This implies that several solutions to the method can be found for a desired period multiplication factor.

Particular solution for minimum dispersion

It is interesting to look for solutions that minimize the total displacement on the temporal Talbot carpet, since such solutions achieve a minimal required amount of dispersion[19]. From an implementation perspective, this is an attractive design specification, as it minimizes the total propagation length and, in turn, the associated propagation loss.

[18] The only restrictions to setting these parameters are that s_1 and q_1 must be mutually-prime, and p_2 and q_2 must be mutually-prime.

[19] This is the case when the spectral phase filtering (SPF) steps are implemented by GVD propagation.

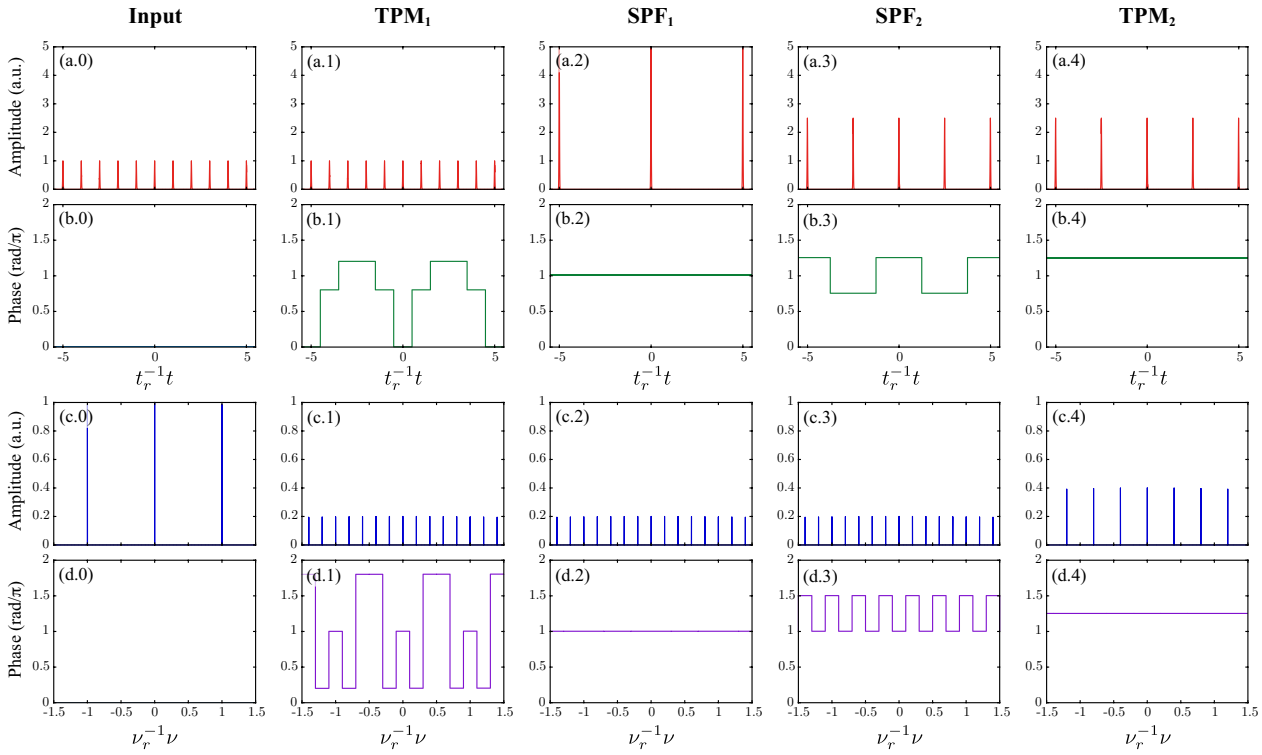

Figure 3.11 – Phase-controlled temporal Talbot method, simulation example. Step-by-step numerical simulation of the method with multiplication factor $r = 5/2 = 2.5$; (a) amplitude and (b) phase of the temporal train of pulses; (c) amplitude and (d) phase of the corresponding frequency comb spectrum. In this simulation, Gaussian pulses with a full width at half maximum equal to a 30-th of the pulse repetition period are used for ease of interpretation (this produces a frequency comb with a power distribution that is mostly flat within the chosen spectral representation window).

From Eq. 3.50 and Table 3.7, the magnitude of the total required dispersion to achieve the desired period multiplication factor is,

$$2\pi|\beta_2|z = \left|\frac{p_2}{q_2} - \frac{p_1}{q_1}\right| (q_1 t_r)^2 \tag{3.79}$$

recall that p_1 is determined by the values of q_1 and s_1.

The solution with minimum dispersion minimizes Eq. 3.79 for the parameters p_1 and p_2. Renaming $d := 2\pi\,|\beta_2|\,z$,

$$d = \left|\frac{p_2}{q_2} - \frac{p_1}{q_1}\right| q_1^2 t_r^2 \tag{3.80}$$

Rearranging terms, Eq. 3.80 rewrites,

$$|p_2 q_1 - p_1 q_2| = \frac{q_2}{q_1}\frac{d}{t_r^2} \tag{3.81}$$

Bézout's identity states that given two nonzero integers, q_1 and q_2, with greatest common divisor g, there exist integers p_2 and p_1 such that [101],

$$p_2 q_1 - p_1 q_2 = g \tag{3.82}$$

Note that g is the smallest[20] natural number that can be written as $p_2 q_1 - p_1 q_2$. Since q_1 and q_2 are mutually-prime, their greatest common divisor is $g = 1$. Using Eq. 3.82 in Eq. 3.81, gives the minimum value of d,

$$\min_{p_1,p_2}\{d\} = \frac{q_1}{q_2} t_r^2 \tag{3.83}$$

and the minimum dispersion is,

$$2\pi|\beta_2|z = \frac{q_1}{q_2} t_r^2 \tag{3.84}$$

The minimum required dispersion is then fixed by the period multiplication factor, $r = q_2^{-1} q_1$, and the input temporal period, t_r. The associated Bézout coefficients, p_2 and p_1, that satisfy Eq. 3.82 are determined by the standard extended Euclidean algorithm [101]. Given the specifications for the input period and the desired multiplication factor, r, the parameters of the phase-controlled temporal Talbot method with minimum dispersion are obtained as follows,

0. Specifications of the method: $r = q_2^{-1} q_1$, and t_r. The minimum dispersion is given by Eq. 3.84.
1. Determine p_1 and p_2 from Eq. 3.82 with $g = 1$, using the standard extended Euclidean algorithm.
2. Determine s_1 from p_1 and q_1, using Eq. 3.27.
3. Determine s_2 from p_2 and q_2, using Eq. 3.27.

It is interesting to note that, since q_1 and q_2 are mutually-prime naturals, the minimum dispersion value satisfies a fractional temporal Talbot condition for the input period t_r. In particular, in the absence of the first temporal phase modulation step, TPM_1, the method will produce a train of pulses with period $q_2^{-1} t_r$.

3.2.3.2 Phase-controlled spectral Talbot method

This Section describes an alternative version (although equivalent in result) to the method described in the previous Section. The goal here is to transform a frequency comb with FSR ν_r into a new comb with FSR $r^{-1}\nu_r$, this time, through transformations along the spectral Talbot carpet. Recall that $r = q_2^{-1} q_1 \; \forall \; \{q_1 \in \mathbb{N}, q_2 \in \mathbb{N} \mid q_2^{-1} q_1 \in \mathbb{Q}\}$, i.e., r is the ratio of two co-prime natural numbers.

Similarly to the PCTTM, if the transformation is entirely completed, in the time domain, this translates into a multiplication of the corresponding pulse repetition period by the factor r, i.e., from $t_r = \nu_r^{-1}$ to $r t_r$.

Also, similarly to the previous method, a number of specifications can be adjusted freely in the calculation of the Talbot phases to achieve a desired value of r, leading to many different possible values for the main design parameters.

[20] The Bézout coefficients, p_2 and p_1, are not unique, and every integer of the form $p_2 q_1 - p_1 q_2$ is a natural multiple of g

This Section describes the general solution of the problem and then provides guidelines to achieve particular solutions that minimize the displacement on the temporal Talbot carpet (corresponding to the case of minimum required dispersion in a practical implementation).

General solution

The general phase-controlled spectral Talbot method is summarized in Fig. 3.12. Recall that the goal here is to transform a frequency comb with FSR ν_r into a new comb with FSR $r^{-1}\nu_r$, where $r = q_2^{-1}q_1$.

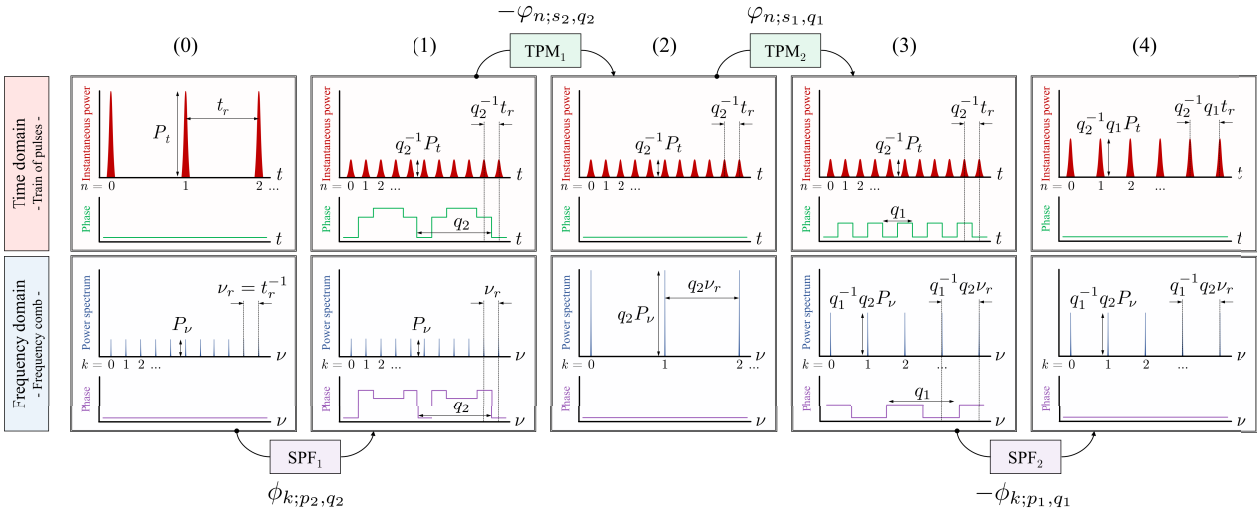

Figure 3.12 – Phase-controlled spectral Talbot method. Steps to transform a frequency comb with FSR ν_r into a new comb with period $r^{-1}\nu_r$, with $r = q_2^{-1}q_1$, through the application of Talbot phases. In the time domain, the corresponding pulse train representation of the comb, with pulse period t_r is transformed into a new train with period rt_r. In the illustrated example, $r = 5/2$.

As such, the method consists of the following four steps.

0. **Input**. The starting point of the method is a frequency comb with FSR ν_r, corresponding to a train of optical pulses with period $t_r = \nu_r^{-1}$ (Figure 3.12(0)).

1. **SPF$_1$** (spectral phase filtering 1). The input comb is phase-filtered with the sequence $\phi_{k;p_2,q_2}$. The resulting pulse train has a period $q_2^{-1}t_r$, while the comb FSR remains equal to ν_r (Fig. 3.12(1)).

2. **TPM$_1$** (temporal phase modulation 1). The acquired temporal phase is canceled by a phase modulation mechanism with the opposite phase profile, $-\varphi_{n;s_2,q_2}$. The result is a flat-phase comb with FSR $q_2\nu_r$ (Fig. 3.12(2)). If the desired FSR multiplication factor is integer, this is the final step. The parameter s_2 is given by Equation 3.27 (with $s \leftarrow s_2$, $p \leftarrow p_2$ and $q \leftarrow q_2$).

3. **TPM$_2$** (temporal phase modulation 2). A second temporal phase $\varphi_{n;s_1,q_1}$ divides the FSR by q_1. If q_2 and q_1 are mutually-prime natural numbers, the overall effect is the division of the input FSR by the rational factor $r = q_2^{-1}q_1$, resulting in $r^{-1}\nu_r$ (Fig. 3.12(3)).

4. **SPF$_2$** (spectral phase filtering 2). The residual spectral phases, acquired due to the application of TPM$_2$, can be canceled out by the application of an additional all-pass filtering step, corresponding to

$-\phi_{k;p_1,q_1}$, where p_1 is given by Equation 3.27 (with $s \leftarrow s_1$, $p \leftarrow p_1$ and $q \leftarrow q_1$). The obtained pulse period is rt_r (Fig. 3.12(4)).

As a note on implementation, since the application of the spectral Talbot propagator does not alter the pulse period of the train in the time domain, the two consecutive temporal phase modulation steps, TPM_1 and TPM_2, can be combined into a single operation,

$$\begin{aligned} \varphi_{n;s_1,q_1} - \varphi_{n;s_2,q_2} &\equiv \varphi_{k;s_1q_2-s_2q_1,q_1q_2} \\ &= -\pi \frac{s_1q_2 - s_2q_1}{q_1q_2} n^2 \end{aligned} \tag{3.85}$$

The global outcome of the method is, as anticipated, the transformation of a frequency comb (pulse train) with FSR ν_r (pulse period t_r) into a new comb (train) with FSR $r^{-1}\nu_r$ (pulse period rt_r), where $r = q_2^{-1}q_1$. Consequent transformations of the peak powers of the comb and train to $r^{-1}P_\nu$ and rP_t, respectively, are also achieved.

Similarly to the temporal method, step 4 (SPF_2) is only necessary if one wishes to obtain a phase-free frequency comb and/or to control the pulse train temporal period. If the objective is only to set the comb FSR, regardless of the pulse period, this step can be omitted. If included, however, it becomes clear that both realizations of phase-controlled Talbot effects achieve identical results through different sets of transformations in the temporal and spectral Talbot carpets. Both methods are then equivalent from a signal processing perspective.

Table 3.8 summarizes the general solution of the PCSTM, and Fig. 3.13 shows the involved transformations on the spectral Talbot carpet for a particular example with $r^{-1} = 5/2$.

Table 3.8 – Phase-controlled spectral Talbot method, general solution. Summary of parameters and outcomes of each step of the phase-controlled spectral Talbot method with FSR multiplication factor $r^{-1} = q_1^{-1}q_2$ (and corresponding pulse period multiplication factor $r = q_2^{-1}q_1$). The listed values ensure an output signal free of temporal and/or spectral Talbot phase variations.

	0. **Input**	1. **SPF_1**	2. **TPM_1**	3. **TPM_2**	4. **SPF_2**
Applied Talbot phase		$\phi_{k;p_2,q_2}$ [a]	$-\varphi_{n;s_2,q_2}$ [b]	$\varphi_{k;s_1,q_1}$ [c]	$-\phi_{k;p_1,q_1}$ [d]
Pulse repetition period Time domain	t_r	$q_2^{-1}t_r$	$q_2^{-1}t_r$	$q_2^{-1}t_r$	$q_2^{-1}q_1t_r$
Free spectral range Frequency domain	ν_r	ν_r	$q_2\nu_r$	$q_1^{-1}q_2\nu_r$	$q_1^{-1}q_2\nu_r$

[a] p_2 is a free parameter.
[b] s_2 is obtained from Eq. 3.27 with $\{p \leftarrow p_2, q \leftarrow q_2\}$.
[c] s_1 is a free parameter.
[d] p_1 is obtained from Eq. 3.27 with $\{s \leftarrow s_1, q \leftarrow q_1\}$.

Once again, the problem reduces to the calculation of four Talbot conditionswith two degrees of freedom (s_1 and p_2).

Particular solution for minimum dispersion

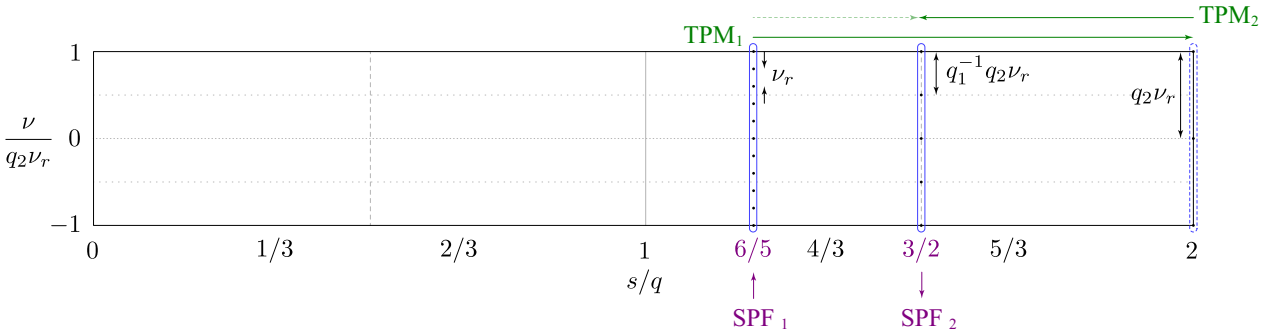

Figure 3.13 – Phase-controlled spectral Talbot method, spectral Talbot carpet. Phase transformations of the PCSTM shown as movements in the spectral Talbot carpet. Shown example for $r^{-1} = 5/2$.

In this version of the method, the two spectral phase filtering steps, SPF_1 and SPF_2, are not consecutive. The total required dispersion is then obtained by adding the magnitudes of both dispersion steps (i.e., without sign). From Eq. 3.50 and Table 3.8,

$$2\pi|\beta_2|z = \frac{p_2}{q_2}t_r^2 + \frac{p_1}{q_1}\left(\frac{q_1}{q_2}t_r\right)^2 \tag{3.86}$$

The minimum displacement in the temporal Talbot carpet is then achieved by minimizing each individual displacement induced by SPF_1 and SPF_2, i.e., by imposing $p_2 = 1$ (s_2 is then obtained from Equation 3.27), and setting s_1 to obtain $p_1 = 1$ using Equation 3.27. The minimum dispersion writes,

$$2\pi|\beta_2|z = \frac{q_1 + q_2}{q_2^2}t_r^2 \tag{3.87}$$

3.2.4 Limits and considerations of the method

In the following, some important considerations of the proposed periodicity control methods are discussed.

3.2.4.1 Limits of the period multiplication factor

In regards to the conventional temporal Talbot effect, using spectral phase filtering only, the maximum pulse period division factor that can be achieved has an upper boundary. This limit is imposed by the temporal duration of the individual pulses of the original train, in order to avoid interference among consecutive rate-multiplied pulse replicas.

In a temporal Talbot sub-image with parameters $\{p, q\}$, q pulses are obtained in the duration of a single input period, where originally only one pulse was present, thus the output temporal period must be longer than the full-width duration of an individual pulse. Naming the full pulse duration Δt, this limit establishes an upper bound for the factor q,

$$q \leq \frac{t_r}{\Delta t} \tag{3.88}$$

This condition can be equivalently enunciated in the frequency domain, where the limit now deals with the number of discrete frequency components that fit within the pulse bandwidth. The spectral Talbot phase that produces the temporal sub-image $\{p, q\}$ is q-periodic. As such, this phase sequence must be applied to a minimum of q consecutive spectral lines. The pulse bandwidth must then fit q comb lines at least.

For the general case of a pulse period multiplication factor of the form $r = q_2^{-1}q_1$, this condition sets a lower boundary,

$$r \geq \frac{\Delta t}{t_r} \tag{3.89}$$

If $r > 1$, there is no fundamental limitation to the pulse period multiplication factor in the PCTTM, since the first transformation to the instantaneous power of the train is a multiplication of its period by q_1 (note that $r >$ automatically satisfies condition 3.89). In the PCSTM, however, the first step is a temporal Talbot effect (SPF_1), resulting in pulse period division by q_2. If condition 3.88 is not satisfied by q_2, the method will fail, even if r satisfies condition 3.89.

From this viewpoint, short pulse durations (corresponding to large frequency bandwidths) are generally preferred.

Regarding the accessible range of period multiplication factors, the described period control methods allow for the design of r factors that can be expressed as an irreducible fraction of two natural numbers, i.e., rational factors. Irrational multiplication factors cannot be achieved by the proposed techniques. However, it is a well-known result of number theory that any real number can be approximated by the ratio of two integers with arbitrary precision. This is known as the Diophantine approximation. Hurwitz's theorem establishes an upper bound to such approximations [101]; for every irrational number, ξ, there are infinite mutually-prime integers v and w, such that,

$$\left|\xi - \frac{v}{w}\right| < \frac{1}{\sqrt{5}w^2} \tag{3.90}$$

This result suggests that the proposed method could, in principle, approximate irrational period multiplication factors with arbitrary precision.

3.2.4.2 Considerations on practical implementation

Here, the specifics of the two processes involved in the methods – spectral phase filtering and temporal phase modulation – are analyzed form the viewpoint of practical implementation through optics and photonics technology.

Spectral phase filtering

Temporal Talbot effect is typically induced by linear propagation through second-order group velocity dispersive media [75]. This is due to the fact that the different temporal Talbot conditions are achieved by a quadratic spectral phase of a certain curvature [56].

Optical media such as dispersive fibers are good approximations to second-order dispersion. However, these approximations lose accuracy for pulses with broad bandwidths, as higher order dispersion effects become significant.

It is important to note that the amount of dispersion, required to induce a temporal Talbot condition, scales with the square of the pulse period (Eq. 3.50). This means that lower repetition rate trains will require longer propagation distances in order to produce a given Talbot (sub-)image, for a given value of the second-order dispersion coefficient of the medium, β_2.

For example, considering a standard single-mode fiber SMF-28, the nominal value of second-order chromatic dispersion at a central wavelength of 1550 nm is $\sim$17 ps/nm/km, with a typical attenuation of 0.275 dB/km. A repetition rate multiplication factor of 2 for a 10 GHz rate pulse train would then require a fiber propagation length of approximately 36 km, with an associated loss of approximately 10 dB (corresponding to a linear power attenuation factor of 10). Propagation loss can be mitigated by the use of special fibers, such as dispersion-compensating fibers, which can be designed to introduce larger amounts of dispersion in shorter propagation lengths. Moreover, linearly-chirped fiber Bragg gratings [104], and superimposed linearly-chirped fiber Bragg gratings [105], further reduce the required propagation lengths by orders of magnitude [OPj16]. These are periodic structures, capable of achieving large amounts of second-order dispersion over broad frequency ranges, and with overall losses that can be below the 1-dB level; e.g., a few meters of linearly-chirped fiber Bragg grating can compensate the dispersion introduced by hundreds of km of SMF-28, thus substantially reducing the loss associated to the propagation of light in the medium.

In this context, it is also interesting to ask whether any of the two realizations of the method offers an optimal solution that minimizes the total required dispersion. To answer this question, the minimum dispersion values of both methods, given in Eqs. 3.84 and 3.87, are compared. Dropping the constant multiplicative factor t_r^2 on the right-hand side of Eqs. 3.84 and 3.87, and renaming the remaining fractions d_{T} and d_{S} respectively,

$$d_{\mathrm{T}} := \frac{q_1}{q_2} \tag{3.91}$$

$$d_{\mathrm{S}} := \frac{q_1 + q_2}{q_2^2} \tag{3.92}$$

The difference between d_{S} and d_{T} writes,

$$d_{\mathrm{S}} - d_{\mathrm{T}} = \frac{q_1 + q_2 - q_1 q_2}{q_2^2} \tag{3.93}$$

Since q_1 and q_2 are positive and nonzero, the sign of this fraction is determined by its numerator. In particular, if $q_1 = 1$ and/or $q_2 = 1$, then $q_1 + q_2 > q_1 q_2$, and $d_{\mathrm{S}} > d_{\mathrm{T}}$. On the other hand, if $q_1 > 1$ and $q_2 > 1$, then $q_1 + q_2 < q_1 q_2$, and $d_{\mathrm{S}} < d_{\mathrm{T}}$.

Alternatively, the ratio of d_{S} to d_{T} writes:

$$\frac{d_{\mathrm{S}}}{d_{\mathrm{T}}} = \frac{1}{q_1} + \frac{1}{q_2} \tag{3.94}$$

Again, since q_1 and q_2 are positive and nonzero, if $q_1 = 1$ and/or $q_2 = 1$, then $q_1^{-1} + q_2^{-1} > 1$, and $d_{\mathrm{S}} > d_{\mathrm{T}}$. On the other hand, if $q_1 > 1$ and $q_2 > 1$, then $q_1^{-1} + q_2^{-1} < 1$, and $d_{\mathrm{S}} < d_{\mathrm{T}}$.

In conclusion, the PCTTM offers a solution with lower dispersion than the phase-controlled spectral Talbot method when either the pulse-period or FSR multiplication factor is an integer (i.e., for $q_1 = 1$ and/or $q_2 = 1$). However, for strictly fractional multiplication factors (i.e., for $q_1 > 1$ and $q_2 > 1$) the PCSTM demands lower dispersion.

Finally, it is important to note that Talbot phases are inherently discrete, i.e., the applied phase must be constant over each period of the initial signal, otherwise distortion will be induced on the signal representation in the dual domain. In fact, temporal Talbot effect can be achieved through a especially designed all-pass filter with a discrete phase profile, introducing a line-by-line spectral Talbot phase sequence [100]. On the other hand, optical fibers and linearly-chirped fiber Bragg gratings introduce continuous spectral phase variations. These continuous phases represent a good approximation to their discrete counterpart in the case of optical frequency combs, as the linewidth of the comb lines is generally narrow enough to neglect any continuous phase variations occurring within each comb line. In general, the linewidth of a frequency comb increases when aperiodicities are introduced across its temporal pulse train representation. For instance, a sequence of pulses with finite duration will have a comb representation with a relatively broad linewidth. Temporal Talbot effect of such a sequence, implemented through continuous (dispersive) spectral filtering, will result in distortion of the individual output pulses [106].

Temporal phase modulation

The temporal phase modulation profiles employed in the described methods are sequences of constant phase levels, applied pulse to pulse. Such is the form of a Talbot phase, i.e., flat within each individual pulse; otherwise, a temporal phase profile with nonlinear variations in time would introduce unwanted modulation of the instantaneous frequency of the pulse (chirp), consequently altering the spectral envelope.

These Talbot phase sequences can be generated electronically and introduced to the train of pulses through electro-optical phase modulation [61]. The limiting factor in this implementation is the available electronic bandwidth (typically in the range of a few tens of GHz).

A possible solution to overcome this limit would be to avoid the use of electro-optic components and to implement the Talbot phases optically. In order to do this, one could use a nonlinear effect with properly shaped optical pump pulses to imprint the desired Talbot phase in the train to be processed. Spectral Talbot effect induced by cross-phase modulation with parabolic-shaped optical pump pulses has been demonstrated [OPj7]. In this situation, one should consider that conditions must be imposed so that the continuous phase modulation closely approaches the desired discrete Talbot phase distribution. In this regard, the pulses of the input train should be sufficiently narrow, so that to avoid the introduction of significant chirp, associated to the temporal phase variations occurring within each pulse. This ultimately leads to undesired distortion of the resulting comb spectral envelope. The specific conditions could be derived as the Fourier-domain counterpart of the equivalent problem studied for temporal Talbot effect [106].

It is important to note that the temporal Talbot phase associated to the sub-image $\{s, q\}$ is q-periodic when reduced modulo 2π, assuming $sq \in \mathbb{E}$. Additionally, since these sequences are derived from quadratic expressions, each period of the sequence is symmetric with respect to its central sample (see Fig. 3.14(a)). A single period of the temporal Talbot phase associated to the sub-image $\{s, q\}$ can then be constructed with q samples that take values in a set of $\lfloor q/2 \rfloor + 1$ levels. This is an important consideration of the signal used to imprint such a phase in the modulation process. In the case of electronics-based implementations (e.g., the voltage output of an arbitrary waveform generator), this means that the vertical resolution of the involved digital-to-analog converters must be sufficient to encode $\lfloor q/2 \rfloor + 1$ voltage levels, and the available depth of

memory must be sufficient to store q samples. For $sq \in \mathbb{O}$, the phase sequence contains an additional linear term. The number of samples becomes $2q$, and the number of levels $q + 1$ (see Fig. 3.14(b)).

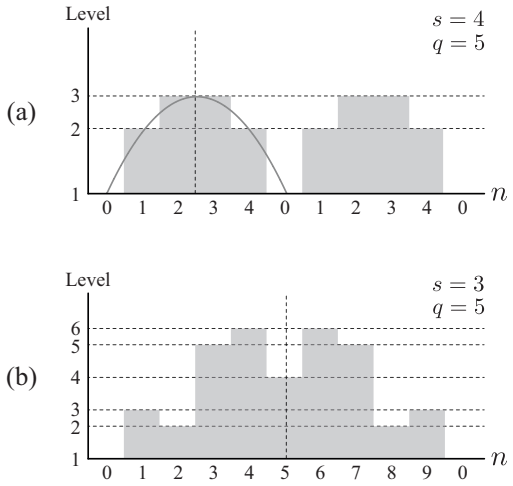

Figure 3.14 – Discretization of temporal Talbot phases. Talbot phases corresponding to $q = 5$ for (a) $s = 4$ ($sq \in \mathbb{E}$) and (b) $s = 3$ ($sq \in \mathbb{O}$). In (a), $q = 5$ samples and $\lfloor q/2 \rfloor + 1 = 3$ levels are needed to build up the sequence. In (b), $2q = 10$ samples and $q + 1 = 6$ levels are needed to build up the sequence.

3.2.4.3 Considerations on energy preservation and noise

This chapter described the operations necessary to arbitrarily manipulate the repetition periods of pulse trains and frequency combs. Such operations are manipulations of the temporal and spectral phase distributions of the signal of interest. As such, ideally, the entire energy carried by the signal is preserved in the process. This is one of the main advantages of the reported methodology.

For pulse period (FSR) multiplication factors higher than 1, the obtained pulses (comb lines) have an increased energy per period of the output signal. The method, however, does not alter the additive noise carried by the signal, as these are incoherent, random fluctuations that do not satisfy the Talbot conditions necessary for period control. Moreover, practical implementations of the described phase manipulations – spectral phase filtering and temporal phase modulation – do not introduce additional external noise in the process. It is possible, then, to obtain output waveforms with lower noise content, relative to the input waveforms, through the application of phase-controlled Talbot effects.

It should be noted that the average power of the signal remains unaltered after the application of the method. This is due to the fact that the described transformations simply redistribute the total energy carried by the signal into a different set of output periods.

In the following chapters, this principle will be demonstrated experimentally.

3.2.5 Generality of the method

All the operations required by the reported methods are linear manipulations of the phase of a wave, along its two Fourier-dual domains of representation; i.e., time and frequency, in the reported model. As per the findings reported in Section 3.1.2, these methods can be extended to any system or framework described by wave equations. One must simply identify the equivalent operations of spectral phase filtering and temporal phase modulation in such a framework (see Table 3.4). In particular, these methods could be readily-applied to the space and transverse momentum (observed in the form of angular spectrum) domains of optical fields,

by direct application of the space-time duality[21]. A similar realization of this method was reported to control the periodicity of repetitive images in two dimensions, even allowing to tailor the spatial repetition periods associated to each dimension independently [OPj11].

Moreover, the generality of the operations involved would, in principle, allow to implement arbitrary period control of signals outside the realm of optical waves. In fact, manifestations of the Talbot effect have been reported across a wide variety of wave regimes, including radio-frequency waves [107], acoustic and mechanical waves [108], X-rays [109], plasmon waves [87] matter waves [88, 89], quantum wavefunctions [90], etc.

Finally, given the beneficial noise-reduction properties of the studied processes (that will be analyzed in more detail in the following chapters), purely computational versions of these methods could be envisioned as techniques to enhance signals and images affected by noise through numerical signal processing operations.

[21] For a review of the space-time duality, consult Appendix B.

CHAPTER 4

Processing of periodic temporal waves

In this chapter, the universal period control method proposed in chapter 3 is applied to a periodic temporal signal. In particular, energy-preserving division of the repetition rate of a train of optical pulses by fractional factors is demonstrated. Considerations on noise mitigation are described, where the process produces a counter-intuitive effect of noise averaging, equivalent to calculating the mean of a non-integer number of noise contributions. The work presented in this Chapter was reported in [APj1, APj4] [APc1].

4.1 Arbitrary period control of pulse trains

In this chapter, the methodology introduced in Section 3.2.3.1 is experimentally validated. In particular, energy-preserving multiplication of the pulse period of a train of optical pulses by a fractional factor, $r \in \mathbb{Q}$, as depicted in Fig. 4.1, is experimentally demonstrated.

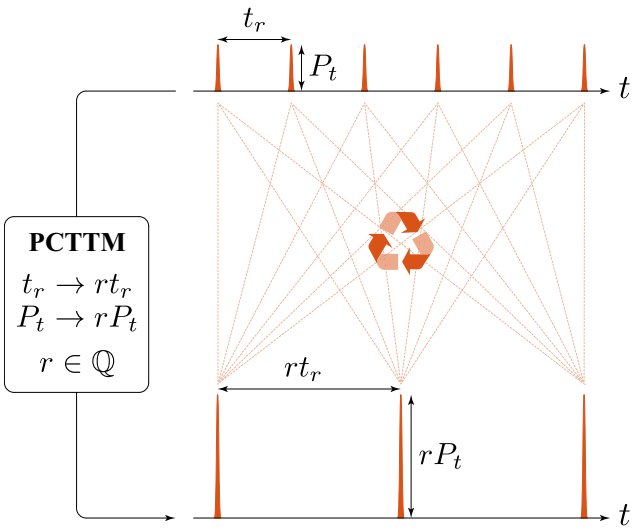

Figure 4.1 – Phase-controlled temporal Talbot method, summary. Transformation of a train of pulses with pulse period t_r into a new train with period rt_r $\forall$ $r \in \mathbb{Q}$, through energy redistribution based on phase manipulations. In the shown example, $r = 5/2$.

Interesting properties of the method to affect the noise content of the processed signal are discussed. In particular, the passive temporal Talbot amplification effect, theoretically discussed in Section 3.2 bears symmetries with the classic operation of numerical averaging, i.e., calculating the mean, or expected value, of a record of samples. Experimental data reported in this chapter shows that, for fractional values of the period multiplication factor, derived form the phase-controlled temporal Talbot method (Section 3.2.3.1), the noise content of the output signal behaves as the result of calculating the mean of a non-integer number of samples (e.g., as if '$2.\overline{6}$ realizations of the process' were measured and processed). Such an operation is simply outside of the scope of classical statistics. This result, though counter-intuitive, perfectly fits the statistical model of averaging of noisy signals, as evidenced by the presented experimental data.

In the following, first, the phase-controlled temporal Talbot method (derived in Section 3.2.3.1) is briefly revisited, and the particular realization of the technique, applied to the reported experiments is introduced. Second, experimental results of energy-preserving pulse period multiplication by fractional factors are presented. Finally, the aforementioned effect on the noise content of the signal is discussed and, the recorded experimental data is compared to the statistical model for signal averaging in the presence of uncorrelated white Gaussian noise.

4.2 PCTTM for fractional repetition rate division of pulse trains

The phase-controlled temporal Talbot method (introduced in Section 3.2.3.1 and summarized in Fig. 4.2) transforms a train of pulses with period t_r into a new train with period rt_r, where $r = q_2^{-1}q_1$. If $q_1 > q_2$, the output train has a higher pulse period than the input train (i.e., a lower repetition rate), and if $q_2 > 1$, the period multiplication factor is a fractional number.

Note that the last step of the method has been omitted (see Fig. 3.9). As a reminder, this last step consists on a second application of a spectral Talbot propagator, i.e., a second temporal phase modulation. Since

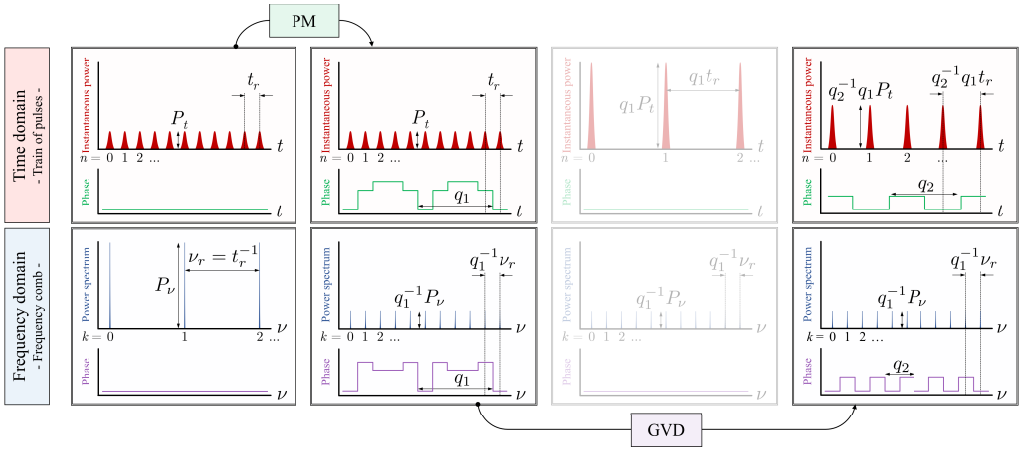

Figure 4.2 – Pulse period control by PCTTM. Combination of phase transformations (PM, phase modulation, and GVD, group velocity dispersion) to implement the phase-controlled temporal Talbot method on a train of optical pulses. In the shown example, $r = 5/2$.

the result of this process only modifies the spectrum of the train, and does not alter its instantaneous power distribution, it was not implemented in the experimental proof of concept reported here (Section 4.2.2). Additionally, the two SPF steps in the PCTTM are combined here into a single group velocity dispersion step for convenience of implementation.

4.2.1 Involved phase manipulations

The phase manipulations required for observation of fractional repetition rate division of a pulse train are implemented here as direct temporal phase modulation (PM) of the pulse train, and propagation of the train through an optical medium exhibiting second-order group velocity dispersion (GVD).

4.2.1.1 Temporal phase modulation

The first step of the method consists on applying a temporal phase $\varphi_{n;s,q_1}$ (general expression in Eq. 3.52) to the n-th pulse of the train of interest.

In the reported experiments, $s = q_1 - 1$, so that the applied phase writes,

$$\varphi_{n;q_1-1,q_1} = -\pi \frac{q_1 - 1}{q_1} n^2 \tag{4.1}$$

4.2.1.2 Group velocity dispersion

The second and third steps of the method, here combined into a single one, consist of the application of the spectral phases $-\phi_{k;p_1,q_1}$ and $\phi_{k;p_2,q_2}$ (general expression in Eq. 3.48) to the k-th line of the frequency comb representation of the train of interest.

In the reported experiments, $p_1 = p_2 = 1$, so that the applied phase writes,

$$\phi_{k;1,q_2} - \phi_{k;1,q_1} = \pi \left(\frac{1}{q_2} - \frac{1}{q_1} \right) k^2 \tag{4.2}$$

As per Eq. 3.50, the required amount of GVD,

$$2\pi\beta_2 z = \left(\frac{1}{q_2} - \frac{1}{q_1} \right) (q_1 t_r)^2 \tag{4.3}$$

Note that $\beta_2 > 0$. This, as explained below, is chosen to fit the sign of the dispersion introduced by the propagation medium used in the experimental demonstration (exhibiting normal dispersion along the working frequency range). Consequently, $\varsigma = 1$ in both Eqs. 4.1 and 4.2 (see Eqs. 3.52 and 3.48).

4.2.2 Experimental demonstration

The proposed fractional repetition rate division technique is demonstrated on a train of near-infrared optical pulses in the C-band of optical telecommunications, and in the GHz regime of repetition rates. These characteristics make for a convenient proof of concept, easy to implement with standard telecommunications equipment.

4.2.2.1 Experimental setup

Fig. 4.3 shows a simplified[1] schematic of the experimental setup used to validate the fractional repetition rate division concept.

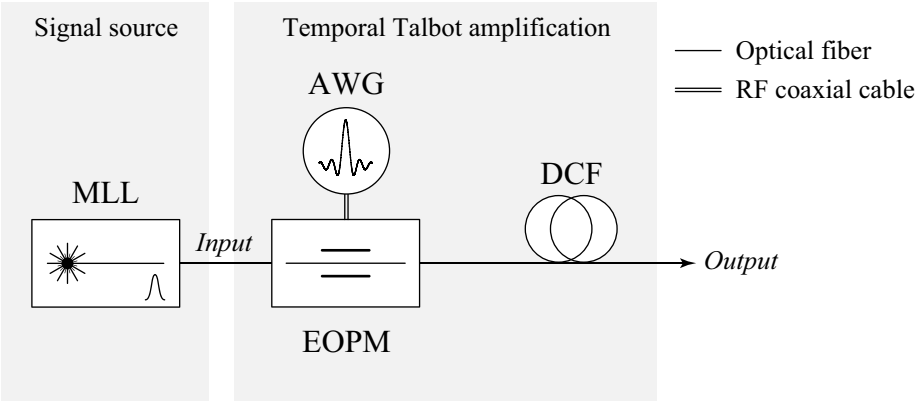

Figure 4.3 – Fractional repetition rate multiplication, experimental setup. MLL, mode-locked laser; AWG, arbitrary-waveform generator; EOPM, electro-optical phase modulator; DCF, dispersion-compensating fiber. For a complete schematic of the experimental setup, see Fig. D.1.

An actively mode-locked laser (MLL) generates the input pulse train. A radio-frequency synthesizer drives the laser to the desired input repetition rate. The laser delivers transform-limited Gaussian-like optical pulses with a full-width at half maximum (FWHM) pulsewidth of approximately 6 ps, at a central wavelength

[1] For a complete schematic of the setup, see Fig. D.1.

of 1550 nm (approximately 193.55 THz). The corresponding spectrum is a coherent optical frequency comb with an FSR dictated by the repetition rate of the laser.

The prescribed temporal phase modulation profile (given by Eq. 4.1) is loaded to the memory of an arbitrary waveform generator (AWG) capable of delivering 24 Gs/s with an analog bandwidth of 7 GHz. The AWG generates an analog voltage signal following the phase levels required by Eq. 4.1 for a given value of q_1, and matching the repetition rate of the generated optical pulses. This voltage signal is amplified and delivered to an electro-optical phase modulator (EOPM), with an RF bandwidth of 40 GHz, that modulates the phase of each pulse accordingly (a tunable optical delay line is used to align the optical signal to the voltage drive, and a polarization controller is used to maximize the modulation efficiency).

Finally, the phase-modulated train propagates through a length of dispersion-compensating fiber (DCF). This optical fiber has normal dispersion ($\beta_2 > 0$) at the working wavelength, and its length is chosen to match the required condition, set by Eq. 4.3.

4.2.2.2 Experimental results

Table 4.1 lists the parameters of the tested input signals, the set of experimental configurations for fractional repetition rate division, and the obtained results.

Table 4.1 – Fractional repetition rate multiplication, experimental conditions and results. List of input and output pulse periods and configuration parameters of the PCTTM for a set of 7 conducted experiments.

	Pulse period		**PCTTM parameters**			
	t_r [a]	rt_r [b]	q_1 [c]	q_2 [d]	r [e]	$\beta_2 z$ [f]
(1)	126.139	168.185	4	3	$1.\overline{3}$	3376.415
(2)	84.092	126.139	3	2	1.5	1688.207
(3)	79.777	132.962	5	3	$1.\overline{6}$	3376.415
(4)	63.568	111.244	7	4	1.75	3376.415
(5)	53.185	132.962	5	2	2.5	3376.415
(6)	63.069	168.185	8	3	$2.\overline{6}$	8441.038
(7)	62.902	220.157	7	2	3.5	11020.156

[a] Input pulse period (ps).
[b] Output pulse period (ps).
[c] Numerator.
[d] Denominator.
[e] Pulse period multiplication factor.
[f] Second-order dispersion (ps^2/rad).

Fig. 4.4 shows a set of measurements corresponding to the experimental conditions and results listed on Table 4.1.

The AWG generates the voltage signals shown in Fig. 4.4(a). These voltage signals drive the EOPM, modulating the phase of the input optical pulse train. This produces spectral Talbot images, resulting in FSR division by the parameter q_1 (Fig. 4.4(b)). The shown optical power spectra are measured by an optical spectrum analyzer.

Propagation of the phase-modulated trains through DCF exhibiting the required amount of GVD (see Table 4.1) produces the anticipated fractional repetition rate division effect, and associated passive ampli-

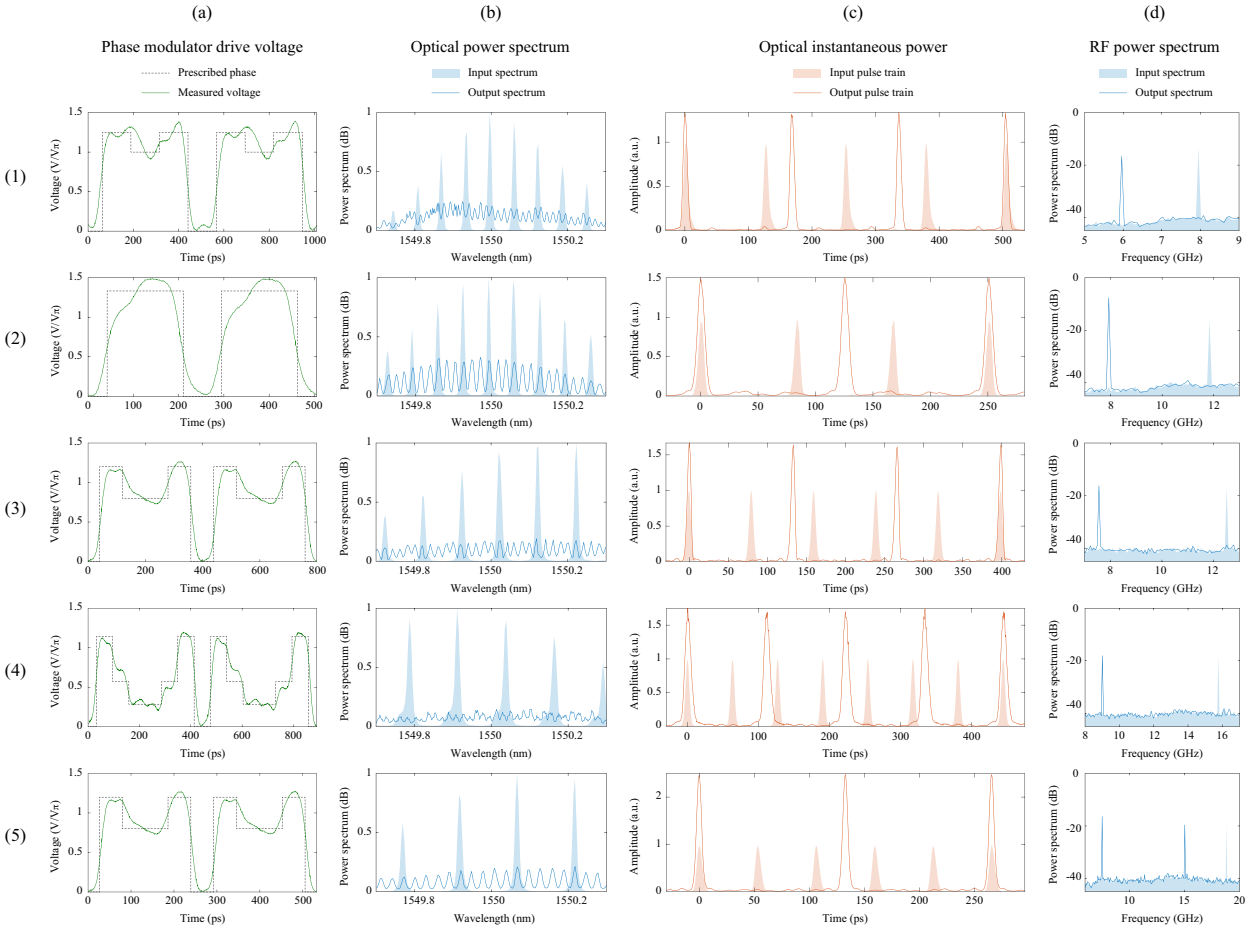

Figure 4.4 – Fractional repetition rate multiplication, experimental results. Set of measurements corresponding to the experimental conditions and results listed on Table 4.1, and following the same numbering (1)-(5). (a) Prescribed temporal phase modulation sequences and applied EOPM drive voltages, where V_π denotes the half-wave voltage of the EOPM (i.e., the required voltage level to apply a phase sift of π rad to the optical signal); (b) optical power spectra of the input and output frequency comb representation of the processed pulse train, normalized to the spectral peak power of the input comb (the anticipated spectral self-imaging effect, leading to FSR division by the factor q_1 is observed); (c) instantaneous power traces of the input and output pulse trains, normalized to the temporal peak power of the input train (the anticipated fractional pulse period multiplication is observed, as well as the corresponding passive amplification effect by energy redistribution); (d) radio-frequency power spectra of the input and output pulse trains, verifying the expected fractional repetition rate division effect.

fication by the rate-division factor, r (Fig. 4.4(c)). The shown temporal traces are measured by an optical sampling oscilloscope with an equivalent acquisition bandwidth of 500 GHz. It is worth noting that the total insertion loss in the optical signal path is of $\sim$13.5 dB for the reported experimental demonstration. The shown temporal traces are normalized to the temporal peak power value of the input signal, accounting for the mentioned insertion loss.

Finally, Fig. 4.4(d) shows the input and output radio-frequency spectra of the pulse trains, measured by a radio-frequency spectrum analyzer equipped with a 45 GHz bandwidth photodiode. The measured measured harmonics in the RF power spectra verify the correct fractional repetition rate division.

4.3 Noiseless amplification of periodic trains of pulses

Talbot amplification, e.g., as a result of the PCTTM exploited here, arises from the coherent addition of properly-delayed frequency components of the periodic signal of interest, as sketched in Fig. 4.5. As such, the noise content of the signal is not affected by the involved coherent phase manipulations of the method. In particular, integer Talbot amplification – energy-preserving pulse period multiplication with $r \in \mathbb{N}$ – has been shown to produce an effect of noise reduction, equivalent to the classical operation of signal averaging.

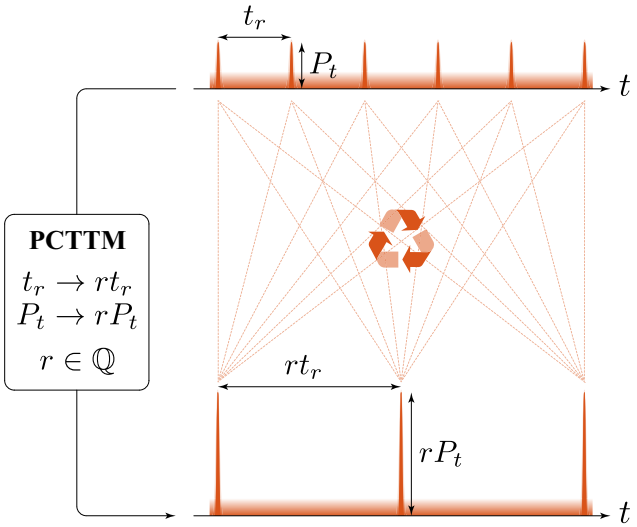

Figure 4.5 – Phase-controlled temporal Talbot method, effect on noise. Depiction of the impact of the phase-controlled temporal Talbot method on the noise content of a periodic train of pulses. In the shown example, $r = 5/2$.

In this Section, the statistics of time-domain signal averaging in the presence of noise are reviewed, and the effects of noise mitigation by fractional Talbot amplification (i.e., with $r \in \mathbb{Q}$) are experimentally demonstrated and compared with the results obtained by classical signal averaging.

4.3.1 Statistics of time-domain signal averaging in the presence of noise

Let S_n be a deterministic variable representing a single realization of the signal level on one period of a repetitive waveform (labeled by n), so that,

$$\mathrm{E}\{S_n\} = \mu \,\forall\, n \in \mathbb{N} \tag{4.4}$$
$$\mathrm{Var}\{S_n\} = 0 \,\forall\, n \in \mathbb{N} \tag{4.5}$$

where $\mathrm{E}\{A\}$ is the expected value of the variable A, i.e., μ is the mean value of S on a particular sampling instant (e.g., the top level of a signal pulse), and $\mathrm{Var}\{A\}$ is the variance[2] of A [110].

Let W_n be a random variable representing a realization of additive white Gaussian noise (AWGN) with zero mean and equal variance,

$$\mathrm{E}\{W_n\} = 0 \,\forall\, n \in \mathbb{N} \tag{4.6}$$
$$\mathrm{Var}\{W_n\} = \sigma^2 \,\forall\, n \in \mathbb{N} \tag{4.7}$$

[2]For a random variable A, $\mathrm{Var}\{A\} := \mathrm{E}\big\{(A - \mathrm{E}\{A\})^2\big\}$.

The following mathematical derivations operate under the premise that different realizations of W_n are uncorrelated, and that signal and noise are independent (and, therefore, uncorrelated), so that,

$$\begin{aligned} \mathrm{Cov}\{W_n, W_k\} &= \begin{cases} 0 & \forall \quad n \neq k \\ \mathrm{Var}\{W_n\} & \forall \quad n = k \end{cases} && (4.8) \\ \mathrm{Cov}\{S_n, W_n\} &= 0 \,\forall\, n \in \mathbb{N} && (4.9) \end{aligned}$$

where $\mathrm{Cov}\{A, B\}$ is the covariance[3] of A and B [110]. This is a reasonable assumption for most practical AWGN sources of interest, including noise generation mechanisms in optical amplifiers. As such, the variable W_n is a fairly accurate model of amplified spontaneous emission (ASE) noise, generated by erbium-doped fiber amplifiers (EDFA), provided that the entire signal bandwidth is contained within a uniform region of the gain spectrum of the amplifier [111].

The measurement of a single signal pulse in the presence of noise is modeled by the process,

$$X_n := S_n + W_n \,\forall\, n \in \mathbb{N} \tag{4.10}$$

The expectation of a single measurement of a noisy pulse, X_n, is then,

$$\begin{aligned} \mathrm{E}\{X_n\} &= \mathrm{E}\{S_n\} + \mathrm{E}\{W_n\} \\ &= \mu \end{aligned} \tag{4.11}$$

and the variance,

$$\begin{aligned} \mathrm{Var}\{X_n\} &= \mathrm{Var}\{S_n + W_n\} \\ &= \mathrm{Var}\{S_n\} + \mathrm{Var}\{W_n\} + 2\mathrm{Cov}\{S_n, W_n\} \\ &= \sigma^2 \end{aligned} \tag{4.12}$$

The dispersion[4] of the probability distribution of a random variable, A, is quantified by the relative standard deviation, also known as the coefficient of variation, $\mathrm{CV}\{A\}$,

$$\mathrm{CV}\{A\} := \frac{\mathrm{Var}\{A\}^{\frac{1}{2}}}{\mathrm{E}\{A\}} \tag{4.13}$$

where $\mathrm{Var}\{A\}^{\frac{1}{2}}$ is the standard deviation of A.

[3] For a pair of random variables A and B, $\mathrm{Cov}\{A, B\} := \mathrm{E}\{(A - \mathrm{E}\{A\})\,(B - \mathrm{E}\{B\})\}$. Note that $\mathrm{Cov}\{A, A\} = \mathrm{Var}\{A\}$.

[4] Note that the term *dispersion* in this context does not refer to chromatic dispersion of transparent media, as used throughout this dissertation, but rather to the *spread* of a probability distribution.

The coefficient of variation of X_n writes,

$$\mathrm{CV}\{X_n\} = \frac{\sigma}{\mu} \tag{4.14}$$

The operation of signal averaging of the process X_n, consists of calculating Y_N, the arithmetic mean of N realizations of X_n,

$$Y_N := \frac{1}{N}\sum_{n=1}^{N} X_n \tag{4.15}$$

The expectation of the average Y_N writes,

$$\begin{aligned} \mathrm{E}\{Y_N\} &= \frac{1}{N}\mathrm{E}\left\{\sum_{n=1}^{N} X_n\right\} \\ &= \frac{1}{N}\sum_{n=1}^{N}\mathrm{E}\{S_n\} + \frac{1}{N}\sum_{n=1}^{N}\mathrm{E}\{W_n\} \\ &= \mu \end{aligned} \tag{4.16}$$

The variance of Y_N can be written as [110],

$$\begin{aligned} \mathrm{Var}\{Y_N\} &= \mathrm{Var}\left\{\frac{1}{N}\sum_{n=1}^{N} X_n\right\} \\ &= \frac{1}{N^2}\sum_{n=1}^{N}\sum_{k=1}^{N}\mathrm{Cov}\{X_n, X_k\} \end{aligned} \tag{4.17}$$

Expanding a single term of the sum in Eq. 4.17, the covariance of two different realizations of a single measurement reduces to,

$$\begin{aligned} \mathrm{Cov}\{X_n, X_k\} &= \mathrm{E}\{(X_n - \mathrm{E}\{X_n\})\,(X_k - \mathrm{E}\{X_k\})\} \\ &= \mathrm{E}\{X_n X_k\} - \mathrm{E}\{X_n\}\mathrm{E}\{X_k\} \\ &= \mathrm{E}\{S_n S_k\} + \mathrm{E}\{S_n W_k\} + \mathrm{E}\{S_k W_n\} + \mathrm{E}\{W_n W_k\} - \mathrm{E}\{S_n\}\mathrm{E}\{S_k\} \\ &= \mathrm{E}\{W_n W_k\} \\ &= \mathrm{Cov}\{W_n, W_k\} + \mathrm{E}\{W_n\}\mathrm{E}\{W_k\} \\ &= \mathrm{Cov}\{W_n, W_k\} \end{aligned} \tag{4.18}$$

and, considering uncorrelated noise (Eq. 4.8), the variance of Y_N writes,

$$\begin{aligned} \mathrm{Var}\{Y_N\} &= \frac{1}{N^2}\sum_{n=1}^{N}\mathrm{Var}\{X_n\} \\ &= \frac{\sigma^2}{N} \end{aligned} \tag{4.19}$$

The coefficient of variation of Y_N,

$$\mathrm{CV}\{Y_N\} = \frac{1}{\sqrt{N}}\frac{\sigma}{\mu} \tag{4.20}$$

Finally, dividing Eq. 4.20 by Eq. 4.14,

$$\frac{\mathrm{CV}\{Y_N\}}{\mathrm{CV}\{X_n\}} = \frac{1}{\sqrt{N}} \tag{4.21}$$

The operation of averaging N realizations of a measurement reduces the dispersion of the probability distribution of the noise variations by a factor $N^{-\frac{1}{2}}$, thus producing a signal trace with lower intensity fluctuations within a period.

The key here, is that the deterministic signal components add coherently, while the uncorrelated noise contributions add incoherently, causing the output signal power to scale with N, while the output noise power scales at the slower rate of $N^{\frac{1}{2}}$. Fig. 4.6 summarizes these results.

It is important to note that, for the case of averaging a photodetected signal on a sampling oscilloscope, this conclusion holds true for high levels of signal mean, μ, relative to the standard deviation σ of the noise. In other words, this analysis is relevant for analyzing the noise affecting high levels of the pulse of interest (e.g., the top level). The reason for this is that the averaged realizations of X_n correspond to values of received power. As such, noise fluctuations around low levels of the signal of interest that would cross zero, will be made positive. Classical signal averaging leaves a background level of noise fluctuations. Furthermore, as per the definition of the coefficient of variation (Eq. 4.13), low values of signal mean could lead to indetermination, arising from a fraction with a small denominator value.

4.3.2 Noise averaging in fractional Talbot amplification

As aforementioned, Talbot amplification by a factor r has an impact on the noise content of the processed signal, equivalent to that of averaging $N = r$ consecutive realizations of the signal.

Fig. 4.7 shows the results of a numerical simulation where a flat-top pulse, S_n, in the presence of strong AWGN fluctuations, W_n, is processed through standard signal averaging of $N = 20$ measurements of the pulse, Y_N, and a single measurement after passive Talbot amplification by $r = 20$. The obtained standard deviations for signal averaging (Fig. 4.7(b)) and Talbot amplification (Fig. 4.7(c)) coincide, and approach the anticipated value of variation reduction by $20^{-\frac{1}{2}} \approx 0.2236$.

Furthermore, as evidenced in Figs. 4.7(b) and (c), Talbot amplification outperforms classical averaging, as it enhances the extinction ratio of the processed pulses. This is due to the fact that Talbot amplification operates directly on the electric field, while classical signal averaging of an instantaneous power trace, as

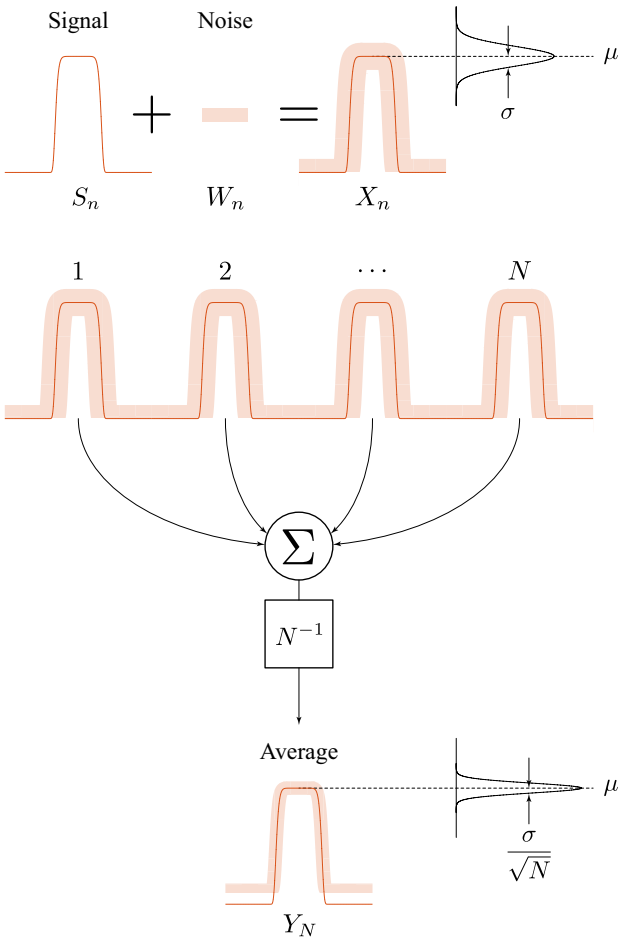

Figure 4.6 – Statistics of signal averaging. Impact of recursive averaging of a periodic signal on the noise content of the measurement (assuming AWGN noise with zero mean). Calculating the arithmetic mean of N consecutive realizations of the signal reduces the noise fluctuations by $N^{-\frac{1}{2}}$. Note that, by definition, $N \in \mathbb{N}$.

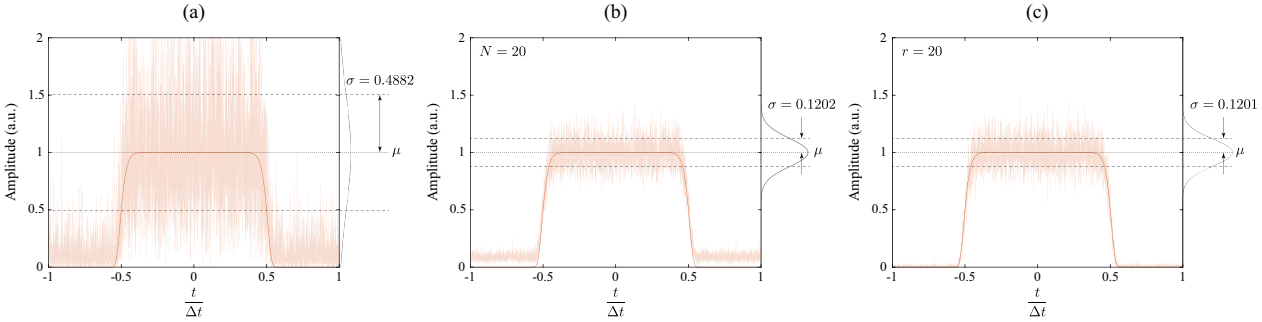

Figure 4.7 – Noise averaging effect of Talbot amplification, numerical simulation. Noise mitigation of a pulsed signal affected by strong AWGN fluctuations (a). Comparison between (b) standard signal averaging of $N = 20$ measurements, and (c) a single measurement after integer Talbot amplification by $r = 20$. A clean trace of the input signal is shown for reference. Δt denotes the FWHM temporal duration of the pulse.

commented in the last paragraph of the previous Section, operates on positive-only levels that will not cancel out for low values of signal power.

Noise averaging on an Talbot amplifier with $r \in \mathbb{N}$ has been experimentally demonstrated on trains of optical pulses affected by ASE noise from an EDFA [57].

It is reasonable to expect that the reported operation of fractional pulse period multiplication by the factor r achieves a similar noise averaging effect, but with a variation reduction factor $r^{-\frac{1}{2}}$, with $r \in \mathbb{Q}$. Note that

this situation would be equivalent to 'averaging a fractional number of measurements', a possibility that is simply not allowed by the basic definition of the sum of a discrete set of samples.

4.3.3 Experimental demonstration

In order to demonstrate the predicted *fractional averaging* effect, the experiment described in Section 4.2.2 is repeated. An AWGN source is incorporated in order to increase the noise content of the input pulse train. The pulse period is then divided by rational numbers, r, following the energy-preserving protocol defined by the PCTTM. Finally, the noise fluctuations on the top level of input and output pulses are quantified, and their respective coefficients of variation are compared in order to extract the observed variation reduction factor and compare it with the expected value for the noise averaging model, $r^{-\frac{1}{2}}$.

4.3.3.1 Experimental setup

In order to test the effect of fractional noise averaging by energy redistribution, an AWGN source is incorporated to the experimental setup depicted in Fig. 4.3.

The noise source is constructed by injecting ASE from an EDFA, leaving the input of the amplifier disconnected, to the input pulse train. This way the amount of ASE injected to the signal is controllable by varying the pump current of the EDFA. A variable optical attenuator is connected to the output of the mode-locked laser generating the input train, in order to set the power level of the signal. In the reported experiments, the optical signal-to-noise ratio (OSNR) – measured with an optical spectrum analyzer as the ratio between the spectral peak power and the noise floor – is set to 10 dB. Fig. 4.8 shows the implementation of this noise source in the experimental setup.

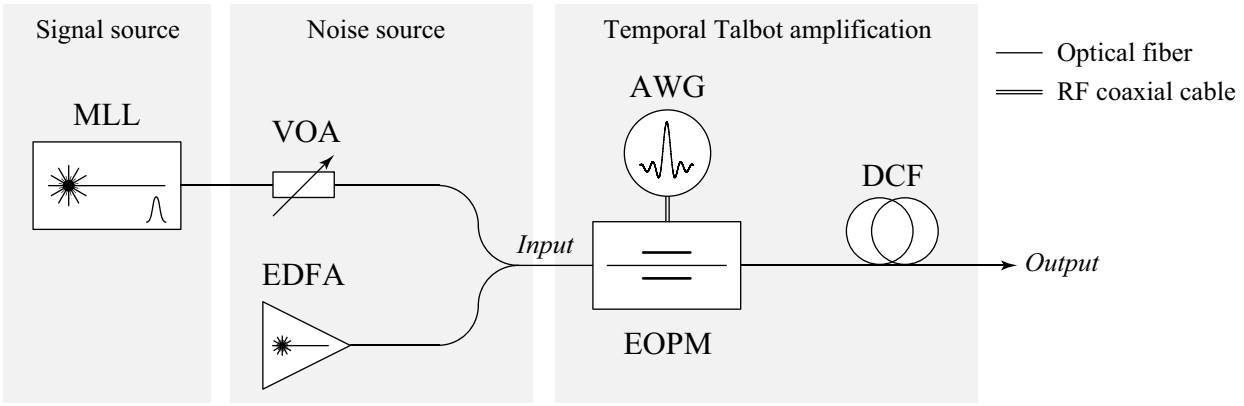

Figure 4.8 – Fractional Talbot amplification and noise averaging, experimental setup. MLL, mode-locked laser; VOA, variable optical attenuator; EDFA, erbium-doped fiber amplifier; AWG, arbitrary-waveform generator; EOPM, electro-optical phase modulator; DCF, dispersion-compensating fiber. For a complete schematic of the experimental setup, see Fig. D.1.

4.3.3.2 Experimental results

Fig. 4.9 shows the temporal traces of a noisy input pulse (OSNR$=10$ dB), the average of 2 measurements of the input pulse, and a single measurement of an output pulse after the fractional repetition rate division process with $r = 8/3 = 2.\overline{6}$ (entry 6 of Table 4.1).

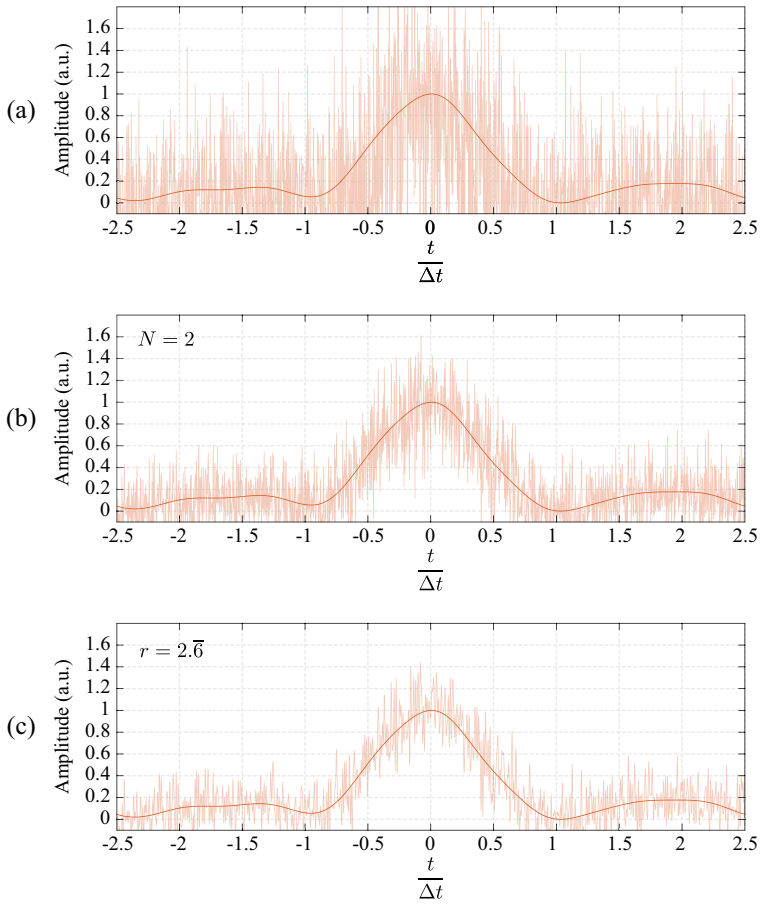

Figure 4.9 – Measured temporal traces resulting of averaging a repetitive train of noisy pulses. Single-shot measured traces of (a) an input noisy pulse with OSNR= 10 dB, (b) integer averaging of the measured power profiles of $N = 2$ input pulses and, (c) an output pulse after the fractional repetition rate division process with $r = 8/3 = 2.\overline{6}$. Δt denotes the FWHM temporal duration of the pulse. A clean trace of the input pulse is shown in all figures for reference. All traces are captured by an electrical sampling oscilloscope equipped with a 45 GHz bandwidth photodiode (see Fig. D.1).

The reduction on the variance of the noise fluctuations within the pulse is clearly observed in Figs. 4.9(b) and 4.9(c). In order to quantify this reduction, the ratio of the coefficients of variation of an input pulse to the average of N pulses, as well as to the output of the fractional Talbot amplifier, are calculated. Fig. 4.10 shows the obtained results for classical averaging in an electrical sampling oscilloscope with $N = 2$, $N = 3$ and $N = 4$, as well as for fractional Talbot amplification by $r = 5/2 = 2.5$, $r = 8/3 = 2.\overline{6}$ and $r = 7/2 = 3.5$ (corresponding to entries 5, 6 and 7 of Table 4.1).

The obtained noise variation reduction factors for the evaluated fractional Talbot amplification cases precisely follows the expected trend $r^{-\frac{1}{2}}$, corresponding to interpolations in between the values obtained by conventional averaging in the oscilloscope, generally following the predicted theoretical trend $N^{-\frac{1}{2}}$ (see Eq. 4.21). Hence, as predicted, the Talbot amplification processes implements an averaging operation, obtaining a result where the record length effectively behaves as if it was equal to a rational number, r.

4.3.4 Additional comments and remarks

As briefly commented on Section 3.2.5, all the operations involved in the realization of the reported experiments are linear manipulations of the phase distributions of the signal of interest in both time and frequency domains. As such, the method could be extrapolated to any system or framework described by wave equations, including other domains of optical waves (e.g., space and transverse momentum), other wave regimes beyond the optical realm (e.g, microwaves, X-rays, matter waves, etc.), and even purely computational re-

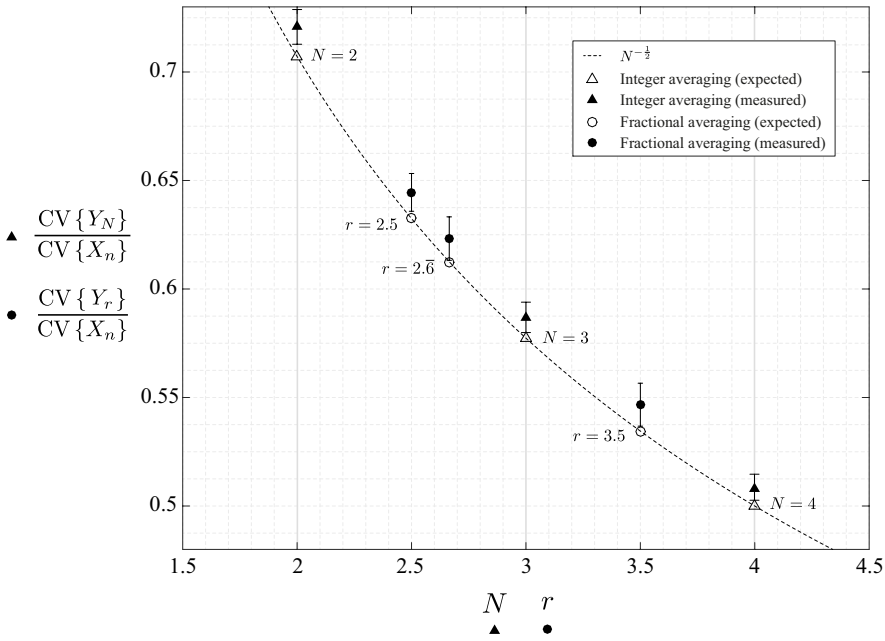

Figure 4.10 – Variation reduction factor for integer and fractional noise averaging. Measured values of the variation reduction factor (the ratio of the coefficient of variation of the average of N pulses or a single pulse resulting from Talbot amplification by the fractional factor r, to that of an input pulse. The shown data points are obtained from 10 measurements for each listed value of N and r; each data point corresponds to the mean of said 10 measurements, while the error bars denote the standard deviation. The expected trend (and specific values) of the variation reduction factor in the statistical model of noise averaging, $N^{-\frac{1}{2}}$, is shown for comparison.

alizations. This is of particular interest, given the ubiquitous nature of noise in any discipline involving the harvesting of information from waves and signals.

In a more general sense, the results reported here indicate that mathematical operations, not defined within the scope of a particular paradigm (calculating the mean, i.e., a sum, of a fractional number of samples, in the case of the reported experiments), could be realized through physical phenomena, enabling an unprecedented, wider range of mathematical and experimental conditions.

CHAPTER 5

Processing of periodic spectral waves

In this chapter, the universal period control method proposed in chapter 3 is applied to periodic spectral signals – frequency combs – to demonstrate arbitrary, energy-preserving control of their frequency spacing. This feat is relevant to many areas of application of frequency combs. The impact of the method on the noise characteristics of the comb is studied, and results showing noiseless spectral amplification of the comb signal are reported. The work presented in this Chapter was reported in [APj5] [APc4, APc6, APc8, APc9, APc14].

5.1 Arbitrary FSR control of frequency combs

In this chapter, the methodology introduced in Section 3.2.3.2 is experimentally validated. In particular, energy-preserving transformations of the free spectral range of an optical frequency comb by an arbitrary factor, $r^{-1} \in \mathbb{Q}$, as depicted in Fig. 5.1, are experimentally demonstrated. As discussed in chapter 1, traditional FSR control methods based on signal processing operations can only achieve FSR multiplication or division by integer factors (e.g., through spectral amplitude filtering or temporal amplitude gating, respectively), and the property of energy preservation has only been demonstrated in the case of integer FSR division through fractional spectral Talbot effect [61].

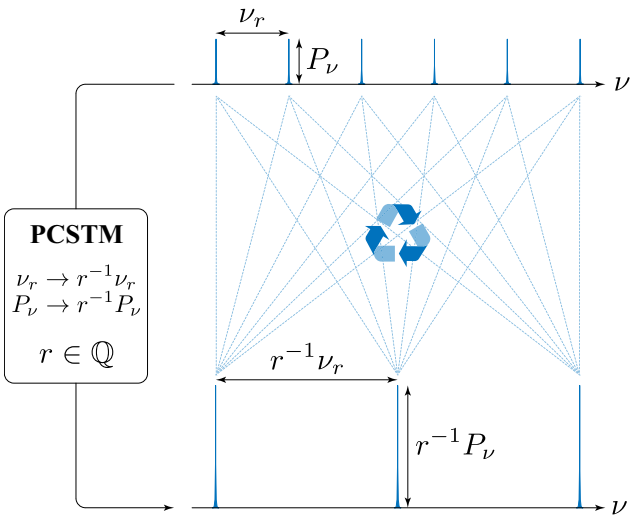

Figure 5.1 – Phase-controlled spectral Talbot method, summary. Transformation of a frequency comb with FSR ν_r into a new train with period $r^{-1}\nu_r \; \forall \; r \in \mathbb{Q}$, through energy redistribution based on phase manipulations. In the shown example, $r^{-1} = 5/2$.

Furthermore, interesting properties of the method to affect the noise content of the processed signal are discussed. In particular, for FSR multiplication factors higher than 1, the PCSTM (derived in Section 3.2.3.2) has the capability of amplifying the coherent components of the power spectrum of a frequency comb over the incoherent background noise floor. Experimental data reported in this chapter shows successful detection of frequency combs originally buried completely under the noise floor, and therefore undetectable through direct spectral measurements.

In the following, the phase-controlled spectral Talbot method is briefly revisited, and the particular realization of the technique, applied to the reported experiments is introduced. Experimental results of energy-preserving, arbitrary FSR control are presented, including the aforementioned effects of noiseless spectral amplification and sub-noise detection of frequency combs.

5.2 PCSTM for arbitrary FSR control of frequency combs

The phase-controlled spectral Talbot method (introduced in Section 3.2.3.2 and summarized in Fig. 5.2) transforms a frequency comb with FSR ν_r into a new comb with FSR $r^{-1}\nu_r$, where $r = q_2^{-1}q_1$.

Note that the last step of the method has been omitted (see Fig. 3.12). As a reminder, this last step consists on a second application of a temporal Talbot propagator, i.e., a second spectral phase filtering. Since the result of this process only modifies the instantaneous power of the train, and does not alter the associated frequency comb spectrum, it was not implemented in the experimental proof of concept reported

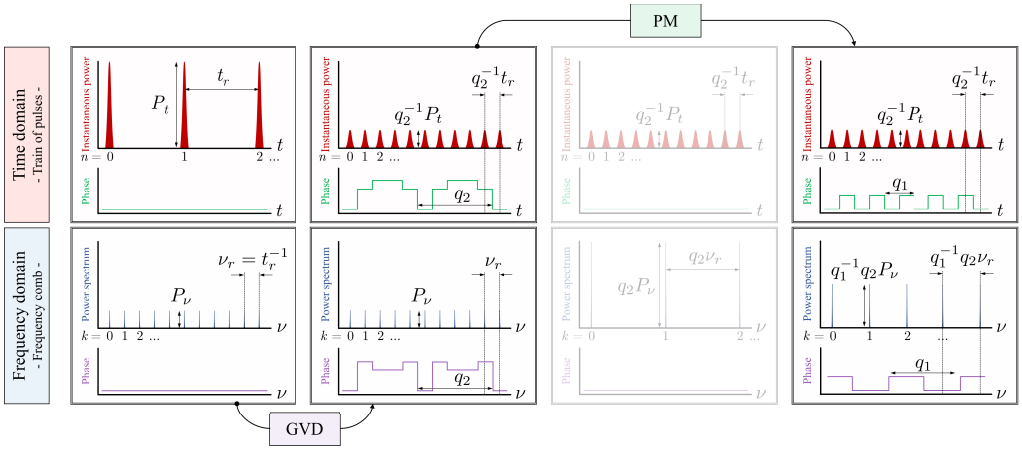

Figure 5.2 – Comb FSR control by PCSTM. Combination of phase transformations (GVD, group velocity dispersion, and PM, phase modulation) to implement the phase-controlled spectral Talbot method on an optical frequency comb. In the shown example, $r^{-1} = 5/2$.

here (Section 5.2.2). Additionally, the two TPM steps in the PCSTM are combined here into a single phase modulation step for convenience of implementation.

5.2.1 Involved phase manipulations

The phase manipulations required for arbitrary FSR control of a frequency comb are implemented here as propagation of through an optical medium exhibiting second-order group velocity dispersion (GVD), and subsequent direct temporal phase modulation (PM) of the resulting pulse train.

5.2.1.1 Group velocity dispersion

The first step of the method consists on applying a spectral phase $\phi_{k;p_2,q_2}$ (general expression in Eq. 3.48) to the k-th line of the comb of interest. In the reported experiments, the value $p_2 = 1$ is chosen to minimize the total required amount of GVD, however, any integer value can be designed, as long as p_2 and q_2 are mutually prime. This way, the applied phase sequence writes,

$$\phi_{k;1,q_2} = \pi \frac{1}{q_2} k^2 \tag{5.1}$$

As per Eq. 3.50, the required amount of GVD,

$$2\pi\beta_2 z = \frac{1}{q_2 \nu_r^2} \tag{5.2}$$

Note that $\beta_2 > 0$. This, as explained below, is chosen to fit the sign of the dispersion introduced by the propagation medium used in the experimental demonstration (exhibiting normal dispersion along the working frequency range). Consequently, $\varsigma = 1$ in both Eqs. 5.1 and 5.3 (see Eqs. 3.48 and 3.52).

5.2.1.2 Temporal phase modulation

The second and third steps of the method, here combined into a single one, consist of the application of the temporal phases $-\varphi_{k;s_2,q_2}$ and $\varphi_{k;s_1,q_1}$ (general expression in Eq. 3.52) to the n-th pulse of the time-domain representation of the comb of interest.

In the reported experiments, $s_2 = q_2 - 1$, and $s_1 = q_1 - 1$, so that the applied phase writes,

$$\begin{aligned} \varphi_{n;q_1-1,q_1} - \varphi_{n;q_2-1,q_2} &\equiv \varphi_{n;q_1-q_2,q_1q_2} \\ &= -\pi \frac{q_1 - q_2}{q_1 q_2} n^2 \end{aligned} \tag{5.3}$$

It is interesting to note that the output comb will preserve the frequency grid reference of the input comb. The output comb lines can be selected within such a grid, by properly delaying the applied temporal phase modulation sequence in the time domain.

Fig. 5.3 shows the results of a numerical simulation where the FSR of a frequency comb is multiplied by the integer factor $r^{-1} = q_2 = 3$. Different results are shown where the temporal phase modulation sequence is delayed in steps of $q_2^{-1} t_r$. The lines of the corresponding FSR-multiplied combs are shifted within the input comb frequency grid in steps of ν_r for each step of temporal delay of the phase sequence. A total delay of t_r restores the phase sequence to its original position in the time domain, resulting on a spectral line shift of $q_2 \nu_r$, which produces the same comb obtained in the case where no temporal delay is introduced.

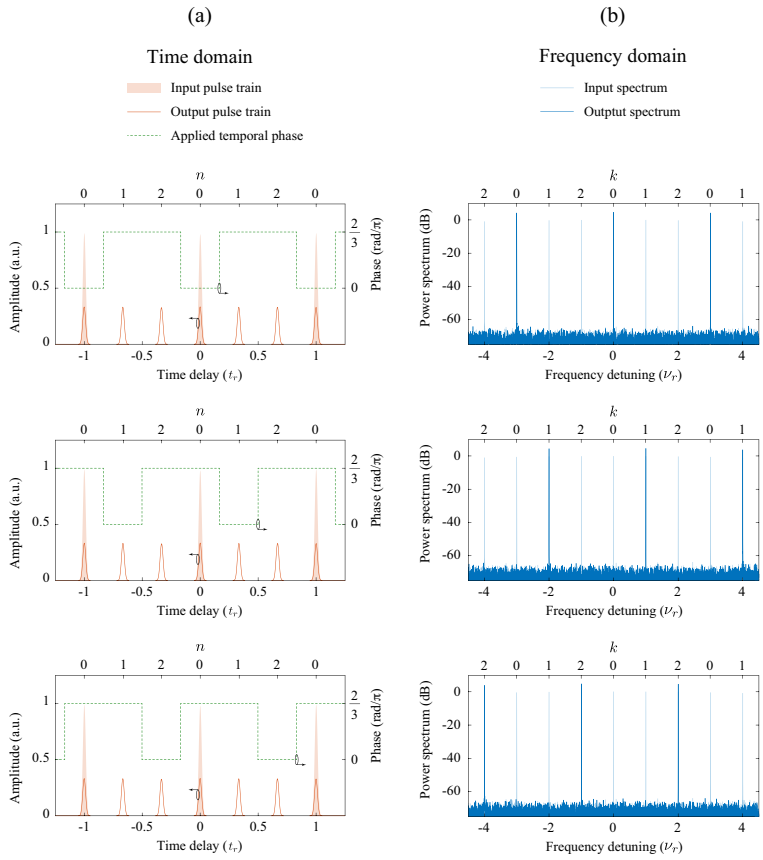

Figure 5.3 – Shifting of comb lines by temporal delay of the phase sequence, numerical simulation. Three examples of application of the PCSTM with $r^{-1} = 3$ to a frequency comb with FSR ν_r are shown. The temporal phase modulation sequence (a) is delayed by $kt_r/3$, with $k = 0, 1, 2$. The output combs (b) have FSR $3\nu_r$, and their comb lines are shifted by $k\nu_r$ (within the input frequency grid) underneath the comb envelope, as a consequence of the temporal delay of the phase modulation sequence.

5.2.2 Experimental demonstration

The proposed technique for arbitrary control of the FSR of frequency combs is demonstrated on a coherent frequency comb corresponding to a train of near-infrared optical pulses in the C-band of optical telecommunications, and in the GHz regime of repetition rates. These characteristics make for a convenient proof of concept, easy to implement with standard telecommunications equipment.

5.2.2.1 Experimental setup

Fig. 5.4 shows a simplified[1] schematic of the experimental setup used to validate the arbitrary FSR control concept.

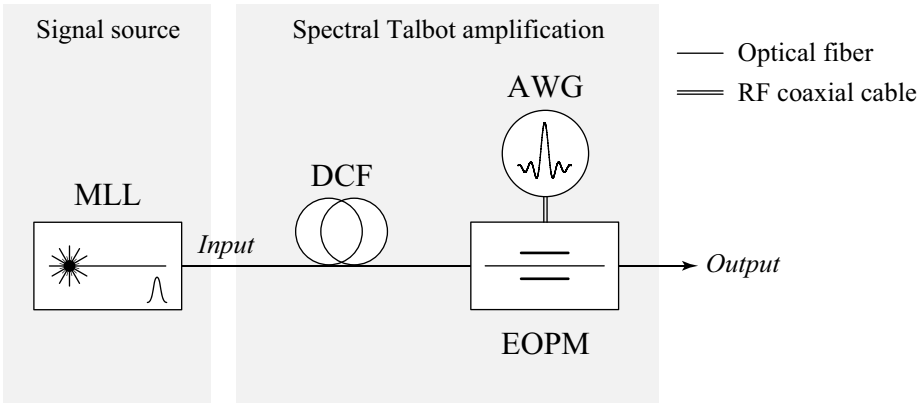

Figure 5.4 – Arbitrary FSR control of frequency combs, experimental setup. MLL, mode-locked laser; DCF, dispersion-compensating fiber; AWG, arbitrary-waveform generator; EOPM, electro-optical phase modulator. For a complete schematic of the experimental setup, see Fig. D.2.

An actively mode-locked (MLL) laser generates the input frequency comb. A radio-frequency synthesizer drives the laser to the desired input FSR, ν_r. The laser delivers transform-limited Gaussian-like optical pulses with a full-width at half maximum (FWHM) pulsewidth of approximately 3 ps, at a central wavelength of 1554.4 nm (approximately 193 THz), and a pulse repetition period, t_r, dictated by the reciprocal FSR.

The input pulse train propagates through a length of dispersion-compensating fiber (DCF). This optical fiber has normal dispersion ($\beta_2 > 0$) at the working wavelength, and its length is chosen to match the required condition, set by Eq. 5.2. The output pulse train corresponds to a temporal Talbot sub-image with pulse period $q_1^{-1} t_r$, while the corresponding comb FSR remains unaltered.

Finally, the prescribed temporal phase modulation profile (given by Eq. 5.3) is loaded to the memory of an arbitrary waveform generator (AWG) capable of delivering 50 Gs/s with an analog bandwidth of 14 GHz. The AWG generates an analog voltage signal following the phase levels required by Eq. 5.3, and matching the repetition rate of the pulses at the output of the GVD medium. This voltage signal is amplified and delivered to an electro-optical phase modulator (EOPM), with an RF bandwidth of 40 GHz, that modulates the phase of each pulse accordingly (a tunable optical delay line is used to align the optical signal to the voltage drive, and a polarization controller is used to maximize the modulation efficiency).

[1] For a complete schematic of the setup, see Fig. D.2.

5.2.2.2 Experimental results

Table 5.1 lists the parameters of the tested input signals, the set of experimental configurations for arbitrary FSR control, and the obtained results.

Table 5.1 – Arbitrary FSR control, experimental conditions and results. List of input and output FSR values and configuration parameters of the PCSTM for a set of 5 conducted experiments.

	FSR		PCSTM parameters				
	ν_r [a]	$r^{-1}\nu_r$ [b]	q_2 [c]	q_1 [d]	r^{-1} [e]	$10\log_{10}(r^{-1})$ [f]	$\beta_2 z$ [g]
(1)	9.451	18.902	2	1	2	3	891.527
(2)	9.463	28.391	3	1	3	4.7	592.369
(3)	9.451	37.804	4	1	4	6	445.455
(4)	7.717	11.575	3	2	1.5	1.7	890.911
(5)	9.451	3.781	2	5	0.4	−4	890.911

[a] Input FSR (GHz).
[b] Output FSR (GHz).
[c] Numerator.
[d] Denominator.
[e] FSR multiplication factor, linear scale.
[f] FSR multiplication factor, logarithmic scale (dB).
[g] Second-order dispersion (ps^2/rad).

Fig. 5.5 shows a detail of the input signal, corresponding to entries (1), (3) and (5) of Table 5.1.

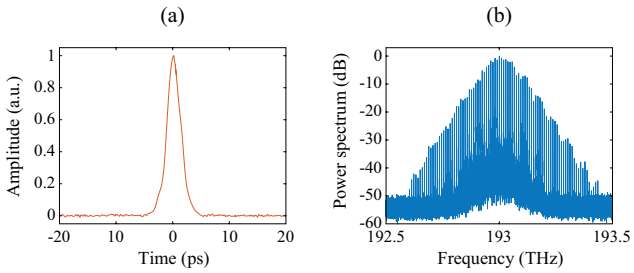

Figure 5.5 – Arbitrary FSR control, input signal. Detail of the input signal (output of the MLL in Fig. 5.4) used for demonstration of the PCSTM, corresponding to entries (1), (3) and (5) of Table 5.1. The measurements show (a) normalized instantaneous power trace of a single input pulse, and (b) full frequency comb power spectrum. The measured FWHM pulsewidth is approximately 3 ps, and the FSR is 9.451 GHz.

Fig. 5.6 shows a set of measurements corresponding to the experimental conditions and results listed on Table 5.1.

The input frequency comb first propagates through a length of DCF exhibiting the required amount of GVD (see Table 5.1). The pulse train obtained at the output of the DCF is a temporal Talbot sub-image (pulse period division by the factor q_2) of the input train, while the power spectrum of the comb at the output of the DCF remains unaltered.

The AWG generates the voltage signals shown in Fig. 5.6(a). These voltage signals drive the EOPM, modulating the phase of the pulse train at the output of the DCF. This produces the expected FSR modification (multiplication of the input FSR by the factor r^{-1}), and associated passive spectral comb line amplification effect. Fig. 5.6(b) shows the input and output power spectra, measured with a 5 MHz resolution optical spectrum analyzer, and normalized to the peak spectral power of the input comb.

It is important to note that the output combs preserve the envelope of the power spectrum of the input comb. Fig. 5.7 shows the measured power spectra and corresponding envelopes of the input and output

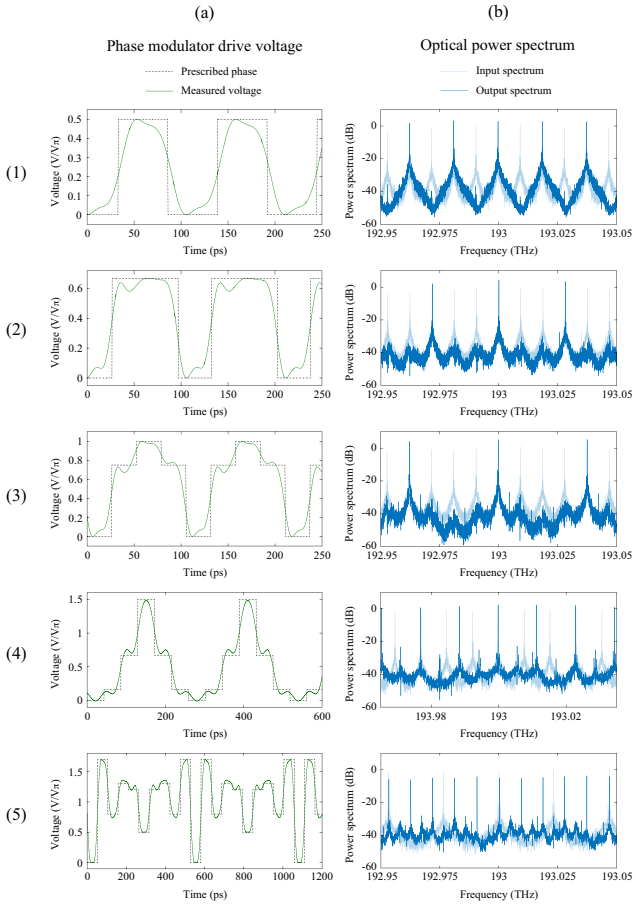

Figure 5.6 – Arbitrary FSR control, experimental results. Set of measurements corresponding to the experimental conditions and results listed on Table 5.1, and following the same numbering (1)-(5). (a) Prescribed temporal phase modulation sequences and applied EOPM drive voltages, where V_π denotes the half-wave voltage of the EOPM (i.e., the required voltage level to apply a phase sift of π rad to the optical signal); (b) optical power spectra of the input and output frequency combs, normalized to the spectral peak power of the input comb (the anticipated FSR multiplication by the factor r^{-1} is observed, as well as the corresponding passive spectral line amplification effect by energy redistribution).

combs used in the demonstration of the PCSTM reported here, corresponding to entries (1)-(3) of Table 5.1. The match between input and output spectral envelopes is clearly observed.

5.3 Noiseless spectral amplification and sub-noise detection of frequency combs

As discussed in Section 1.4, the presence of random noise fluctuations across the frequency spectrum of a frequency comb has a critical impact on the performance quality of the comb in practical applications. The origin of these fluctuations is tied to amplification stages outside of the comb generation system, commonly referred to as extracavity noise [68], which are often required to induce spectral broadening through nonlinear effects. Active gain processes amplify both the comb lines and the background noise floor, while additionally introducing an external noise contribution (e.g., amplified spontaneous emission, ASE, on erbium-doped fiber amplifiers, EDFA, that can be considered additive white Gaussian noise, AWGN, as long as the entire comb spectrum is contained within a uniform region of the gain spectrum of the EDFA).

Naming the spectral peak power of the comb P_ν, and the spectral power level of the background noise floor N_ν, the visibility of the comb lines can be defined as the ratio of these two magnitudes,

$$\eta := \frac{P_\nu}{N_\nu} \tag{5.4}$$

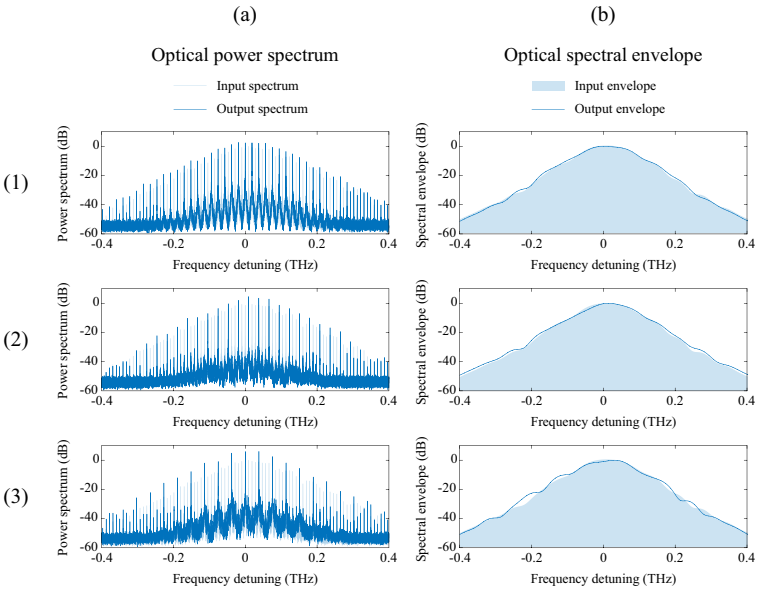

Figure 5.7 – Preservation of the comb envelope after application of the PCSTM, experimental results. Optical power spectra (a) and associated spectral envelopes (b) of the frequency combs listed in entries (1)-(3) of Table 5.1. In all cases, the envelope of the output comb matches that of the input comb.

In a simple approximation, an active amplifier with power gain $r^{-1} > 1$, introducing an external noise term N_{ASE}, produces a frequency comb at its output, with a visibility,

$$\eta = \frac{r^{-1}P_\nu}{r^{-1}N_\nu + N_{\text{ASE}}} \tag{5.5}$$

It is easy to see that, not only the gain term does not enhance the visibility, but rather that the additional noise contribution degrades it.

Reducing the noise floor of a frequency comb poses significant challenges. For instance, the most straightforward noise mitigation method based on direct frequency filtering of individual comb lines would require extremely precise fine-tuning, alignment and stabilization of the filter [67], including accurate a priori knowledge of the absolute frequencies of the comb lines.

The reported method for comb FSR manipulation has the capability of redistributing the energy of the comb lines into a completely different set of lines in the output comb (see Fig. 5.6). When the FSR multiplication factor, r^{-1}, is designed to be higher than 1, energy conservation ensures that the output spectral peak power increases with respect to the input spectral peak power, by a factor r^{-1}. Since the noise content of the background noise floor is incoherent and does not satisfy any of the designed Talbot conditions in the PCSTM, this suggests the possibility of increasing the visibility of the comb lines through the application of the method with $r^{-1} > 1$, so that,

$$\eta = r^{-1}\frac{P_\nu}{N_\nu} \tag{5.6}$$

Fig. 5.8 shows a simplified model of the classical active amplification process (Fig. 5.8(a)) and the energy redistribution process resulting from the PCSTM (Fig. 5.8(b)).

Indeed, similarly to the process described and demonstrated in Section 4.3, an effect of passive amplification occurs in the power spectrum of a frequency comb, as a consequence of the PCSTM, if $r^{-1} > 1$. Fig. 5.9 shows the results of a numerical simulation where the noise floor of a frequency comb is reduced, with respect to the spectral peak power, through application of the PCSTM with $r^{-1} = 20$. A visibility

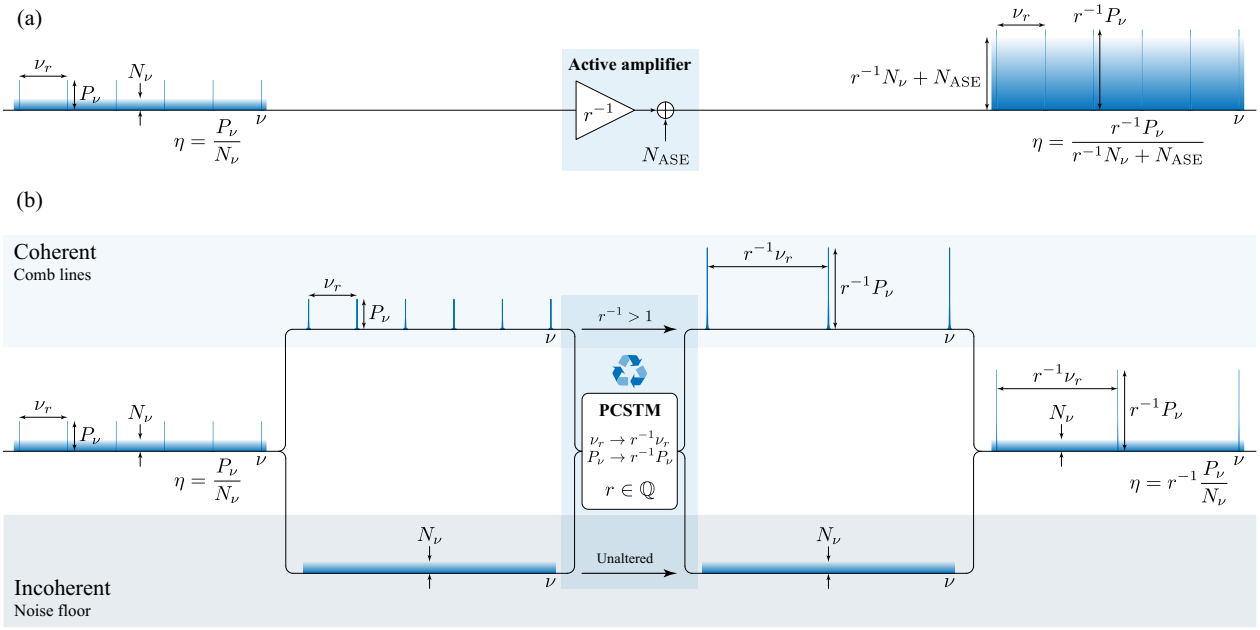

Figure 5.8 – Impact of amplification on the noise floor of a frequency comb. Simplified steady-state frequency domain model of (a) a classical active amplifier and (b) the passive spectral amplification effect, consequence of the PCSTM with $r^{-1} > 1$. Active amplification increases both the signal power, P_ν and the noise power, N_ν while introducing an additional noise term, N_{ASE}, thus deteriorating the visibility of the comb lines, η. Passive spectral Talbot amplification ($r^{-1} > 1$) redistributes the energy of the comb lines into a set of fewer comb lines, thus increasing their spectral peak power, while keeping the noise content of the comb unaffected. The comb visibility is then enhanced, increasing by the FSR multiplication factor, r^{-1}.

increase of 13 dB is observed, in agreement with the expected enhancement value, $10\log_{10}(r^{-1})$. Furthermore, the proposed technique compares favorably to classical averaging[2] of $N = 20$ measurements of the power spectrum. The outcome in this situation is a spectrum with smooth power variations, however, the noise floor level remains unchanged, and so the visibility is not enhanced.

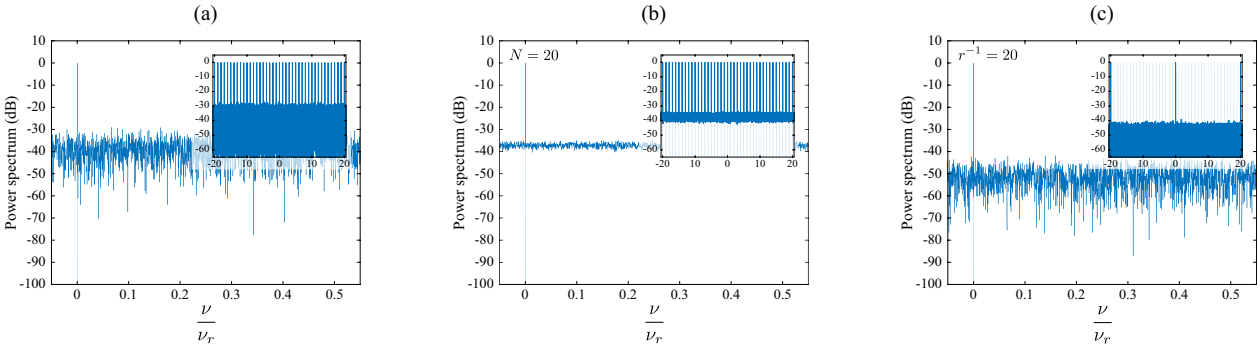

Figure 5.9 – Visibility enhancement by noiseless spectral Talbot amplification, numerical simulation. Noise mitigation of a frequency comb affected by strong AWGN fluctuations (a). Comparison between (b) standard signal averaging of $N = 20$ measurements, and (c) a single measurement after integer spectral Talbot amplification by $r^{-1} = 20$. A clean trace of the input signal is shown for reference.

[2]This result is equivalent to the effect of averaging the instantaneous power distribution of a train of optical pulses in the presence of noise, where the extinction ratio of the pulse is not enhanced by averaging, while temporal Talbot amplification does enhance it (see Section 4.3).

This suggest the possibility of detecting sub-noise spectral events through energy redistribution in the frequency domain, allowing to detect signals whose power spectra is completely buried underneath the background noise floor.

5.3.1 Experimental demonstration

In order to demonstrate the predicted *noiseless spectral amplification* effect, the experiment described in Section 5.2.2 is repeated. An AWGN source is incorporated in order to increase the noise content of the input comb, to the spectral peak power value of the input comb. The FSR period is then multiplied by integer numbers, r^{-1}, following the energy-preserving protocol defined by the PCSTM, thus increasing the comb spectral peak power over the noise floor level.

5.3.1.1 Experimental setup

In order to test the effect of noiseless spectral amplification by energy redistribution, an AWGN source is incorporated to the experimental setup depicted in Fig. 5.4.

The noise source is constructed by injecting ASE from an EDFA, leaving the input of the amplifier disconnected, to the input comb. This way the amount of ASE injected to the signal is controllable by varying the pump current of the EDFA. A variable optical attenuator is connected to the output of the mode-locked laser generating the input comb, in order to set the power level of the signal. In the reported experiments, the input comb visibility is set to 0 dB, i.e., the noise floor is at the same level as the spectral peak power of the input comb. Fig. 5.10 shows the implementation of this noise source in the experimental setup.

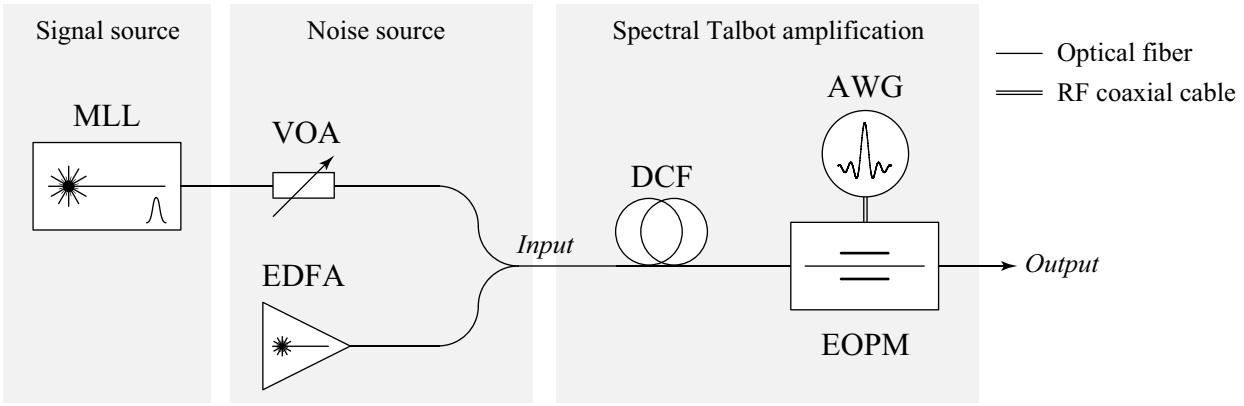

Figure 5.10 – Noiseless spectral amplification of frequency combs, experimental setup. MLL, mode-locked laser; VOA, variable optical attenuator; EDFA, erbium-doped fiber amplifier; DCF, dispersion-compensating fiber; AWG, arbitrary-waveform generator; EOPM, electro-optical phase modulator. For a complete schematic of the experimental setup, see Fig. D.2.

5.3.1.2 Experimental results

Fig. 5.11(a) shows a set of measured spectra of input combs with a visibility of 0 dB (see Table 5.1 for a list of experimental conditions). The PCSTM is subsequently applied to multiply the FSR of these combs by $r^{-1} = 2, 3,$ and 4.

Fig. 5.11(b) shows the spectra of the output combs, where the comb lines are clearly visible over the noise floor, due to the expected energy redistribution. The visibility of the obtained combs is consistent with the expected value, $10\log_{10}(r^{-1})$.

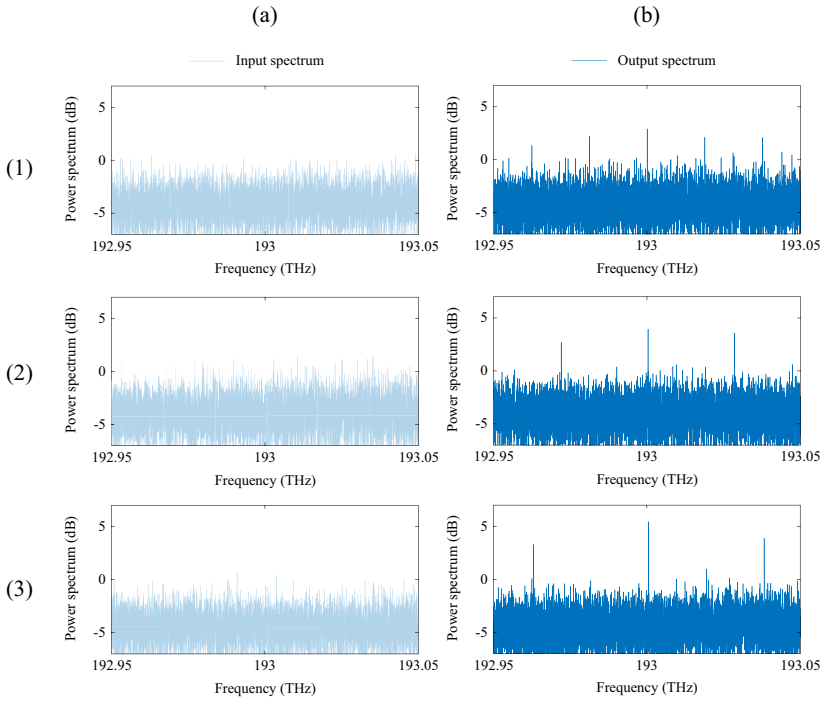

Figure 5.11 – Noiseless spectral amplification of frequency combs, experimental results. Set of measurements corresponding to the experimental conditions and results listed on Table 5.1, and following the same numbering (1)-(3). The noise floor level of the input combs (a) is increased up to the level of the comb lines, so that the comb visibility is of 0 dB. The output comb lines, after application of the PCSTM with $r^{-1} > 1$, rise over the noise floor by an amount equal to the FSR multiplication factor, so that the output visibility is $10\log_{10}(r^{-1})$.

A particularly interesting feature of the described process is that it does not require any a priori knowledge of the absolute frequencies of the comb lines to increase the comb visibility. Such a feat compares favorable with techniques that rely on direct amplitude filtering of the comb spectrum.

5.4 Generation of frequency combs with user-defined FSR

In principle, the PCSTM – generalized self-imaging-induced spectral energy redistribution – applies to any coherent frequency comb. The method, however, relies on applying a suitable quadratic spectral phase to the comb – temporal Talbot effect – prior to the temporal phase modulation process with the corresponding Talbot phase sequence – spectral Talbot effect. In practice, the required amounts of GVD can be challenging to meet in the current technological framework. The spectral phase filtering step in the PCSTM requires phase variations between adjacent lines of the comb of the order of π rad (see Eq. 5.1). This condition can be met using specially engineered optical dispersive media, such as linearly-chirped fiber Bragg gratings or dispersive optical fibers when the FSR of the input comb exceeds a few GHz. It becomes particularly challenging to meet the required GVD specifications for combs with FSR in the MHz regime, as encountered in conventional passively mode-locked lasers.

For instance, at a central wavelength of 1550 nm, the PCSTM achieves FSR multiplication by a factor 2 from an input FSR of 10 GHz with a total GVD of $|\beta_2|\, z \approx 795.775$ ps^2/rad; this corresponds to propagation through $\sim$37 km of standard SMF-28 optical fiber[3] [76]. If the original FSR is 100 MHz, the required GVD scales up to $|\beta_2|\, z \approx 7957747.155$ ps^2/rad, corresponding to a length of $\sim$367010 km of SMF-28, a highly

[3]For this comparison, a typical value of 17 ps/nm/km is used as the reference dispersion value of SFM-28 optical fiber, operated at 1550 nm (see Fig. 2.6).

unpractical[4] specification. Fig. 5.12 shows the length of SMF-28, z, required by the PCSTM for different values of the parameter q_2 and the input FSR, ν_r.

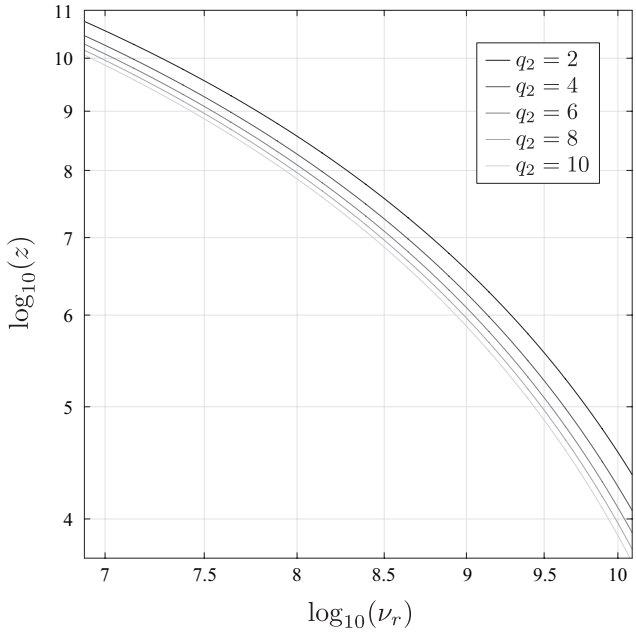

Figure 5.12 – Dispersive propagation length required for FSR control. Estimated length (z, measured in m) of standard SMF-28 optical fiber required by the PCSTM for FSR manipulation for different values of the FSR multiplication factor (parameter q_2, for integer FSR multiplication) and the input FSR (ν_r, measured in Hz). A typical value of 17 ps/nm/km is used as the reference dispersion value of SFM-28 at a central wavelength of 1550 nm.

It is worth noting that, as per the formulation of the Talbot phases, the required spectral phase variations can be introduced through multilevel spectral phase filters. However, optical filters with complex phase variations and the high level of finesse required for processing a comb with FSR values in the MHz regime are extremely difficult to implement, if at all possible. Indeed, line-by-line pulse shaping techniques would fail to provide the required spectral phase profile, due to the limited frequency resolution of conventional pulse shapers (typically in the order of tens of GHz) [31, 32].

The temporal phase modulation operation, however, becomes less problematic at lower values of the input FSR. A lower FSR translates into a longer pulse period, thus allowing the use of lower frequency RF equipment (e.g., arbitrary waveform generators and amplifiers) to generate the required temporal Talbot phase sequences.

In order to overcome these GVD limitations, the use of a special resonant cavity, known as a *frequency-shifted feedback loop* [92], was proposed as a platform for versatile frequency comb generation based on the PCSTM [APj7]. Such a cavity, when seeded by a CW laser, behaves as a mode-locked laser with a built-in tunable quadratic spectral phase, capable of emulating propagation of a phase-coherent frequency comb through thousands of km of optical fiber. When used in conjunction with a temporal phase modulator, the phase transformations involved in the PCSTM can be implemented. Frequency comb generation with tunable FSR over 6 orders of magnitude, from a few kHz to a few GHz, was experimentally achieved, even allowing to induce very high and user-defined chirp – frequency modulation – values to the associated temporal pulses [APj7]. A detailed description of this technique is reported in Appendix E.

[4]Note that, as per Eq. 5.2, there is an inversely-quadratic relationship between the total required GVD and the input FSR.

CHAPTER 6

Generalized spectral Talbot effect on aperiodic waves

The effects of the universal period control method on aperiodic signals are studied in this chapter. The method has the capability to introduce free spectral regions – frequency gaps – to the continuous spectra of aperiodic waves. Two applications are discussed; (i) a method for full-field invisibility cloaking in the frequency domain and, (ii) a method for compressing the spectrum of sequences of modulated pulses (e.g., telecommunication data signals) while preserving the original pulse duration and overall temporal shape. The latter is additionally used as a robust, energy-efficient technique for format conversion of modulated pulse sequences. The work presented in this Chapter was reported in [APj6] [APc2, APc3, APc7, APc10].

6.1 Talbot effect on aperiodic waves

As introduced in Section 2.4 and mathematically demonstrated in Section 3.1, Talbot effect requires a wave described by a periodic function of its representation domain. This allows to write the Fourier-domain representation of the wave as a Dirac comb, which is key in the formulation of the Talbot phases.

However, the linear transformations derived from the theory of Talbot effect reported in this dissertation can be applied to aperiodic structures and waves, obtaining interesting results. Typically, in such situations, the application of an intrinsically periodic Talbot phase introduces a certain degree of periodicity to the wave of interest, in a loose sense; e.g., a CW laser, phase-modulated by a Talbot phase sequence, acquires a spectrum consisting of a Dirac comb. Additionally, aperiodic waves with an *underlying periodic component* (e.g., digitally-modulated data signals with an underlying clock frequency) also produce interesting Talbot (sub-)images when processed through different self-imaging phenomena. The latter case gives rise to the fascinating self-healing property of the Talbot effect, where an aperiodic structure produces Talbot images with an emphasized periodic component.

6.1.1 Talbot array illuminators

A Talbot array illuminator (TAI) is an example of self-imaging of an object that, under normal circumstances, would not produce Talbot sub-images. These structures were demonstrated in the Fresnel diffraction domain of waves, as a way of transforming a uniform beam of light into a collection of localized bright spots [112–114]. A TAI is observed when a plane wave diffracts off a phase mask, introducing a spatial Talbot phase profile, to an integer Talbot length. At the observation plane, a periodic image of squared spots is obtained, with a period that depends on the introduced Talbot phase. Fig. 6.1 shows a 1D numerical simulation, depicting the formation of a TAI from a continuous constant function.

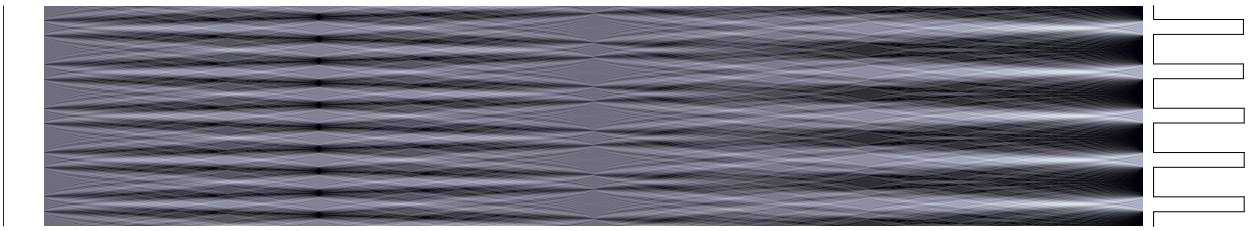

Figure 6.1 – Talbot array illuminator, numerical simulation. Talbot carpet obtained in the formation of a TAI. The simulated phase mask corresponds to a spatial 1D Talbot phase with $q_1 = 3$.

A temporal version of the Talbot array illuminator (T-TAI), is observed when a CW beam is phase-modulated with a temporal Talbot phase sequence, prior to propagation through a GVD medium satisfying a Talbot condition for the applied phase modulation, resulting on a train of rectangular pulses[1]. An easy way of understanding this is by picturing a train of rectangular pulses where the repetition period is an integer multiple of the pulsewidth, q_1. A temporal Talbot sub-image of said pulse train, with denominator q_1 (see Eq. 3.19), will produce a signal with a constant instantaneous power level. The T-TAI is observed by reversing the process, i.e., starting from the continuous signal, applying an adequate temporal Talbot phase profile to emulate the mentioned sub-image with denominator q_1 (thus making the complex amplitude of the signal q_1-periodic), and reversing the GVD propagation. The T-TAI was recently introduced as a method to generate trains of optical pulses from CW lasers with high energetic efficiency and high levels of

[1]Note that this implementation arises from direct application of the space-time duality (see Appendix B) to the processes involved in the formation of a spatial TAI.

extinction ratio [115]. This method can be understood as an application of the PCTTM with integer period multiplication factor, $r > 1$, on a limit case signal with a constant instantaneous power distribution. Fig. 6.2 shows a sketch summary of the wave transformations involved in the generation of a T-TAI.

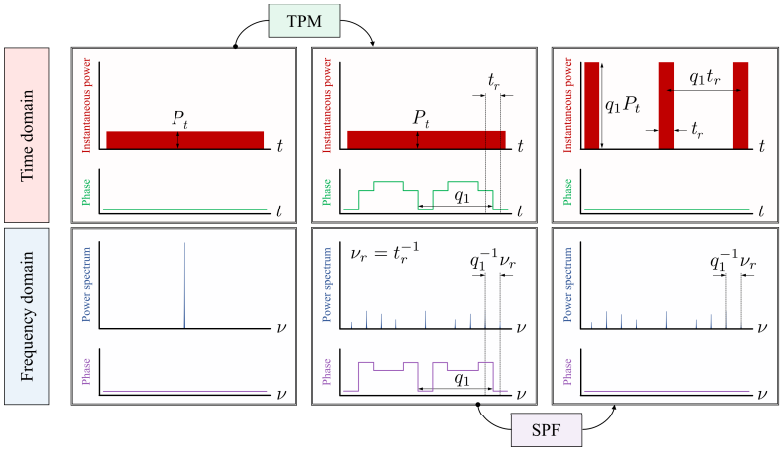

Figure 6.2 – Temporal Talbot array illuminator as a limit case of the PCTTM. Combination of phase transformations (TPM, temporal phase modulation; SPF, spectral phase filtering) of a CW beam to generate a train of rectangular pulses through energy redistribution based on the PCTTM. In the shown example, $r = q_1 = 5$.

It should be noted that while, strictly speaking, a CW beam satisfies the condition for a function to be periodic[2], the fundamental period is not defined (all values of a constant function repeat themselves infinitely). Consequently, the spectrum of a constant function is a single component in the Fourier domain. From the viewpoint of generating Talbot sub-images, constant functions are considered aperiodic here.

6.1.2 Self-healing property of Talbot effect

Another category of aperiodic structures, susceptible of producing Talbot (sub-)images, is obtained by introducing non-uniformity to an originally periodic object, thus disrupting its periodicity. Common examples of such "faulty" periodic structures are imperfect images of periodic optical gratings, in the position (space) domain, and modulated temporal data signals, used in digital telecommunications systems to convey information. In the latter case, the introduced non-uniformity codifies the information of interest, carried by the signal.

Talbot effect on faulty periodic structures renders images where the underlying periodicity of the object is partially recovered. The reason behind this phenomenon, is that the output individual features of a Talbot (sub-)image are not constructed from a specific feature of the input waveform. In other words, there is no one-to-one relationship between input and output features of a Talbot (sub-)image. This way, variations between periods of the input waveform are washed out in the output image. This effect is enhanced in the case of Talbot amplification, e.g., as observed through the application of the PCTTM with $r > 1$ to modulated trains of pulses. This is because in the process of Talbot amplification, images with higher energy per output feature are obtained. Fig. 6.3 shows a numerical simulation example of Talbot self-healing on a periodic one-dimensional object, where input features are randomly eliminated.

The self-healing property of Talbot effect has been used as a way to reconstruct two-dimensional images from periodic objects affected by faults in the image acquisition process [83,112], achieving improved results

[2]In general, a function, ψ, is periodic in the representation domain u if $\psi(u) = \psi(u \pm n u_r)\ \forall\ n \in \mathbb{N}$, where $u_r > 0$ is the fundamental period.

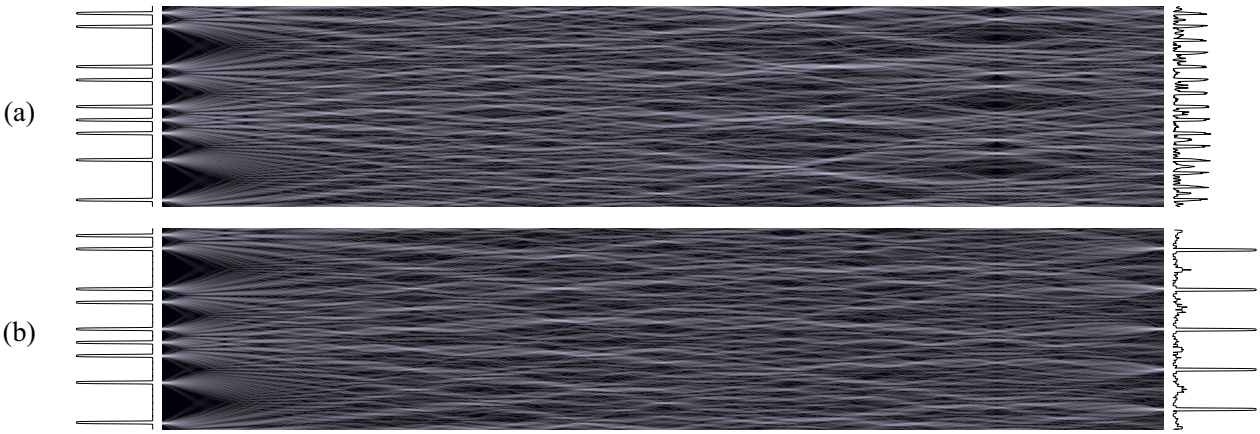

Figure 6.3 – Self-healing property of Talbot effect, numerical simulation. Talbot effect on faulty periodic objects – aperiodic objects with an underlying periodicity – renders Talbot images where the underlying periodicity of the object is reconstructed. (a) Reconstruction of a periodic image from an aperiodic object through integer Talbot effect. While the underlying periodicity of the object is reconstructed, strong amplitude fluctuations are introduced. (b) Reconstruction of a periodic image from an aperiodic object through integer Talbot amplification, by application of the PCTTM with $r = 3$. The reconstructed period is r times longer than the underlying period of the input object, however, the level of amplitude fluctuations on the obtained image is substantially reduced with respect to the amplitude level of the output amplified features. For a fair comparison, the carpet shown in (a) represents the third integer Talbot image; this way the output images in (a) and (b) are obtained from equal propagation lengths.

when processed through a spatial realization of the PCTTM [OPc17]. Moreover, the same principle has been applied to modulated digital data signals in the time domain, as a method to recover the periodic clock component, necessary for synchronization purposes on a telecommunications receiver [95]. In this context, temporal Talbot amplification has been used as a successful method for reconstructing sub-harmonic – decimated – clocks from such data signals, achieving clock signals with higher quality than those obtained through the basic application of integer temporal Talbot effect [OPj4].

6.1.3 Processing aperiodic waves through the PCSTM

Although, as listed above, some some properties of Talbot (sub-)images obtained from aperiodic objects are relatively well-known, the impact on their spectra is less understood. Nevertheless, interesting phenomena can be observed in the frequency domain of Talbot (sub-)images when the input object processed presents aperiodicity.

6.1.3.1 Spectral Talbot array illuminators

Following a similar procedure to the formulation of the T-TAI (see Fig. 6.2), it should be possible to obtain a spectral manifestation of the effect, a spectral Talbot array illuminator (S-TAI). Recall that in a T-TAI, a CW beam is focused into a train of short (ideally rectangular) optical pulses following periodic phase modulation of the input CW and dispersive propagation of the modulated signal, where both the phase modulation profile and the dispersive length are designed accordingly to the PCTTM (see Section 6.1.1). An exchange of the time and frequency domains on the phase transformations of the PCTTM should obtain the desired T-TAI effect; this would first involve the application of a discrete spectral Talbot phase to a wave featuring a uniform continuous spectrum, followed by a cancellation of the consequently induced temporal phase profile, as illustrated in Fig. 6.4(a).

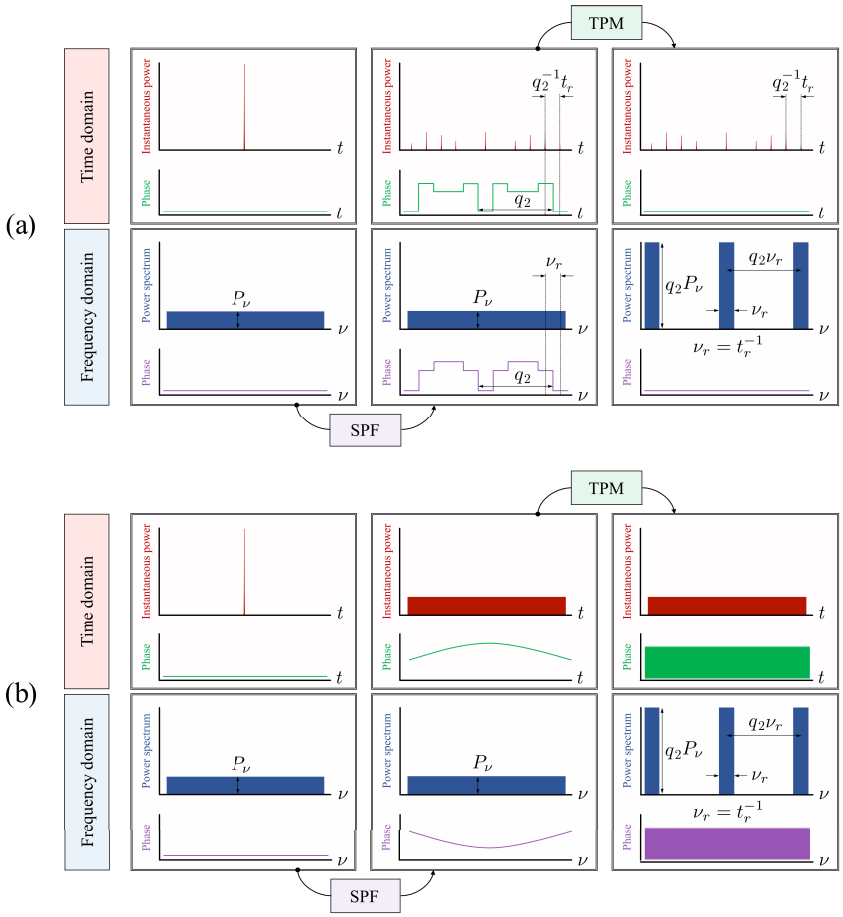

Figure 6.4 – Spectral Talbot array illuminator as a limit case of the PCSTM. Combination of phase transformations (SPF, spectral phase filtering; TPM, temporal phase modulation) of a uniform continuous spectrum to generate a sequence of spectral peaks and gaps through energy redistribution based on the PCSTM. (a) Formulation of the problem using discrete spectral Talbot phases. (b) Formulation of the problem using continuous spectral Talbot phases, such as those introduced by conventional GVD media. Note that that the TPM operation in (b) still follows the exact same discrete temporal Talbot phase sequence required in (a). In the shown examples, $r^{-1} = q_2 = 5$.

Remarkably, if a continuous spectral Talbot phase (i.e., one satisfying the condition given in Eq. 3.50) is used instead of a discrete spectral phase sequence, the S-TAI still forms after the application of the corresponding discrete temporal Talbot phase sequence, as illustrated in Fig. 6.4(b). This finding is interesting from a signal processing perspective, as the period of the obtained S-TAI spectrum becomes an arbitrary factor set by the period of the applied temporal phase sequence. This is also of great interest from a practical implementation viewpoint, as the required continuous quadratic spectral phase transformation can be easily implemented by conventional GVD media, which presents practical advantages such as the lack of need for frequency alignment between the filter and the signal.

Note that the S-TAI configuration corresponds to direct application of the PCSTM, with integer spectral period multiplication factor $r^{-1} > 1$, to a temporally-localized waveform (in practical terms, a short coherent pulse), corresponding to a broad spectrum. This chapter deals with the application of the PCSTM to temporally-aperiodic waves, and it studies the resulting effects on their continuous spectra. Two application examples of the PCSTM to aperiodic temporal signals are reported and discussed: (i) a method to reversibly transform the energy spectrum of a broadband wave, so as to avoid interaction between the wave and an object with the purpose of concealing the object from detection (Section 6.2), and (ii) a technique to compress

the spectrum of a sequence of modulated short pulses, e.g., a telecommunications signal, without altering the temporal shape, including the duration, of the individual pulses of the sequence (Section 6.3). Moreover, the latter sets the principles for a robust and energy-efficient method for converting the modulation format of a data sequence, from return-to-zero to nonreturn-to-zero (Section 6.4).

6.2 Spectral invisibility cloaking

This section discusses the application of energy redistribution methods based on phase-controlled Talbot effects to the field of invisibility cloaking. A method to produce phase-preserving, broadband invisibility is presented, based on reversible transformations of the frequency spectrum of broadband waves.

6.2.1 Concealment of objects from detection

The capability of making objects invisible has captivated mankind's imagination for centuries, becoming fairly standard plot devices in the world of fantasy and science fiction. In real life, invisibility can be achieved by manipulating the ways in which waves travel through space, 'tricking' light into not illuminating the object one wishes to conceal from detection.

In general, an observer is able to detect and study an object by analyzing the interaction between said object and a probe wave, coming from a known illumination source. Such an interaction imprints a signature to the illumination wave, allowing the observer to detect and, to some extent, study the properties of the target object. A spatial invisibility cloak is a device capable of redirecting the illumination wave around a prescribed area [10, 116]. This way, objects located within the cloaked region avoid interaction with the wave. The observer is then unable to detect the presence of the object. Fig. 6.5 illustrates the principle.

The last decade has witnessed a flourishing production of novel concepts and methods for concealing objects from detection, including invisibility cloaks operating over different regions of the electromagnetic spectrum [10, 116–131], and even for waves of very different nature, such as acoustic and thermal waves [132, 133].

Similarly, temporal events, which are detected by the transient variation – temporal signature – they imprint on a probe wave, can be concealed from detection through a temporal invisibility cloak. Such a device, appropriately slows down the wave propagation speed before the target event takes place, and speeds it up after the event is finished, effectively creating a time period during which the wave carries no energy [134–136]. Fig. 6.6 illustrates the principle.

It should be noted that the ultimate goal of an invisibility cloak is to prevent the detection of both the object and the cloaking device. Indeed, simply obstructing the observer's field of view would effectively obscure the object, however, the observer would immediately realize that an undesired external agent is interfering with the detection process.

6.2.1.1 Broadband invisibility invisibility: Cloaking multiple colors

Early demonstrations of invisibility cloaking featured metamaterial designs based on transformation optics, in which a conformal coordinate transformation is applied to Maxwell's equations, obtaining the set of electromagnetic parameters required to achieve the desired wave propagation paths [117–119]. The main limitation of such designs was the fact that invisibility was only achieved at a single wavelength.

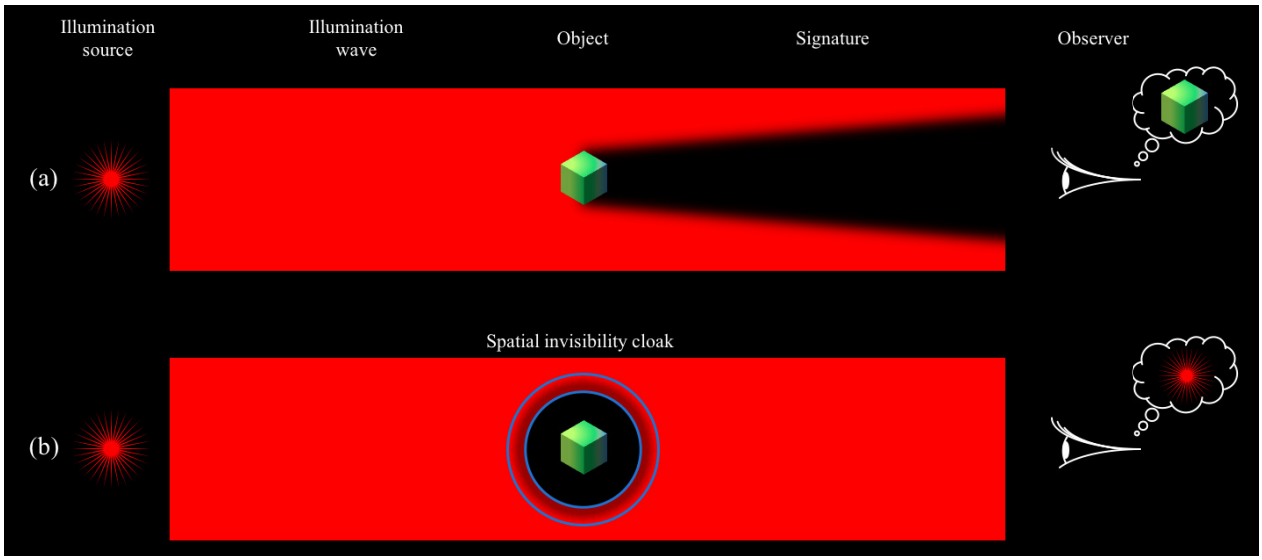

Figure 6.5 – Concept of spatial invisibility cloaking. (a) Detection of an object through the spatial signature resulting from the interaction between said object and an illumination wave. (b) Concealment of the object from detection through the operation of a spatial invisibility cloak. The cloaking device redistributes the energy of the illumination wave in space, forming a 'space gap'.

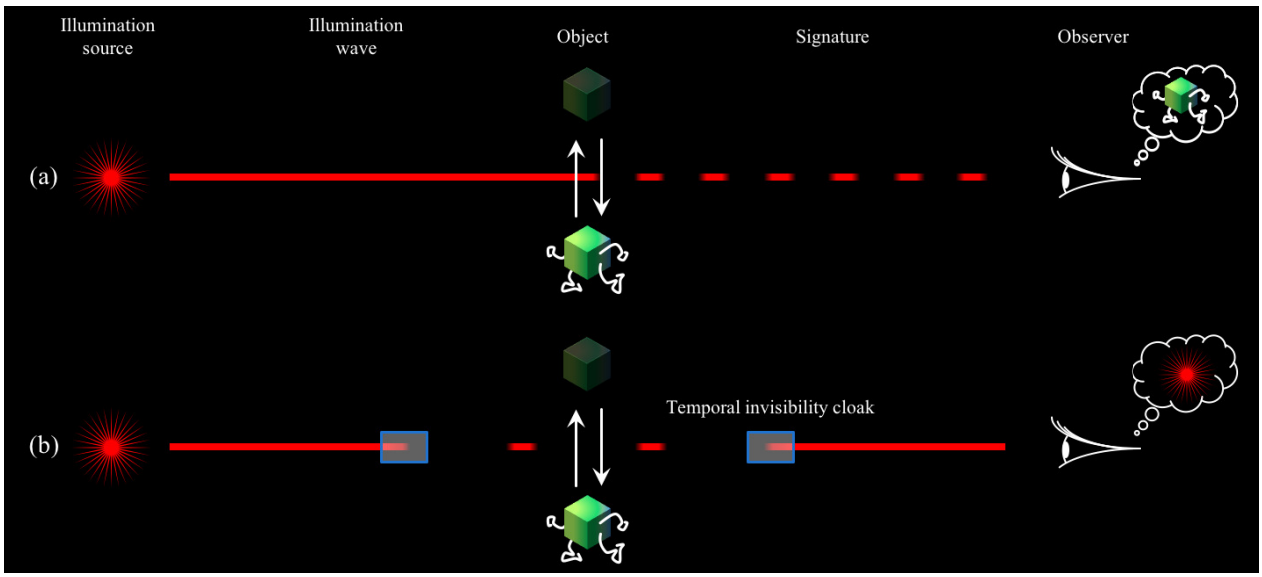

Figure 6.6 – Concept of temporal invisibility cloaking. (a) Detection of an event (e.g., the movement of an object, a temporal modulation process…) through the temporal signature resulting from the interaction between said event and an illumination wave. (b) Concealment of the event from detection through the operation of a temporal invisibility cloak. The cloaking device redistributes the energy of the illumination wave in time, forming a 'time gap'.

Recent advances in the field have given rise to invisibility cloaks featuring large operation bandwidths, usually relying on precise engineering of the electromagnetic response of an exotic material or a complex optical system [120–131].

6.2.1.2 *True* invisibility: The problem of full-field cloaking

One of the main fundamental challenges in the field of invisibility cloaking is the issue of phase preservation. For an object to be fully concealed, an invisibility device must be able to restore the exact amplitude and phase variations of the illumination wave, both spatially and temporally (i.e., the full field), at its output.

By fundamental design principles, current cloaking strategies are expected to alter the phase variations among the different frequency components of a broadband illumination wave [125–129]. This is due to the fact that an invisibility cloak forces different frequency components of the illumination wave to propagate through different optical paths, thus undergoing different delays. Such phase distortion unavoidably alters the illumination temporal profile, and current cloaking approaches are thus vulnerable to detection by straightforward observation methods. For instance, a phase-coherent short pulse (corresponding to a continuous, broadband frequency spectrum) incident in the cloaking device will be severely distorted due to phase distortion. An observer equipped with common phase-sensitive or temporal detection instruments could easily detect such distortion, thus revealing the presence of the cloak [125–129]. Furthermore, recent in-depth studies, using full electromagnetic analysis, have additionally predicted that traditional spatial invisibility cloaks also induce further distortions directly across the energy spectrum profile of the broadband illumination wave [128].

These fundamental shortcomings are intrinsic to invisibility designs and strategies proposed to date, so that demonstration of full-field broadband invisibility, even for the simplest one-dimensional case (single illumination direction), remains a significant challenge [116,125–129]. It has been argued that fundamentally new concepts, beyond conventional invisibility solutions proposed to date, become necessary for realization of phase-preserving, broadband cloaking [129–131].

6.2.2 Invisibility in the frequency domain through energy redistribution

Fig. 6.7 schematically illustrates the process of observation of an object through the distinct signature it imprints on the continuous frequency spectrum of a broadband illumination wave. Such a signature can be observed either by direct frequency-domain measurements, or through observation of the associated changes in the temporal and/or spatial properties of the wave.

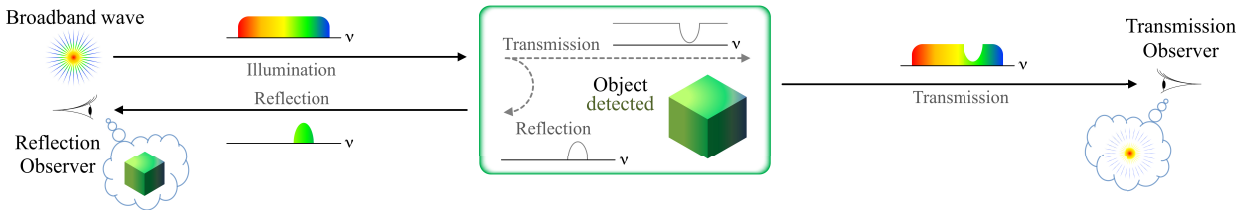

Figure 6.7 – Detection of an object through its frequency-domain siganture on a broadband illumination wave. For simplicity of illustration, only scattering of the wave by the target is represented.

The concept proposed here is based on redistributing the incoming wave energy toward frequency regions that will not be affected by interaction with the object to be cloaked, through energy-preserving transformations. These transformations are designed to create a reversible 'frequency gap' across the desired region(s) of the illumination spectrum. The wave then propagates through the object without interacting with it, and subsequent application of the opposite transformations restores the wave spectrum to its exact original state – both in amplitude and in phase – when the wave has cleared the object. This ensures that both the target

and the cloaking device remain invisible to any observer, including through broadband, phase-sensitive or time-domain detection. Fig. 6.8 illustrates the principle.

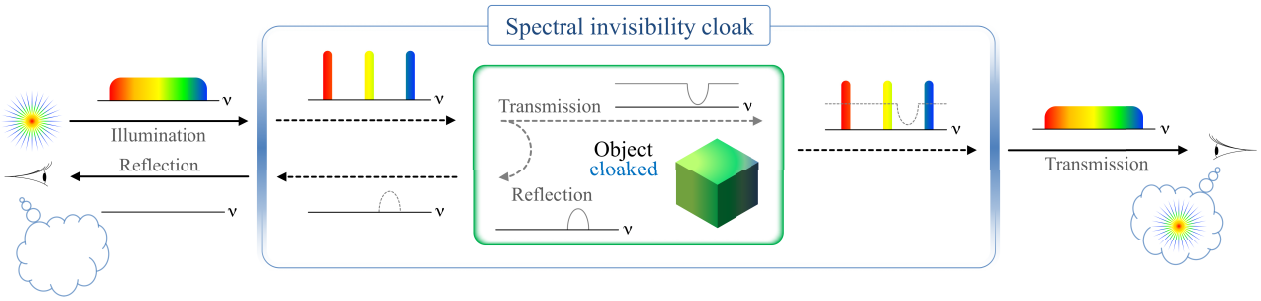

Figure 6.8 – Concealment of the frequency-domain signature of an object through spectral invisibility cloaking. A frequency gap is generated in the spectrum of the illumination wave through energy-preserving, reversible wave transformations. The spectral response of the object, located within such a gap, does not interact with the illumination wave, and thus, a signature is not imprinted. Once the wave clears the object, the opposite wave transformations restore the illumination spectrum (both in amplitude and in phase) to its exact original state.

Not only this method has the capability of preserving the phase distribution of coherent broadband illumination waves, but it also provides a new avenue towards application of invisibility concepts to the realm of spectral analysis of waves. More generally, this concept suggests a way to tailor at will the interaction between an incoming wave and a medium (i.e., a material, device, system, etc.), through reversible, energy-preserving transformations of the wave spectrum. To give just a basic example, the spectrum of a wave of interest could be reversibly transformed to avoid interaction with undesired frequency bands of a medium or system (e.g., high-absorption spectral regions), thus preventing loss and/or distortion. Such a capability could prove useful for many important applications, from enhanced control of linear and nonlinear wave dynamics to unprecedented opportunities in sensing, communications and signal processing.

6.2.2.1 Operation principle

Many different implementations of energy redistribution concepts based on reversible wave transformations could be envisioned to generate frequency gaps in the continuous spectra of coherent broadband waves. The wave transformations defined by the PCSTM (see Section 3.2.3.2) successfully produce the desired effect.

For simplicity of explanation, consider first a train of pulses with repetition period t_r as the illumination wave. This corresponds to a frequency comb with FSR $\nu_r = t_r^{-1}$. In this situation, the PCSTM can be used to multiply the comb FSR by an integer factor, $r^{-1} = q_2$. Recall that, as per the PCSTM derivations in Section 3.2.3.2, fist, a spectral phase shift $\phi_{k;p_2,q_2}$ (general expression in Eq. 3.48) must be applied to the k-th comb line. In the reported experiments, the value $p_2 = 1$ is chosen to minimize the total required amount of GVD, however, any integer value can be designed, as long as p_2 and q_2 are mutually prime. This way, the applied phase sequence writes,

$$\phi_{k;1,q_2} = \varsigma\pi\frac{1}{q_2}k^2 \tag{6.1}$$

As per Eq. 3.50, the required amount of GVD,

$$2\pi|\beta_2|z = \frac{1}{q_2\nu_r^2} \tag{6.2}$$

The obtained wave is a pulse train with repetition period $q_2^{-1}t_r$. Next, a temporal phase shift $-\varphi_{n;s_2,q_2}$ (general expression in Eq. 3.52, where s_2 is obtained from Eq. 3.27, for the given values of q_2 and p_2) is applied to the n-th pulse of the resulting train. In the reported experiments, $s_2 = q_2 - 1$, so that,

$$-\varphi_{n;q_2-1,q_2} = \varsigma\pi\frac{q_2-1}{q_2}n^2 \tag{6.3}$$

The FSR multiplication factor obtained in this configuration of the PCSTM is $r^{-1} = q_2$ (see Section 3.2.3.2), resulting in a comb with FSR,

$$\nu_c = r^{-1}\nu_r \tag{6.4}$$

Due to the energy-preserving nature of the transformation (only phase manipulations are involved), the FSR-multiplied comb can be restored to its original state by applying the opposite phase manipulations. Fig. 6.9(a) illustrates the entire process, where the labels -PM and -GVD denote application of said opposite phase transformations.

As described in Section 6.1.3.1, when the described transformations are applied to a coherent broadband illumination wave with a purely continuous frequency spectrum (e.g., a single, short temporal pulse), a periodic set of wideband frequency gaps is generated across the wave spectrum, forming an S-TAI with a spectral repetition period of ν_c. Fig. 6.9(b) illustrates the process. The described situation can be understood as a limit case where the pulse period of the input train in Fig. 6.9(b) is increased so that consecutive illumination pulses do not interact with each other through the applied phase transformations.

The required phase transformations in the case of a continuous illumination spectrum are the same ones described above for a periodic train of pulses. However, the values of r and ν_r can now be chosen arbitrarily to achieve the desired frequency gap bandwidth, set by,

$$\Delta\nu_g = (r^{-1} - 1)\nu_r \tag{6.5}$$

This makes the operation of the cloak independent of the properties of the illumination wave (e.g., repetition rate). As discussed above, the illumination wave can be subsequently restored to its exact original state through application of the opposite phase transformations. Fig. 6.10 shows a numerical simulation of the process with $r^{-1} = 4$, where the original illumination spectrum is assumed to exhibit uniform intensity and phase distributions, though it should be noted that the described process for frequency gap generation can be generally produced on non-uniform illumination spectra (further discussions below).

Fig. 6.11 shows a numerical simulation of the process for different values of the parameter r^{-1}.

6.2.3 Experimental demonstration

The proposed technique for phase-preserving spectral invisibility cloaking is demonstrated on a phase-coherent optical pulse in the near-infrared. It should be noted, however, that due to the nature of the wave transformations involved in the process, practical implementations could, in principle, be designed in any region of the electromagnetic spectrum, and for any wave-based platform where basic wave operations – spectral phase filtering and temporal phase modulation – are defined (e.g., acoustics, matter waves, etc.).

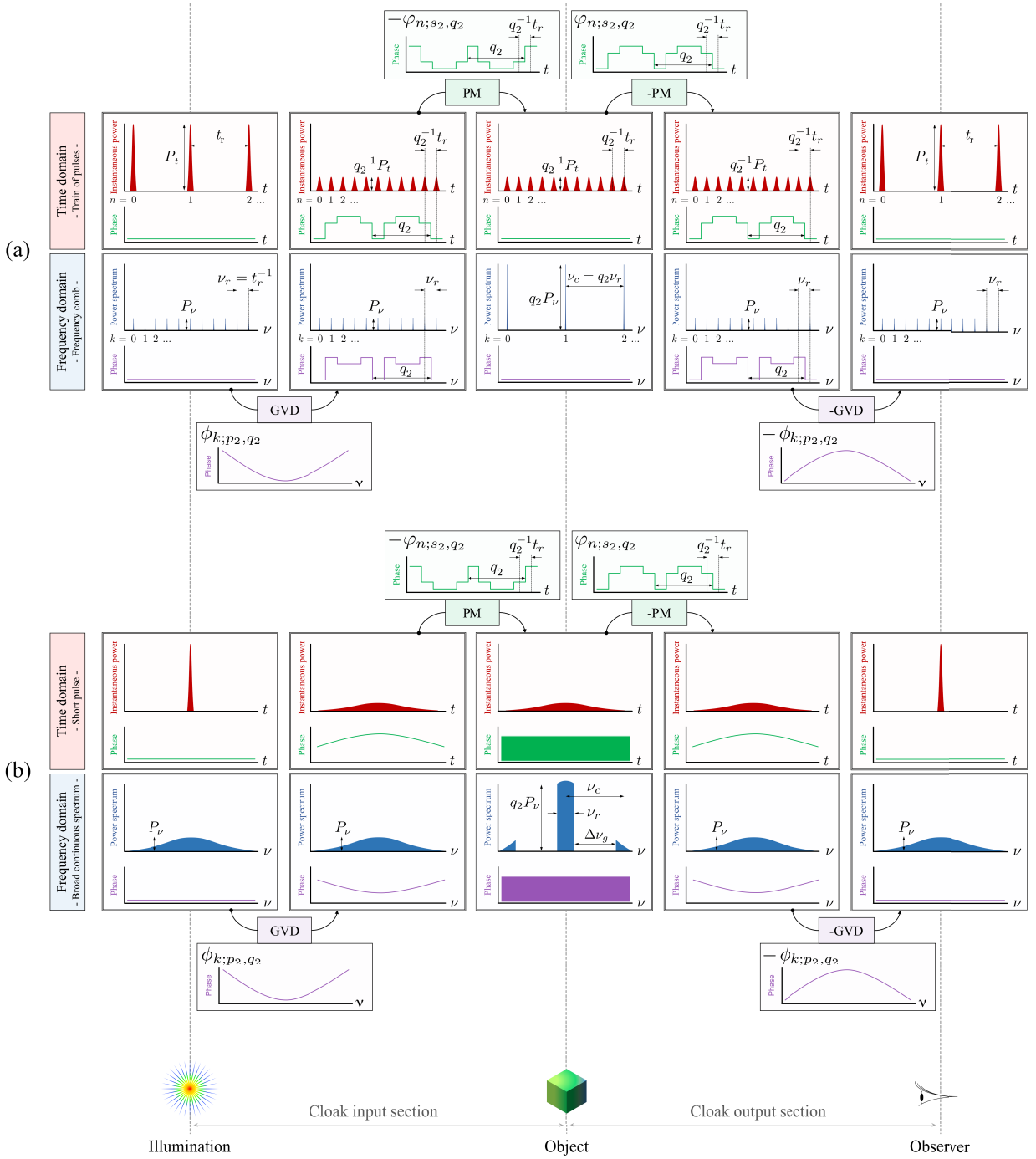

Figure 6.9 – Spectral invisibility cloaking, operation principle. Summary of the steps involved in the spectral cloaking process, based on the phase-only manipulations of the PCSTM (temporal phase modulation, PM, and group-velocity dispersion, GVD, respectively, see Section 3.2.3.2), with $r^{-1} = q_2$ (integer) for (a), a frequency comb illumination wave, and (b), the general case of an illumination wave with a continuous spectrum, where no interaction occurs between neighbouring pulses in the cloaking device at any given time.

6.2.3.1 Experimental setup

Fig. 6.12 shows a simplified[3] schematic of the experimental setup used to validate the spectral invisibility cloaking concept.

[3]For a complete schematic of the setup, see Fig. D.3.

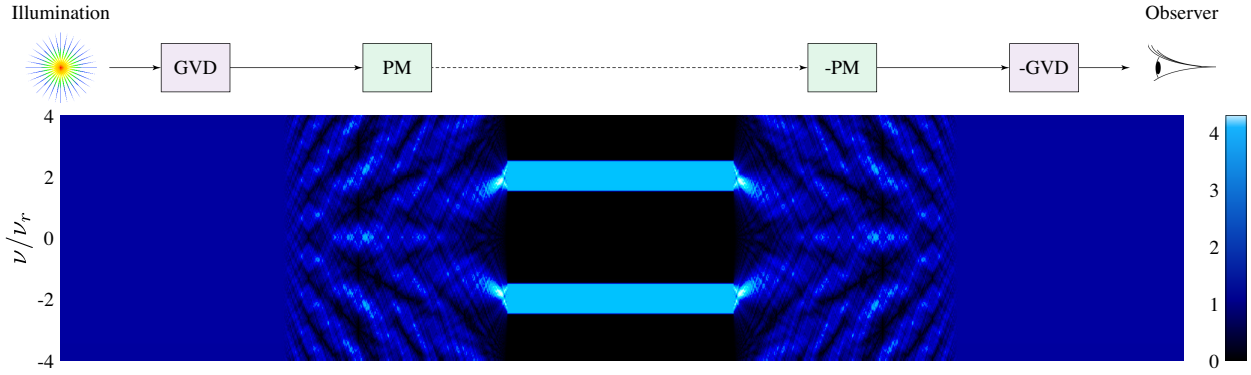

Figure 6.10 – Frequency gap generation process, numerical simulation. The operation of the PCSTM transformations on a wave with a continuous, broadband spectrum produces spectral regions free of energy (frequency gaps). In the shown numerical simulation, with $r = 4$, the original illumination spectrum is assumed to exhibit uniform intensity and phase distributions. The effect of phase modulation (PM) is here depicted as a progressive process in order to reveal the intricate mechanism leading to the formation, and subsequent reversal, of the frequency gaps.

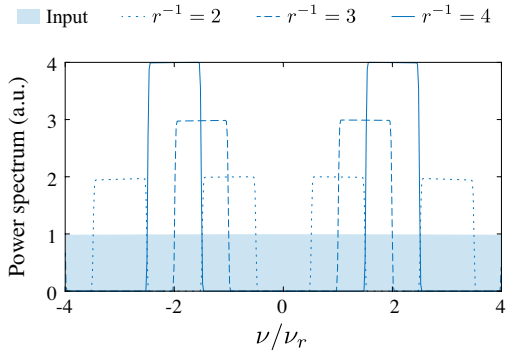

Figure 6.11 – Frequency gaps of different bandwidths, numerical simulation. Three examples of frequency gap generation in the spectrum of a broadband illumination wave are shown, for values of $r^{-1} = 2$, 3, and 4.

The used illumination source consists of a mode-locked laser with a repetition rate of 250 MHz, and an optical filter, used to select a 4 nm bandwidth around a central wavelength of 1554.5 nm (corresponding to a 3 dB bandwidth of ∼500 GHz around 192.85 THz). The resulting phase-coherent broadband frequency spectrum corresponds to a ∼1.4 picosecond temporal pulse.

As depicted in Fig. 6.12, the cloaking device consists of two sections of optical fiber for implementation of the input and output GVD media, with equal dispersion magnitude and opposite signs; and two electro-optic phase modulators driven by a radio-frequency synthesizer.

A spool of 10 km of standard single-mode fiber (SMF) was used as the input dispersive section of the cloaking device, with a total second-order dispersion of 173 ps/nm (corresponding to -222.6 ps^2/rad). The output dispersive section is matched to the input one by concatenating a spool of dispersion-compensating fiber, designed to compensate the dispersion of 20 km of SMF at the working wavelength, with an additional 10 km SMF spool. These dispersion values satisfy the desired Talbot condition for $\nu_r = 19$ GHz and $r^{-1} = 2$ (see Eq. 6.2). Note that this value of ν_r is 76 times higher than the repetition rate of the illumination laser; as such, the illumination repetition rate clearly does not satisfy a Talbot condition for the dispersion provided by the cloak. Moreover, the amount of dispersion in the cloak is insufficient to induce interference between any two consecutive pulses, thus ensuring no interaction among incoming pulses in the system.

Both electro-optical phase modulators are driven by a single-frequency tone at 19 GHz from the radio-frequency synthesizer. The generated driving voltage corresponds to a first-order approximation of the $r^{-1} = 2$ temporal Talbot phase sequence. The alignment of the applied driving voltage signal to the optical signal

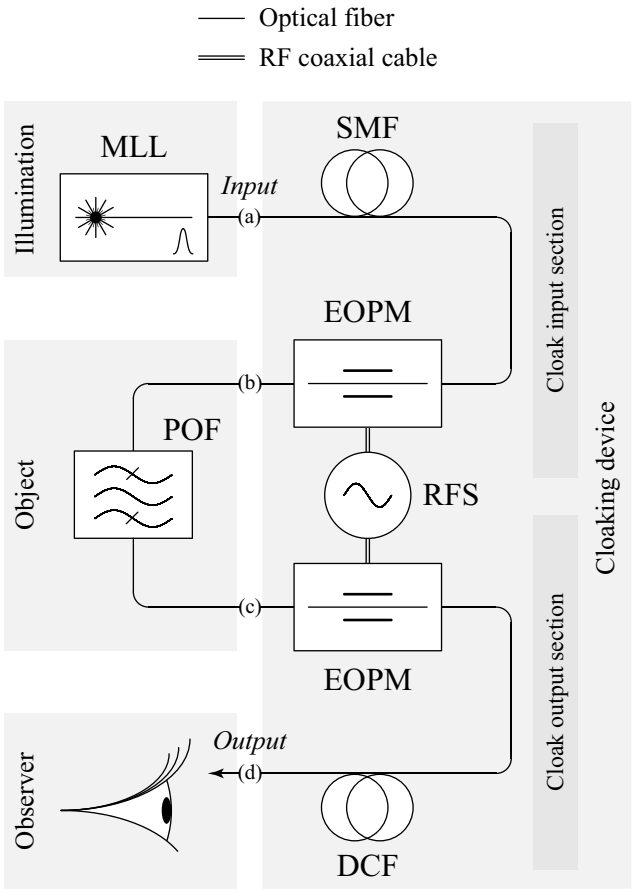

Figure 6.12 – Spectral invisibility cloaking, experimental setup. MLL, mode-locked laser; SMF, single-mode fiber; EOPM, electro-optical phase modulator; RFS, radio-frequency synthesizer; POF, programmable optical filter; DCF, dispersion-compensating fiber. For a complete schematic of the experimental setup, see Fig. D.3.

is achieved by a tunable optical delay line. Polarization controllers are used at the input of each modulator in order to maximize the modulation efficiency. Two radio-frequency amplifiers are used to boost the output of the synthesizer before each modulation stage, in order to adapt the radio-frequency tone to the half-wave voltage of the phase modulators. Fig. 6.13 shows a measurement of the phase modulation driving voltage, together with a trace of the dispersed pulse to which it is applied within the cloaking device.

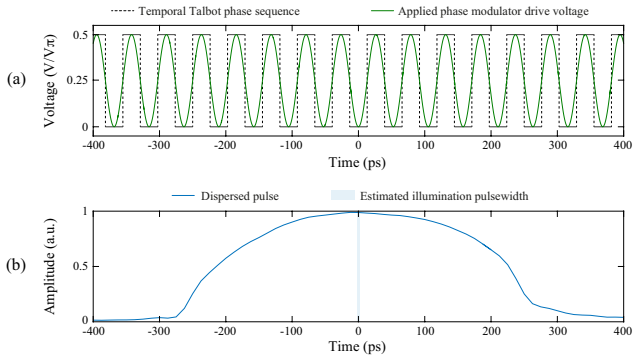

Figure 6.13 – Phase modulation and dispersed pulse propagating through the spectral invisibility cloak. (a) Periodic temporal Talbot phase profile associated to a Talbot condition with $r^{-1} = 2$. V_π represents the half-wave voltage of the electro-optical phase modulator. (dashed line) Prescribed phase obtained from the theory of Talbot effect. (solid line) Measured phase modulator drive voltage used in the experiments, approximating the Talbot phase by a single frequency component. The number of periods of the phase sequence occurring within the temporal duration of the dispersed pulse approximately equals the number of generated frequency gaps in the illumination spectrum (see Fig. 6.15). (b) Photodetected temporal amplitude trace of the dispersed pulse (after the first dispersive fiber section, see Fig. 6.12), shown with respect to the estimated 1.4 ps duration of the original illumination pulse, measured by a 28 Gsa/s real-time oscilloscope equipped with a 43 GHz photodiode.

The object to be concealed (frequency domain characterization shown in Fig. 6.14) is a programmable optical filter, loaded with a linear frequency response consisting of a set of resonances spaced by 38 GHz, each with a 3 dB width of 17.5 GHz.

Figure 6.14 – Test object used in the experimental demonstration of spectral invisibility cloaking. Phase (top) and log-scale magnitude of the transmission (bottom) spectral profiles of the linear optical filter, used as the object to be concealed in the experimental demonstration of spectral invisibility cloaking. The measurements are performed with an optical vector analyzer with a frequency resolution of 200 MHz. In this representation, the transmission spectral response corresponds to the reciprocal of the object absorption as a function of frequency; this way, a transmission value of 0 dB indicates transparency, while a transmission value of -35 dB corresponds to 35 dB of optical power absorption. The object consists of a set of 11 resonances spaced 38 GHz apart, which sets the value of ν_c that is used for design in the reported transformations for spectral invisibility cloaking. Each resonance has a 3 dB bandwidth of 17.5 GHz. The peak absorption is measured to be approximately 35 dB. Each resonance introduces an additional phase shift of π rad.

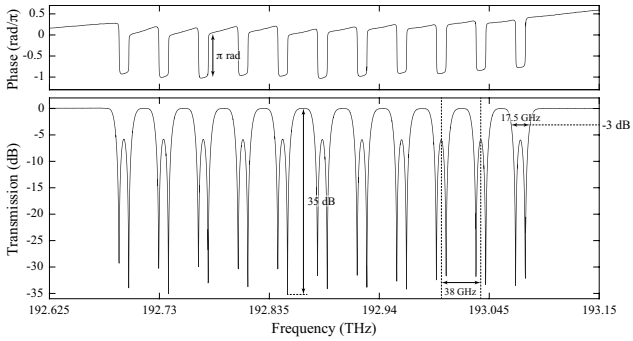

6.2.3.2 Experimental results

Fig. 6.15 shows a set of measured spectral traces of the waves involved in the spectral cloaking process, captured by an optical spectral analyzer with a frequency resolution of 2 GHz.

Figure 6.15 – Spectral invisibility cloaking, experimental results, frequency domain. Measured optical power spectra of the involved waves, normalized to the illumination peak spectral intensity, illustrating the implemented transformations for frequency gap generation and reversal. The transmission spectrum of the object to be concealed (full characterization in Fig. 6.14) is shown for reference. Measurement points, as marked in Fig. 6.12, are indicated. (a) Illumination spectrum (Fig. 6.12(a)). (b) Spectral amplitude signature of the object, detected on the illumination wave when the transformations are not applied (Fig. 6.12(d)). (c) Frequency gaps induced in the illumination wave when the transformations are applied (Fig. 6.12(b)). (d) Object spectral response inserted in the frequency gaps (Fig. 6.12(c)). (e) Effect of the spectral cloak on the output illumination spectrum in the absence of the object (Fig. 6.12(d)). (f) Measured output spectrum when the object is present and the cloak is on, showing successful prevention of wave-object interaction, and consequent concealment of the object (Fig. 6.12(d)). The residual ripples on the recovered spectrum are attributed to the fact that the object resonances are slightly wider than the generated frequency gaps.

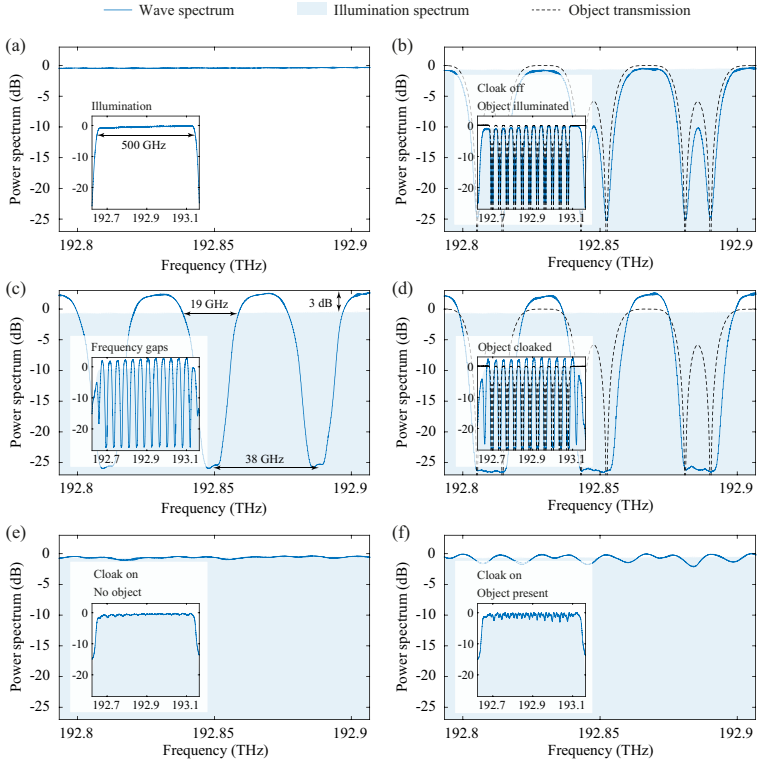

Fig. 6.15(a) shows the spectrum of the coherent broadband illumination wave. The spectral amplitude signature of the object is clearly observed in Fig. 6.15(b), when the phase modulators are not driven (cloak off). When the cloak is turned on, this configuration produces the expected set of frequency gaps in the illumination spectrum, with a 3 dB gap bandwidth of $\Delta\nu_g = 19$ GHz, and a spectral period of $\nu_c = 38$ GHz (Fig. 6.15(c)). Note that a 3 dB increase in the peak intensity (corresponding to a linear factor of $\sim$2) is observed in the frequency gap spectrum, in agreement with the expected conservation of energy, from the designed parameter r^{-1}.

The presence of the frequency gaps in the illumination spectrum allows the wave to propagate unaltered through the filter (Fig. 6.15(d)) without interacting with it. In this situation, an observer monitoring the output spectrum will detect the exact original illumination wave, as if the object was not present (Figs. 6.15(e) and (f)).

For completeness, Fig. 6.16 shows a higher resolution measurement of the spectrum of the illumination wave, before and after the generation of frequency gaps.

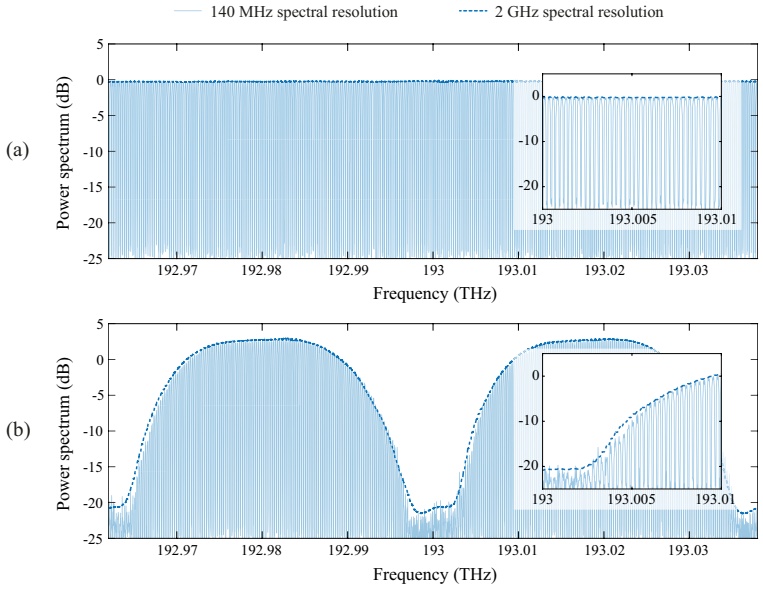

Figure 6.16 – Spectral invisibility cloaking, experimental results, frequency domain – detail. The solid line corresponds to a measured power spectrum with a frequency resolution of 140 MHz, the dashed line shows the same measurement with a frequency resolution of 2 GHz. (a) Detail of the illumination spectrum. (b) Detail of the spectrum of the frequency gaps. The illumination wave has a repetition rate of 250 MHz (observable in the high resolution measurements in the form of spectral lines with a 250 MHz frequency spacing). The designed spectral transformations introduce frequency gaps in the complex envelope of the spectrum, regardless of the pulse repetition rate. Note that, at 250 MHz, the illumination repetition rate clearly does not satisfy the designed Talbot condition in the shown example.

In order to demonstrate that the spectral cloak preserves the exact original incoming illumination wave, both in amplitude and phase, time-domain measurements of the propagating wave at the input and output of the cloak are performed (Fig. 6.17).

Fig. 6.17(a) shows the measured autocorrelation trace of the illumination pulse. This trace is compared to the expected autocorrelation, computed from the measured illumination spectrum, assuming a a constant spectral phase profile. The good agreement between both traces suggests that the illumunation pulse is Fourier transform-limited[4].

When the cloak is turned off, the measured output autocorrelation is significantly distorted, revealing the time-domain signature of the object (Fig. 6.17(b)). In contrast, the wave propagates without any observable distortion when the cloak is turned on, regardless of whether the object is present or not (Figs. 6.17(c) and (d)).

To quantify the similarity between the measured autocorrelation traces of the illumination and output waves, their cross-correlation coefficient, ρ, is calculated. The cross-correlation coefficient is a widely-

[4]A Fourier transform-limited pulse has both its temporal and spectral phase distributions linear, and thus, its temporal duration is the shortest possible, given its bandwidth.

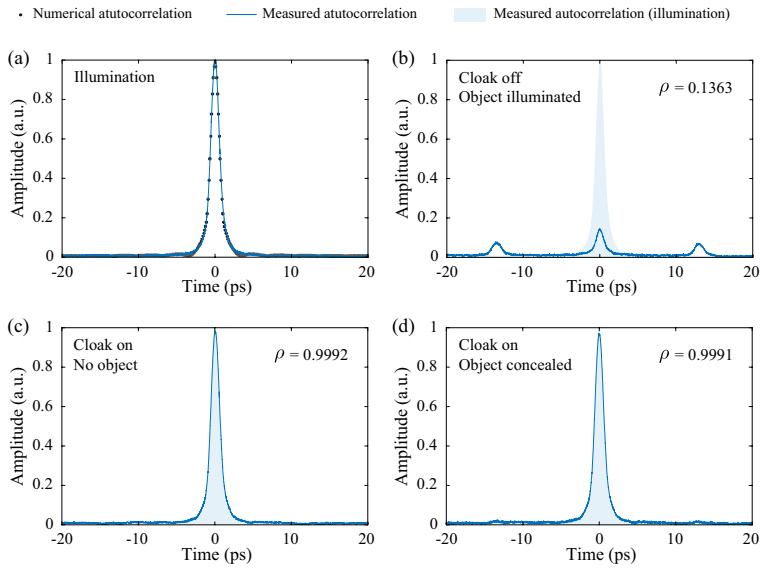

Figure 6.17 – Spectral invisibility cloaking, experimental results, temporal autocorrelation. Measured temporal autocorrelation traces of the involved waves. Measurement points, as marked in Fig. 6.12, are indicated. (a) Autocorrelation trace of the illumination wave (Fig. 6.12(a)), and numerical fit of the expected trace for a transform-limited pulse (i.e., with a constant spectral phase profile). (b) Temporal signature of the object when the cloak is turned off (Fig. 6.12(d)). (c) Autocorrelation trace of the wave at the output of the cloak without the target object (Fig. 6.12(d)). (d) Autocorrelation trace when the object is present and the cloak is on (Fig. 6.12(d)), showing a successful concealment of the object.

employed metric for quantitative comparison of real-valued signals. It corresponds to the zero-lag sample of the cross-correlation between two signals, normalized to the zero-lag sample of the autocorrelations of each signal. For two real-valued signals $\psi_1(t)$ and $\psi_2(t)$, the definition of the cross-correlation coefficient, ρ, is,

$$\rho = \frac{\displaystyle\int_{-\infty}^{\infty} \psi_1(\tau)\psi_2(\tau)\,\mathrm{d}\tau}{\sqrt{\displaystyle\int_{-\infty}^{\infty} |\psi_1(\tau)|^2\,\mathrm{d}\tau \int_{-\infty}^{\infty} |\psi_2(\tau)|^2\,\mathrm{d}\tau}} \tag{6.6}$$

This coefficient takes values between -1 and 1. Two real-valued signals satisfying $\psi_1(t) = \psi_2(t)$ yield a cross-correlation coefficient $\rho = 1$, while its value becomes -1 when $\psi_1(t) = -\psi_2(t)$. If the two signals are real-valued and positive, the cross-correlation coefficient is defined between 0 and 1. The closer this coefficient is to 0, the more dissimilar the signals $\psi_1(t)$ and $\psi_2(t)$ are. Similarly, the degree of similitude between the signals $\psi_1(t)$ and $\psi_2(t)$ is then higher the closer the value of ρ is to 1.

When the cloak is turned off and the object is illuminated, the similarity between the illumination and output pulses is found to be just over 13.6% ($\rho = 0.1363$ in Fig. 6.17(b)). The operation of the cloak conceals both the object's signature and the presence of the cloaking device itself, increasing the similarity between illumination and output pulses to a value higher than 99.9%, regardless of the presence of the object ($\rho = 0.9992$ and 0.9991 Figs. 6.17(c) and (d) respectively).

Additionally, an indirect reconstruction of the complex – amplitude and phase – temporal envelope of the illumination and output pulses is performed. This is achieved through spectral measurements, using a frequency-domain version of the phase reconstruction through optical ultrafast differentiation technique (PROUD) [137], referred to as S-PROUD (spectral phase reconstruction through optical ultrafast differentiation) [138]. The method reconstructs the complex temporal envelope (including both amplitude and phase profiles) of a signal under test (SUT), of the form,

$$\psi_{\mathrm{i}}(t) = |\psi_{\mathrm{i}}(t)|e^{i\triangleleft\psi_{\mathrm{i}}(t)} \tag{6.7}$$

where i is the imaginary unit and $|\psi_{\mathrm{i}}(t)|$ and $\lhd\psi_{\mathrm{i}}(t)$ are the temporal amplitude and phase profiles of the SUT, respectively.

This reconstruction requires the measurement of two power spectra: $|\Psi_{\mathrm{i}}(\omega)|^2$, the power spectrum of the SUT, (where $\omega = 2\pi\nu$ is the radial frequency variable, measured in rad), and $|\Psi_{\mathrm{o}}(\omega)|^2$, the power spectrum of the signal resulting from modulating the amplitude of $\psi_{\mathrm{i}}(t)$ with a linear monotonic function of time. Following the properties of the Fourier transform[5], the result of such a modulation translates into a differentiation of the spectrum of the SUT, $\Psi_{\mathrm{i}}(\omega)$. In the reported experiments, this spectral differentiation was achieved through electro-optical temporal amplitude modulation of the incoming optical waveform (SUT) in a Mach-Zehnder intensity modulator (MZM). The electronic modulation driving signal was a sinusoidal function, slowly-varying as compared to the temporal envelope of the SUT, where the required linear monotonic function was approximated by the rising slope of a single sinusoidal cycle. For this purpose, the MZM was biased at the quadrature point (i.e., in the linear operation region, half way between the maximum and minimum transmission points). The group delay distribution of $\Psi_{\mathrm{i}}(\omega)$ (the derivative of the phase of $\Psi_{\mathrm{i}}(\omega)$ with respect to radial frequency) can be numerically reconstructed by means of the following equation [138],

$$\frac{\mathrm{d}}{\mathrm{d}\omega}\lhd\Psi_{\mathrm{i}}(\omega) = \frac{1}{A\Omega}\left(1 - \frac{1}{|\Psi_{\mathrm{i}}(\omega)|}\sqrt{\frac{2}{T_0}|\Psi_{\mathrm{o}}(\omega)|^2 - \left(A\Omega\frac{\mathrm{d}}{\mathrm{d}\omega}|\Psi_{\mathrm{i}}(\omega)|\right)^2}\right) \tag{6.8}$$

where the parameters A, Ω and T_0 are associated to the temporal amplitude modulation process: A is the half amplitude of the RF tone referred to the half-wave voltage of the MZM, Ω is the frequency of the RF tone, and T_0 is the maximum throughput of the MZM. The values of these parameters in the reported experiment are: $A\Omega \simeq 7.8$ ns^{-1} and $T_0 \simeq 1$. Note that the derivative of $|\Psi_{\mathrm{i}}(\omega)|$ on the right-hand side of Eq. 6.8 is performed numerically on the measured input amplitude spectrum.

The spectral phase profile of the SUT, $\lhd\Psi_{\mathrm{i}}(\omega)$, is then obtained (except for an additive constant term) by numerical integration of the calculated group delay profile. The time-domain waveform of the SUT is finally reconstructed by simply calculating the inverse Fourier transform of the measured spectral amplitude, $|\Psi_{\mathrm{i}}(\omega)|$, with the numerically calculated spectral phase profile, $\lhd\Psi_{\mathrm{i}}(\omega)$, such that,

$$\Psi_{\mathrm{i}}(\omega) = |\Psi_{\mathrm{i}}(\omega)|e^{i\lhd\Psi_{\mathrm{i}}(\omega)} \tag{6.9}$$

Fig. 6.18 shows the reconstructed temporal amplitude and phase profiles of the illumination pulse and the pulse at the output of the cloaking device when the object is present and the cloak is operational. The output pulse shows a high similarity with the illumination pulse, quantified by a cross-correlation coefficient higher than 0.99 for the amplitude profile, and 0.95 for the phase profile, confirming that the complex temporal envelope of the illumination wave is entirely preserved.

6.2.4 Selective spectral cloaking

The proposed cloak design has the capability to continuously shift the positions of the frequency gaps without shifting the global envelope of the illumination spectrum, by simply delaying the temporal phase modulation profile. When the temporal delay equals one period of the phase modulation signal (52.6 ps in the reported experiment), the gaps are shifted to their original relative frequencies. The relationship between the fre-

[5]For details on the properties of the Fourier transform, consult Appendix A.

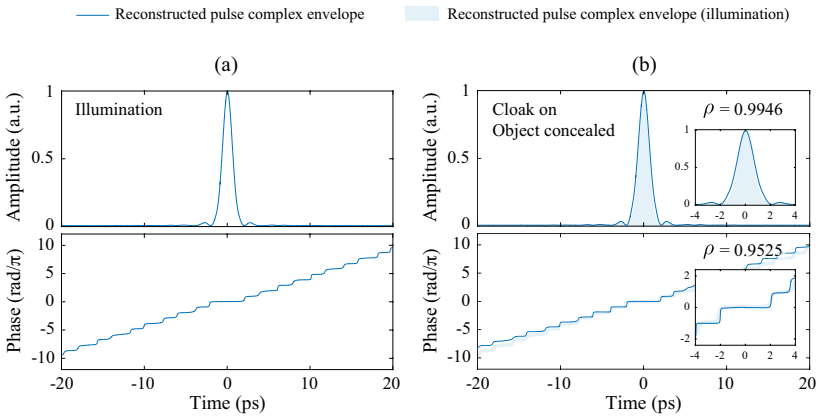

Figure 6.18 – Spectral invisibility cloaking, experimental results, temporal phase reconstruction. Indirect reconstruction of the complex (amplitude and phase) temporal envelope of the involved waves through the S-PROUD method. (a) Illumination pulse. (b) Pulse with the object present and the cloak turned on. The estimated full-width at half maximum temporal width of the pulse is of approximately 1.4 ps.

quency sift experienced by the gaps, $\delta\nu$, and the associated time delay of the phase modulation signal, δt, writes,

$$\frac{\delta\nu}{\delta t} = r^{-1}\nu_r^2 \tag{6.10}$$

Fig. 6.19 shows a set of 12 measured traces of the power spectrum of the illumination wave after the first section of the cloak. For each trace, the temporal phase modulation sequence was delayed, producing the expected continuous shift of the frequency gaps.

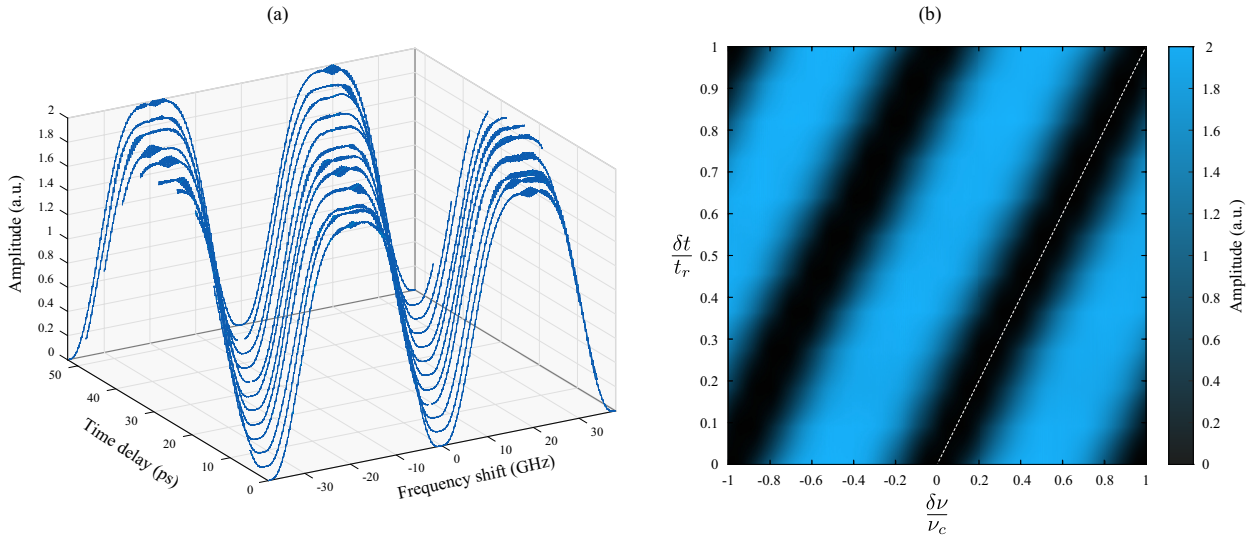

Figure 6.19 – Spectral invisibility cloaking, experimental results, continuous shift of the frequency gaps. (a) 12 measured spectra of the frequency gaps for different values of temporal delay of the phase modulation signal. (b) interpolation of the 12 measured spectra, showing the linearity of the observed frequency shift with the applied time delay. The dashed white line indicates the trend of Eq. 6.10.

This capability of shifting the frequency gaps grants a unique feature to the reported reversible wave-spectrum control method. One could selectively determine the specific frequency region(s) along which the wave-object interaction is permitted and/or avoided. For instance, this allows one to conceal only a part of the frequency spectrum of the object, deliberately leaving the rest detectable, by strategically selecting the positions of the frequency gaps. This could be understood as selecting a range of colors of a multicolor object to be cloaked, while allowing the rest of the object to remain visible. An experimental demonstration

example is reported in Fig. 6.20, showcasing the enhanced degree of flexibility offered by the proposed concept to selectively control the interaction between wave and object.

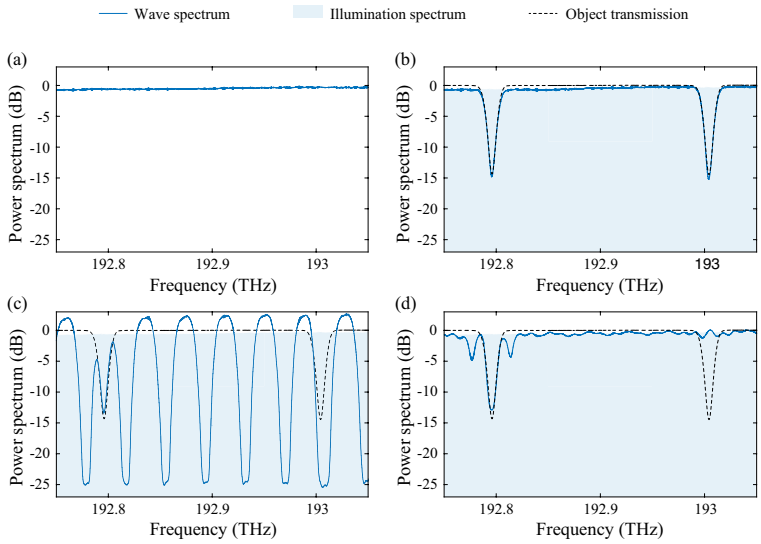

Figure 6.20 – Spectral invisibility cloaking, experimental results, selective cloaking. An object with several absorption bands (or equivalently, several objects with different absorption bands) can be selectively targeted by the cloak spectral transformations. (a) Measured spectrum of the illumination wave. (b) Measured transmission spectrum of the object (comprising a pair of stop bands) and signature on the illumination wave when the cloak transformations are not applied. (c) Measured wave spectrum at the output of the first phase modulator (Fig. 6.12(b)), showing the generation of frequency gaps. The cloak is designed so that one of the resonances of the object fits in a frequency gap, while the other one is located outside of the gaps. (d) Measured wave spectrum at the output of the cloaking device (Fig. 6.12(d)). The resonance located at a frequency gap is cloaked (wave-object interaction avoided), while the one located outside of the gaps is detected (wave-object interaction permitted).

6.2.5 Spectral cloaking with nonuniform spectra

The proposed energy-preserving wave spectrum manipulation method also performs the desired frequency gap generation operation for illumination waves with strong spectral amplitude and phase variations. Fig. 6.21 shows a numerical simulation example of frequency gap generation and reversal on an illumination wave with a nonuniform spectrum.

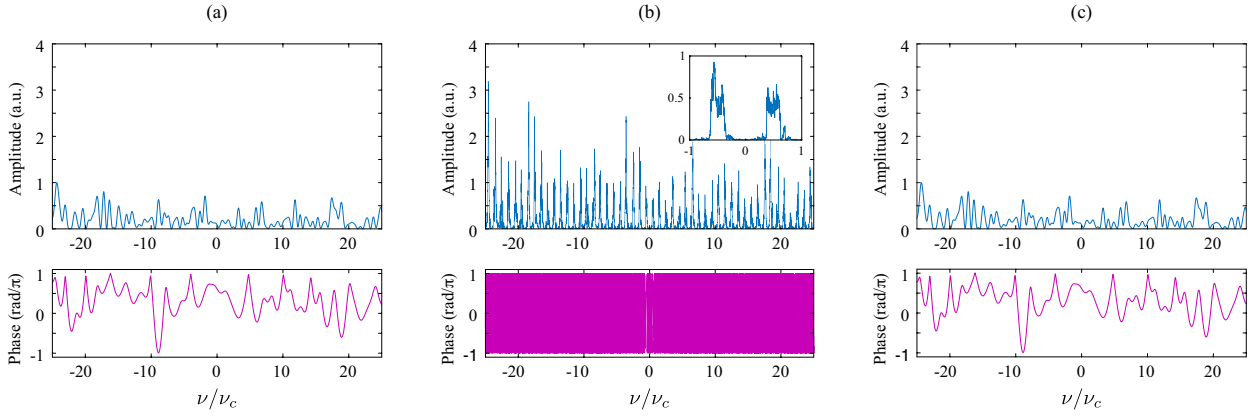

Figure 6.21 – Spectral invisibility cloaking, nonuniform illumination. Numerical simulations of the spectral transformations implementing the full-wave cloaking operation (shown example with $r^{-1} = 4$) with a nonuniform illumination spectrum. (a) Broadband illumination spectrum, presenting strong fluctuations in both amplitude and phase; (b) frequency gaps resulting from application of the spectral cloak transformations; (c) reconstruction of the original illumination wave after reversal of the applied transformations.

From a practical viewpoint, such spectral variations could actually be understood as the signature of other surrounding objects. Furthermore, since the proposed spectral cloak design has a symmetric architecture, the

cloaking process is bidirectional. These two features would allow to indistinctly exchange the positions of the source and the observers, potentially enabling an observer to see behind the cloaked object without distortion, and without detecting the cloaking device (see illustration in Fig. 6.22).

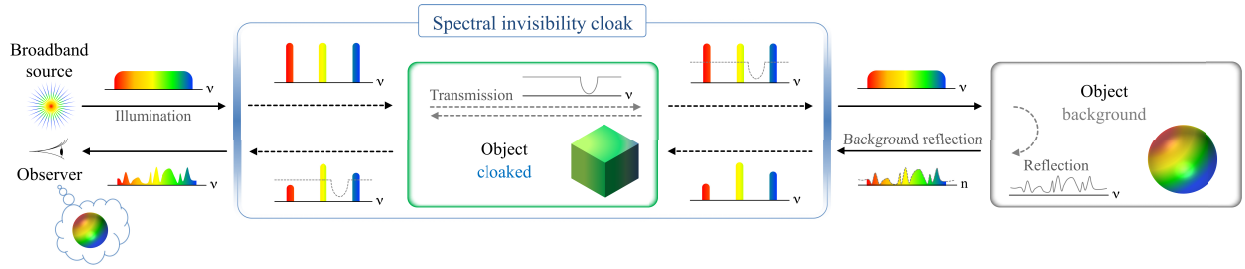

Figure 6.22 – Spectral invisibility cloaking, bidirectional operation. Conceptual illustration of the detection of a target located in the background of a cloaked object. This is enabled by the inherent symmetric architecture of the spectral cloak, combined with the capability of the energy redistribution transformations to successfully operate with nonuniform illumination spectra. In this case, the non-uniform spectral shape 'encodes' the reflection signature of the background target.

6.2.6 Additional comments and remarks

As aforementioned (see Section 6.1.3.1), the reported methodology for redistributing the spectrum of a broadband wave into a periodic set of frequency gaps could be conceptually understood as a frequency-domain realization of a temporal Talbot array illuminator (T-TAI) [115]. In a T-TAI, a CW beam is focused into a train of short (ideally rectangular) optical pulses following periodic phase modulation of the input CW and dispersive propagation of the modulated signal, where both the phase modulation profile and the dispersive length are prescribed by the PCTTM, with t_r being a free parameter. Such a concept has been previously exploited for temporal cloaking, namely to hide information in the temporal gaps that are created in between the output short pulses [136]. The reported frequency gap generation process could then be conceptually interpreted as a spectral TAI (S-TAI), in that it produces a train of rectangular spectral peaks with high extinction ratio from a broadband wave.

Nonetheless, it is important to note that from a mathematical viewpoint, there is a key difference between the implementations of the phase transformations involved in a T-TAI and those of the reported spectral cloak realization. For the formation of a T-TAI, a continuous-wave beam is first phase- modulated by a periodic Talbot phase sequence (i.e., a sequence of periodic phase steps satisfying the required Talbot condition), after which, the phase-modulated wave propagates through a certain GVD length, implementing a continuous quadratic phase filtering operation. In the reported spectral cloak implementation, the order of these operations is exchanged (GVD before PM), however, their definition remains identical, i.e., the first operation in the S-TAI (GVD) is still a continuous quadratic phase filter, while the second operation (PM) is a periodic step-like phase modulation. A direct duality between the realizations of a T-TAI and an S-TAI would involve a direct exchange of the time and frequency domains, so that the S-TAI would consist of a first periodic step-like phase filter followed by a continuous quadratic temporal phase modulation, as opposed to the method reported here. This shows that wave operations based on Talbot phase manipulations can be designed to affect the envelope of a coherent broadband wave, regardless of its repetition rate (as demonstrated in Fig. 6.16). Furthermore, from an implementation viewpoint, this finding implies that periodic or discrete spectral phase filters (potentially difficult to implement with good spectral resolution) are not an indispensable requisite for implementation of the proposed spectral cloaking approach, and that the approach could still be implemented using a continuous quadratic spectral phase, such as that provided by widely available

second-order dispersive media (also avoiding the need for precise alignment of the signal's spectrum to the filter).

6.3 Waveform-preserving spectral compression of modulated pulse sequences

In the previous section, it was shown how the spectral invisibility cloaking concept successfully generates frequency gaps in nonuniform spectra, effectively liberating frequency regions, originally occupied by the wave of interest. Such spectral variations could actually be the result of temporal modulation of the wave of interest, in such a way that the mentioned nonuniformity encodes the information of the modulation pattern. In this section, this result is used as a means to introduce frequency gaps to the spectra of data signals, consisting on sequences of modulated short pulses, effectively liberating originally occupied bandwidth. Owing to the properties of the Talbot effect, this operation results on the spectral compression of the signal, while the associated temporal pulses maintain their original shape, including their temporal duration. As discussed below, this feat could have important implications in ultra-wideband technologies, telecommunications and information processing systems.

6.3.1 The Fourier transform limit

By its own definition, the Fourier transform establishes a strict relationship between the temporal duration of a pulse and the extent of its frequency content. This relationship is ultimately dictated by the so-called uncertainty principle.

6.3.1.1 The time/frequency uncertainty principle

The uncertainty principle is a fundamental consequence of the Fourier transform [73]. In short, this principle states that the spreads of a function and its Fourier transform cannot be arbitrarily small simultaneously. Any pair of Fourier-conjugate variables entails an uncertainty principle. In its original application in quantum mechanics, Werner Heisenberg formulated the principle as the uncertainty relation of the position/momentum pair [139, 140]. Later, Dennis Gabor established a generalization in the time/frequency representation of waves by applying Heisenberg's mathematical apparatus to arbitrary signals [141, 142].

Considering the Fourier-conjugate pair of variables t and ω, representing time and radial frequency respectively, if most of the energy of a wave, represented by a complex function $\psi(t)$, is concentrated over a given time period, the energy of its Fourier-domain representation, $\Psi(\omega)$, must have a minimum spread in frequency, related to the temporal spread by a scaling factor. In particular, taking $|\psi(t)|^2$ and $|\Psi(\omega)|^2$ as probability distributions[6], with standard deviations σ_t and σ_ω, respectively, so that,

[6]Note that this implies absolute square normalization, so that,

$$\int_{-\infty}^{\infty} |\psi(\tau)|^2 \, \mathrm{d}\tau = \frac{1}{2\pi} \int_{-\infty}^{\infty} |\Psi(\Omega)|^2 \, \mathrm{d}\Omega = 1$$

where the Parseval's theorem was used (for further details, consult Appendix A).

$$\sigma_t^2 := \int_{-\infty}^{\infty} \tau^2 |\psi(\tau)|^2 \, \mathrm{d}\tau \tag{6.11}$$

$$\sigma_\omega^2 := \int_{-\infty}^{\infty} \Omega^2 |\psi(\Omega)|^2 \, \mathrm{d}\Omega \tag{6.12}$$

the time/frequency uncertainty principle writes,

$$\sigma_t \sigma_\omega \geq \frac{1}{4\pi} \tag{6.13}$$

where the equality is achieved when $\psi(t)$ is a Gaussian function.

6.3.1.2 Time-bandwidth product of pulsed waveforms

In the context of pulsed signals, the uncertainty principle determines the minimum bandwidth (range of frequencies), $\Delta\nu$ (measured in Hz), necessary to build up a pulse of a certain duration, Δt (measured in s); or equivalently, the minimum duration a pulse can achieve given a certain available bandwidth.

Consider an arbitrary pulsed waveform, $\psi(t)$, and its linear frequency spectrum, $\Psi(\nu)$. If Δt is defined as the FWHM duration of $|\psi(t)|^2$, and $\Delta\nu$ as the 3 dB bandwidth of $|\Psi(\nu)|^2$, the product $\Delta t \Delta\nu$ is known as the time-bandwidth product (TBP), and it satisfies the uncertainty relation,

$$\Delta t \Delta\nu \geq C \tag{6.14}$$

where C is a constant that depends on the complex envelope of the pulse, $\psi(t)$. For instance, taking a pulse with an instantaneous power profile defined by a Gaussian function of time, $C = \pi^{-1} 2 \log(2) \simeq 0.441$ [75].

6.3.1.3 Transform-limited pulses

When Eq. 6.14 is satisfied with strict equality, $\psi(t)$ is said to be a bandwidth-limited, Fourier-transform-limited, or simply transform-limited pulse. Transform-limited pulses have the minimum possible duration for a given available bandwidth Fig. 6.23(a) shows a sketch of the temporal and spectral power and phase distributions of a transform-limited pulse.

In general, both the temporal and spectral phase distributions of a transform-limited pulse are linear functions of time and frequency, respectively [74, 75]. Linear phase transformations can be applied to a pulse to extend its temporal duration without altering the composition of its frequency spectrum, e.g., in the form of group velocity dispersion in a transparent optical propagation medium [75]. Similarly, the spectrum of a pulse can be broadened without affecting its temporal duration, through nonlinear or linear time-variant phase transformations, e.g., such as those induced by Kerr nonlinearity in optical media [75]. In both situations, the uncertainty relationship is satisfied with strict inequality (see Fig. 6.23(b)). This is due to the fact that variations of the temporal and spectral phases of the pulse remain uncompensated for after the corresponding transformation has taken place. If such phase variations are flattened, a pulse can be temporally compressed, but at the expense of broadening its frequency spectrum [75]. Similarly, one can compress the spectrum of a pulse at the expense of increasing its temporal duration [143]. The obtained pulses in both cases are then transform-limited, and the uncertainty relation holds with strict equality (see

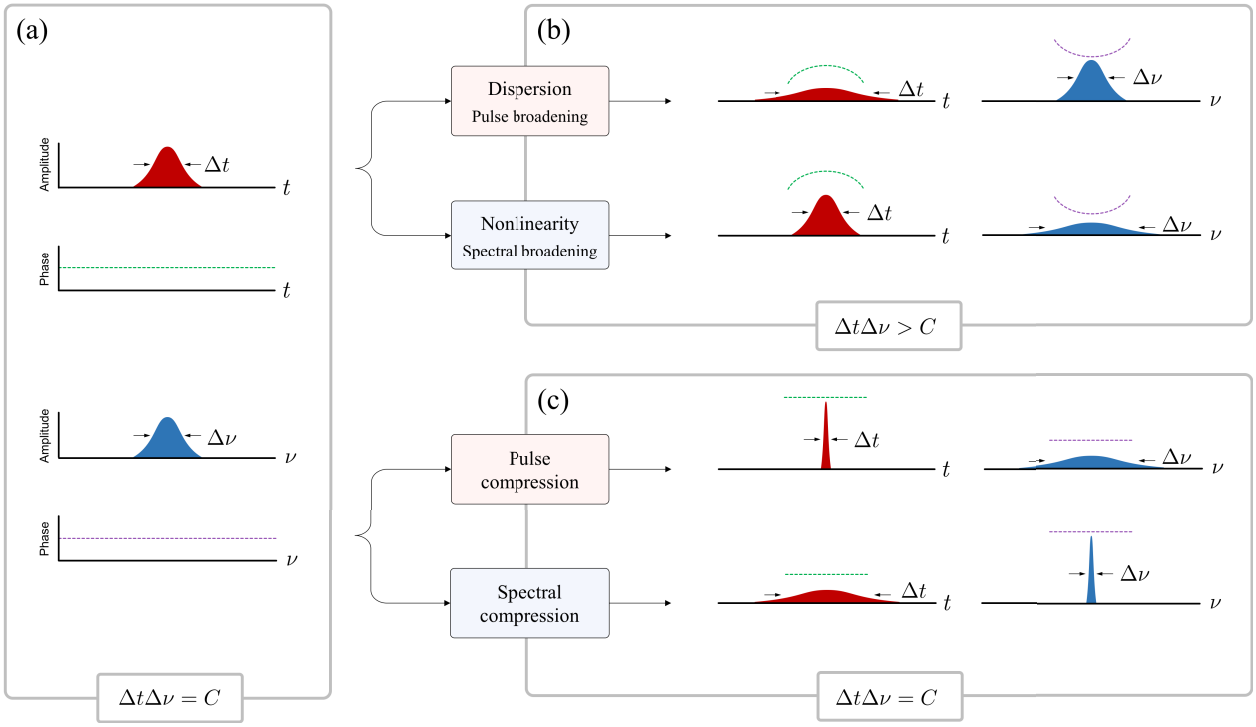

Figure 6.23 – Fourier uncertainty relations in temporal/spectral compression mechanisms. Formulation of the time/frequency uncertainty principle of the Fourier transform in different scenarios. (a) Amplitude and phase of a transform-limited pulse (top) and its spectrum (bottom). (b) Propagation through a linear dispersive medium, resulting on the temporal stretching of the pulse while its spectrum remains unaltered (top); the process corresponds to a quadratic transformation of the spectral phase distribution of the pulse. Propagation through a nonlinear medium, resulting on the spectral broadening of the pulse, while its temporal shape remains unaltered (bottom); the process corresponds to a quadratic transformation of the temporal phase distribution of the pulse. In both cases the obtained pulses are not transform-limited. (c) Pulse compression (top), and spectral compression (bottom), produced by combinations of temporal and spectral phase manipulations. The obtained pulses are transform-limited.

Fig. 6.23(c)). It is not possible, however, to compress a pulse or its frequency spectrum below the limit set by the uncertainty principle. This leads to critical design constraints in applications that involve the use of pulsed waveforms, such as for processing and communication of data signals.

6.3.2 Advantages and disadvantages of short pulses for practical applications

Data-modulated pulse sequences (e.g., as used in telecommunication and information processing systems) are fundamental for processing, storage and transmission of information [14]. In general, a data signal can be interpreted as a sequence of periodic pulses that are consecutively modulated to carry the desired arbitrary (e.g., random) complex data pattern, symbol to symbol (i.e., pulse to pulse). The duration of the coded pulses cannot exceed the inter-symbol temporal period, i.e., the inverse of the symbol rate[7]. In the frequency domain, such an arbitrary-modulated pulse sequence exhibits a continuous frequency spectrum along the full bandwidth of the individual pulses [14, 74]. The amount of information that can be transmitted or processed per time period over the available bandwidth (i.e., the spectral efficiency) is ultimately limited by the extent

[7] A data pulse sequence follows a nonreturn-to-zero (NRZ) coding format when temporal duration of the pulses is fixed to coincide with the inter-symbol period, so that there are no guard times between consecutive symbols. When the pulse duration is shorter than the inter-symbol period, the sequence follows a return-to-zero (RZ) coding format, leaving guard times between consecutive symbols.

of the data signal frequency spectrum, so that a narrower data signal spectrum translates into an increased spectral efficiency (for a prescribed number of bits per symbol, and a symbol rate).

Particularly, the use of short pulses – in the form of return-to-zero (RZ) modulation formats – provides critical advantages, including lower power consumption, higher net data rates and simpler synchronization operations, among others [14, 144–146]. In the particular case of optical communication and information processing systems, short-pulse data signals offer higher tolerance to noise, nonlinear effects and polarization-mode dispersion, all of them critical impairments in present high-capacity fiber-optics communication links [147–149]. Indeed, fear of the so-called *capacity crunch* of fiber-optics communications, where the mentioned propagation impairments compromise the available channel capacity, is fueling the development of new technologies and strategies that can help fulfilling the increasing demand of data transmission [147–154].

Optical coding and modulation formats based on short pulses have also been demonstrated to provide important performance improvements in free-space communication systems under adverse atmospheric conditions [155]. Power-constrained optical communication systems, deep space communications and transmission through turbulent media also favor the use of short pulses, typically in the form of pulse-position modulation schemes [156].

Sequences of data-modulated short pulses are then favored by time-division multiplexing (TDM) methods to aggregate information (e.g., optical TDM, OTDM, in the context of fiber-optics telecommunication systems). On the other hand, as previously discussed, a shorter temporal pulse needs a broader spectral bandwidth, resulting in a reduced spectral efficiency, as compared to nonreturn-to-zero (NRZ) data sequences, which require a lower bandwidth than RZ sequences for a given data rate. As a result, NRZ signals are preferred by frequency-division multiplexing (FDM) strategies (e.g., optical wavelength-division multiplexing, WDM, in the context of fiber-optics telecommunication systems), which are, in general, easier to implement and operate than their TDM counterparts [14, 18, 157]. This is because, in principle, the time/frequency uncertainty relationship prevents the spectrum of a modulated data pulse sequence to be arbitrarily compressed without increasing the temporal duration of its pulses.

6.3.3 Reversible spectral compression of pulsed data sequences by energy redistribution

The spectral energy redistribution concepts studied in this chapter can be exploited to compress the spectrum of a sequence of arbitrary (e.g., random) data-modulated short pulses, without altering the temporal shape – including the temporal duration – of its constituent pulses.

This section provides a simple linear processing scheme for waveform-preserving spectral compression of short pulse data signals, based on the PCSTM. Owing to the phase-only nature of the involved signal operations (GVD and PM), the process is fully reversible, in such a way that the original signal can be subsequently recovered without any loss of information, (including full recovery of the exact original pulsed data waveform). Fig. 6.24 illustrates the concept.

The proposed waveform-preserving spectral compression process is similar to the spectral invisibility cloaking concept, explained in Section 6.2, with the particularity that the pulse rate of the input signal, in this case, satisfies the designed Talbot condition, as in the original formulation of the PCSTM, applied to frequency combs (see Chapter. 5). In this situation, the temporal aperiodicity introduced by the modulation sequence – data – produces a continuous spectrum where frequency gaps can be generated, following a methodology identical to that introduced in Section 6.2.2.1 for implementation of spectral invisibility cloaking. Also, similarly to the spectral cloak implementation, reversal of the PCSTM transformations fully restores the original input signal. Fig. 6.25 illustrates the process.

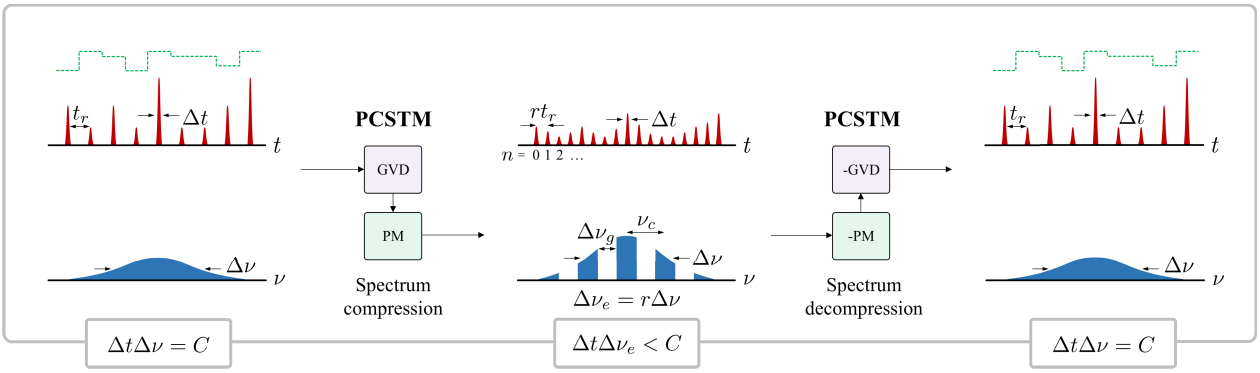

Figure 6.24 – Waveform-preserving spectral compression of modulated pulse sequences. Illustration of the proposed concept to overcome the spectrum spread constraint of an arbitrary data-modulated pulse sequence through application of the reversible phase-only linear transformations of the PCSTM (GVD: second-order group-velocity dispersion; PM: quadratic temporal phase modulation). Such phase transformations act on the entire pulse sequence, rather than on individual pulses. The result is the desired compression of the total occupied bandwidth, while maintaining the original individual pulse shape: the overall spectral width remains unchanged, but periodic frequency gaps are introduced in the spectrum, reducing the effective occupied bandwidth. The original data signal waveform can be fully recovered by application of the inverted linear phase transformations (-GVD, -PM).

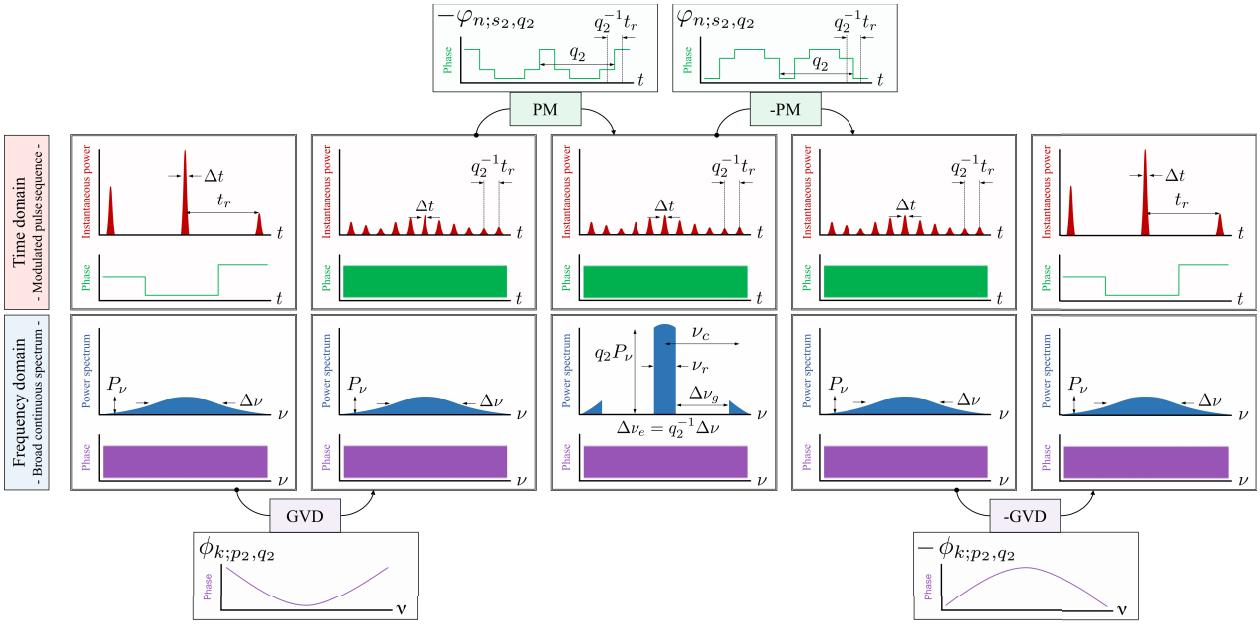

Figure 6.25 – Spectral compression of pulsed data signals by PCSTM, operation principle. Summary of the steps involved in the process of waveform-preserving spectral compression of modulated pulse sequences, based on the phase-only manipulations of the PCSTM (temporal phase modulation, PM, and group-velocity dispersion, GVD, respectively, see Section 3.2.3.2.), with $r^{-1} = q_2$ (integer).

Such an energy-preserving method for spectral compression of data signals could find immediate application for multiplexing signals in the frequency domain, while still maintaining short temporal pulses, thus combining the spectral efficiency and convenient operation of FDM systems with the performance, versatility and robustness advantages of short-pulse data transmission. Additionally, applications such as optical label switching [158], and radio-over-fiber communications [159], that require data sequences to be multiplexed within the bandwidth of broadband pulsed signals, necessarily introducing undesired distortions in these signals (e.g., associated with the need to filter out part of the signal spectrum), could immediately benefit from the proposed spectral compression technique. The proposed method could be used to generate the needed

spectral gaps to accommodate the additional data without affecting the original optical waveforms. Finally, ultra-wideband radar and telecommunication technologies, using coded short pulses, could also benefit from multiplexing techniques based on the reported spectral compression method, allowing to exploit simultaneously several data pulse sequences without interfering with neighbouring frequency bands [160, 161].

6.3.3.1 Operation principle

The case under consideration here is that of a data-modulated sequence of pulses with duration Δt, obtained by temporal modulation an originally periodic pulse train in amplitude and/or phase, pulse-to-pulse, following an arbitrary data pattern. The symbol rate, ν_r, is defined by the pulse period of the sequence, $t_r = \nu_r^{-1}$. In the frequency domain, following such a modulation process, the resulting data sequence exhibits a continuous energy spectrum along the full frequency bandwidth, $\Delta\nu$, of the short pulses in the sequence. Assuming transform-limited pulses, the relationship between the temporal pulse duration and the frequency bandwidth writes $\Delta t \Delta\nu = C$, for some constant C depending of the temporal envelope of the pulses.

The spectral compression process consists on the application of the spectral and temporal phase transformations defined by the PCSTM (identical to the ones given in Eqs. 6.2 and 6.3[8]) to the input modulated pulse sequence. Fist, a spectral phase shift $\phi_{k;p_2,q_2}$ (general expression in Eq. 3.48) is applied to the k-th comb line. In the reported experiments, the value $p_2 = 1$ is chosen to minimize the total required amount of GVD, however, any integer value can be designed, as long as p_2 and q_2 are mutually prime. This way, the applied phase sequence writes,

$$\phi_{k;1,q_2} = \varsigma\pi\frac{1}{q_2}k^2 \tag{6.15}$$

As per Eq. 3.50, the required amount of GVD,

$$2\pi|\beta_2|z = \frac{1}{q_2\nu_r^2} \tag{6.16}$$

The obtained signal is a pulse train with repetition period $q_2^{-1}t_r$, where the individual pulses maintain their original temporal profile, including the pulsewidth Δt.

Next, a temporal phase shift $-\varphi_{n;s_2,q_2}$ (general expression in Eq. 3.52, where s_2 is obtained from Eq. 3.27, for the given values of q_2 and p_2) is applied to the n-th pulse of the resulting train through a temporal phase modulation process (PM). In the reported experiments, $s_2 = q_2 - 1$, so that,

$$-\varphi_{n;q_2-1,q_2} = \varsigma\pi\frac{q_2-1}{q_2}n^2 \tag{6.17}$$

As in the spectral invisibility cloaking method, a periodic set of frequency gaps is generated across the signal's continuous frequency spectrum, with a spectral period ν_c, and gap bandwidth $\Delta\nu_g$, given by,

[8]Note that, in this case, t_r is no longer an arbitrary constant, but rather it is fixed by the symbol rate of the signal of interest, similarly to the original formulation of the PCSTM for frequency combs.

$$\nu_c = r^{-1}\nu_r \tag{6.18}$$
$$\Delta\nu_g = (r^{-1}-1)\nu_r \tag{6.19}$$

This produces a compression of the overall frequency range that is occupied by the modulated pulse sequence, reducing the effective bandwidth of the sequence to,

$$\Delta\nu_e = r\Delta\nu \tag{6.20}$$

while the spectral envelope maintains its original shape and width, $\Delta\nu$.

As a result, the effective TBP of the output sequence is reduced with respect to the input, and specifically, the uncertainty relation for the effective occupied bandwidth writes,

$$\Delta t\Delta\nu_e = rC \tag{6.21}$$

Finally, application of the opposite phase transformations (-PM and -GVD) restores the data pulse sequence to its exact original state in both the time and frequency domains.

6.3.4 Experimental demonstration

The proposed technique for waveform-preserving spectral compression is demonstrated on a typical optical RZ pulsed data signal for fiber-optics telecommunications. It should be noted, however, that due to the nature of the signal transformations involved in the process, practical implementations could, in principle, be designed for other regions of the electromagnetic spectrum (e.g., for radio communications, microwave links, etc).

6.3.4.1 Experimental setup

Fig. 6.26 shows a simplified[9] schematic of the experimental setup used to validate the waveform-preserving spectral compression concept.

A mode-locked laser generates optical pulses at a repetition rate of $\nu_r = 9.45$ GHz (corresponding pulse repetition period $t_r = 105.82$ ps), at a central frequency of 193.4 THz (corresponding to a central wavelength of 1551.2 nm). These pulses have a temporal FWHM of $\Delta t = 2.58$ ps. The associated spectrum is a frequency comb with FSR ν_r, and a 3 dB spectral width $\Delta\nu = 126.2$ GHz. The estimated TBP is $\sim$0.326, close to the expected value of $C \simeq 0.315$ for transform-limited sech^2 pulses.

An electro-optical Mach-Zehnder modulator is used to introduce a $2^7 - 1$ pseudo-random binary (`0/1`) sequence (PRBS)[10], generated by a 12 Gb/s bit pattern generator, to the pulse train, through direct amplitude modulation of the incoming optical pulses, generating an RZ data signal.

[9] For a complete schematic of the setup, see Fig. D.4.

[10] A 2^N-1 pseudo-random binary sequence is a deterministic succession of 2^N-1 bits ($N \in \mathbb{N}$) where the value of each element is independent of any other element in the sequence. This way, a PRBS emulates a fully random bit sequence over 2^N-1 consecutive bits. These sequences are commonly used as test probes for communication, computing and signal processing equipment.

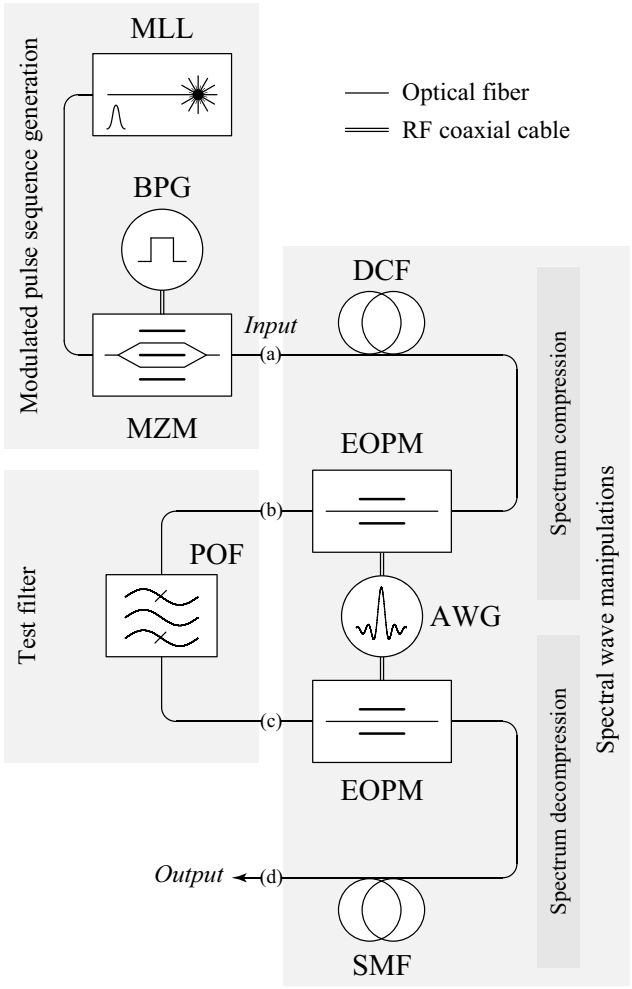

Figure 6.26 – Waveform-preserving spectral compression, experimental setup. MLL, mode-locked laser; BPG, bit pattern generator; MZM, Mach-Zehnder modulator; DCF, dispersion-compensating fiber; EOPM, electro-optical phase modulator; AWG, arbitrary waveform generator; POF, programmable optical filter; SMF, single-mode fiber. For a complete schematic of the experimental setup, see Fig. D.3.

The input dispersive medium of the spectral compressor is a length of dispersion-compensating fiber, providing a total second-order dispersion of -349.5 ps/nm at the working wavelength. This corresponds to a value of $\beta_2 z = 446.5$ ps^2/rad, satisfying the required temporal Talbot condition for the designed values of ν_r GHz and $r^{-1} = 4$ (see Eq. 6.16). At the working wavelength, this corresponds to the opposite dispersion of approximately 20 km of standard single mode fiber, which is used as the output dispersion of the spectral decompressor.

Two 40 GHz electro-optical phase modulators are used to introduce the required temporal Talbot phases to the dispersed optical signals. A 50 Gsa/s arbitrary waveform generator with 14 GHz analog bandwidth generates a voltage signal with the required temporal profile, shown in Fig. 6.27.

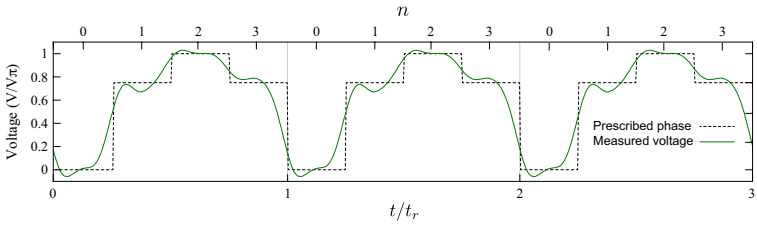

Figure 6.27 – Phase modulation function for waveform-preserving spectral compression. Periodic temporal Talbot phase profile associated to a Talbot condition with $r^{-1} = 4$. V_π represents the half-wave voltage of the electro-optical phase modulator. (dashed line) Prescribed phase obtained from the theory of Talbot effect. (solid line) Measured phase modulator drive voltage used in the experiments.

A programmable optical filter is used to verify that the generated frequency gaps contain no significant amount of energy.

6.3.4.2 Experimental results

This section contains the results of an experimental demonstration of the described waveform-preserving spectral compression concept. The concept is first validated on the RZ signal described above, analyzing both its temporal and spectral properties. Then, a second experiment (supported by numerical simulation) showcases an application scenario where a narrow-band NRZ signal is multiplexed in frequency, alongside the spectrally-compressed RZ signal. This NRZ signal is inserted into one of the frequency gaps generated on the RZ spectrum, in such a way that no additional bandwidth is occupied int he multiplexing process.

Waveform-preserving spectral compression

Fig. 6.28 compiles the results of an experiment where the waveform-preserving spectral compression concept is validated.

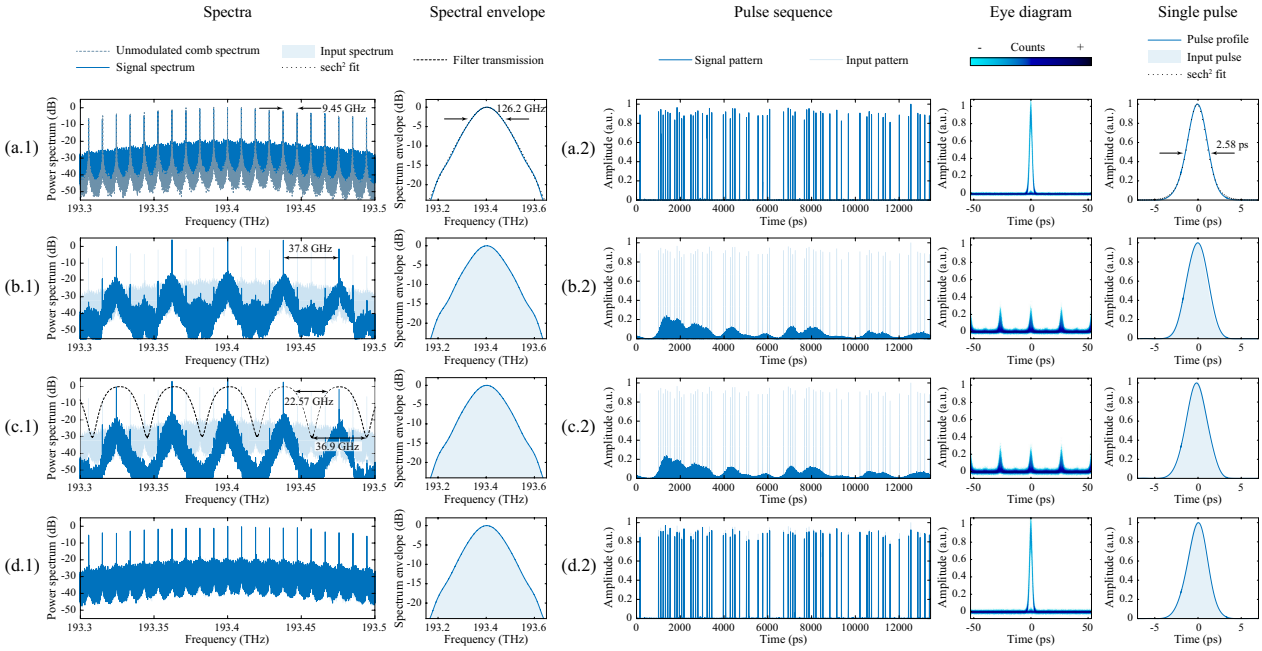

Figure 6.28 – Waveform-preserving spectral compression, experimental results. Generation of frequency gaps in a sequence of short optical pulses with binary (on-off-keying, OOK) intensity modulation. Measurement points, as marked in Fig. 6.26, are indicated. (a.1) Spectrum of the original sequence, obtained by direct amplitude modulation of a repetitive optical pulse train or periodic optical frequency comb (shown for reference) with a binary $2^7 - 1$ PRBS (Fig. 6.26(a)). (a.2) Temporal profile, eye diagram and detail of a single pulse of the original sequence (Fig. 6.26(a)). (b.1) Spectrum and, (b.2) temporal profile, eye diagram and single pulse detail of the sequence after application of the spectral compression process (Fig. 6.26(b)). The overall spectral envelope and temporal pulse shape – including duration – remain unaltered, while periodic frequency gaps are induced in the sequence. (c.1), (c.2) A periodic band-stop filter is introduced in the frequency gaps for testing purposes (Fig. 6.26(c)). Due to the energy redistribution mechanism giving rise to the frequency gaps, the temporal sequence is unaffected by the filter, a result that confirms that the created gaps contain no information. (d.1), (d.2) Output sequence after the application of the reverse phase transformations, closing the frequency gaps and reverting the modulated temporal data sequence to its exact original state (Fig. 6.26(c)).

Fig. 6.28(a.1) shows the spectra of the initial frequency comb and the modulated RZ data signal, as well as the envelope of its power spectrum. As expected, the modulated signal spectrum is a continuum over the full frequency bandwidth of the individual pulses, with discrete clock components at the frequencies of the original comb lines. The corresponding time-domain representation is shown in Fig. 6.28(a.2), including the modulated pulse train, its eye diagram[11], and a detail of a single pulse of the sequence. As expected, both the spectrum and the instantaneous power profile fit a transform-limited sech^2 pulse shape, in line with the estimated value of the TBP above.

Fig. 6.28(b.1) shows the spectrum resulting from the gap-generation process (i.e., after the GVD and PM operations). As expected, the achieved frequency gap period is $\nu_c = 37.8$ GHz, corresponding to the suppression of 3 out of each 4 clock components (original comb lines), consistent with the designed value of $r^{-1} = 4$. Fig. 6.28(b.2) shows that the original pulse sequence is spread out into a larger number of short pulses, with an equivalent pulse rate increased by 4 with respect to the input one (see eye diagram on Fig. 6.28(b.2)). As predicted, the newly obtained pulses retain the original time-width and overall temporal shape (see single pulse detail on Fig. 6.28(b.2)).

In order to confirm the spectral compression capability of the process, a linear optical test filter with a frequency response consisting of a set of stop bands with a spectral period $\nu_T = 36.9$ GHz (close in value to ν_c), overlapping with the generated frequency gaps (see measured spectra in Fig. 6.28(c.1)), is introduced. The 3-dB bandwidth of each of the stop bands is $\Delta\nu_T = 22.57$ GHz. Due to the presence of the frequency gaps, the signal propagates through the filter without interacting with it, and the temporal waveform remains entirely unaffected (see time-domain measurements in Fig. 6.28(c.2)). This demonstrates that the effective bandwidth of the modulated signal was compressed, at least, by a factor $\nu_T^{-1}\Delta\nu_T = 0.612$; in other words, over 60% of the frequency spectrum occupied by the input data signal was freed, while maintaining the original temporal shape of the pulses in the sequence. It should be noted that, ideally, for the designed value of $r^{-1} = 4$, the expected spectral compression should reach 75%; however, practical imperfections in the implementation of the phase modulation (limited by available electronic bandwidth) and dispersion (associated to small deviations of fiber length from the ideal) lead to an imperfect suppression of the signal energy in the frequency gaps, up to $\sim$20 dB in the reported experiments.

Finally, application of the opposite temporal phase modulation profile and propagation through an optical fiber with opposite GVD restores the data signal to its exact original state (including the original data modulation pattern), both in the frequency and time domains (see Figs. 6.28(d.1) and (d.2), respectively).

In-band frequency-division multiplexing of data-modulated signals

The reported process for spectral compression provides a simple method for increasing the spectral efficiency of short-pulse arbitrary data signals. As demonstrated by the results shown in Fig. 6.28, the generated frequency gaps contain no useful information for the reconstruction of the original data sequence. Such free spectral regions could be used by other signals in order to share a common transmission medium and resources, through frequency-domain multiplexing (FDM) [14, 18].

Indeed, the spectral compression process reported here significantly enhances the spectral efficiency of RZ pulse sequences by liberating occupied bandwidth. In this way, several RZ data sequences could be multiplexed in frequency without occupying additional bandwidth, a strategy that would enable to combine the performance, versatility and robustness advantages of short-pulse data transmission with the convenient op-

[11] The eye diagram of a digital data signal is a superposition of consecutive symbol intervals – periods – of the sequence, recorded over a sufficiently long period of time. This representation is a powerful tool for evaluation of the combined effects of noise and inter-symbolic interference, since it contains a combination of all possible realizations of the digital modulation sequence [14].

eration of FDM. This is possible because the specific locations of the created frequency bands can be shifted by simply delaying the Talbot temporal phase modulation pattern with respect to the incoming dispersed optical data signal. In particular, a temporal delay of the phase modulation sequence corresponding to rt_r, shifts the central frequencies of the gaps by ν_r, (note that a temporal delay of t_r corresponds to a spectral sift of the frequency gaps by ν_c, returning the gaps to their original positions).

A numerical example of frequency-division multiplexing and demultiplexing of two RZ optical pulse data sequences through the proposed method is shown Fig. 6.29. In this example, the simulated data sequences exhibit a 16-symbols quadrature amplitude modulation (16-QAM) scheme. This shows how the described signal transformations produce a similar frequency gap generation effect in the more general case of pulse sequences with multi-level complex (amplitude and phase) modulation formats, such as those typically used in coherent communication systems [14].

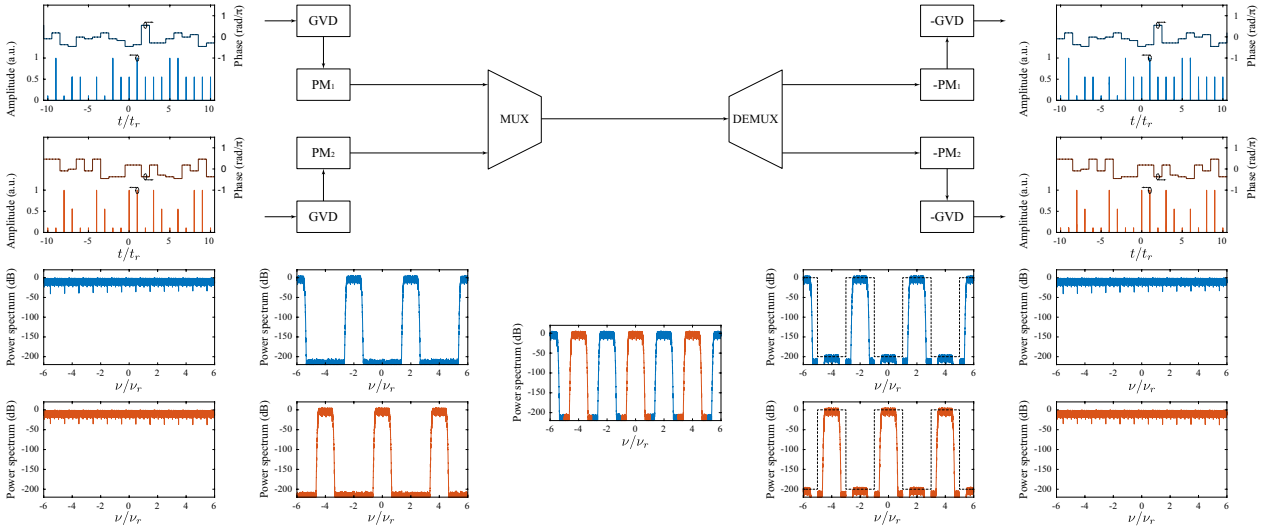

Figure 6.29 – In-band frequency-division multiplexing, numerical simulation. Two optical RZ pulse sequences are modulated in amplitude and phase following a 16-QAM scheme. Frequency gaps are introduced to the spectra of the two signals through the phase manipulations of the spectral compression method with $r^{-1} = 4$, so that they can be multiplexed in frequency without occupying additional bandwidth. The multiplexed signals are spectrally orthogonal (separable in frequency); this way, two periodic band-pass filters can be used to demultiplex them. Application of the reverse phase manipulations restore both signals to their original states.

In order to experimentally demonstrate this capability, a NRZ signal is inserted in one of the frequency gaps of the RZ signal in Fig. 6.28. Fig. 6.30 shows a simplified[12] schematic of the experimental setup used to validate the concept of in-band FDM through waveform-preserving spectral compression.

The NRZ signal to be inserted is obtained by direct binary amplitude modulation of a continuous wave laser at a bit rate equal to that of the RZ sequence, 9.45 Gb/s. Figs. 6.31(a) and (b) show the spectra of the RZ and NRZ signals, respectively. Figs. 6.32(a.1) and (b.1) show the the corresponding instantaneous power profiles and associated eye diagrams.

After the spectral compression process, the NRZ signal is inserted in-band, in one of the frequency gaps introduced to the RZ spectrum; this is possible because both signals are spectrally orthogonal (i.e., their spectra do not overlap when sharing the same transmission medium). This is illustrated in Fig. 6.31(c). The two signals are easily separable – demultiplexed – in the frequency domain using conventional selective amplitude filters, as shown in Fig. 6.31(d).

[12]For a complete schematic of the setup, see Fig. D.4.

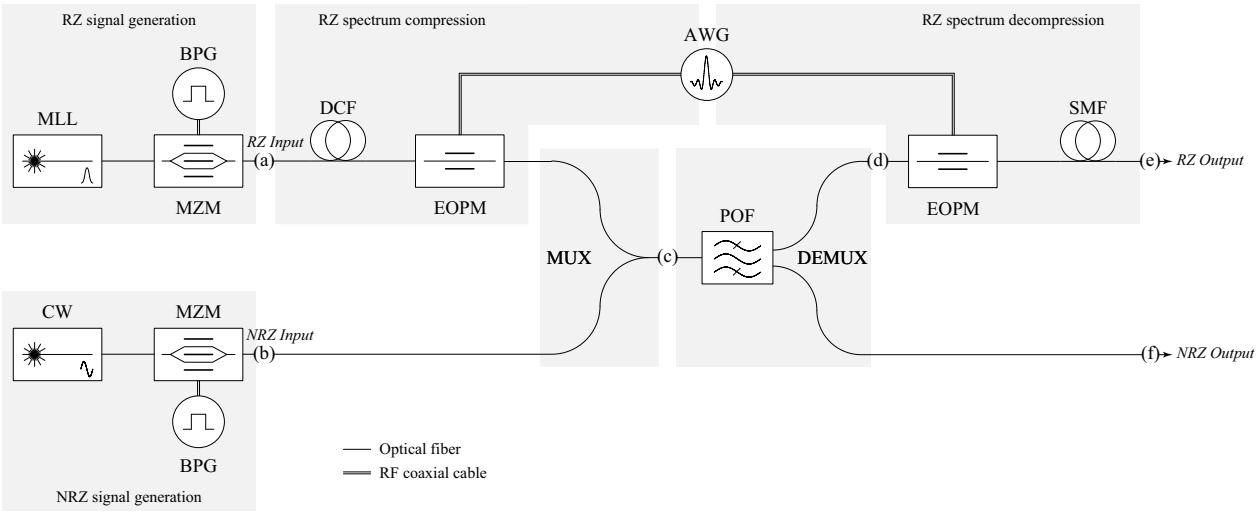

Figure 6.30 – In-band frequency-division multiplexing, experimental setup. MLL, mode-locked laser; CW, continuous-wave laser; BPG, bit pattern generator; MZM, Mach-Zehnder modulator; DCF, dispersion-compensating fiber; EOPM, electro-optical phase modulator; AWG, arbitrary waveform generator; POF, programmable optical filter; SMF, single-mode fiber. For a complete schematic of the experimental setup, see Fig. D.3.

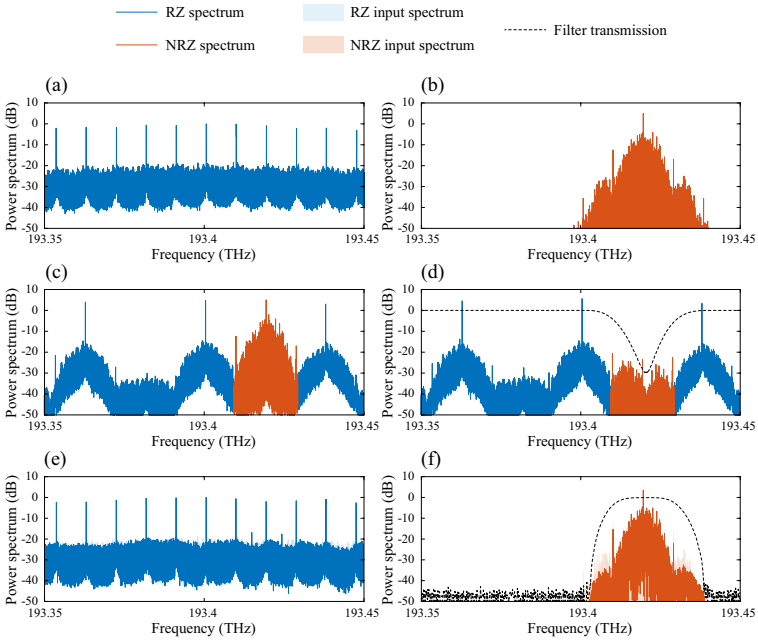

Figure 6.31 – In-band frequency-division multiplexing, experimental results, frequency domain. Frequency-division multiplexing/demultiplexing of a NRZ data signal within the bandwidth occupied by a RZ data signal, using the described process for frequency gap generation. Measurement points, as marked in Fig. 6.30, are indicated. (a) Spectrum of the RZ signal (Fig. 6.30(a)). (b) Spectrum of the NRZ signal (Fig. 6.30(b)). (c) Spectrum of the NRZ signal inserted in one of the frequency gaps induced in the RZ spectrum (Fig. 6.30(c)). (d) Extraction of the NRZ signal by use of an add/drop optical filter (Fig. 6.30(d)). (e) Output RZ spectrum after the frequency gaps are closed, after the extraction of the NRZ signal (Fig. 6.30(e)). (f) Output NRZ spectrum (Fig. 6.30(f)).

Subsequent application of the inverse phase manipulations (-PM and -GVD) decompresses the RZ signal and restores it to its original state, in both the frequency and time domains (see spectrum in Fig. 6.31(e), and instantaneous power and eye diagram in Fis. 6.32(a.2)). Fig. 6.31(f) shows the output NRZ spectrum, and Fig. 6.32(b.2) shows the corresponding instantaneous power distribution and eye diagram.

It should be noted that, since the NRZ format leaves no guard times between consecutive bits, multiplexing along the time domain (TDM) would not be possible for the two signals used here. The reported spectral compression process provides a way to perform FDM (referred to as WDM in optical communication systems) without additional bandwidth usage.

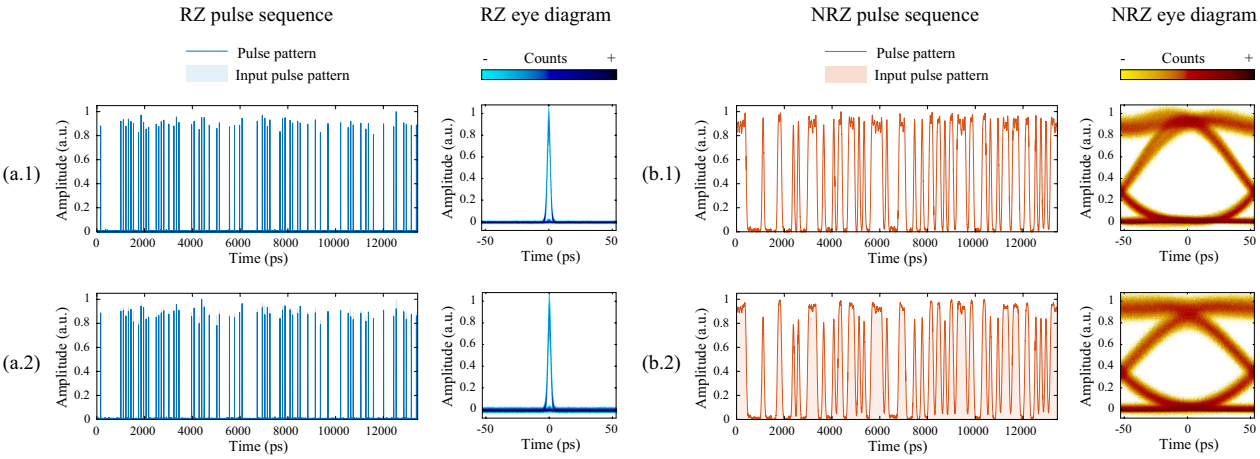

Figure 6.32 – In-band frequency-division multiplexing, experimental results, time domain. Frequency-division multiplexing/demultiplexing of a NRZ data signal within the bandwidth occupied by a RZ data signal, using the described process for frequency gap generation. Measurement points, as marked in Fig. 6.30, are indicated. Measured temporal sequence (instantaneous power trace) and eye diagrams of, (a.1) input RZ signal (Fig. 6.30(a)), (b.1) input NRZ signal (Fig. 6.30(b)), (a.2) output RZ signal (Fig. 6.30(e)), and (b.2) output NRZ signal (Fig. 6.30(f)).

In order to study the potential degradation of signal quality due to the spectral compression/decompression process and overall multiplexing/demultiplexing operation, two figures of merit are measured: the quality factor of the temporal eye diagram, Q, and the bit error rate (BER) [162].

The Q factor of the eye diagram is defined as a metric of the eye aperture,

$$Q = \frac{\mu_1 - \mu_0}{\sigma_1 + \sigma_0} \tag{6.22}$$

where μ_1 and μ_0 are the average optical power on the top and bottom levels respectively, and σ_1 and σ_0 are the standard deviations of the optical power around the sampling time.

The BER is the number of erroneous bits received per unit time, and it is measured by an error performance analyzer (EPA).

Both metrics can be used to quantify the degradation that a process under test (PUT, the spectral compression/decompression process in this case) introduces on a signal under test (SUT). Fig. 6.33 shows a simplified schematic of the BER measurement circuit.

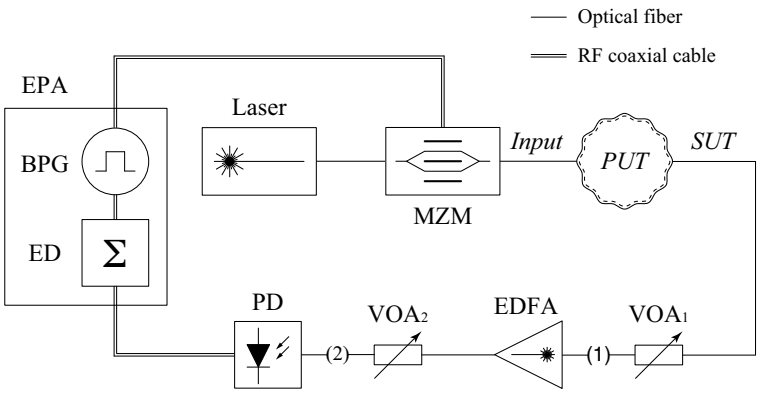

Figure 6.33 – BER measurement circuit. EPA, error performance analyzer; BPG, bit pattern generator; ED, error detector; MZM, Mach-Zehnder modulator; PUT, process under test; SUT, signal under test; VOA, variable optical attenuator; EDFA, erbium-doped fiber amplifier; PD, photodiode.

The SUT is obtained as a result of the PUT acting on the input signal. The SUT is photodetected and the EPA measures the BER by comparing the transmitted and received bits. This process is repeated for different values of average SUT power. The SUT power (optical power at point (1) in Fig. 6.33) is scanned by acting on a variable optical attenuator (VOA_1 in Fig. 6.33). An EDFA and a second VOA ensure that the received power (optical power at point (2) in Fig. 6.33) is always equal to 0 dBm. This way, measurements with lower SUT power correspond to higher values of amplified spontaneous emission noise from the EDFA. The measured average SUT power (with fixed 0 dBm received optical power at point (2) in Fig. 6.33) is then a metric for the optical signal-to-noise ratio of the measurement. In the back-to-back configuration (B2B), the PUT is not present, and the SUT (corresponding to the input signal in this case) is only affected by the BER measurement process itself. This serves as a point of comparison to study system performance.

The Q factor is calculated directly from eye diagram measurements, captured over intervals of 10 minutes, following an identical protocol to that of the BER measurement (i.e., for constant 0 dBm received signal power).

Figs 6.34(a) and (b) show the measured Q factor and BER, respectively.

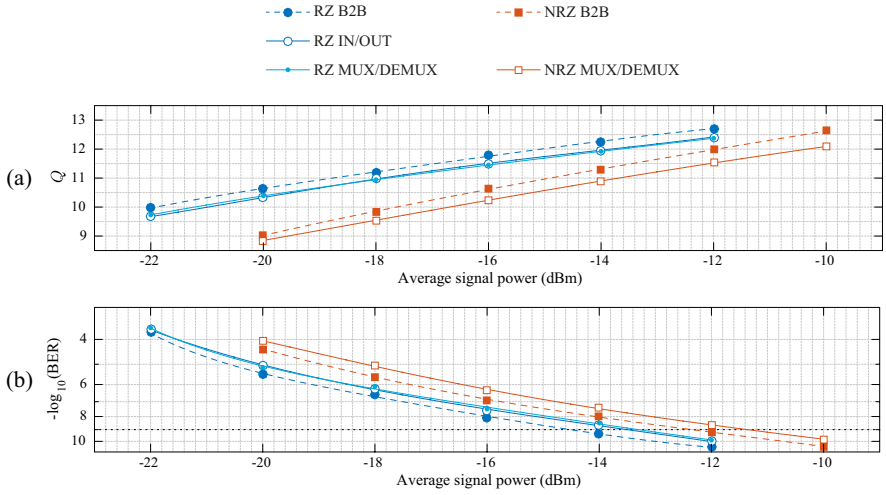

Figure 6.34 – In-band frequency-division multiplexing, experimental results, bit error rate analysis. Measured Q factor of the eye diagram (a), and BER (b), for different values of transmitted signal power. Studied scenarios: B2B, back-to-back configuration; IN/OUT, RZ signal compressed/decompressed in the absence of NRZ signal; MUX/DEMUX, NRZ signal inserted in a frequency gap induced on the RZ signal spectrum and subsequently extracted.

The B2B configuration corresponds to measurements on the RZ and NRZ input signals (before spectral compression). Fig 6.34 shows measurements of Q and BER on the RZ signal when it undergoes the spectral compression/decompression process without the NRZ signal inserted (IN/OUT configuration). When compared to the B2B configuration, the observed degradation is minimal; in particular, only 1 dB of additional optical power is required by the IN/OUT configuration to achieve the BER of the B2B configuration (power penalty measured at the standard error-free telecommunication threshold, BER$= 10^{-9}$). Finally, a scenario where the NRZ signal is inserted and extracted from the frequency gap generated in the RZ signal spectrum (MUX/DEMUX configuration) is analyzed. Interestingly, no degradation of the RZ signal is observed in this configuration with respect to the IN/OUT configuration (where no additional signal was multiplexed). This further demonstrates that no information is contained within the frequency gaps induced by the spectral compression process, as both signals are recovered without loss of information.

6.4 Robust RZ-to-NRZ modulation format conversion

This section presents and discusses a method for robust and energy-preserving conversion of return-to-zero data signals to nonreturn-to-zero data signals. The method is a direct application of the energy-preserving spectrum compression technique, proposed in Section 6.3.

6.4.1 Need for format conversion in telecommunication networks

The fast increase in the demand of transmission capacity in optical networks has led to envision hybrid network architectures where different coding formats and multiplexing strategies, e.g., optical time-division multiplexing and wavelength-division multiplexing, naturally co-exist [163, 164].

The requirement for high spectral efficiency in conventional frequency-division multiplexing networks calls for the use of a coding format that enables narrow-bandwidth operation, typically NRZ. On the other hand, the operation of a temporal multiplex (as in OTDM) requires the use of narrow return-to-zero pulses [14, 18]. It should be noted that while the spectral compression method described in Section 6.3 provides a way for enhancing the spectral efficiency of short-pulse data sequences, RZ-to-NRZ conversion methods are still necessary at the interfaces between current telecommunication networks exploiting different coding and modulation formats. Indeed, the conversion between RZ and NRZ coding formats have been the target of substantial research effort. Current approaches include the use of injection-locking methods [164, 165], Kerr-based nonlinear interactions in optical fibers [166], and linear optical amplitude filtering [167–170], the latter being particularly interesting for its linear and passive nature.

6.4.2 Shortcomings of current solutions for RZ-to-NRZ format conversion

The typical spectrum of a broadband RZ signal has a periodic clock component, repeating at the symbol rate. Data modulation produces an equal broadening of the clock components, causing them to overlap, giving rise to a broadband continuous spectrum. The most popular and straightforward technique for RZ-to-NRZ conversion based on optical filtering consists of two stages: first, a periodic notch filter – typically a multi-resonant photonic structure – is employed to suppress all spectral clock lines except for the central one; second, a band-pass filter is used to select a narrow band in around this central component, in order to produce a smooth temporal signal [168–170]. Fig. 6.35(a) schematically illustrates the process.

Such a technique is entirely based on linear signal processing operations, and thus, no external energy contribution is necessary. However, the design of the involved optical filters is critical. An efficient line suppressor requires multiple high-finesse, high-suppression resonances with a very well defined free spectral range, closely matching the symbol rate of the signal of interest. Such specifications may be challenging to achieve in practical designs. Additionally, this configuration requires a precise matching between the clock components of the RZ signal and the resonances of the line suppressor. Systems based on linear amplitude filtering solutions are sensitive to the expected frequency drifts of the RZ signal and resonant filters. Furthermore, a considerable amount of energy of the original RZ signal is discarded by the smoothing band-pass filter, potentially incurring in degradation of the signal-to-noise ratio, and consequent bit error rate increase.

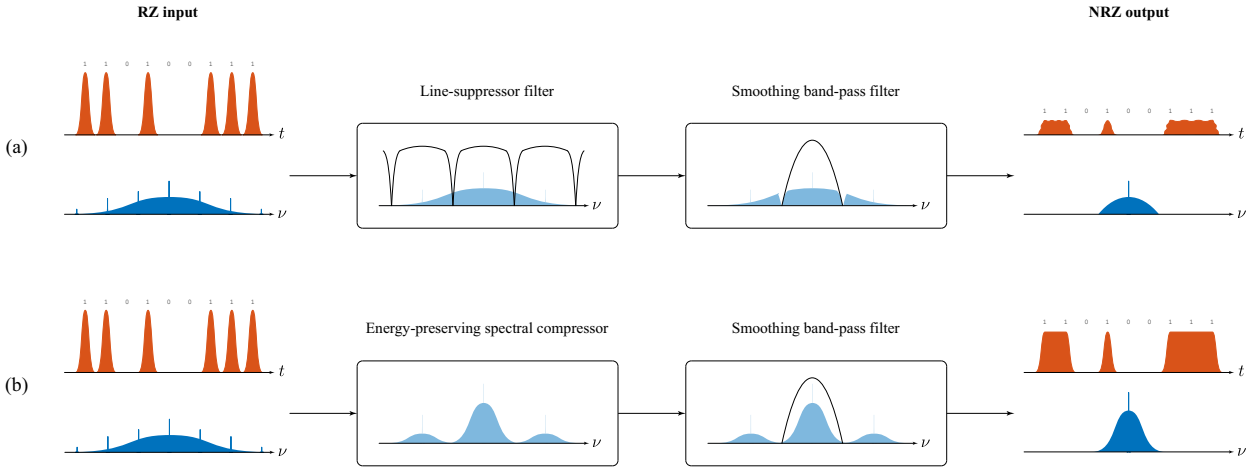

Figure 6.35 – Principle of RZ-to-NRZ format conversion. (a) Conventional format conversion method based on direct linear optical amplitude filtering. (b) Proposed format conversion method based on the PCSTM-assisted, energy-preserving spectral compression technique.

6.4.3 RZ-to-NRZ format conversion by energy redistribution

The energy-preserving spectrum compression technique, proposed in Section 6.3, provides a way of performing RZ-to-NRZ conversion in an energy-efficient fashion, while avoiding the need for a line suppressor filter altogether.

6.4.3.1 Operation principle

The energy of the RZ signal of interest can be distributed towards the central region of its spectrum through direct application of the PCSTM, exactly as used in Section 6.3. The required phase transformations (spectral phase filtering and temporal phase modulation) are the same ones described by Eqs. 6.16 and 6.17, for the particular configuration $q_2 = 2$.

Such spectral energy redistribution process generates frequency gaps on the spectrum of the RZ signal, effectively suppressing the unwanted clock components without the use of a resonant filtering structure. Subsequent processing of the obtained signal through a smoothing band-pass filter, similar to the ones used in the second step of conventional methods based on resonant line-suppressors, produces the desired NRZ signal. This completely avoids the need for tight spectral alignment and fine tuning that makes direct amplitude filtering methods sensitive to unavoidable frequency drifts. It should be noted that the smoothing band-pass filter still requires some degree of alignment to the spectrum of the optical signal, however, the effect of misalignment at this stage has a much lower impact on the quality of the obtained NRZ sequence, since the bandwidth of such a filter is of the order of magnitude of the output NRZ signal bandwidth. Moreover, since the spectral compression method simply redistributes the energy of the RZ signal towards the desired regions of its frequency spectrum, subsequent use of a smoothing band-pass filter discards a lower amount of energy, as compared to conventional methods. Fig. 6.35(b) schematically illustrates the process.

6.4.4 Experimental demonstration

The proposed robust RZ-to-NRZ format conversion method is demonstrated on a $\sim$10 Gb/s intensity-modulated pulsed data signal in the C-band of optical telecommunications.

6.4.4.1 Experimental setup

Fig. 6.36 shows a simplified[13] schematic of the experimental setup used to validate the proposed robust RZ-to-NRZ format conversion method.

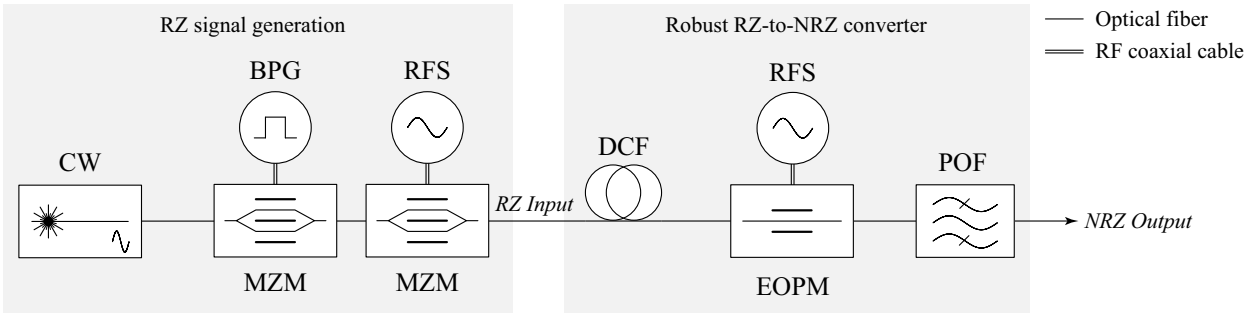

Figure 6.36 – Robust RZ-to-NRZ format conversion, experimental setup. CW, continuous-wave laser; BPG, bit pattern generator; RFS, radio-frequency synthesizer; MZM, Mach-Zehnder modulator; DCF, dispersion-compensating fiber; EOPM, elctro-optical phase modulator; POF, programmable optical filter.

A continuous-wave laser (CW), tuned at a wavelength of 1551.2 nm (corresponding to a central frequency of $\sim$193.4 THz), is used as the optical carrier. A Mach-Zehnder modulator (MZM), driven by a 12 Gb/s bit pattern generator (BPG) introduces a $2^7 - 1$ PRBS to the optical carrier. A second MZM, biased slightly out of the quadrature point, is used in conjunction with a radio-frequency synthesizer to carve a train of RZ 45-ps FWHM pulses out of the modulated CW beam, at a bit rate of 9.45 GHz.

The RZ signal is then injected into the converter circuit, where its spectrum is compressed following the procedure detailed in Section 6.3.4. The used dispersive medium is a spool of dispersion-compensating fiber (DCF) providing a total GVD of 890.91 ps^2/rad. This configuration satisfies the required Talbot conditions for $r^{-1} = 2$ (see Eq. 6.16). An electro-optical phase modulator (EOPM) introduces the required temporal Talbot phase sequence to the dispersed pulse train (see Eq. 6.17). This sequence is approximated by a single RF tone, generated by a radio-frequency synthesizer.

The final smoothing step is implemented by a programmable optical filter, where a band-pass filtering function with a bandwidth of 10 GHz (corresponding to the approximate frequency separation between the two central frequency gaps induced to the input RZ spectrum by the spectral compression process) is programmed. The resulting signal is a NRZ version of the input RZ pulse sequence.

6.4.4.2 Experimental results

In order to assess the performance quality of the proposed RZ-to-NRZ format conversion method, the results of two experiments are compared. First, the input RZ signal described in the previous section is converted to NRZ by direct amplitude filtering, as in conventional RZ-to-NRZ conversion methods. The POF is used to implement a filtering function combining both the response of a resonant line-suppressor and a smoothing band-pass filter. Second, the described technique for robust RZ-to-NRZ format conversion based on the PCSTM (with $r^{-1} = 2$) is implemented on the same input RZ signal.

Fig. 6.37 shows the measured optical spectra of the signals involved in the RZ-to-NRZ conversion processes by the conventional direct amplitude filtering method (Fig. 6.37(b)), and the proposed robust method based on energy-preserving spectral compression (Figs. 6.37(c.1) and (c.2)). The input RZ signal is shown

[13]For a complete schematic of the setup, see Fig. D.5.

for reference in Fig. 6.37(a). All signal traces are measured by an optical spectrum analyzer with a frequency resolution of 140 MHz, while the filter transmission traces are measured by an optical vector analyzer with a frequency resolution of 200 MHz.

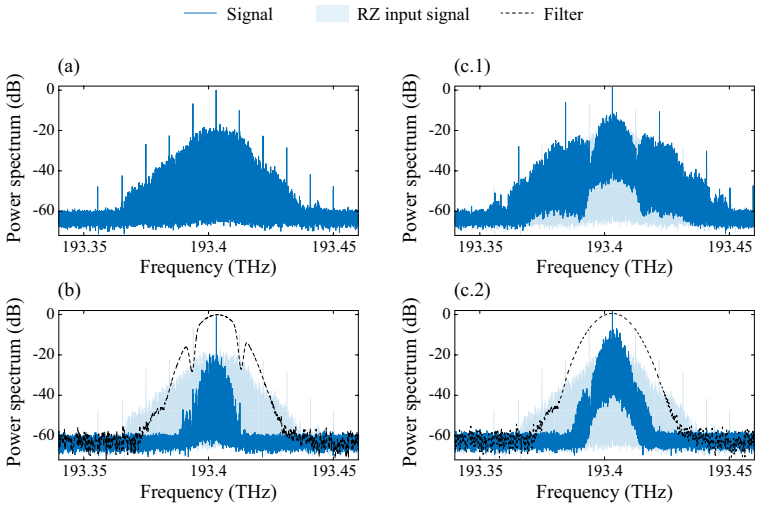

Figure 6.37 – Robust RZ-to-NRZ format conversion, experimental results, frequency domain. Comparison between the conventional direct amplitude filtering method and the proposed robust method based on spectral energy redistribution. All shown traces are normalized to the peak spectral power of the input RZ signal. (a) Input RZ signal spectrum. (b) Output NRZ signal spectrum obtained through the conventional direct amplitude filtering method (line-suppressor + smoothing filter). (c.1) Energy-preserving spectral compression of the input RZ signal by a factor $r^{-1} = 2$; one out of each two clock components of the input RZ signal is suppressed, and its energy is redistributed towards the surviving regions of the spectrum. (c.2) Output NRZ signal spectrum obtained through the proposed method (energy-preserving spectral compression + smoothing filter).

From Figs. 6.37(b) and (c.2), it can be seen how the energy redistribution process produces output signals with higher energy than those obtained by the conventional method based on direct spectral line suppression.

The corresponding time domain instantaneous power traces are shown in Fig. 6.38, including the complete 2^7-1 PRBS pulse sequence, a zoomed-in detail of the traces, and associated eye diagrams, all measured by an optical sampling oscilloscope with an effective acquisition bandwidth of 500 GHz.

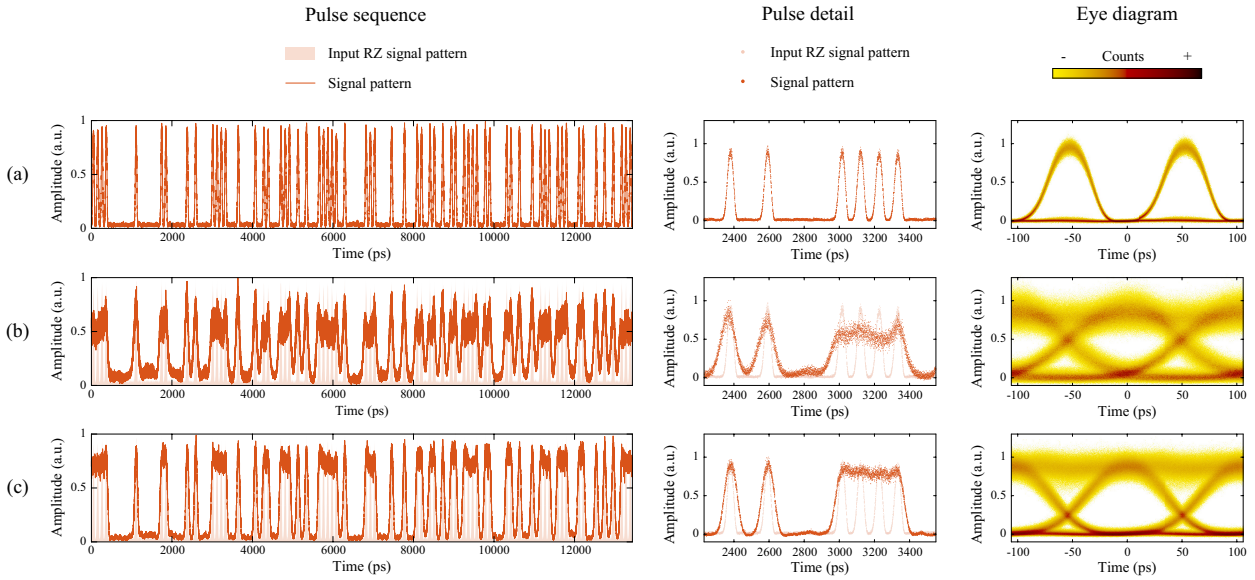

Figure 6.38 – Robust RZ-to-NRZ format conversion, experimental results, time domain. Comparison between the conventional direct amplitude filtering method and the proposed robust method based on spectral energy redistribution. From left to right: instantaneous power trace of the complete $2^7 - 1$ PRBS pulse sequence, detail of the power trace, and eye diagram. (a) Input RZ signal. (b) Output NRZ signal obtained through the conventional direct amplitude filtering method (line-suppressor + smoothing filter). (c.2) Output NRZ signal obtained through the proposed method (energy-preserving spectral compression + smoothing filter).

The BER of the obtained NRZ signals is measured following a procedure similar to the one detailed in Section 6.3.4 (see Fig. 6.33). Fig. 6.39(a) shows the BER vs. average signal power traces of the two compared methods and the back-to-back (B2B) configuration, shown for reference. The conventional RZ-to-NRZ conversion method incurs in a power penalty of $\sim$9 dB (signal power difference with respect to the B2B configuration, measured at the standard telecommunications error-free threshold, BER$= 10^{-9}$). This is in sharp contrast to the $\sim$2 dB power penalty incurred by the proposed technique based on energy redistribution.

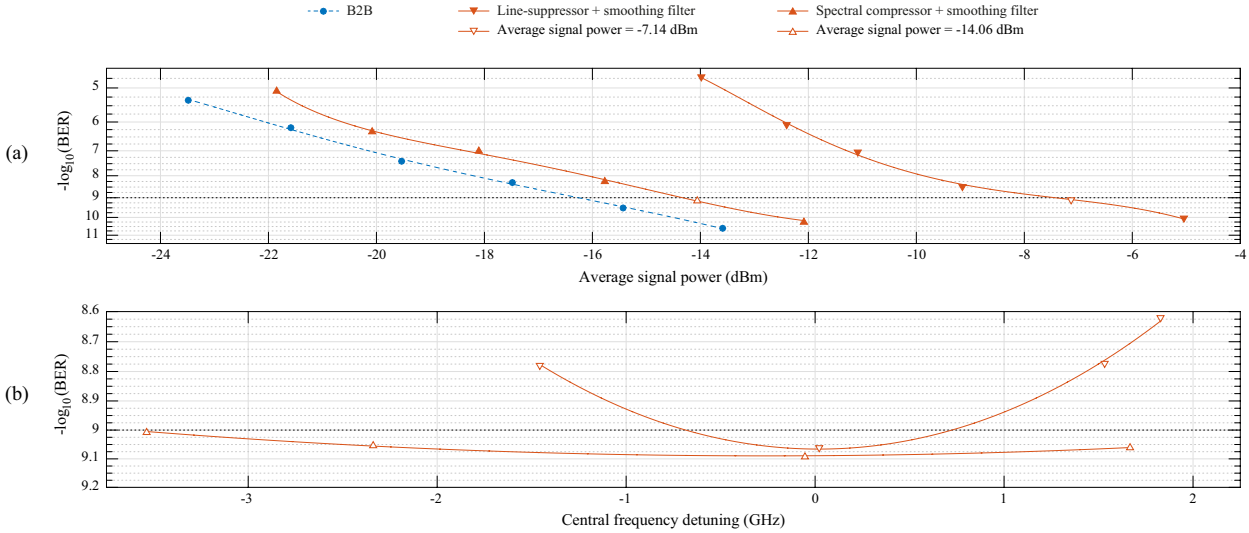

Figure 6.39 – Robust RZ-to-NRZ format conversion, experimental results, bit error rate analysis. Comparison between the conventional direct amplitude filtering method and the proposed robust method based on spectral energy redistribution. (a) BER vs. average signal power for constant received average optical power (the average signal power level is indicative of the SNR value). (b) BER vs. frequency detuning, measured at an average signal power level corresponding to BER$\simeq 10^{-9}$ in the case of no frequency deviation.

Finally, the robustness of the technique against central frequency drifts is studied by detuning the emission wavelength of the CW laser. Fig. 6.39(b) shows the measured values of the BER achieved by both methods for different values of central frequency detuning. The measurements are performed, with average signal power levels that, for perfectly tuned central frequency, yield BER values close to the error-free threshold (these correspond to -7.14 dBm and -14.06 dBm for the conventional method and the method proposed here, respectively). It can be seen how the BER for the conventional method quickly degrades when the laser frequency deviates from the central frequency of the filters. The method based on energy redistribution, on the other hand, retains a lower BER level for large frequency deviations, measuring a BER degradation lower than $10^{0.1}$ for a frequency deviation as high as 3.8 GHz (still remaining below the error-free threshold). It is important to mention that a proper implementation of the conventional scheme requires the design and fabrication of an application-specific optical periodic notch filter. A multipurpose programmable filter, as the one used in the reported experimental demonstration, is not optimized for format conversion specifically. However, a high-finesse filter with narrower stop-bands, specifically designed for more effective line suppression will compromise even further the tolerance of the technique against frequency drifts of the input signal and/or the optical filter.

CHAPTER 7

Conclusion and perspectives

This chapter summarizes the work presented in this dissertation and discusses its potential prospects, as well as tentative paths of future work.

7.1 Conclusion

Talbot effect – or self-imaging – is observed when a periodic object or wave is affected by a propagator imposing a phase variation across its Fourier domain representation (e.g., the discrete frequency spectrum of a periodic temporal signal) with a specific quadratic dependence with the corresponding Fourier-conjugate variable. The phenomenon, first reported in the Fresnel diffraction regime of paraxial optical waves, has been independently observed in the temporal, spectral and angular domains of wave optics, as well as through different realizations of waves, such as matter waves and quantum wavefunctions.

In this Ph.D. thesis, a general description of the Talbot effect has been reported, unifying all manifestations of the phenomenon under a single mathematical framework. Such a formalism, introduced in Chapter 3, describes the phenomenon in terms of the phase distributions of the involved waves in any pair of Fourier-conjugate variables, with independence of the observation domain (e.g., time/frequency, position/-momentum, etc). The ability to calculate Talbot phases in Fourier-dual domains allowed for the formulation of a general wave transformation method to turn an original periodic wave into a new wave, where the new period can be arbitrarily set. Furthermore, since the method involves only transformations of the phase distributions of the wave, its entire energy content is preserved in the process.

Particularly interesting cases of periodic waveforms are trains of optical pulses and their spectral counterpart, optical frequency combs. These signals find extensive application in a myriad of areas of science and engineering, in some cases, becoming the enabling factor of important recent technological advances. The repetition period of such signals is a key factor for their use in different applications. The universal periodicity control methodology, reported in Chapter 3, is an attractive signal processing solution to the arbitrary manipulation of periodic signals, offering high flexibility in the design of the desired output period, as well as the attractive feature of potentially preserving the energy of the signal to be processed. This is in sharp contrast to conventional methods based on direct amplitude modulation and amplitude filtering, where a large amount of signal energy is deliberately discarded in the process, negatively impacting the noise characteristics of the signal, and where only period multiplication/division by integer factors is accessible.

In Chapter 4, the described universal period control method was applied to processing trains of optical pulses, achieving energy-preserving division of the repetition period by fractional factors. This was achieved through coherent redistribution of the energy content of the original signal, leaving its noise content unaffected. Such coherent mechanism allowed for noiseless amplification of the obtained optical pulses, where the energy per output pulse is increased by the period multiplication factor, without any external energy injection mechanism. Not only this prevents amplification of the noise already present alongside the signal of interest, but it also avoids external noise sources, typical of conventional active amplification schemes. Furthermore, an interesting effect of fractional averaging of the noise fluctuations accompanying the train was observed.

In Chapter 5, the described universal period control method was applied to processing optical frequency combs, achieving arbitrary control of the spectral comb line spacing (free spectral range, FSR). Similarly, the coherent energy redistribution capabilities of the method allowed for passive amplification of the individual comb lines by the FSR multiplication factor, maintaining the original noise floor level unaltered. Such a feat could have important implications for applications that require frequency combs with high levels of visibility, and even for the frequency-domain detection of signals, originally buried under the noise floor. The last section of the chapter mentions the recent application of the universal period control method to the generation of frequency combs with tunable FSR over 6 orders of magnitude (from the kHz regime to the GHz regime) on a single laser platform.

In chapter Chapter 6, the described universal period control method was applied to processing the spectra of arbitrary, aperiodic signals. Two applications were reported: (i) a method for introducing reversible frequency gaps (frequency bands free of energy in the spectrum of a wave) to the spectrum of isolated waveforms, allowing for implementation of a novel technique for invisibility cloaking, capable of preserving the phase distributions of broadband, coherent illumination waves; and (ii) a method for compressing the spectra of modulated sequences of short pulses, while preserving the temporal shape – including duration – of the pulses, thus combining the performance advantages and robustness of short pulses for transferring and processing information with the convenience of frequency-domain multiplexing and processing operations. The mentioned waveform-preserving spectral compression method, was further used as the basis for an energy-efficient RZ-to-NRZ format conversion technique, with increased energy efficiency and robustness against frequency drifts of the involved signals, typically harmful in such systems.

As a general conclusion, considering the wide range of application of periodic temporal and spectral optical signals (trains of pulses and frequency combs), interest in the methods reported in this dissertation can be foreseen, based on their high flexibility and energetic efficiency. Furthermore, this project could inspire the development of new applications that would take advantage of the energy redistribution strategies for the design of signal processing systems and techniques. For instance, methods for noise mitigation of arbitrary – not necessarily periodic – signals, based on energy redistribution, could be envisioned (some additional details are discussed below, as lines of future work). Finally, the generality of the reported wave transformations make the proposed methods attractive for application to electromagnetic waves across the entire energy spectrum, and even to fundamentally different wave platforms, such as matter waves, quantum wavefunctions, and potentially even acoustic and thermal waves.

7.2 Future work

This section describes possible paths of future work, considered interesting and of relevance by the author.

7.2.1 Generality of the Talbot condition

The generalization of the Talbot effect, described in depth in Section 3.1, provides a closed solution to the problem of calculating the phases associated to Talbot sub-images in a pair of Fourier conjugate domains (e.g., time and radial frequency).

It is worth mentioning that during the course of the work leading to completion of this Ph.D. dissertation, a more compact solution for the Talbot coefficients, motivated by the mathematical findings reported in Section 3.1 of this document [APj2, APj3], was formulated by Carlos Rodríguez Fernández-Pousa [102]. This further simplification represents, in the candidate's humble opinion, an elegant final piece of the intricate puzzle that is the mathematical description of the Talbot effect.

7.2.1.1 Universality of the results

The main focus of this dissertation is on the the manipulation of periodic signals, represented in the time/frequency picture, with particular attention to the effect of phase transformations, inspired by the mathematical formalism of the Talbot effect, in the frequency domain of optical waves.

The reported methodology, however, should apply to any wave platform where basic operations – phase modulation and phase filtering in particular – can be implemented. This includes most regions of the elec-

tromagnetic spectrum [171]; e.g., radio-frequency, microwaves, terahertz radiation, optics etc. Furthermore, the reported concepts could be designed for application to wave systems of very different nature, such as matter waves and quantum wavefunctions, where realizations of the Talbot effect have already been reported [88–90], as well as potentially to acoustics and thermal waves [108].

7.2.2 Arbitrary control of 2D periodic images

The reported methods and techniques directly apply to the wave representation domains of position (space) and transverse momentum (angular spectrum). Let us not forget that Talbot effect was, in fact, first observed and explained in the paradigm of paraxial Fresnel diffraction of optical waves.

A spatial version of the PCTTM (see Section 3.2.3.1) can be formulated through direct application of the space-time duality (see Section B.3). Such a technique allows for arbitrary control of 2D periodic wavefronts, or images.

Furthermore, for periodic images with two different spatial periods (one along each transverse dimension, x and y), independent control of the period along each coordinate is possible. Such a generalization of the spatial Talbot effect has been recently reported, including independent period control of 2D periodic images [OPj11].

7.2.2.1 Noise mitigation of 2D periodic images

Considering the noise mitigation properties of the PCTTM (see Section 4.3), a space domain implementation for processing of 2D images should be expected to produce similar results.

Preliminary results on this topic have been reported, showing successful noiseless Talbot amplification of 2D periodic images [OPc11]. Such a methodology could be useful to image acquisition systems for applications relying on bright, clear, high-quality images, which are key to a large range of fundamental and applied disciplines, including optics, materials science, astronomy and biomedical sciences, among many others [65]. Computational processing methods for image denoising could also be envisioned, based on the reported phase-controlled Talbot effects.

7.2.2.2 Enhanced restoration of faulty images

The self-healing property of the Talbot effect (see Section 6.1.2) was reported as a means to correct faults on periodic images [83, 112], and later, its time domain version has been used as a clock recovery method [95], including sub-harmonic clock recovery through temporal Talbot amplification [OPj4].

A space-domain implementation of the PCTTM should produce equivalent results on 2D periodic images presenting aperiodicities – faults – on their periodic structure. Preliminary results on this topic have been reported, showing enhanced restoration of faulty images through spatial Talbot amplification [OPc17].

Such a feat could find application in imaging of periodic structures, as well as in signal processing methods for 2D periodic wavefronts (such as those generated by antenna and microphone arrays). Computational processing methods for periodic image restoration could also be envisioned, based on the phase-controlled Talbot effects.

7.2.2.3 Arbitrary control of 2D angular spectra

Similarly, a spatial version of the PCSTM (see Section 3.2.3.2) can be formulated through direct application of the space-time duality (see Section B.3). Such a technique would allow for arbitrary control of the angular spectra of 2D periodic wavefronts, potentially applicable to methods for beamsteering, beamforming, and far-field wavefront processing.

Similarly, the developed concept for spectral invisibility cloaking (see Section 6.2) could be directly transferred to the transverse momentum domain of waves. In this way, a method based on such concepts could be envisioned to cloak anisotropic spatial objects, i.e., objects sensitive to the specific direction in which they are illuminated, by only allowing light to shine the object in a controlled set of angles.

7.2.3 Processing and generation of CEO-stable frequency combs

The first reported application of the PCSTM (see Section 3.2.3.2) in this dissertation was to energy-preserving processing of frequency combs, in order to arbitrary tailor their frequency spacing (see Section 5.2). Several areas of application of frequency combs require stabilization of the carrier-envelope offset (CEO), so that the comb lines are tightly aligned to a specific reference spectral component, avoiding any frequency drifting. High-resolution spectroscopy techniques and high-precision spectrograph calibration methods are examples of such applications, the first one requiring comb FSR values in the MHz regime, while the second one steps deep into the GHz regime.

The reported theory and numerical simulations suggest that the output combs, generated through the PCSTM, do retain the exact original frequency grid reference of the input comb. This way, the method should preserve the state of CEO stabilization of the comb being processed. A preliminary experimental verification of this hypothesis has been reported, showing that basic spectral Talbot effect, through temporal phase modulation of a CEO-stable, broadband optical frequency comb, does not deteriorate its state of CEO stabilization [OPc30]. Experimental validation of CEO-stable comb generation and processing through the complete PCSTM would be an interesting achievement, as it would signify that the methods reported in this dissertation are compatible with applications of frequency combs where CEO stabilization is indispensable, such as the aforementioned ones.

7.2.4 Arbitrary coherent control of quantum frequency combs

Particularly interesting applications of the theory and methodology reported in this dissertation could be found in the field of quantum optics. Linear signal processing methods have already been applied to the generation and coherent control of quantum states, supported by single-photon optical frequency combs [43] [OPj13], which are a promising emerging technological candidate for future quantum computing and information processing systems. The capability of manipulating the comb spacing of such platforms could substantially enhance their versatility, as well as providing new avenues towards the arbitrary control of single- and multi-photon quantum states.

7.2.5 Spectral control and noise mitigation of arbitrary signals

The energy-preserving methods for coherent manipulation of the spectra of aperiodic signals, studied in Chapter 6, could be generalized to the coherent control of arbitrary spectra through phase-only transformations (not necessarily limited to, but including, the reported methods based on Talbot effect). For instance,

appropriately designed phase manipulations could be envisioned to compress the bandwidth of arbitrary data signals, not limited to the case of short pulses reported in Section 6.3.

Schemes similar to the spectral invisibility cloaking concept (see Section 6.2) could be used to redistribute the energy spectrum of a weak signal with a high noise content, allowing for sub-noise detection and accurate measurement of arbitrary signals, including isolated events, beyond the periodic frequency comb case reported in Section 5.3.

Similarly, continuous aperiodic signals, such as modulated data sequences, could be temporally sampled, thus introducing redundancy to their spectra, and subsequently processed through a method similar to the robust RZ-to-NRZ format conversion method reported in Section 6.4, in order to increase their energy content while reducing the impact of noise. Such a technique would allow for in-band noise mitigation of arbitrary signals, a feat of prime importance, not only in communications, but in general metrology.

Finally, the mentioned generalization of the process to denoising of arbitrary temporal and spectral waveforms could be implemented in the domain of arbitrary spatial 2D images.

APPENDIX A

Review of continuous-variable Fourier analysis

This Appendix provides a brief review of basic concepts of the Fourier transform for functions of continuous independent variables. The contents of this Appendix are a summary of concepts, compiled from the following sources: [73, 74].

A.1 Harmonic decomposition

Fourier analysis deals with the representation of functions as superpositions of fundamental periodic oscillatory functions, generally, complex exponentials.

A complex exponential oscillates with period 2π. Euler's formula[1] gives the form of the complex exponential in terms of trigonometric functions, as its real and imaginary parts,

$$e^{i\frac{2\pi}{u_r}u} = \cos\left(\frac{2\pi}{u_r}u\right) + i\sin\left(\frac{2\pi}{u_r}u\right) \tag{A.1}$$

where $u \in \mathbb{R}$ is the independent variable, and $u_r \in \mathbb{R}$ is the period of the complex exponential.

These functions are harmonic, with a unique oscillation frequency, U_r, given by,

$$U_r = \frac{2\pi}{u_r} \tag{A.2}$$

A.1.1 Fourier series

A function $\psi(u)$ is periodic in u if,

$$\psi(u \pm Nu_r) = \psi(u) \; \forall \; N \in \mathbb{N} \tag{A.3}$$

where $u_r > 0$ is the fundamental period of $\psi(u)$.

Any *reasonably well-behaved* periodic function[2] can be expressed as a sum of weighted complex exponentials,

$$\psi(u) = \sum_{k=-\infty}^{\infty} c_k e^{i\frac{2k\pi}{u_r}u} \tag{A.4}$$

where the coefficient $c_k \in \mathbb{C}$ writes,

$$c_k = \frac{1}{2\pi}\int_{u_0}^{u_0+u_r} \psi(u) e^{-i\frac{2k\pi}{u_r}u}\,\mathrm{d}u \tag{A.5}$$

with u_0, an arbitrary point in the domain of definition of $\psi(u)$.

[1] Euler's formula writes,

$$e^{i\theta} = \cos(\theta) + i\sin(\theta)$$

[2] A useful criterion of convergence of the Fourier series is that the function under analysis, $\psi(u)$, is absolutely integrable in one period,

$$\int_{u_0}^{u_0+u_r} |\psi(\mu)|\,\mathrm{d}\mu < \infty$$

where u_0 is an arbitrary point in the domain of definition of $\psi(u)$.

Note that the oscillation period of each complex exponential in the sum in Eq. A.4 is an integer multiple of the fundamental period of $\psi(u)$, u_r.

Eq. A.4 is a synthesis equation, as it constructs the function $\psi(u)$ from its harmonic components. Eq. A.5, on the other hand, is the associated analysis equation, as it gives the set of harmonic components, constituents of the function $\psi(u)$. Applying Euler's formula to Eq. A.4 gives an alternative formulation of the Fourier series,

$$\psi(u) = \frac{a_0}{2} \sum_{k=1}^{\infty} \left(a_k \cos\left(\frac{2k\pi}{u_r} u\right) + b_k \sin\left(\frac{2k\pi}{u_r} u\right) \right) \tag{A.6}$$

where,

$$a_k = \frac{2}{u_r} \int_{u_0}^{u_0+u_r} \cos\left(\frac{2k\pi}{u_r} u\right) \mathrm{d}u \tag{A.7}$$

$$b_k = \frac{2}{u_r} \int_{u_0}^{u_0+u_r} \sin\left(\frac{2k\pi}{u_r} u\right) \mathrm{d}u \tag{A.8}$$

The complex Fourier coefficients, c_k, are related to the real coefficients of the trigonometric Fourier series, a_k and b_k, by,

$$a_k = c_k + c_{-k} \tag{A.9}$$

$$b_k = i(c_k - c_{-k}) \tag{A.10}$$

and,

$$c_k = \frac{1}{2}(a_{|k|} - i\mathrm{sgn}\{k\} b_{|k|}) \tag{A.11}$$

where $\mathrm{sgn}\{k\}$ is the sign of the index k, so that,

$$\mathrm{sgn}\{k\} := \begin{cases} -1 & \Longleftrightarrow \quad k < 0 \\ 0 & \Longleftrightarrow \quad k = 0 \\ +1 & \Longleftrightarrow \quad k > 0 \end{cases} \tag{A.12}$$

A.1.1.1 Parseval's relationship

A u_r-periodic function of the variable u, $\psi(u)$, with Fourier coefficients c_k, satisfies the following relationship,

$$\frac{1}{u_r} \int_{u_0}^{u_0+u_r} \psi^*(u)\psi(u) \, \mathrm{d}u = \sum_{k=-\infty}^{\infty} c_k^* c_k \tag{A.13}$$

where $\cdot^*$ indicates complex conjugation[3].

This relationship is particularly useful for calculating the energy of a periodic signal over the duration of one period, from the coefficients of its Fourier series decomposition.

A.2 Fourier transform

Similarly to the Fourier series, the Fourier transform decomposes a function $\psi(u)$ into its harmonic components. Fourier transforms, however, operate on aperiodic functions. The synthesis and analysis equations write, respectively,

$$\psi(u) = \frac{1}{\sqrt{(2\pi)^{1+a}}} \int_{-\infty}^{\infty} \Psi(U) e^{iUu} \, \mathrm{d}U \tag{A.14}$$

$$\Psi(U) = \frac{1}{\sqrt{(2\pi)^{1-a}}} \int_{-\infty}^{\infty} \psi(u) e^{-iUu} \, \mathrm{d}u \tag{A.15}$$

where U is the Fourier-conjugate variable of u, $\Psi(U)$ is often referred to as the spectrum of $\psi(u)$, and a is an arbitrary real constant. The normalization factors in Eqs. A.14 and A.15 are arbitrary, as long as their product equals $(2\pi)^{-1}$. In the following, $a = 1$.

The analysis equation, Eq. A.15, is often referred to as the Fourier transform, denoted by the operator $\mathscr{F}\{\cdot\}$. The synthesis equation, Eq. A.14, is known as the inverse Fourier transform, denoted by the operator $\mathscr{F}^{-1}\{\cdot\}$.

A.2.1 Properties of the Fourier transform

Table A.1 lists some useful properties of the Fourier transform. These can be proved by direct application of Eqs. A.14 and A.15.

An operation of interest here is the convolution integral. Given two functions $\psi_1(u)$ and $\psi_2(u)$, their convolution integral is defined as,

$$\psi_1(u) * \psi_2(u) := \int_{-\infty}^{\infty} \psi_1(\mu) \psi_2(u - \mu) \, \mathrm{d}\mu \tag{A.16}$$

The convolution operation is commutative, associative and, owing to the linearity of the integral, distributive.

A.2.1.1 Uncertainty principle

There exists a reciprocity between the spreads of a function and its Fourier transform, in that both cannot be arbitrarily concentrated simultaneously. In short, if most of the area under the squared value of a function, $|\psi(u)|^2$, is concentrated over a given interval in u, the area under the absolute squared value of its Fourier

[3]Note that, for a complex-valued quantity, c, the product $c^* c = |c|^2$

Table A.1 – Properties of the Fourier transform.

Property	**Representation domain**	
	Real space, u	Fourier space, U
Fourier transform pair	$\psi(u)$	$\Psi(U)$
Linearity	$\sum_{k=1}^{K} c_k \psi_k(u)$	$\sum_{k=1}^{K} c_k \Psi_k(U)$
Shift in real space	$\psi(u-u_0)$	$\Psi(U)e^{-iUu_0}$
Shift in Fourier space	$\psi(u)e^{iU_0u}$	$\Psi(U-U_0)$
Domain inversion	$\psi(-u)$	$\Psi(-U)$
Convolution	$\psi_1(u) * \psi_2(u) * \cdots * \psi_K(u)$	$\prod_{k=1}^{K} \Psi_k(U)$
Multiplication	$\prod_{k=1}^{K} \psi_k(u)$	$\frac{1}{(2\pi)^K}\Psi_1(U) * \Psi_2(U) * \cdots * \Psi_K(U)$
Scaling	$\psi(u_0u)$	$\frac{1}{\lvert u_0\rvert}\Psi\left(\frac{U}{u_0}\right)$
Differentiation in real space	$\frac{\mathrm{d}^K}{\mathrm{d}u^K}\psi(u)$	$(iU)^K\Psi(U)$
Differentiation in Fourier space	$(-iu)^K\psi(u)$	$\frac{\mathrm{d}^K}{\mathrm{d}u^K}\Psi(U)$
Symmetry	$\Psi(u)$	$2\pi\psi(-U)$

transform, $|\Psi(U)|^2$, must have a minimum spread in the domain U, related to the spread in the real domain, by a scaling factor.

In particular, taking $|\psi(u)|^2$ and $|\Psi(U)|^2$ as probability distributions[4], with standard deviations σ_u and σ_U, respectively, so that,

[4]Note that this implies absolute square normalization, so that,

$$\int_{-\infty}^{\infty} |\psi(\mu)|^2 \, \mathrm{d}\mu = 1$$

$$\sigma_u^2 := \int_{-\infty}^{\infty} \mu^2 |\psi(\mu)|^2 \, \mathrm{d}\mu \tag{A.17}$$

$$\sigma_U^2 := \int_{-\infty}^{\infty} \Omega^2 |\psi(\Omega)|^2 \, \mathrm{d}\Omega \tag{A.18}$$

the Fourier uncertainty principle writes,

$$\sigma_u \sigma_U \geq \frac{1}{4\pi} \tag{A.19}$$

The equality in Eq. A.19 is achieved when $\psi(u)$ is a Gaussian function.

A.2.1.2 Parseval's relationship

A function, $\psi(u)$, and its Fourier transform, $\Psi(U)$, satisfy the following relationship,

$$\int_{-\infty}^{\infty} \psi^*(u)\psi(u) \, \mathrm{d}u = \frac{1}{2\pi} \int_{-\infty}^{\infty} \Psi^*(U)\Psi(U) \, \mathrm{d}U \tag{A.20}$$

This relationship is particularly useful for calculating the energy of a signal, from its spectrum.

A.2.2 Fourier transform of periodic functions

The Fourier transform can be generalized to periodic functions by introducing the Dirac's delta function.

A.2.2.1 Dirac's delta

Dirac's delta is a generalized function, typically used to model abstractions such as a point mass, a point charge, an infinitely-short impulse, etc.

The delta can be loosely thought of as a function of the real line, defined as zero everywhere except at the origin, where it is infinite,

$$\delta(u) := \begin{cases} \infty & \forall \quad u = 0 \\ 0 & \forall \quad u \neq 0 \end{cases} \tag{A.21}$$

and whose area is defined to be unitary,

$$\int_{-\infty}^{\infty} \delta(\mu) \, \mathrm{d}\mu := 1 \tag{A.22}$$

From Eqs. A.21 and A.22, important properties of the delta can be derived. In particular,

$$\int_{-\infty}^{\infty} \psi(\mu)\delta(\mu) \, \mathrm{d}\mu = \psi(0) \tag{A.23}$$

is known as the sampling property. This way, the delta function is the unitary element of the convolution, defining the identity,

$$\psi(u) * \delta(u) = \psi(u) \tag{A.24}$$

The two properties formulated above can be generalized as follows,

$$\int_{-\infty}^{\infty} \psi(\mu)\delta(\mu - u_0)\,\mathrm{d}\mu = \psi(u_0) \tag{A.25}$$

$$\psi(u) * \delta(u - u_0) = \psi(u - u_0) \tag{A.26}$$

Using Eq. A.23 in Eq. A.15 gives the Fourier transform of the delta function,

$$\mathscr{F}\{\delta(u)\} = 1 \;\forall\, U \tag{A.27}$$

which can also be found by taking Fourier transforms in Eq. A.24 and applying the convolution property (see Table A.1).

A.2.2.2 Discrete spectra of periodic functions

Consider a periodic function, $\psi(u)$, with fundamental period u_r. Defining $\psi_r(u)$ as a windowed version of $\psi(u)$ over a single period,

$$\psi_r(u) := \begin{cases} \psi_r(u) & \forall \quad u \in [u_0, u_0 + u_r] \\ 0 & \forall \quad u \notin [u_0, u_0 + u_r] \end{cases} \tag{A.28}$$

where u_0 is an arbitrary point in the domain of definition of $\psi(u)$, the periodic function $\psi(u)$ can be described in terms of a summation of Dirac's deltas,

$$\psi(u) = \psi_r(u) * \sum_{n=-\infty}^{\infty} \delta(u - nu_r) \tag{A.29}$$

The spectrum of $\psi(u)$, $\Psi(U)$ is obtained by calculating the Fourier transform of Eq. A.29,

$$\Psi(U) = U_r \sum_{k=-\infty}^{\infty} \Psi_r(kU_r)\delta(U - kU_r) \tag{A.30}$$

where $U_r = u_r^{-1}2\pi$, and $\Psi_r(U) = \mathscr{F}\{\psi_r(u)\}$.

Periodic functions have then discrete spectra. The spectrum of a periodic function is a weighted Dirac comb, i.e., a sum of delta functions with coefficients given by the Fourier transform of a single windowed period of the function. The separation between deltas is the harmonic oscillation frequency, U_r, associated with the period u_r.

A.2.2.3 Poisson's summation formula

Poisson's summation formula relates the Fourier series coefficients of the periodic summation of a function to values of the function's continuous Fourier transform.

$$\sum_{n=-\infty}^{\infty} \psi_r(u - nu_r) = \frac{1}{u_r} \sum_{k=-\infty}^{\infty} \Psi_r(kU_r) e^{ikU_r u} \tag{A.31}$$

The periodic summation of a function and, consequently, any periodic function, is completely defined by discrete samples of the original function's Fourier transform, related to the Fourier series as described by Eq. A.32. Conversely, the periodic summation of a function's Fourier transform is completely defined by discrete samples of the original function. Nyquist's sampling theorem[5] is a corollary of this result.

As stated above, Poisson's formula relates the Fourier series representation of a periodic function with the Fourier transform of the function in a single period. Indeed, Eq. A.30 has the form of a continuous expansion of a Fourier series, where the complex coefficients, c_k, take the value,

$$c_k = \frac{1}{u_r} \Psi_r \left(\frac{2k\pi}{u_r} \right) \tag{A.32}$$

A.2.3 Useful Fourier transform pairs

Table. A.2 lists some useful Fourier transform pairs.

A.2.4 Multidimensional Fourier transforms

A scalar function $\psi(\mathbf{u})$ of $\mathbb{R}^N$, where,

$$\mathbf{u} = \sum_{n=1}^{N} u_n \hat{\mathbf{u}}_n \tag{A.33}$$

has a Fourier transform defined in $\mathbf{U} \in \mathbb{R}^N$, where,

$$\mathbf{U} = \sum_{n=1}^{N} U_n \hat{\mathbf{U}}_n \tag{A.34}$$

The N-dimensional Fourier transform pair $\psi(\mathbf{u}) \leftrightarrow \Psi(\mathbf{U})$ writes,

[5] Nyquist's sampling theorem roughly states that periodic sampling of a signal is enough to perfectly reconstruct the signal, provided that its maximum frequency is at most half the sampling rate.

Table A.2 – Useful Fourier transform pairs.

Function	**Representation domain**	
	Real space, u	Fourier space, U
Fourier transform pair	$\psi(u)$	$\Psi(U)$
Fourier series	$\sum_{k=-\infty}^{\infty} c_k e^{ikU_r u}$	$2\pi \sum_{k=-\infty}^{\infty} c_k \delta(U - kU_r)$
Dirac's delta	$\delta(u)$	$1 \,\forall\, U$
Constant	$1 \,\forall\, u$	$2\pi\delta(U)$
Sinusoidal function	$\cos(U_r u + \theta)$	$\pi\left(\delta(U - U_r)e^{i\theta} + \delta(U + U_r)e^{-i\theta}\right)$
Complex exponential	$e^{i(U_r u+\theta)}$	$2\pi\delta(U - U_r)e^{i\theta}$
Rectangular function	$\begin{cases} 1 & \forall \quad \lvert u\rvert \leq \frac{1}{2} \\ 0 & \forall \quad \lvert u\rvert > \frac{1}{2} \end{cases}$	$\dfrac{\sin(U/2)}{U/2}$
Sinc function	$\dfrac{\sin(u/2)}{u/2}$	$\begin{cases} 2\pi & \forall \quad \lvert U\rvert \leq \frac{1}{2} \\ 0 & \forall \quad \lvert U\rvert > \frac{1}{2} \end{cases}$
Step function	$\begin{cases} 0 & \forall \quad u < 0 \\ 1 & \forall \quad u \geq 0 \end{cases}$	$\pi\delta(U) + \dfrac{1}{iU}$
Gaussian function	e^{-u^2}	$\sqrt{\pi}e^{-\frac{U^2}{4}}$
Decaying exponential	$\begin{cases} 0 & \forall \quad u < 0 \\ e^{-u} & \forall \quad u \geq 0 \end{cases}$	$\dfrac{1}{1 + iU}$
Dirac comb	$\sum_{n=-\infty}^{\infty} \delta(u - nu_r)$	$\dfrac{2\pi}{u_r} \sum_{k=-\infty}^{\infty} \delta\left(U - k\dfrac{2\pi}{u_r}\right)$

$$\psi(\mathbf{u}) = \frac{1}{\sqrt{(2\pi)^{N(1+a)}}} \int_{\mathbb{R}^N} \Psi(\mathbf{U}) e^{i\mathbf{U}\cdot\mathbf{u}} \,\mathrm{d}\mathbf{U} \tag{A.35}$$

$$\Psi(\mathbf{U}) = \frac{1}{\sqrt{(2\pi)^{N(1-a)}}} \int_{\mathbb{R}^N} \psi(\mathbf{u}) e^{i\mathbf{U}\cdot\mathbf{u}} \,\mathrm{d}\mathbf{u} \tag{A.36}$$

The two-dimensional case with $a = 1$, is commonly used in the analysis of images and wavefronts,

$$(2\pi)^2\psi(u_1,u_2) = \int_{-\infty}^{\infty}\int_{-\infty}^{\infty}\Psi(U_1,U_2)e^{i(U_1u_1+U_2u_2)}\,\mathrm{d}U_1\,\mathrm{d}U_2 \tag{A.37}$$

$$\Psi(U_1,U_2) = \int_{-\infty}^{\infty}\int_{-\infty}^{\infty}\Psi(u_1,u_2)e^{i(U_1u_1+U_2u_2)}\,\mathrm{d}u_1\,\mathrm{d}u_2 \tag{A.38}$$

A.3 Fourier analysis formalism for continuous-variable signals and systems

In a broad sense, a signal is any measurable variation of a physical quantity that typically conveys information about the process that generated it. These include sound, pressure, heat, light, etc. Signals are mathematically described as generally complex functions of an independent variable (which can be of vector nature if the signal is represented in a multidimensional space), commonly referred to as the support or representation domain of the signal. A system can then be defined as a process that takes a number of input signals and produces a generally different number of output signals, which can be represented in either the same support or in a different one. The input-output relationship of a general multiple-input multiple-output (MIMO) system is given by a mathematical operator, $\hbar$, that transforms a set of N functions $\psi_{\mathrm{i};n}(\mathbf{u}_\mathrm{i})$ (the input signal space) into a different set of L functions $\psi_{\mathrm{o};l}(\mathbf{u}_\mathrm{o})$ (the output signal space),

$$[\psi_{\mathrm{o};1}(\mathbf{u}_\mathrm{o}),\psi_{\mathrm{o};2}(\mathbf{u}_\mathrm{o}),\ldots,\psi_{\mathrm{o};L}(\mathbf{u}_\mathrm{o})] = \hbar\left\{[\psi_{\mathrm{i};1}(\mathbf{u}_\mathrm{i}),\psi_{\mathrm{i};2}(\mathbf{u}_\mathrm{i}),\ldots,\psi_{\mathrm{i};N}(\mathbf{u}_\mathrm{i})]\right\} \tag{A.39}$$

where $\{\psi_{\mathrm{i};n},\psi_{\mathrm{o};l}\} \in \mathbb{C}\ \forall\ \{n,l\} \in \mathbb{N}$, and $\mathbf{u}_\mathrm{i}$ and $\mathbf{u}_\mathrm{o}$ are generally complex-valued vectors of different dimension; although, in the context of this dissertation, the real-valued scalar u, representing domains such as position, momentum, time and frequency, is considered as the common support for both input and output sets of signals.

A.3.1 Linear and shift-invariant systems

A linear system satisfies the superposition principle, so that the net response caused by a given set of input signals is the sum of the responses associated to each signal, individually exciting the system. The system must be both additive and homogeneous in order to be linear, so that,

$$\hbar\left\{\sum_{n=1}^{N}c_n\psi_n(u)\right\} = \sum_{n=1}^{N}c_n\hbar\left\{\psi_n(u)\right\} \tag{A.40}$$

where $c_n \in \mathbb{C}\ \forall\ n \in \mathbb{N}$ are constant values, independent of u.

A shift-invariant system preserves displacements of the representation domain. This way, if a system generates an output signal $\psi_\mathrm{o}(u)$ in response to an input signal $\psi_\mathrm{i}(u)$, such a system is shift-invariant if its response to $\psi_\mathrm{i}(u-u_0)$ is $\psi_\mathrm{o}(u-u_0)$ for any value of the shift u_0.

Linear and shift-invariant (LSI) systems satisfy both properties, and they are extremely important in disciplines relying on the signals and systems formalism to represent physical phenomena. In particular, when the variable u represents time, LSI systems are known as linear and time-invariant (LTI).

A.3.1.1 Impulse response and transfer function

LSI systems can be mathematically described in terms of an unambiguous, generally complex function of the representation domain u, referred to as the impulse response, $\hbar(u)$. The input-output relationship of such systems is described by a convolution integral operation,

$$\psi_{\mathrm{o}}(u) = \int_{-\infty}^{\infty} \hbar(\mu)\psi_{\mathrm{i}}(u-\mu)\,\mathrm{d}\mu \tag{A.41}$$

The Fourier transform of the impulse response, $\mathscr{H}(U) = \mathscr{F}\{\hbar(u)\}$, describes the system in Fourier space, also unambiguously, where U is the Fourier-conjugate of u. Given the Fourier spectra of the input and output signals, $\Psi_{\mathrm{i}}(U) = \mathscr{F}\{\psi_{\mathrm{i}}(u)\}$ and $\Psi_{\mathrm{o}}(U) = \mathscr{F}\{\psi_{\mathrm{o}}(u)\}$, respectively, the input-output relationship of the system in Fourier space is reduced to a product (see Section A.2.1),

$$\Psi_{\mathrm{o}}(U) = \mathscr{H}(U)\Psi_{\mathrm{i}}(U) \tag{A.42}$$

This way, LSI systems describe filters, as the output spectrum is obtained from the product of the input spectrum and the generally complex operator $\mathscr{H}(U)$. The magnitude of the transfer function, $|\mathscr{H}(U)|$, describes the ranges in U along which input signals linearly exchange energy with the system. The phase of the transfer function, $\sphericalangle\mathscr{H}(U)$, provides information of the ways in which the system shifts the different spectral components of the input signal in real space u. In the time-frequency picture (where $u \leftarrow t$ and $U \leftarrow \omega$) this is quantified by the group delay of the system,

$$t_g(\omega) := -\frac{\mathrm{d}}{\mathrm{d}\omega}\sphericalangle\mathscr{H}(\omega) \tag{A.43}$$

A MIMO LSI system is described by a transfer matrix, where each output signal is obtained as a linear superposition of each input signal, weighted by a specific transfer matrix element.

$$\begin{pmatrix} \Psi_{\mathrm{o};1}(U) \\ \Psi_{\mathrm{o};2}(U) \\ \vdots \\ \Psi_{\mathrm{o};L}(U) \end{pmatrix} = \begin{pmatrix} \mathscr{H}_{1,1}(U) & \mathscr{H}_{1,2}(U) & \cdots & \mathscr{H}_{1,N}(U) \\ \mathscr{H}_{2,1}(U) & \mathscr{H}_{2,2}(U) & \cdots & \mathscr{H}_{2,N}(U) \\ \vdots & \vdots & \ddots & \vdots \\ \mathscr{H}_{L,1}(U) & \mathscr{H}_{L,2}(U) & \cdots & \mathscr{H}_{L,N}(U) \end{pmatrix} \cdot \begin{pmatrix} \Psi_{\mathrm{i};1}(U) \\ \Psi_{\mathrm{i};2}(U) \\ \vdots \\ \Psi_{\mathrm{i};N}(U) \end{pmatrix} \tag{A.44}$$

where the Fourier spectrum of the l-th output signal is obtained as,

$$\Psi_{\mathrm{o};l}(U) = \sum_{n=1}^{N} \mathscr{H}_{l,n}(U)\Psi_{\mathrm{i};n}(U) \tag{A.45}$$

A.3.1.2 Unitary elements and eigenfunctions

As shown in Section A.2.2.1, the delta function is the unitary element of the convolution. Using this property in Eq. A.41, it follows that a system excited by $\delta(u)$ will respond with its impulse response, $\hbar(u)$. In the Fourier space picture, this is easily understood from Eq. A.42 by noting that the Fourier transform of the

delta function is $1 \; \forall \, U$. A stimulus exciting every spectral component of a system with equal amplitude and phase will result in a response perfectly mapping the Fourier spectrum of the system, $\mathscr{H}(U)$.

A signal, $\psi_{\mathrm{e}}(u)$, is an eigenfunction of a system if the corresponding response of the system is the same signal multiplied by a constant, generally complex, eigenvalue, λ_{e}, so that,

$$\hbar\{\psi_{\mathrm{e}}(u)\} = \lambda_{\mathrm{e}}\psi_{\mathrm{e}}(u) \tag{A.46}$$

In the case of LSI systems,

$$\begin{aligned} \hbar(u) * \psi_{\mathrm{e}}(u) &= \lambda_{\mathrm{e}}\psi_{\mathrm{e}}(u) && \text{(A.47)} \\ \mathscr{H}(U)\Psi_{\mathrm{e}}(U) &= \lambda_{\mathrm{e}}\Psi_{\mathrm{e}}(U) && \text{(A.48)} \end{aligned}$$

where $\Psi_{\mathrm{e}}(U) = \mathscr{F}\{\psi_{\mathrm{e}}(u)\}$.

Each LSI system has its own set of eigenfunctions, however, the complex exponential is always an eigenfunction of any LSI system. This is easy to verify from Eq. A.48 by noting that the Fourier transform of a complex exponential is a shifted Dirac's delta function,

$$\begin{aligned} \hbar(u) * e^{iU_r u} &= \mathscr{H}(U_r)e^{iU_r u} && \text{(A.49)} \\ \mathscr{H}(U)\,(2\pi\delta(U - U_r)) &= \mathscr{H}(U_r)\,(2\pi\delta(U - U_r)) && \text{(A.50)} \end{aligned}$$

The associated eigenvalue is the the complex value of the spectrum of the system at the oscillation frequency of the complex exponential. This property is extensively used as a method to test the response of an LTI system to a single input frequency.

APPENDIX B

Review of Fourier optics and the space-time duality

This Appendix provides a brief summary of the Fourier optics formalism for modeling the paraxial propagation of waves, as well as the space-time duality, a mathematical symmetry between the equations describing paraxial wave propagation and temporal wave evolution. The contents of this Appendix are a summary of concepts, compiled from the following sources: [16, 56, 71, 96].

B.1 Propagation of paraxial waves

As described in Chapter 2 (Section 2.2.2.2), the complex amplitude of a plane wave writes

$$\psi(\mathbf{r}) = \psi_0 e^{-i\mathbf{k}\cdot\mathbf{r}} \tag{B.1}$$

where ψ_0 is a generally complex constant, and $\mathbf{k}$ is the wavevector.

Taking z as the reference dimension, the wavevector makes angles θ_x and θ_y with the planes $\{y, z\}$ and $\{x, z\}$, respectively, as shown in Fig. 2.2 (repeated here as Fig. B.1 for convenience of the reader), so that,

$$\hbar \sin(\theta_x) = \hbar_x \tag{B.2}$$
$$\hbar \sin(\theta_y) = \hbar_y \tag{B.3}$$

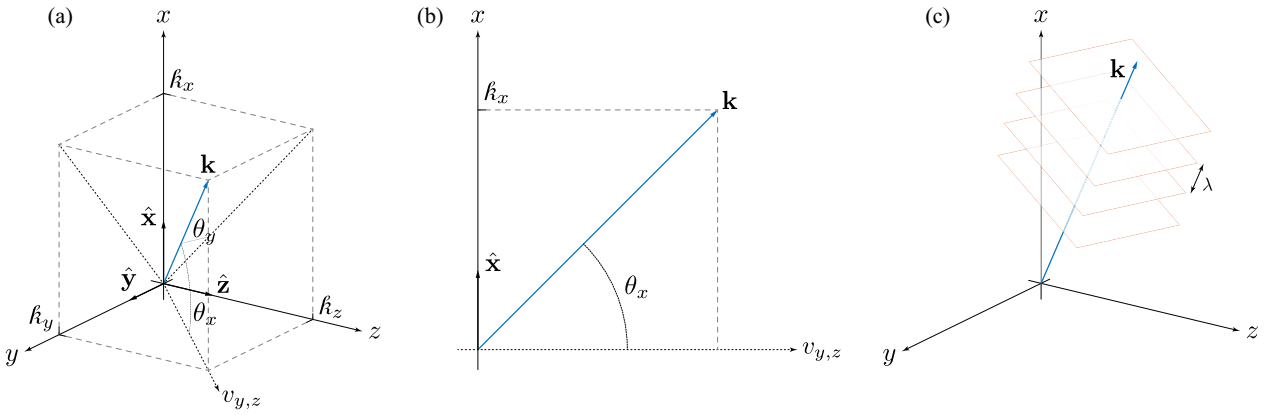

Figure B.1 – The wavevector. The wavevector, $\mathbf{k} = \hbar_x\hat{\mathbf{x}} + \hbar_y\hat{\mathbf{y}} + \hbar_z\hat{\mathbf{z}}$, unambiguously describes a plane wave with wavenumber $\hbar = |\mathbf{k}|$, propagating in the direction of $\mathbf{k}$. (a) Components of the wavevector in Cartesian coordinates; $v_{y,z}$ denotes the direction of the projection of the vector $\mathbf{k}$ onto the plane $\{y, z\}$. (b) Detail of the wavevector components in the plane that contains the vector $\mathbf{k}$ and its projection onto the plane $\{y, z\}$. (c) Wavefronts of a plane wave (note that the equiphase surfaces of a plane wave are boundless planes, here depicted as squares for illustration purposes).

If $\hbar_x \ll \hbar$ and $\hbar_y \ll \hbar$, the angles θ_x and θ_y are small. Taking the first term of the Taylor series expansion of the sine function, and noting that $\lambda = \hbar^{-1}2\pi$, the angles write,

$$\theta_x \approx \lambda\frac{\hbar_x}{2\pi} \tag{B.4}$$
$$\theta_y \approx \lambda\frac{\hbar_y}{2\pi} \tag{B.5}$$

This is known as the paraxial approximation, and it holds true when the normal directions of the wavefronts make small angles with the propagation axis.

Consider an arbitrary wave propagating in the positive direction of the z axis. The complex amplitude writes,

$$\psi(\mathbf{r}) = \tilde{\psi}(\mathbf{r})e^{-i\hbar z} \tag{B.6}$$

The amplitude $\tilde{\psi}(\mathbf{r})$ is known as the complex envelope of the wave. If this envelope is a slowly varying function of position, so that $\tilde{\psi}(\mathbf{r})$ remains approximately constant within a wavelength, $\psi(\mathbf{r})$ is a paraxial wave. In this situation, the envelope experiences a change $\delta\tilde{\psi}(\mathbf{r})$ over a distance $\delta z = \lambda$, that satisfies $\delta\tilde{\psi}(\mathbf{r}) \ll \tilde{\psi}(\mathbf{r})$. Taking the rate of change of $\delta\tilde{\psi}(\mathbf{r})$ in the z direction as the partial derivative,

$$\frac{\partial}{\partial z}\tilde{\psi}(\mathbf{r}) \ll \hbar\tilde{\psi}(\mathbf{r}) \tag{B.7}$$

$$\frac{\partial^2}{\partial z^2}\tilde{\psi}(\mathbf{r}) \ll \hbar^2\tilde{\psi}(\mathbf{r}) \tag{B.8}$$

Using Eq. B.6 in the formulation of the Helmholtz equation (Eq. 2.7), and neglecting the appropriate terms, as per the relationships B.7 and B.8, gives the paraxial Helmholtz equation for the complex envelope,

$$\left(\frac{\partial}{\partial z} - \frac{i}{2\hbar}\tilde{\nabla}^2\right)\tilde{\psi}(\mathbf{r}) = 0 \tag{B.9}$$

where $\tilde{\nabla}^2$ is the transverse Laplacian operator,

$$\tilde{\nabla}^2 := \frac{\partial^2}{\partial^2 x} + \frac{\partial^2}{\partial^2 y} \tag{B.10}$$

B.2 Fourier optics

Fourier optics provides a powerful and convenient mathematical formalism for describing wave propagation in terms of linear operators, based on the principle of harmonic decomposition, governing the Fourier transform.

B.2.1 Plane-wave decomposition and the angular spectrum

The complex amplitude $\psi(\mathbf{r})$ in Eq. B.1 is a harmonic function of space. For instance, in the plane, $z = 0$,

$$\psi(x, y, 0) = \psi_0 e^{-i(\hbar_x x + \hbar_y y)} \tag{B.11}$$

According to the principles of Fourier analysis[1], an arbitrary function of an arbitrarily-dimensional space can be written as a superposition of harmonic functions of said space. This suggests that the wavefront of an arbitrary monochromatic wave – taking z as the propagation direction – can be expressed as a superposition of plane waves with different amplitudes, characterized by wavevectors with different angles θ_x and θ_y.

[1] For a review of Fourier analysis, consult Appendix A.

Assuming propagation under paraxial conditions, where the approximations B.4 and B.5 are satisfied, the transverse wavevector components of such spatial harmonics, $\hbar_x$ and $\hbar_y$, play the roles of spatial radial frequencies, measured in rad/m (see Fig. B.2).

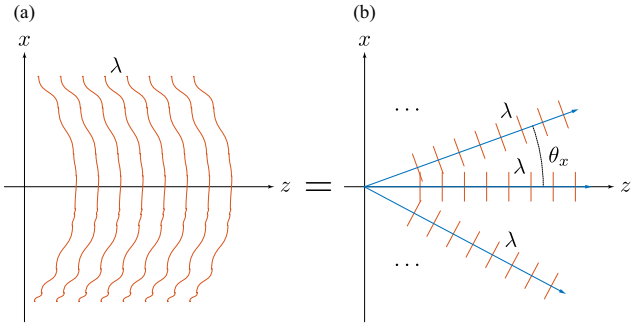

Figure B.2 – Plane wave spectrum. Decomposition of a wave with an arbitrary wavefront (a), taken at a fixed spatial point, as a collection of plane waves propagating at different angles (b). For simplicity, only the plane $\{x, z\}$ is shown.

The set of complex amplitudes of the plane-wave decomposition at a given point along the propagation axis, z, represents the transverse momentum distribution of the wave, and it is often referred to as the angular spectrum, $\tilde{\Psi}(\mathbf{k})$. The spatial complex amplitude and the angular spectrum are related by a two-dimensional Fourier transform pair,

$$\tilde{\Psi}(\hbar_x, \hbar_y) = \iint_{-\infty}^{\infty} \tilde{\psi}(x, y) e^{-i(\hbar_x x + \hbar_y y)} \, \mathrm{d}x \, \mathrm{d}y \tag{B.12}$$

$$(2\pi)^2 \tilde{\psi}(x, y) = \iint_{-\infty}^{\infty} \tilde{\Psi}(\hbar_x, \hbar_y) e^{i(\hbar_x x + \hbar_y y)} \, \mathrm{d}\hbar_x \, \mathrm{d}\hbar_y \tag{B.13}$$

B.2.2 Spatial wave propagators

Within the formalism of Fourier optics, the propagation of scalar electromagnetic waves through optical media can be described in the context of linear signals and systems[2].

An optical system is characterized by a linear operator, known as a wave propagator, that describes the evolution of the wave of interest along its propagation through the optical system. The propagator can be expressed both in real space, $h(x, y)$, and in transverse-momentum space (angular spectrum), $\mathcal{H}(\hbar_x, \hbar_y)$. If the operation is linear and invariant to displacements in x and y, $h(x, y)$ is said to be the impulse response of the system, and $\mathcal{H}(\hbar_x, \hbar_y)$ its transfer function, forming a Fourier transform pair. Fig. B.3 shows a schematic depiction of the Fourier optics wave propagation model.

Most linear phenomena of scalar waves can be described within this formalism. In the following, two important examples of wave propagation through optical systems – diffraction and spatial modulation – are discussed.

B.2.2.1 Spatial modulation

Spatial modulation is the process by which an optical system introduces a localized change to the complex amplitude of a wave in real space. The process is described by the multiplication of the complex amplitude

[2]For a review of the mathematical formalism of signals and systems theory, consult Appendix A.

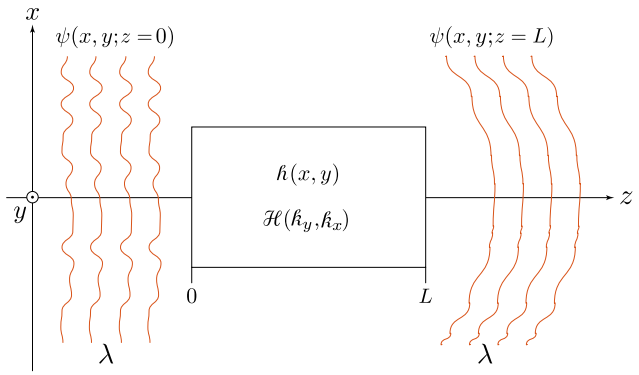

Figure B.3 – Operator model of wave propagation. Transmission of a wave through an optical system of length L, described as an operator, following the postulates of Fourier optics.

of the wave of interest in real space, $\psi(x, y; z = 0)$, by the complex amplitude transmittance function of the system, $\hbar_{\text{SM}}(x, y)$, so that,

$$\psi(x, y; z = L) = \hbar_{\text{SM}}(x, y)\psi(x, y; z = 0) \tag{B.14}$$

where L is used here as an indicator of the length of the optical system, assuming that the wave enters the system at $z = 0$, and then travels through it along the propagation axis, z.

In the Fourier domain, the operation is described by the convolution integral between the angular spectrum of the wave, $\Psi(\hbar_x, \hbar_y; z = 0)$, and the Fourier transform of the complex transmittance function, $\mathcal{H}_{\text{SM}}(\hbar_x, \hbar_y)$,

$$\Psi(\hbar_x, \hbar_y; z = L) = \frac{1}{(2\pi)^2} \iint_{-\infty}^{\infty} \mathcal{H}_{\text{SM}}(\kappa_x, \kappa_y)\Psi(\hbar_x - \kappa_x, \hbar_y - \kappa_y; z = 0)\, \mathrm{d}\kappa_x\, \mathrm{d}\kappa_y \tag{B.15}$$

The complex amplitude transmittance can be a purely real function, in which case the process is referred to as amplitude modulation, a complex function with uniform magnitude, in which case the process is referred to as phase modulation, or a combination of both, in which case the process is referred to as complex modulation. Apertures are examples of spatial amplitude modulation, while lenses are examples of spatial phase modulation. Spatial light modulators are devices capable of applying a user-defined spatial modulation pattern to an impinging optical wave.

If $\psi(x, y; z = 0)$ is a plane wave (i.e., a wave consisting of a single spatial frequency pair $\{\hbar_x, \hbar_y\}$), the spatial modulation process will generate an output angular spectrum, $\Psi(\hbar_x, \hbar_y; z = L)$, with additional spatial frequency components.

Fig. B.4 schematically depicts the operation.

B.2.2.2 Diffraction

Diffraction is most commonly defined as the transformation that a wave experiences when it propagates away from an object. The wavefront of a plane wave retains its shape along its propagation through free space; the wavefront of an arbitrary wave, made out of a set of plane waves, will experience variations along its propagation. This is due to the fact that the different constituent plane waves have different spatial

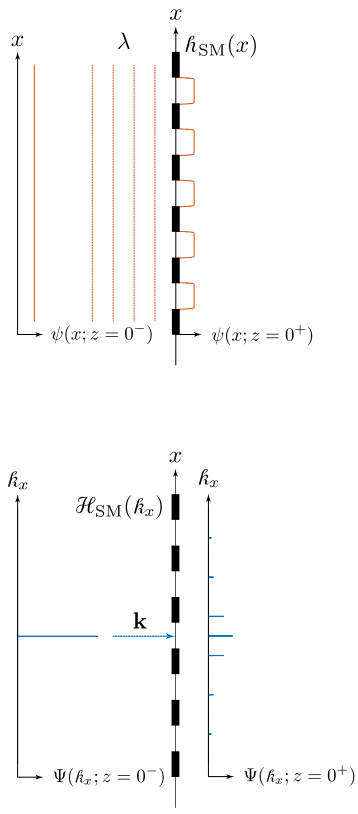

Figure B.4 – Spatial modulation. Operator model of the spatial modulation process. The shown example consist on a periodic object, with a binary amplitude transmittance (i.e., alternating regions of full transparency with regions of full opacity). The object is considered infinitesimally thin, making the process spatially localized; the notation $z = 0^+$ and $z = 0^-$ refer to the planes immediately before and after the object, respectively. (top) Real space. (bottom) Fourier space.

frequencies, thus making different angles with the propagation axis (see Eqs. B.4 and B.4). Diffraction is the result of the different constituent spatial harmonics of a wavefront propagating away from each other.

Diffraction is mostly observed when a plane wave, incident on a spatial modulation system (e.g., an aperture), propagates away from the system (e.g., producing a blurred shadow of the aperture function). The wave phenomenon responsible for diffraction is simply free space propagation. The process is described by the multiplication of the angular spectrum of the wave of interest, $\Psi(\hbar_x, \hbar_y; z = 0)$, by the transfer function of free space, $\mathcal{H}_{\mathrm{D}}(\hbar_x, \hbar_y)$, so that,

$$\Psi(\hbar_x, \hbar_y; z = L) = \mathcal{H}_{\mathrm{D}}(\hbar_x, \hbar_y)\Psi(\hbar_x, \hbar_y; z = 0) \tag{B.16}$$

where the transfer function of free space, in the paraxial approximation, can be written as a two-dimensional phase factor presenting a quadratic variation with spatial frequency,

$$\mathcal{H}_{\mathrm{D}}(\hbar_x, \hbar_y) = e^{i\frac{\hbar_x^2 + \hbar_y^2}{2\hbar}z} \tag{B.17}$$

where $z = L$ indicates the propagation length.

This is known as the Fresnel approximation. Similarly, the process in real space is described by the convolution integral of the complex amplitude of the wave $\psi(x, y; z = 0)$, with the impulse response of free space, $\hbar_{\mathrm{D}}(x, y)$, so that,

$$\psi(x, y; z = 0) = \iint_{-\infty}^{\infty} \hbar_{\mathrm{D}}(\chi, \xi)\psi(x - \chi, y - \xi; z = 0)\,\mathrm{d}\chi\,\mathrm{d}\xi \tag{B.18}$$

where the impulse response of free space, in the paraxial approximation, writes,

$$h_{\mathrm{D}}(x,y) = e^{-i\frac{x^2+y^2}{2z}k} \tag{B.19}$$

Fig. B.5 schematically depicts the operation.

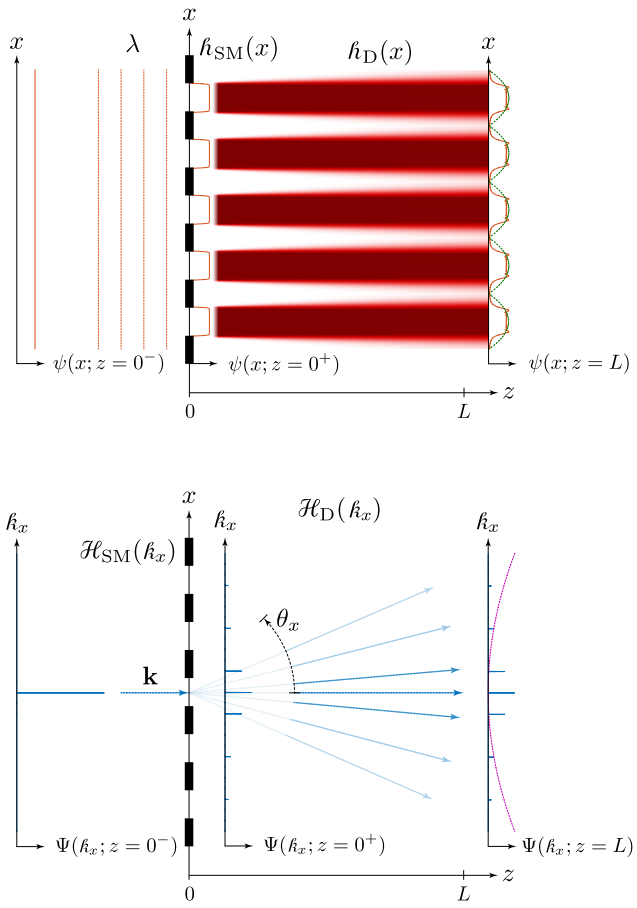

Figure B.5 – Diffraction. Operator model of the paraxial diffraction modulation process. In the shown example, the wave obtained after the spatial modulation process shown in Fig. B.4 propagates a distance L away from the periodic object. (top) Real space. (bottom) Fourier space.

B.3 The space-time duality

The space–time duality originates from the similarity of the equations describing spatial diffraction of an electromagnetic beam and temporal dispersion of an electromagnetic pulse, along their propagation. This elegant symmetry has inspired substantial development in optical technology, and it is an extremely powerful tool in the design and analysis of optical systems.

B.3.1 Formulation

Following the approximations used in Section 2.3.1.2, the nonlinear Schrödinger equation[3] (see Eq. 2.22) can be written in a simplified form as follows,

$$\left(\frac{\partial}{\partial z} - i\frac{\beta_2}{2}\frac{\partial^2}{\partial t^2}\right)\tilde{\psi}(t,z) = 0 \tag{B.20}$$

Eq. B.20 describes the temporal evolution of optical waves along their linear propagation through transparent media, under the narrow-band approximation. This equation is isomorphic to the paraxial Helmholtz equation (see Eq. B.9), written here in one transverse dimension,

$$\left(\frac{\partial}{\partial z} - \frac{i}{2k}\frac{\partial^2}{\partial x^2}\right)\tilde{\psi}(x,z) = 0 \tag{B.21}$$

The mathematical symmetry existing between Eqs. B.20 and B.21 establishes a duality between the temporal dynamics of optical waveforms and the spatial evolution of optical beams. This symmetry is known as the space-time duality of optical waves.

B.3.2 Equivalence between wave parameters in space and time

In short, the outcome of an optical system, operating over a the spatial wavefront of a wave, can be replicated on the temporal envelope of a wave if one manages to emulate an equivalent transformation in the time domain. From Eqs. B.20 and B.21, the relationship between temporal and spatial parameters is clear. Table B.1 lists such relationships.

Similarly, a direct equivalence can be established between the operators governing processes in space and time (see Section 2.3.2). For instance, The narrow-band chromatic dispersion operator, $\mathscr{H}_{\mathrm{GVD}}(\omega)$ (see Section 2.3.2.2), acting over the frequency spectrum of a temporal waveform, is analogous to the paraxial diffraction operator, $\mathscr{H}_{\mathrm{D}}(k_x)$ (taken along a single spatial dimension), acting over the angular spectrum of a spatial wavefront. A similar relationship exists between their corresponding impulse responses, as well as between the operators governing spatial and temporal modulation (see Section 2.3.2.1).

Fig. B.6 illustrates the symmetry existing between the spatial modulation and temporal modulation process, as well as between the paraxial diffraction and narrow-band group velocity dispersion processes, modeled as wave propagators in the Fourier optics paradigm.

B.3.3 Space-time duality of the Talbot effect

The spatial and temporal realizations of the Talbot effect (briefly described in Section 2.4 and further related in Section 3.1.2), are mathematically related by the space-time duality. Recall that spatial Talbot effect is a particular case of Fresnel diffraction of spatially-periodic wavefronts (with wavelength λ and transverse spatial period x_r, along the x dimension), while temporal Talbot effect is a particular case of second-order

[3] Recall that the nonlinear Schrödinger equation models the temporal evolution of optical waves along their propagation through dielectric media.

Table B.1 – Space-time duality. Relationship between spatial and temporal parameters of waves in the paraxial diffraction and narrow-band dispersion regimes. Space-domain magnitudes are expressed in one transverse dimension, here represented by the coordinate x.

Space domain		**Time domain**	
Paraxial Helmholtz equation	Eq. B.21	Eq. B.20	Narrow-band Schrödinger equation
Propagation direction	z	z	Propagation direction
Wavefront dimension	x	t	Waveform dimension
Spatial radial frequency	$\hbar_x$	ω	Radial frequency
Spatial wavefront	$\tilde{\psi}(x)$	$\tilde{\psi}(t)$	Temporal waveform
Angular spectrum	$\tilde{\Psi}(\hbar_x)$	$\tilde{\Psi}(\omega)$	Frequency spectrum
Paraxial diffraction	$\frac{1}{2\hbar}$	$\frac{\beta_2}{2}$	Narrow-band dispersion

dispersion of temporally-periodic waveforms (with second-order dispersion coefficient β_2 and temporal period t_r).

From Eqs. 2.44 and 2.47, it is easy to verify that the second order dispersion coefficient in temporal Talbot effect, plays the role of the wavelength in spatial Talbot effect. The spatial and temporal Talbot conditions[4] write,

$$\lambda z = \frac{p}{q} x_r^2 \tag{B.22}$$

$$2\pi|\beta_2|z = \frac{p}{q} t_r^2 \tag{B.23}$$

respectively, where p and q are two mutually prime natural numbers. Fig. B.7 shows the distribution of spatial and temporal Talbot images and sub-images for some values of the fraction $q^{-1}p$.

Using the definitions for the Talbot length, z_{T}, given in Eqs. 2.44 and 2.47 for spatial and temporal Talbot effects, respectively, the Talbot condition can be written for both realizations of the effect as,

$$z = \frac{p}{q} z_{\mathrm{T}} \tag{B.24}$$

Finally, a realization of the Talbot effect in the transverse momentum domain of optical waves – known as angular Talbot effect – can also be formulated by direct application of the space-time duality to the mathematical description of the spectral Talbot effect. This phenomenon was first postulated and observed by José Azaña and Hugues Guillet de Chatellus in 2014 [103].

[4]Note that the temporal Talbot condition is written here for the particular case or propagation through a dispersive medium. A more general formulation of the temporal Talbot condition is given in Eqs. 2.46 and 3.7.

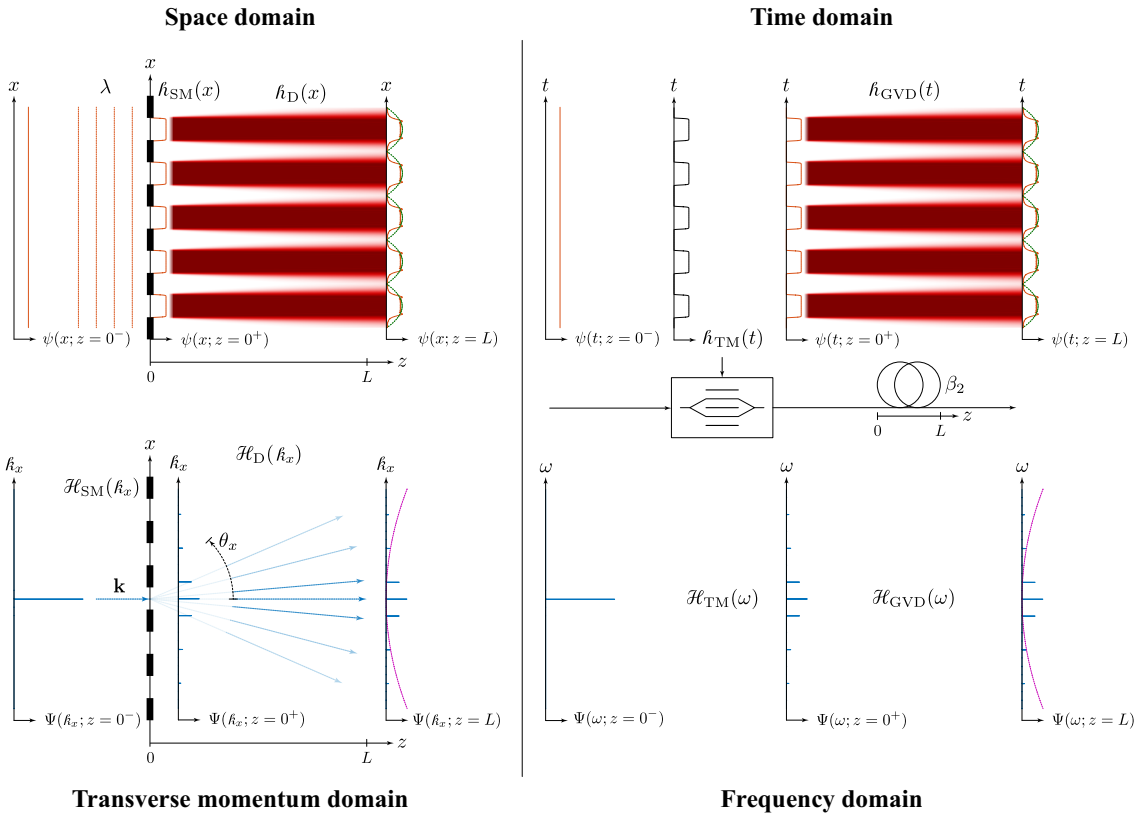

Figure B.6 – Space-time duality. Illustration of the mathematical symmetry between the operators describing the spatial modulation and temporal modulation process, as well as between the paraxial diffraction and narrow-band group velocity dispersion processes.

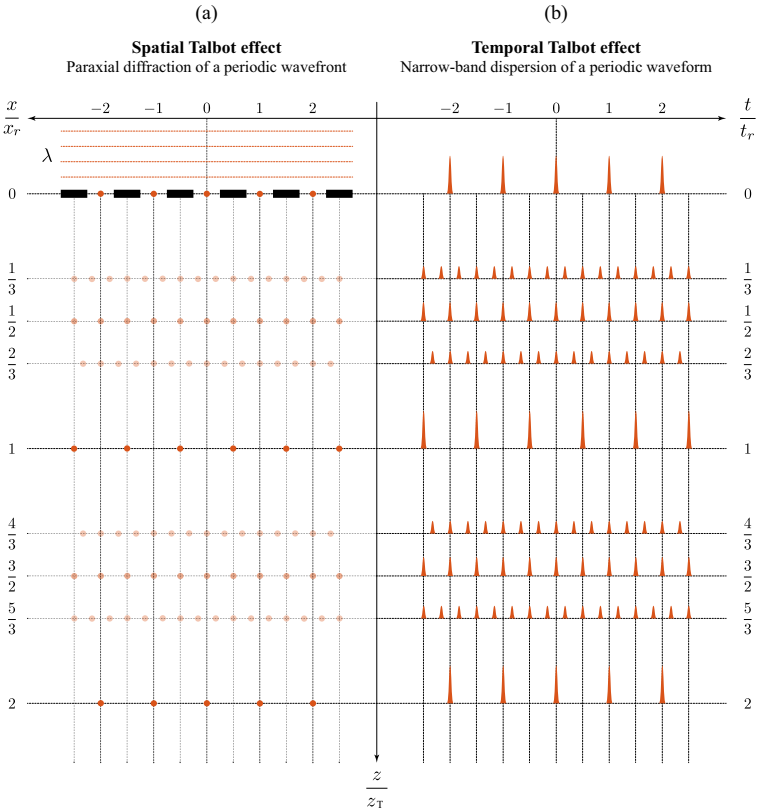

Figure B.7 – Space-time duality of the Talbot effect. Distribution of Talbot images and sub-images along the propagation of a wave with a periodic transverse profile. (a) Spatial Talbot effect, observed in the paraxial diffraction of a periodic transverse wavefront (here, depicted as the spatial modulation of a monochromatic plane wave by a periodic amplitude transmittance). (b) Temporal Talbot effect, observed in the narrow-band dispersion of a periodic train of pulses.

APPENDIX C

MATLAB code listings

This Appendix contains the MATLAB code used in the calculation of Fourier-dual Talbot phase profiles.

C.1 Modular arithmetic functions

Listing C.1 – Computation of the modular multiplicative inverse. Based on Eq. 3.22

```
%% Modular multiplicative inverse

function a = invmod(p,q)

[~,a,~] = gcd(p,q);
a = mod(a,q);

end
```

Listing C.2 – Computation of the Jacobi symbol. Based on Eq. 3.23

```
%% Jacobi symbol

function J = jacobi(a,b)

if mod(b,2)==0
    error('lower parameter must be odd');
end

a = mod(a,b);

if a == 0
    J = 0;
elseif a == 1
    J = 1;
elseif mod(a,2) == 0
    if abs(mod(b,8)) == 1
        J = jacobi(a/2,b);
    else
        J = -jacobi(a/2,b);
    end
else
    if mod(b,4)==3 && mod(a,4)==3
        J = -jacobi(b,a);
    else
        J = jacobi(b,a);
    end
end

end
```

C.2 Gauss sums

Listing C.3 – Computation of the quadratic Gauss sum. Based on Eq. 3.18

```
%% Evaluation of quadratic Gauss sum

function [G] = GaussSum(n,p,q)

N = length(n);
```

```
6
7  G = zeros(1,N);
8  for l = 0:q-1
9
10     G_l = exp(1i*pi/q*(p*l^2+(p*q^2+2*n)*l));
11     G = G+G_l;
12
13 end
```

C.3 Computation of the Talbot phases

Listing C.4 – Computation of Talbot parameters. Based on Table 3.3

```
1  %% Talbot phase parameters in Fourier-dual domains
2
3  function [s,m,c] = TalbotParameters(p,q)
4
5  if ((rem(p,1) ~= 0) || (rem(q,1) ~= 0)) || ((p < 1) || (q < 1))
6      error('p and q must be possitive integers');
7  end
8
9  if gcd(p,q) ~= 1
10     error('p and q must be mutually prime');
11 end
12
13 m = q;
14
15 if      (mod(p,2) == 0) && (mod(q,2) == 1) % p even, q odd
16
17     s = p.*invmod(p,q).^2;
18     c = (q-1)/4+1/2.*(1-jacobi(p,q));
19
20 elseif (mod(p,2) == 1) && (mod(q,2) == 1) % p odd,  q odd
21
22     s = 8.*p.*invmod(2,q).*invmod(2*p,q).^2;
23     c = (q-1)/4+1/2.*(1-jacobi(p,q));
24
25 elseif (mod(p,2) == 1) && (mod(q,2) == 0) % p odd,  q even
26
27     s = p.*invmod(p,q).^2;
28     c = -p/4-1/2.*(1-jacobi(q,p));
29
30 end
31
32 s = mod(s,2*m);
33 c = mod(c,2);
34
35 end
```

C.4 Execution example

Listing C.5 – Benchmark code for computation of Talbot phases. Shown example with $p = 1$, $q = 5$

```
1  close all
```

```
clear variables
clc


%% Talbot phase, domain U

p = 1;
q = 5;

K = 4*q;
k = 0:K;

phi_k = mod(pi*p/q*k.^2,2*pi);


%% Talbot phase, domain u

%  Analytic definition

[s,m,c] = TalbotParameters(p,q);

N = 4*q;
n = 0:N;

phi_n = mod(-pi*s/m*n.^2-pi*c,2*pi);

%  Evaluation of Gauss sum

G_n = GaussSum(n,p,q);


%% Results

disp(['p = ' num2str(p) ', q = ' num2str(q)])
disp(['s = ' num2str(s) ', m = ' num2str(m) ', c = ' num2str(c)])
disp(['sqrt(q) = ' num2str(sqrt(q)) ...
      ', |G_{1,' num2str(p) ',' num2str(q) '}| = ' num2str(abs(G_n(1)))])

figure

subplot(2,1,1)
bar(k,phi_k/pi,1,'facecolor',[0 0 0])
xlabel('k')
ylabel('Phase (rad/\pi), domain U')
axis([k(1)-0.5 k(end)+0.5 0 2])
box on

subplot(2,1,2)
hold on
bar(n,phi_n/pi,1,'facecolor',[0.6 0.6 0.6],'edgecolor',[0.6 0.6 0.6])
plot(n,mod(angle(G_n),2*pi)/pi,'kx')
xlabel('n')
ylabel('Phase (rad/\pi), domain u')
legend('Analytical','Gauss sum')
axis([n(1)-0.5 n(end)+0.5 0 2])
box on
```

Listing C.6 – Command prompt output. Result of execution of Code C.5

```
p = 1, q = 5
s = 6, m = 5, c = 1
sqrt(q) = 2.2361, |G_{1,1,5}| = 2.2361
```

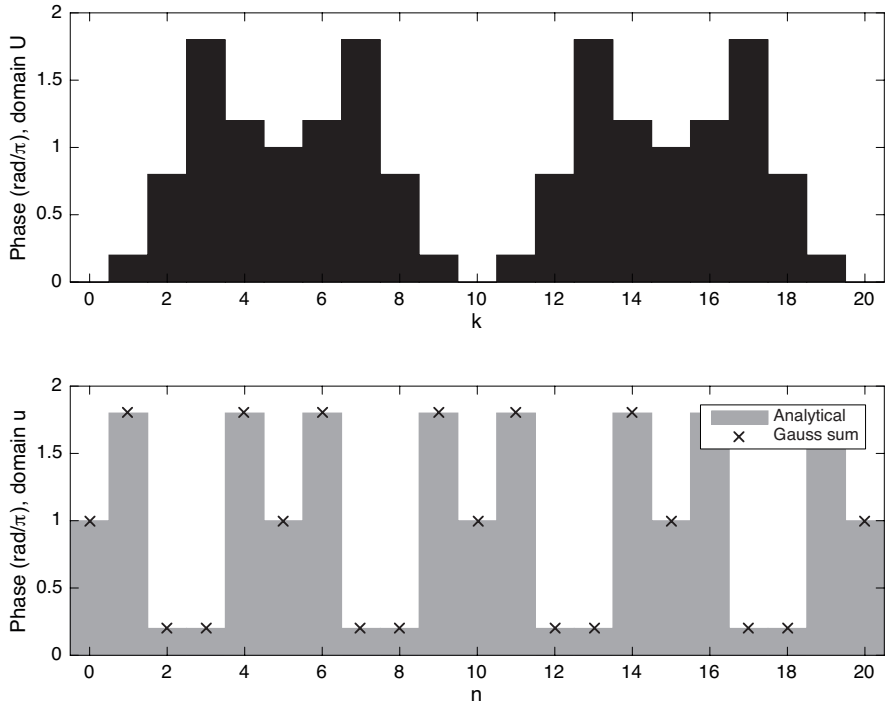

Figure C.1 – MATLAB figure output of benchmark code. Result of execution of Code C.5.

APPENDIX D

Detailed circuit schematics

This Appendix contains detailed schematics of the electro-optical circuits used in the experimental demonstration of the systems, techniques and phenomena reported in this dissertation.

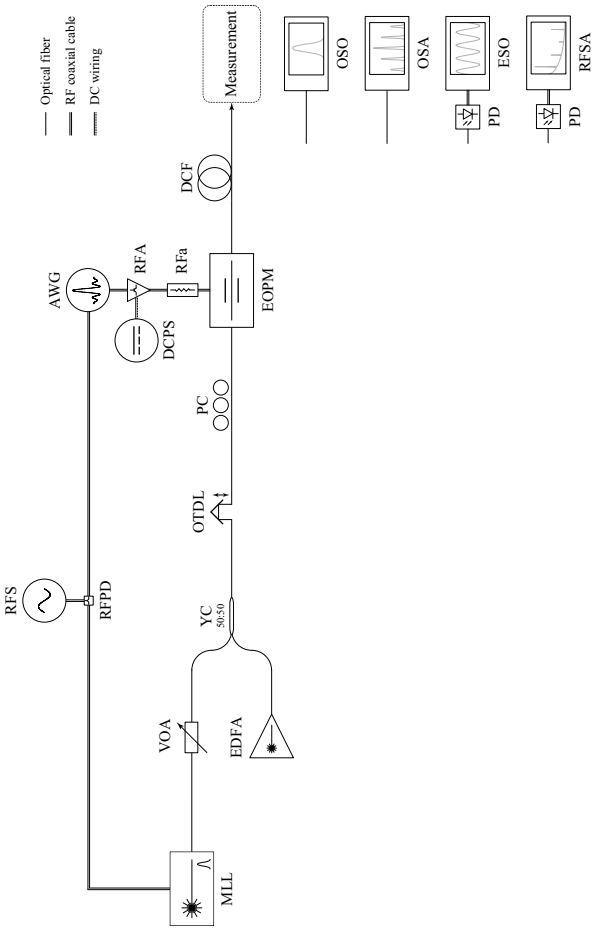

Figure D.1 – Fractional repetition rate multiplication, detailed experimental setup.

***Setup components*:** MLL, mode-locked laser; RFS, radio-frequency synthesizer; RFPD, radio-frequency power divider; VOA, variable optical attenuator; EDFA, erbium-doped fiber amplifier; YC, optical Y-coupler; OTDL, optical tunable delay line; PC, polarization controller; AWG, arbitrary-waveform generator; DCPS, direct current power supply; RFA, radio-frequency amplifier; RFa, radio-frequency attenuator; EOPM, electro-optical phase modulator; DCF, dispersion-compensating fiber.

***Measurement components*:** OSO, optical sampling oscilloscope; OSA, optical spectrum analyzer; ESO, electrical sampling oscilloscope; RFSA, radio-frequency spectrum analyzer; PD, photodiode.

Figure D.2 – Arbitrary FSR control of frequency combs, detailed experimental setup.

***Setup components*:** MLL, mode-locked laser; RFS, radio-frequency synthesizer; RFPD, radio-frequency power divider; VOA, variable optical attenuator; EDFA, erbium-doped fiber amplifier; YC, optical Y-coupler; DCF, dispersion-compensating fiber; OTDL, optical tunable delay line; PC, polarization controller; AWG, arbitrary-waveform generator; DCPS, direct current power supply; RFA, radio-frequency amplifier; RFa, radio-frequency attenuator; EOPM, electro-optical phase modulator.
***Measurement components*:** OSA, optical spectrum analyzer.

Figure D.3 – Spectral invisibility cloaking, detailed experimental setup.

***Setup components*:** MLL, mode-locked laser; POF, programmable optical filter; EDFA, erbium-doped fiber amplifier; SMF, single-mode fiber; OTDL, optical tunable delay line; PC, polarization controller; RFS, radio-frequency synthesizer; RFPD, radio-frequency power divider; DCPS, direct current power supply; RFA, radio-frequency amplifier; RFa, radio-frequency attenuator; EOPM, electro-optical phase modulator; DCF, dispersion-compensating fiber.
***Measurement components*:** OSA, optical spectrum analyzer; OAC, optical autocorrelator.

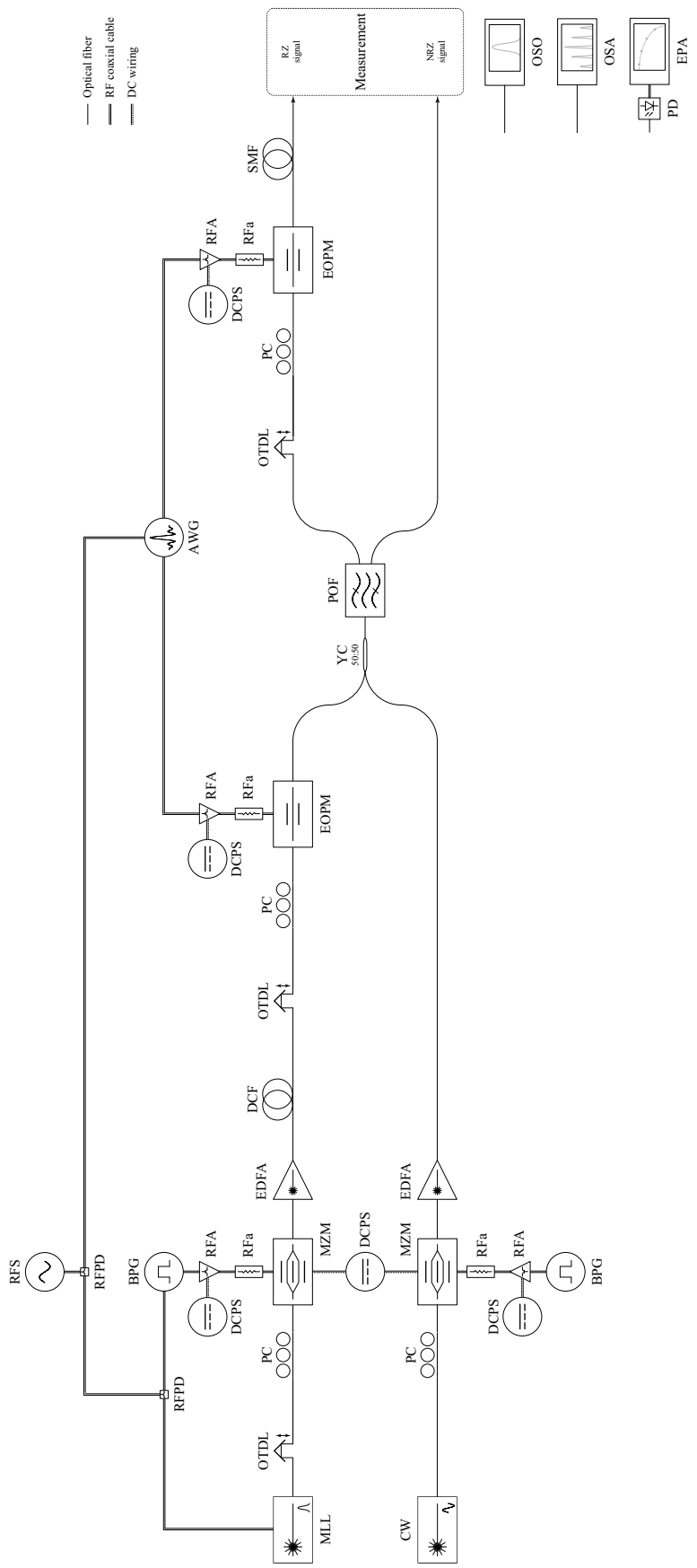

Figure D.4 – Waveform-preserving spectral compression and in-band frequency-division multiplexing, detailed experimental setup.

***Setup components*:** MLL, mode-locked laser; CW, continuous-wave laser; OTDL, optical tunable delay line; PC, polarization controller; RFS, radio-frequency synthesizer; RFPD, radio-frequency power divider; BPG, bit pattern generator; RFA, radio-frequency amplifier; RFa, radio-frequency attenuator; MZM, Mach-Zehnder modulator; DCPS, direct current power supply; EDFA, erbium-doped fiber amplifier; DCF, dispersion-compensating fiber; EOPM, electro-optical phase modulator; AWG, arbitrary waveform generator; YC, optical Y-coupler; POF, programmable optical filter; SMF, single-mode fiber.

***Measurement components*:** OSO, optical sampling oscilloscope; OSA, optical spectrum analyzer; EPA, error performance analyzer; PD, photodiode.

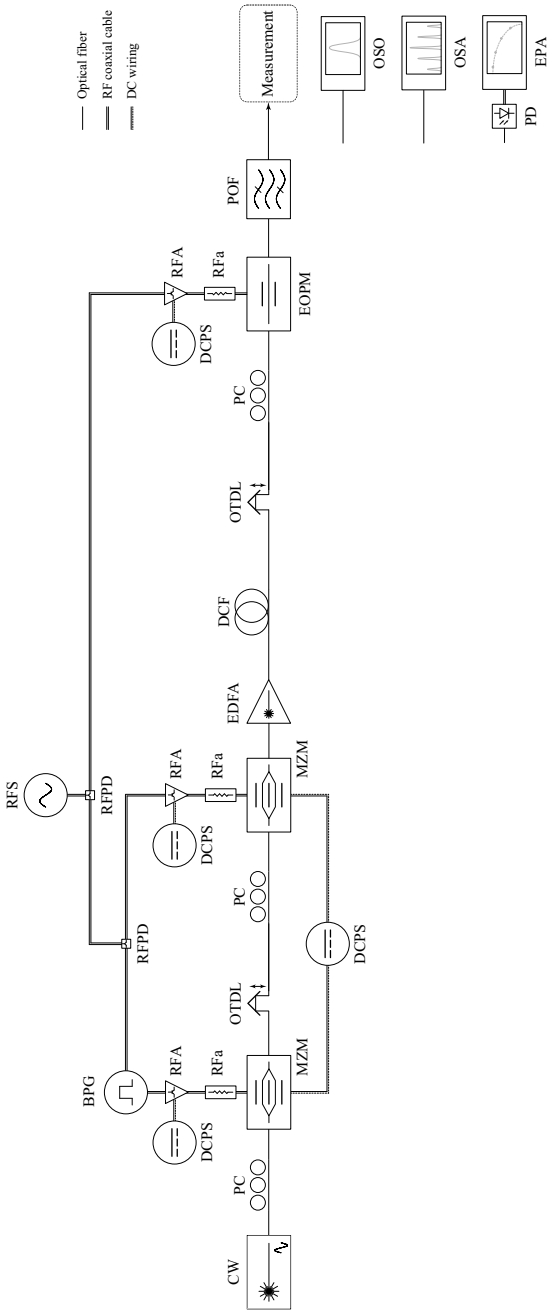

Figure D.5 – Robust RZ-to-NRZ format conversion, detailed experimental setup.

***Setup components*:** CW, continuous-wave laser; PC, polarization controller; BPG, bit pattern generator; RFA, radio-frequency amplifier; RFa, radio-frequency attenuator; MZM, Mach-Zehnder modulator; DCPS, direct current power supply; OTDL, optical tunable delay line; EDFA, erbium-doped fiber amplifier; RFS, radio-frequency synthesizer; RFPD, radio-frequency power divider; DCF, dispersion-compensating fiber; EOPM, electro-optical phase modulator; POF, programmable optical filter.
***Measurement components*:** OSO, optical sampling oscilloscope; OSA, optical spectrum analyzer; EPA, error performance analyzer; PD, photodiode.

Figure D.6 – Generation of frequency combs with user-defined FSR, detailed experimental setup.

***Setup components*:** CW, continuous-wave laser; YC, optical Y-coupler; PC, polarization controller; FAS, fiber alignment stage; AOFS, acousto-optical frequency shifter; RFS, radio-frequency synthesizer; DCPS, direct current power supply; RFA, radio-frequency amplifier; OI, optical isolator; POF, programmable optical filter; EDFA, erbium-doped fiber amplifier; AWG, arbitrary waveform generator; RFa, radio-frequency attenuator; EOPM, electro-optical phase modulator; VOA, variable optical attenuator.
***Measurement components*:** OSA, optical spectrum analyzer; ESO, electrical sampling oscilloscope; PD, photodiode.

APPENDIX E

Generation of frequency combs with user-defined FSR

This Appendix reports the theoretical foundations and experimental demonstration of a technique for frequency comb generation with user-defined line frequency spacing, based on a realization of phase-controlled Talbot phenomena on a CW-seeded frequency-shifted feedback loop cavity. The work presented in this Appendix was reported in [APj7] [APc4].

E.1 CW-seeded frequency-shifted feedback loop

A frequency-shifted feedback loop is a resonant cavity with a frequency up/down-converting element – typically an acousto-optical frequency shifter – and a gain mechanism that compensates for the loss accumulated in a cavity round-trip. Fig. E.1(a) shows a schematic sketch of the steady-state model of the FSFL structure.

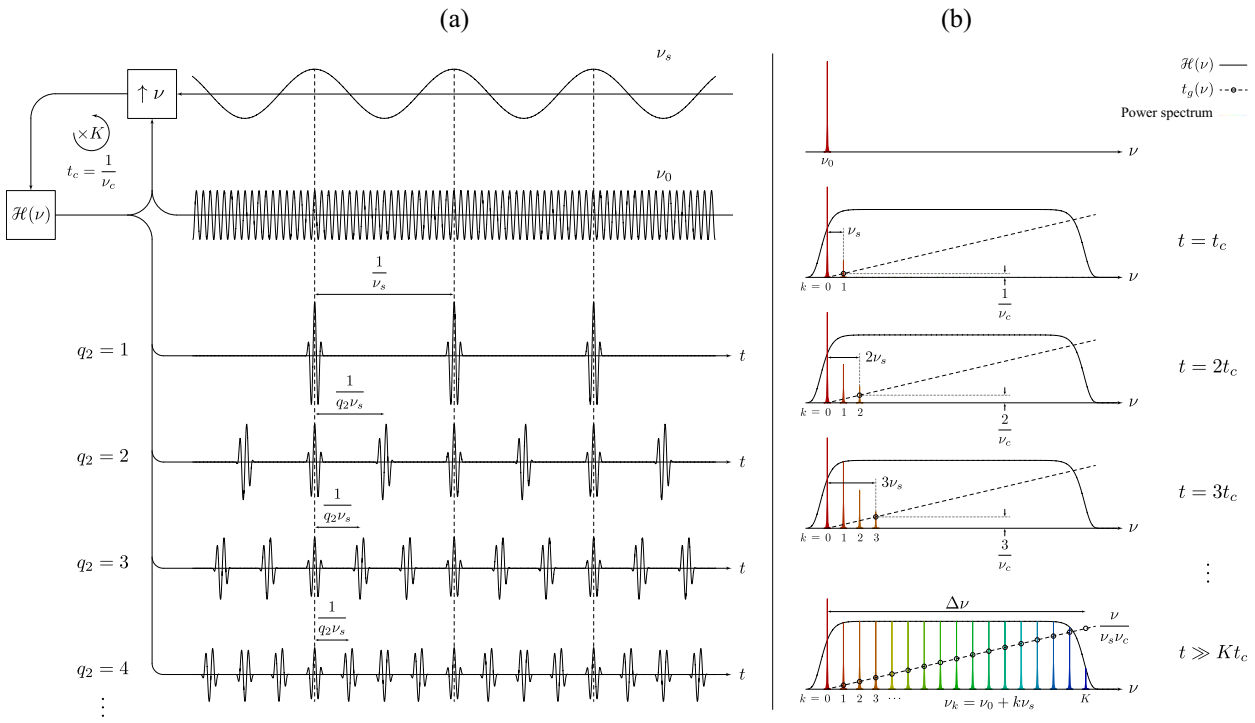

Figure E.1 – Steady-state model of a CW-seeded frequency-shifted feedback loop. A CW-seeded FSFL, in the steady state, behaves as a mode-locked laser with a tunable quadratic spectral phase. If the loop is designed to achieve an equivalent GVD value that satisfies a temporal Talbot condition, a train of pulses is obtained at its output, with the characteristics of a temporal Talbot (sub-)image. (a) Simple model of the loop, assuming a bandwidth of the cavity spectral response $\mathcal{H}(\nu)$, satisfying $\Delta\nu \leq K\nu_s$, where ν_s is the shifting frequency (up-shifting, $\uparrow \nu$, is assumed in the depicted sketch), and ν_0 is the seed frequency (note that, in general $\nu_0 \gg \nu_s$). Depending on the value of the fraction $\nu_c^{-1}\nu_s \equiv q_2^{-1}p_2$, the loop generates a train of pulses with repetition rate $q_2\nu_s$ and a pulse-to-pulse temporal Talbot phase. (b) Simplified depiction of the transient dynamics in the generation of the FSFL comb spectrum. The seed frequency is simultaneously shifted (by ν_s) and delayed (by $t_c = \nu_c^{-1}$) upon completion of each round-trip in the loop. In the steady state ($t \gg Kt_c$), a frequency comb with FSR ν_s and linear group delay distribution (corresponding to a quadratic spectral phase) is obtained. Note that both the FSR and equivalent GVD parameter – the slope of the group delay distribution – are tunable by the parameters ν_s and ν_c.

E.1.1 Expression of the output field amplitude

A comprehensive analysis of the derivations reported in this section can be found in [92].

The FSFL structure is seeded with a single optical frequency, ν_0, e.g., a CW laser,

$$\psi_s(t) := \psi_0 e^{i\omega_0 t} \tag{E.1}$$

where ψ_0 is the initial seed amplitude, and $\omega_0 = 2\pi\nu_0$.

In this situation, the optical seed frequency is up/down-converted in discrete steps of the shifting frequency, ν_s, upon completion of each round-trip. In particular, assuming frequency up-conversion in the cavity, the field amplitude obtained after K round-trips (see Fig. E.1) can be written as the summation of the field resulting from each round-trip, adequately delayed by the round-trip time,

$$\begin{aligned}
\psi(t) &= \psi_0 \mathcal{H}'_0 e^{i\omega_0 t} \\
&+ \psi_0 \mathcal{H}'_0 \mathcal{H}'_1 e^{i(\omega_0+\omega_s)t} e^{i(\omega_0+\omega_s)t_c} \\
&+ \psi_0 \mathcal{H}'_0 \mathcal{H}'_1 \mathcal{H}'_2 e^{i(\omega_0+2\omega_s)t} e^{i(\omega_0+\omega_s)t_c} e^{i(\omega_0+2\omega_s)t_c} \\
&+ \psi_0 \mathcal{H}'_0 \mathcal{H}'_1 \mathcal{H}'_2 \mathcal{H}'_3 e^{i(\omega_0+3\omega_s)t} e^{i(\omega_0+\omega_s)t_c} e^{i(\omega_0+2\omega_s)t_c} e^{i(\omega_0+3\omega_s)t_c} \\
&+ \cdots \\
&+ \psi_0 \prod_{k=0}^{K} \mathcal{H}'_k e^{i(\omega_0+K\omega_s)t} e^{i(K\omega_0 t_c)} e^{i\frac{1}{2}K(K+1)\omega_s t_c}
\end{aligned} \tag{E.2}$$

where,

$\mathcal{H}'_k$ is the single-pass gain coefficient of a cavity mode with frequency $\nu_0 + k\nu_s$,
$\omega_s = 2\pi\nu_s$ is the radial shifting frequency,
t_c is the cavity round-trip time,

The envelope of the optical spectrum of the cavity, $\mathcal{H}(\nu)$, results from the competition between gain and loss mechanisms. The total gain coefficient seen by the k-th cavity mode, i.e., $\mathcal{H}_k = \mathcal{H}(\nu_0 + k\nu_s)$ is then,

$$\mathcal{H}_k := \prod_{n=0}^{k} \mathcal{H}'_n \tag{E.3}$$

Assuming that $\mathcal{H}(\nu)$ has a bandwidth $\Delta\nu = K\nu_s$, i.e., $\mathcal{H}_k = 0 \; \forall \; k > K$, the field amplitude at the output of the loop, in the steady state, writes,

$$\psi(t) = \psi_0 e^{i\omega_0 t} \sum_{n=0}^{K} \mathcal{H}_n e^{in(\omega_s t+\omega_0 t_c)} e^{i\frac{1}{2}n(n+1)\omega_s t_c} \tag{E.4}$$

Rearranging Eq. E.4 and isolating all phase terms that are linear in n, the complex amplitude of each cavity mode writes,

$$c_n := \psi_0 \mathcal{H}_n e^{in\left(\omega_0+\frac{1}{2}\omega_s\right)t_c} \tag{E.5}$$

and the field amplitude,

$$\psi(t) = e^{i\omega_0 t} \sum_{n=0}^{K} c_n e^{in\omega_s t} e^{i\frac{1}{2}n^2\omega_s t_c} \tag{E.6}$$

Noting the Fourier series structure of Eq. E.6, the spectrum of the FSFL in the steady state writes,

$$\Psi(\nu) = \sum_{k=0}^{K} c_k \delta(\nu - \nu_0 - k\nu_s) e^{i\pi \frac{\nu_s}{\nu_c} k^2} \tag{E.7}$$

where $\nu_c = t_c^{-1}$.

This spectrum is, indeed, a Dirac comb with a frequency spacing dictated by the shifting frequency, ν_s, and where the first component oscillates at the seed frequency, ν_0 (see Fig. E.1(b)). The bandwidth, $\Delta\nu$, and overall spectral envelope, $\mathcal{H}(\nu)$, are set by the resulting competition of gain and loss mechanisms in the cavity.

The key point to notice here is the quadratic dependence of the spectral phase sequence with the comb line index parameter k,

$$\phi_k := \pi \frac{\nu_s}{\nu_c} k^2 \tag{E.8}$$

Remarkably, this sequence is isomorphic to a spectral Talbot phase (see Eq. 3.48), where,

$$\frac{\nu_s}{\nu_c} \equiv \frac{p_2}{q_2} \tag{E.9}$$

Provided that the term $\nu_c^{-1}\nu_s$ can be expressed as an irreducible fraction of two natural numbers, $q_2^{-1}p_2$, the output of the FSFL in the time domain has the form of a temporal Talbot (sub-)image (see Fig. E.1(a)); i.e., it is a train of pulses with repetition period,

$$t_r = \frac{1}{q_2 \nu_s} \tag{E.10}$$

E.1.2 Group delay and equivalent dispersion

A wave circulating within the FSFL cavity completes a cycle with the round-trip time, t_c, and its simultaneously up(down)-converted by the shifting frequency ν_s. Each frequency component of the comb is then delayed a time t_c with respect to the previous comb line. The group delay distribution of the comb writes then,

$$t_g(\nu) = \frac{\nu}{\nu_s \nu_c} \tag{E.11}$$

As per the definition of the group delay[1],

$$t_g(\omega) := -\frac{\mathrm{d}}{\mathrm{d}\omega} \phi(\omega) \tag{E.12}$$

where $\phi(\omega)$ is the spectral phase distribution as a function of radial frequency.

[1] For further details, consult Section 2.3.2.2

Solving Eq. E.12,

$$\begin{aligned}\phi(\omega) &= -\int t_g(\omega)\,\mathrm{d}\omega \\ &= -\frac{1}{2\pi\nu_s\nu_c}\int \omega\,\mathrm{d}\omega \\ &= -\frac{\omega^2}{4\pi\nu_s\nu_c} + C \end{aligned} \tag{E.13}$$

where C is an undetermined integration constant that simply translates into a uniform spectral phase shift for all components of the comb, and can, thus, be neglected for practical purposes.

Identifying terms with the general expression of the second-order approximation of a dispersive medium[2], and using $t_r = \nu_s^{-1}$, the equivalent dispersion of the FSFL writes,

$$2\pi|\beta_2|z = \frac{\nu_s}{\nu_c}t_r^2 \tag{E.14}$$

Note that, while Eq. E.14 has interest in that it follows the exact mathematical structure of the temporal Talbot condition for a GVD medium (see Eq. 3.50), it can be written in a more convenient form for calculation of experimental parameters as,

$$2\pi|\beta_2|z = \frac{t_c}{\nu_s} \tag{E.15}$$

E.1.3 Tunability

As per Eq. E.7, the shifting frequency, ν_s determines the FSR of the comb at the output of the FSFL. In a practical implementation, the up(down)-converter element can be implemented by an acousto-optical frequency shifter. The shifting frequency is then set by a radio-frequency synthesizer, driving the shifter. This parameter can be electronically reconfigured, without the need for altering the physical architecture of the loop. Typical acousto-optical frequency shifters operate in the MHz regime, where RF signals can be easily generated and amplified.

The bandwidth of the obtained comb is determined by $\mathcal{H}(\nu)$. Factors at play include the gain/loss balance in the cavity, the conversion efficiency of the shifting element (typically, a function of frequency), and the coupling efficiency of the FSFL output. A gain mechanism is required to compensate for the intrinsic cavity loss, as well as for the fraction of the wave coupled outside of the loop. A band-pass filter can be inserted in the cavity to limit the impact of noise arising from the gain mechanism, as well as to shape the output spectrum.

As shown above, the output field amplitude of the FSFL depends on the value of the factor $\nu_c^{-1}\nu_s$, and when this fraction produces a rational number, the FSFL generates a train of pulses that emulates a temporal Talbot (sub-)image. A particular desired Talbot condition can be achieved by modifying the shifting frequency, ν_s and/or, the cavity length (and associated round-trip time, t_c). The cavity round-trip time can

[2]For details on modeling dispersive media as linear filters, consult Section 2.3.2.2.

be calculated, as a first approximation, from the cavity length, L_c, and the effective refractive index of the propagation medium, n_{eff}, so that,

$$t_c = n_{\text{eff}} \frac{L_c}{c_0} \tag{E.16}$$

where c_0 is the speed of light in the vacuum. It should be noted that this derivation assumes that every cavity mode sees the same effective refractive index. This is a reasonable assumption for FSFL implementations in fiber optics technology with optical bandwidths ranging from a few tens to a few hundreds of GHz.

For an FSF implemented in fiber-optics technology, a cavity length of a few m of fiber will translate into round-trip times in the order of tens of ns; with associated values of ν_c in the order of tens to a few hundreds of MHz. For instance, taking a value of $n_{\text{eff}} = 1.468$, with a cavity length of $L_c = 10$ m, the round-trip time is of approximately 50 ns, corresponding to $\nu_c = 20$ MHz. As per Eq. E.15, a shifting frequency of 100 MHz in this configuration produces an equivalent dispersion value of $|\beta_2|\, z \approx 79577471.546$ ps^2/rad, corresponding to an emulated propagation through $\sim$3670104.1562 km of standard SMF-28 optical fiber at a working wavelength of 1550 nm (see Fig. 2.6). Such an extreme propagation length is simply unattainable, and renders the dispersion steps of the PCSTM impractical.

E.2 PCSTM in a CW-seeded FSFL

Taking advantage of the properties of the CW-seeded FSFL architecture, in particular, the capability to generate frequency combs with built in tunable quadratic spectral phase distributions, the phase-controlled spectral Talbot method, as presented and demonstrated in Section 5.2, can be used to generate frequency combs with user-defined FSR, tunable over several orders of magnitude. This is due to the extremely high amounts of GVD that the FSFL can emulate, thus providing access to a wide range of Talbot conditions, typically inaccessible due to stringent implementation requirements. It should be noted that, as explained in the previous Section, the capability for re-configuring the emulated GVD without modifying the system is an interesting feature of the proposed architecture; in a direct implementation using dispersive media, GVD tunability is limited, if at all possible, and only attainable through manipulation of the physical properties (e.g., length) of the propagation medium itself.

The FSFL generates a frequency comb with FSR ν_s and a quadratic spectral phase distribution that emulates the dispersion value given in Eq. E.15. In order to transform the FSR ν_s into a new FSR $r^{-1}\nu_s$ – where $r^{-1} = q_1^{-1} q_2$ – through application of the PCSTM, the required GVD is calculated following the directives given in Section 3.2.3.2, with $\nu_r \leftarrow \nu_s$. The the loop is then configured to generate a frequency comb with the desired *input* FSR, ν_s, and the desired emulated dispersion value, from Eq. E.15, by adjusting the round-trip time, t_c. Finally, also following Section 3.2.3.2, the required temporal phase modulation sequence is computed normally, as if the method started from a phase-free comb with input FSR ν_s. Fig. E.2 shows the realization of the method, using the CW-seeded FSFL as the generator of the signal in step 2 (see Section 3.2.3.2).

E.2.1 Experimental demonstration

In the following the proposed variation of the PCSTM, using a CW-seeded FSFL architecture as the starting point, is experimentally validated. The combs generated by the FSFL have FSR in the vicinity of 80 MHz (well within the RF bandwidth specifications of widely-available commercial acousto-optical frequency

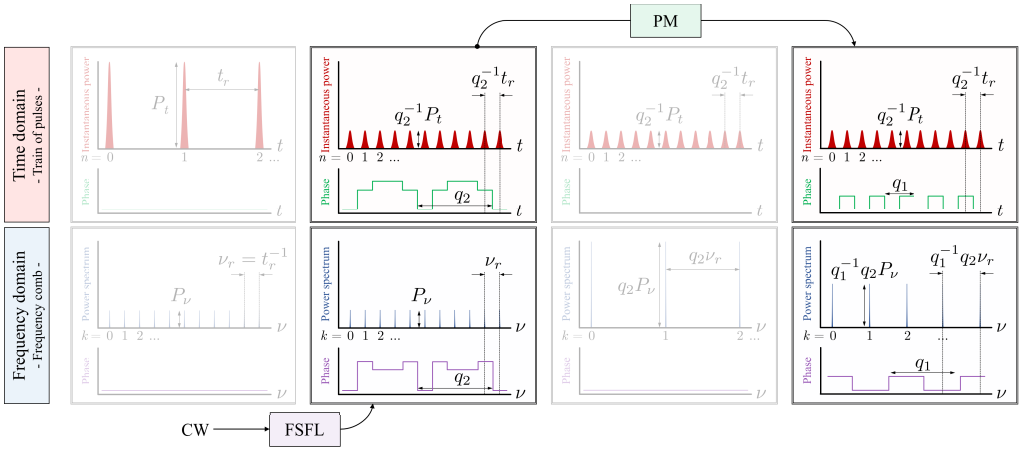

Figure E.2 – PCSTM implemented with a CW-seeded FSFL. Phase modulation of the frequency comb generated by a frequency-shifted feedback loop (a frequency comb with a built-in tunable quadratic spectral phase profile, designed to satisfy a temporal Talbot condition). The PM operation completes the sets of transformations of the phase-controlled spectral Talbot method to arbitrarily tailor the FSR of the generated comb. In the shown example, $r^{-1} = 5/2$.

shifters). The obtained output combs, after the temporal phase modulation step, have FSR ranging from $\sim$8 kHz to $\sim$8 GHz. This represents an FSR tunability range of 6 orders of magnitude, achieved through variations of electronic and RF parameters exclusively, i.e., the shifting frequency and the voltage output of the AWG that follows the temporal Talbot phase sequence.

E.2.1.1 Experimental setup

Fig. E.3 shows a simplified[3] schematic of the experimental setup used in the experimental demonstration of frequency comb generation with user-defined FSR.

A continuous-wave laser (CW) generates the seed, at a wavelength of 1550 nm ($\nu_0 \approx 193.55$ THz). The seed is then coupled into the loop, where an erbium-doped fiber amplifier (EDFA) compensates for the losses in the cavity, and an optical band-pass filter (BPF) sets the bandwidth of the comb (adjustable between a few GHz and a few hundreds of GHz), and removes excess noise from the EDFA. A free-space acousto-optical frequency shifter (AOFS), driven by a radio-frequency synthesizer around $\nu_s \sim 80$ MHz, acts as the shifting element in the cavity. The AOFS is set to down-convert the signal frequency. An RF amplifier boosts the driving signal, in order to maximize the AOFS conversion efficiency.

A fraction of the optical field circulating in the loop is coupled out and directed to an electro-optical phase modulator (EOPM), with an RF bandwidth of 40 GHz. The modulator is driven by an arbitrary waveform generator (AWG) capable of delivering 24 Gs/s with an analog bandwidth of 7 GHz. The AWG generates an analog voltage signal following the phase levels given by Eq. 5.3, and matching the repetition rate of the pulses at the output of the FSFL. A tunable optical delay line is used to align the optical signal to the voltage drive, and a polarization controller is used to maximize the modulation efficiency.

All the experimental results reported in the following section are obtained with a FSFL designed for a round-trip time of $t_c = 76.2$ ns, corresponding to $\nu_c \approx 13.13$ MHz. Different configurations of the loop are obtained by electronically modifying the value of ν_s.

[3]For a complete schematic of the setup, see Fig. D.6.

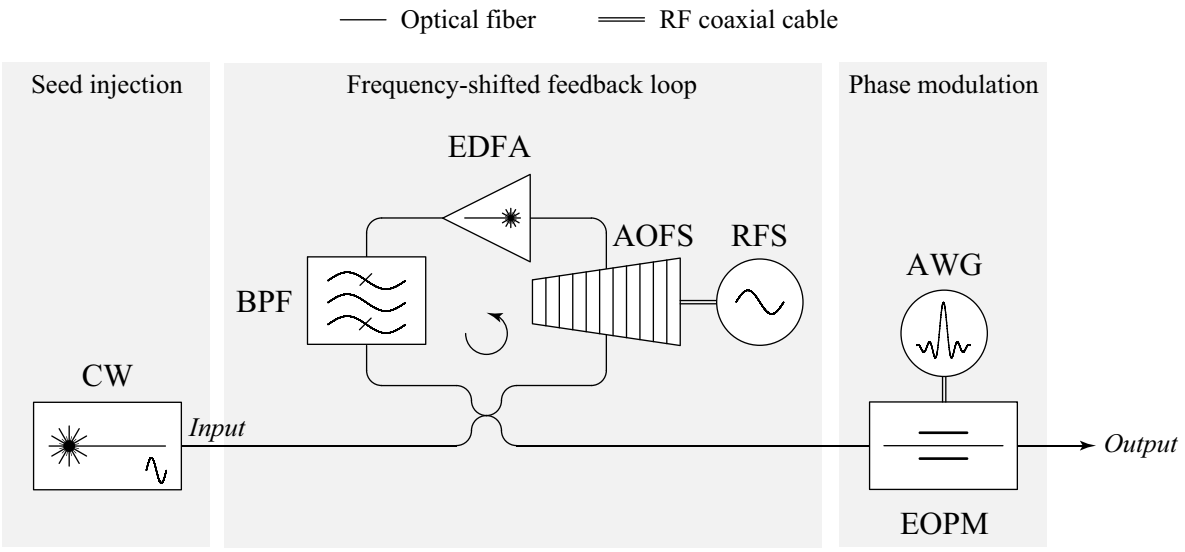

Figure E.3 – Generation of frequency combs with user-defined FSR, experimental setup. CW, continuous-wave laser; RFS, radio-frequency synthesizer; AOFS, acousto-optical frequency shifter; EDFA, erbium-doped fiber amplifier; BPF, band-pass filter; AWG, arbitrary waveform generator; EOPM, electro-optical phase modulator. For a complete schematic of the experimental setup, see Fig. D.6.

E.2.1.2 Experimental results

First, the output signal of the CW-seeded FSFL is analyzed in the absence of temporal phase modulation. Fig. E.4 shows a typical trace of the output spectrum of the CW-seeded FSFL, measured with an optical spectrum analyzer.

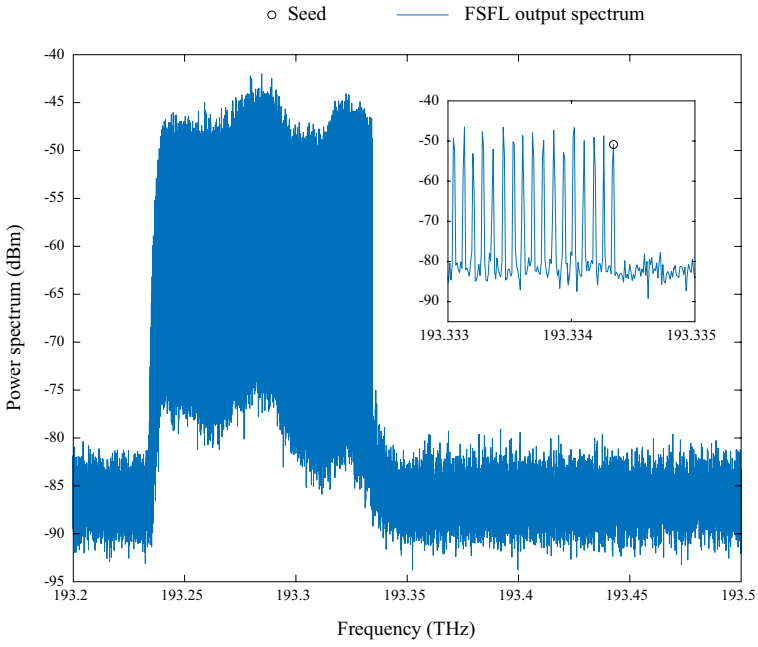

Figure E.4 – Typical output spectrum of a CW-seeded fiber FSFL. Measured optical power spectrum at the output of the fiber loop. The shown spectrum has a bandwidth of $\Delta\nu \approx 96$ GHz. The AOFS is driven at $\nu_s \approx 80$ MHz in the down-shifting configuration (i.e., the rightmost comb line corresponds to the seed frequency). The resulting frequency comb has then $K \approx 1200$ lines, starting from the seed frequency, $\nu_0 \approx 193.55$ THz.

Table E.2 lists for tested values of the shifting frequency, ν_s, the emulated Talbot parameters, p_2 and q_2, and corresponding emulated GVD.

Table E.2 – FSFL operation, experimental conditions and results. List of parameters of the CW-seeded FSFL and the obtained output signals for a set of 4 conducted tests in the absence o temporal phase modulation. In all cases, $t_c = 76.2$ ns.

	FSFL parameters		**FSFL signal characteristics**				
	ν_s [a]	ν_c [b]	p_2 [c]	q_2 [d]	ν_r [e]	t_r [f]	$\lvert\beta_2\rvert z$ [g]
(1)	78.80	13.13	6	1	78.80	12.690	$1.539 \cdot 10^8$
(2)	78.84	13.13			78.84	12.684	$1.538 \cdot 10^8$
(3)	80.42	13.13	49	8	80.42	12.435	$1.508 \cdot 10^8$
(4)	81.41	13.13	31	5	81.41	12.284	$1.490 \cdot 10^8$

[a] Shifting frequency (MHz).
[b] Inverse cavity round-trip time (MHz).
[c] Numerator of the Talbot condition emulated by the FSFL.
[d] Denominator of the Talbot condition emulated by the FSFL.
[e] FSR of the generated frequency comb (MHz).
[f] Repetition period of the generated pulse train (ns).
[g] Equivalent second-order dispersion (ps^2/rad).

Fig. E.5 shows a set of measurements corresponding to the experimental conditions and results listed on Table E.2. The traces in Fig. E.5(a) show the measured line-to-line spectral phase distribution of the generated frequency comb. These traces are obtained by mixing the generated comb with a fraction of the seed CW laser[4] in a 28 GHz bandwidth photodiode, a process commonly referred to as optical heterodyning. The resulting photocurrent is captured by an oscilloscope and the phase of its Fourier transform is computed, resulting on the represented traces. The traces in Fig. E.5(b) show the photocurrent resulting from direct detection of the output pulse train of the FSFL.

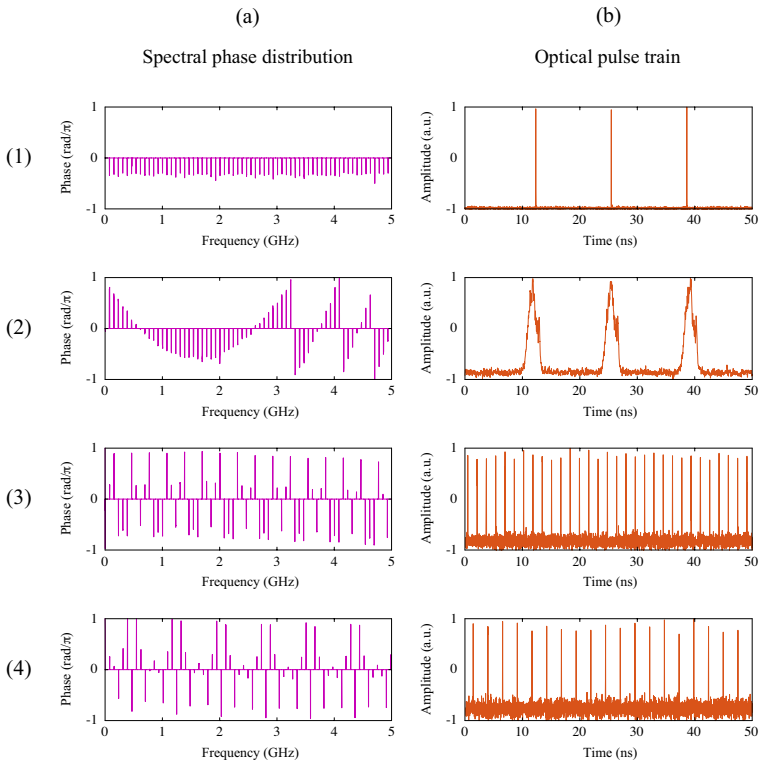

Figure E.5 – FSFL operation, experimental results. Set of measurements corresponding to the experimental conditions and results listed on Table E.2, and following the same numbering (1)-(4). (a) Spectral line-to-line phase distribution of the generated optical frequency combs, and, (b) instantaneous power traces of the generated trains of optical pulses. Experiment (1) corresponds to an integer temporal Talbot condition; the spectral phase is flat and the obtained pulse train repeats at the rate set by the shifting frequency, ν_s. Experiments (3) and (4) corresponds to fractional Talbot conditions, resulting in rate-multiplied optical trains, by the emulated Talbot parameter q_2 (see Table E.2(3),(4)). The configuration of the loop in experiment (2) does not correspond to a Talbot condition; a train of stretched (chirped) optical pulses is then obtained.

[4] For a detailed depiction of the heterodyne measurement process, see Fig. D.6.

Experiment (1) corresponds to a configuration of the FSFL to emulate an integer Talbot condition; the obtained optical signal is a transform-limited (no spectral phase variations) train of optical pulses with a repetition rate dictated by the cavity shifting frequency, ν_s (also setting the FSR of the corresponding frequency comb). Note that the values of ν_s and ν_c listed on entry (2) of Table E.2 do not satisfy a Talbot condition. The generated optical signal behaves as a train of pulses with excess dispersion, thus resulting in broader optical pulses with a quadratic spectral phase distribution (see Fig. E.5(2)), resulting on linear frequency modulation of the pulses, or chirp. The loop satisfies fractional Talbot conditions for experiments (3) and (4), thus obtaining rate-multiplied optical pulse trains with associated spectral Talbot phases.

Next, the PCSTM is tested with the proposed FSFL architecture as its starting point. For this purpose, the required temporal Talbot phase sequences are introduced to the pulse trains generated by the loop. Table E.3 lists the parameters of the generated FSFL signals, applied temporal Talbot phases and obtained results.

Table E.3 – Generation of frequency combs with user-defined FSR, experimental conditions and results. List of experimental conditions and results of 7 experiments showing generation of frequency combs with tunable FSR, ranging from $\sim$8 kHz to $\sim$8 GHz.

	FSFL parameters		**PCSTM parameters**				**Output comb**	
	ν_s [a]	ν_c [b]	p_2 [c]	q_2 [d]	q_1 [e]	r^{-1} [f]	$r^{-1}\nu_s$ [g]	$\lvert\beta_2\rvert z$ [h]
(1)	78.91	13.13	601	100	1	100	$7.89 \cdot 10^3$	$1.537 \cdot 10^8$
(2)	82.46	13.13	157	25	2	12.5	$1.03 \cdot 10^3$	$1.471 \cdot 10^8$
(3)	83.16	13.13	19	3	11	$0.\overline{27}$	22.68	$1.458 \cdot 10^8$
(4)	78.80	13.13	6	1	10	0.1	7.88	$1.539 \cdot 10^8$
(5)	78.80	13.13	6	1	100	0.01	$7.88 \cdot 10^{-1}$	$1.539 \cdot 10^8$
(6)	78.80	13.13	6	1	1000	0.001	$7.88 \cdot 10^{-2}$	$1.539 \cdot 10^8$
(7)	78.80	13.13	6	1	10000	0.0001	$7.88 \cdot 10^{-3}$	$1.539 \cdot 10^8$

[a] Shifting frequency (MHz).
[b] Cavity round-trip frequency, t_c^{-1} (MHz).
[c] Numerator of the Talbot condition emulated by the FSFL.
[d] Denominator of the Talbot condition emulated by the FSFL (numerator of the FSR multiplication factor).
[e] Denominator of the FSR multiplication factor (set by the PM process).
[f] FSR multiplication factor.
[g] Output FSR (MHz).
[h] Equivalent second-order dispersion (ps^2/rad).

Fig. E.6(a) shows the optical spectrum of the signal generated by the FSFL, measured with an optical spectrum analyzer, as well as the output of the EOPM, showing energy-preserving multiplication of the original FSR by $r^{-1} = 100$. Fig. E.6(b) shows the voltage signal applied to the EOPM, compared to the Talbot phase sequence prescribed by the PCSTM for the desired FSR multiplication factor. The shown results correspond to entry (1) of Table E.3.

The measured results, shown in Fig. E.6(a) confirm multiplication of the FSR of the comb generated by the FSFL, 78.91 MHz, by the desired factor $r^{-1} = 100$, producing an FSR of 7.89 GHz. As per the characteristics of the PCSTM, the overall comb energy is nearly preserved; the power ratio between the measured output and input comb lines is $\sim$17 dB, approaching the expected ideal value of $10\log_{10}(100) = 20$ dB. Residual energy remains in the output spectrum at discrete frequencies corresponding to the input comb lines. This imperfect realization of the process is mainly attributed to practical deviations in the temporal PM profile imposed on the FSFL output, as compared with the theoretical prescription (Fig. E.6(b)). The spectral envelope, bandwidth, and frequency grid of the input comb are not modified by the FSR multiplica-

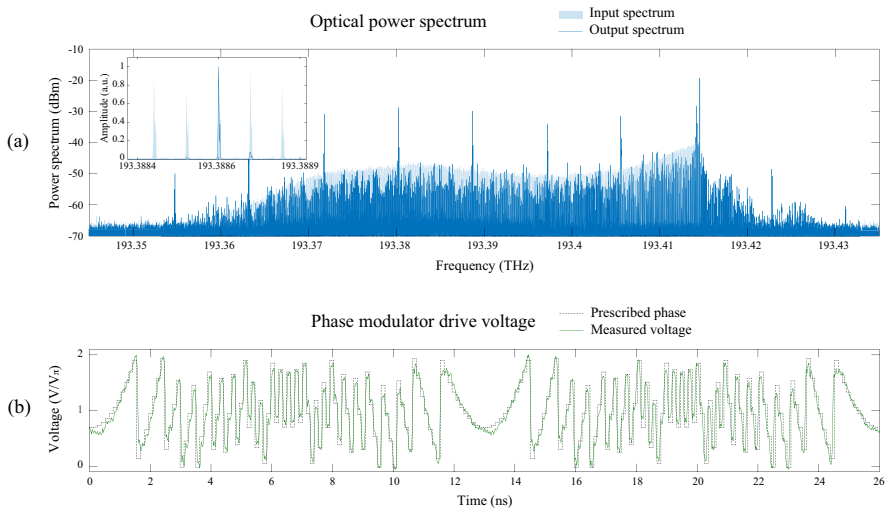

Figure E.6 – FSR multiplication of the FSFL output comb by a factor 100, experimental results. (a) Measured optical spectra of the comb generated by the FSFL (78.91 MHz FSR) and the obtained output comb after energy-preserving FSR multiplication by a factor 100 (7.89 GHz FSR). Conservation of the comb energy, spectral envelope, and input frequency grid is observed. (b) Temporal phase modulation sequence and generated EOPM driving voltage, required by the PCSTM for the FSR multiplication process. The shown example corresponds to the parameters listed in Table E.3(1).

tion process. Additionally, the individual output lines (inset of Fig. E.6(a)) show no noticeable broadening (within the limit of the measurement integration time). Finally, as expected in the application of the PCSTM, the spectral noise floor level of the comb – mainly due to amplified spontaneous emission in the FSFL cavity – is not affected by the FSR multiplication process.

Fig. E.7 shows a set of measurements of the frequency combs generated by the FSFL, and the output combs, after application of the temporal phase modulation. The shown traces are obtained following the same procedure used in the characterization of the spectral phase sequences of the FSFL combs, shown in Fig. E.5(a), i.e., by mixing the seed laser with the generated comb in a 28 GHz photodiode, and calculating the Fourier spectrum of the resulting photocurrent in an electrical real-time oscilloscope.

Fig. E.7(1) (corresponding to Table E.3(1)) shows the RF spectra corresponding to the optical spectra shown in Fig. E.6(a). The FSR multiplication factor and energy redistribution effects are clearly noticeable.

Fig. E.7(2) (corresponding to Table E.3(2)) shows an example of FSR multiplication by a fractional factor, $r^{-1} = 12.5 > 1$, from 82.46 MHz at the output of the FSFL to 1.03 GHz after the PM process. The measured power ratio between output and input comb lines is $\sim$9 dB, slightly short of the expected $10\log_{10}(12.5) \approx 11$ dB. Once more, this is mainly attributed to practical deviations in the temporal PM profile.

Fig. E.7(3) (corresponding to Table E.3(3)) shows an example of FSR multiplication by a fractional factor, $r^{-1} = 0.\overline{27} < 1$, from 83.16 MHz at the output of the FSFL to 22.68 MHz after the PM process.

Fig. E.7(4)-(7) (corresponding to Table E.3(4)-(7)) show examples of FSR multiplication by the factors 0.1, 0.01, 0.001 and 0.0001, respectively. The resulting combs have respective FSR values of 7.88 MHz, 788 kHz, 78.8 kHz and 7.88 kHz. These combs are generated from an input FSFL comb with FSR of 78.8 MHz and uniform spectral phase distribution (i.e., starting from an integer temporal Talbot condition).

These results demonstrate the unique capabilities of the FSFL architecture to generate frequency combs with user-defined FSR, through the application of the PCSTM. The reported results illustrate the unprecedented tunability of the FSR by purely electronic means (simply modifying the frequency of an RF tone in the MHz regime), here demonstrated over 6 orders of magnitude on the generated frequency combs (from $\sim$8 kHz to $\sim$8 GHz), while preserving the energy and overall characteristics (bandwidth, spectral envelope and frequency grid) of the generated input comb.

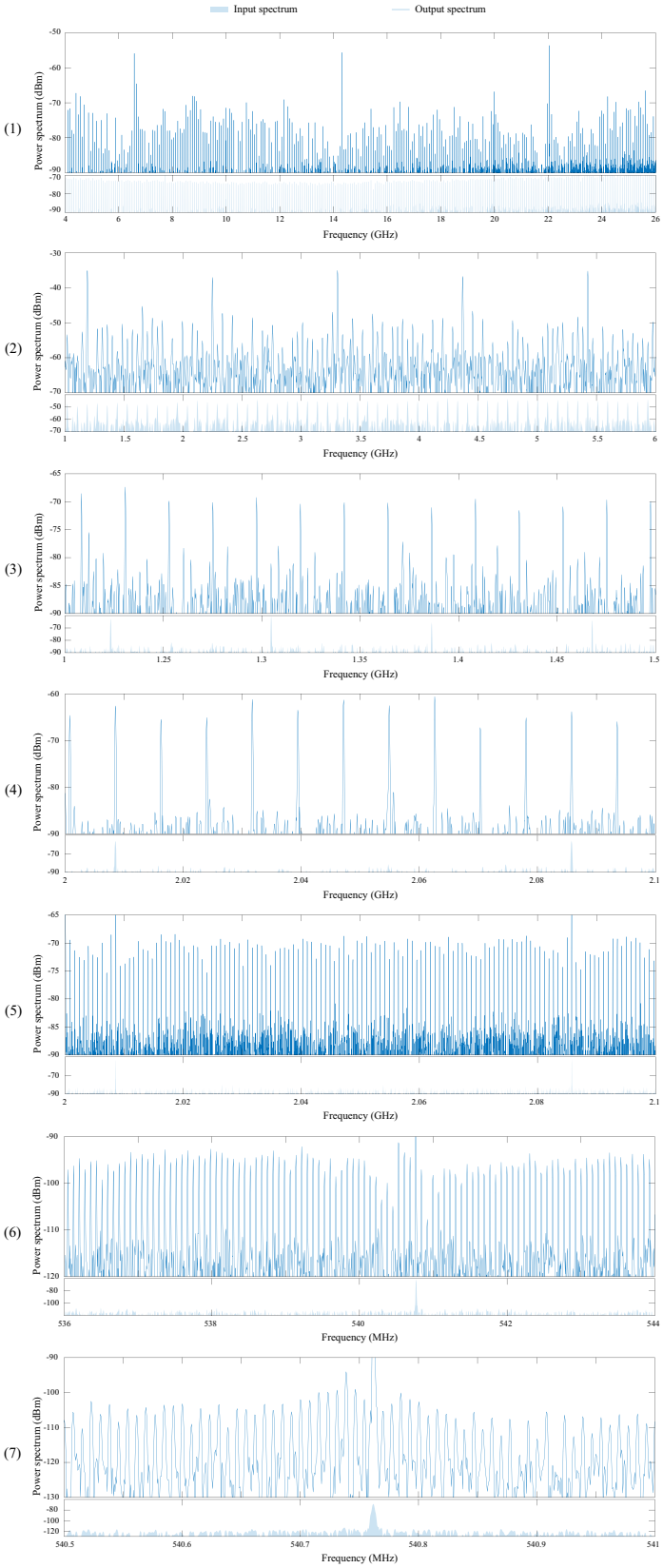

Figure E.7 – Arbitrary FSR comb generation by the PCSTM with a FSFL, experimental results. Measured RF spectra of frequency combs generated by the FSFL and processed by the PCSTM. The figure numbering corresponds to the entry list of Table E.3.

References

[1] W. H. Bragg and S. W. L. Bragg, "The reflection of X-rays by crystals," *Proc. Royal Soc. Lond. A*, **88**, 428–438 (1913).

[2] J. M. Cowley *Diffraction physics*, Elsevier (1995).

[3] E. G. Loewen and E. Popov *Diffraction gratings and applications*, CRC Press (1997).

[4] P. M. Morse and K. U. Ingard *Theoretical Acoustics*, Princeton University Press (1968).

[5] H. Chen, C. T. Chan, and P. Sheng, "Transformation optics and metamaterials," *Nat. Mater.*, **9**, 387–96 (2010).

[6] T. G. Mackay and A. Lakhtakia, "Negative refraction, negative phase velocity, and counterposition," *Phys. Rev. B*, **79**, 235 121 (2009).

[7] F. Aieta, P. Genevet, M. A. Kats, Nanfang, R. Blanchard, Z. Gaburro, and F. Capasso, "Aberration-free ultrathin flat lenses and axicons at telecom wavelengths based on plasmonic metasurfaces," *Nano Lett.*, **12**, 4932–4936 (2012).

[8] X. Zhang and Z. Liu, "Superlenses to overcome the diffraction limit," *Nat. Mater.*, **7**, 435–441 (2008).

[9] R. W. Boyd and D. J. Gauthier, "Controlling the velocity of light pulses," *Science*, **326**, 1074–1077 (2009).

[10] G. Gbur, "Chapter 2 - Invisibility physics: past, present, and future," *Progress in Optics*, **58**, 65–114 (2013).

[11] G. Hobbs, W. Coles, R. N. Manchester, M. J. Keith, R. M. Shannon, D. Chen, M. Bailes, N. D. R. Bhat, S. Burke-Spolaor, D. Champion, A. Chaudhary, A. Hotan, J. Khoo, J. Kocz, Y. Levin, S. Oslowski, B. Preisig, V. Ravi, J. E. Reynolds, J. Sarkissian, W. van Straten, J. P. W. Verbiest, D. Yardley, and X. P. You, "Development of a pulsar-based time-scale," *Mon. Notices Royal Astron. Soc.*, **427**, 2780–2787 (2012).

[12] M. I. Skolnik *Radar handbook*, McGraw-Hill Education (2008).

[13] P. Dong and Q. Chen *LiDAR remote sensing and applications*, CRC Press (2017).

[14] B. Sklar *Digital communications: fundamentals and applications*, Pearson Education (2009).

[15] P. W. Smith, M. A. Duguay, and E. P. Ippen *Mode-locking of lasers*, Pergamon Press (1974).

[16] B. E. A. Saleh and M. C. Teich *Fundamentals of photonics*, Wiley (2007).

[17] S. E. Harris, B. J. McMurtry, and A. E. Siegman, "Modulation and direct demodulation of coherent and incoherent light at a microwave frequency," *Appl. Phys. Lett.*, **1**, 37–39 (1962).

[18] G. P. Agrawal *Fiber-optic communication systems*, Wiley (1997).

[19] G. T. Reed, G. Mashanovich, F. Y. Gardes, and D. J. Thomson, "Silicon optical modulators," *Nat. Photon.*, **4**, 518–526 (2010).

[20] L. Alloatti, R. Palmer, S. Diebold, K. P. Pahl, B. Chen, R. Dinu, M. Fournier, J.-M. Fedeli, T. Zwick, W. Freude, C. Koos, and J. Leuthold, "100 GHz silicon-organic hybrid modulator," *Light Sci. Appl.*, **3** (2014).

[21] J. Willis E. Lamb, "Theory of an optical maser," *Phys. Rev.*, **134**, A1429 (1964).

[22] T. Gaumnitz, A. Jain, Y. Pertot, M. Huppert, I. Jordan, F. Ardana-Lamas, and H. J. Wörner, "Streaking of 43-attosecond soft-X-ray pulses generated by a passively CEP-stable mid-infrared driver," *Opt. Express*, **22**, 27 506–27 518 (2017).

[23] R. Paschotta *Encyclopedia of laser physics and technology*, John Wiley & Sons (2008).

[24] E. Ding, W. H. Renninger, F. W. Wise, P. Grelu, E. Shlizerman, , and J. N. Kutz, "High-energy passive mode-locking of fiber lasers," *Int. J. Opt.*, **2012** (2012).

[25] S. A. Diddams, L. Hollberg, and V. Mbele, "Molecular fingerprinting with the resolved modes of a femtosecond laser frequency comb," *Nature*, **445**, 627–630 (2007).

[26] K. Plamann, F. Aptel, C. L. Arnold, A. Courjaud, C. Crotti, F. Deloison, F. Druon, P. Georges, M. Hanna, J.-M. Legeais, F. Morin, E. Mottay, V. Nuzzo, D. A. Peyrot, and M. Savoldelli, "Ultrashort pulse laser surgery of the cornea and the sclera," *J. Opt.*, **12**, 084 002 (2010).

[27] H. Hora, S. Eliezer, G. J. Kirchhoff, N. Nissim, J. X. Wang, P. Lalousis, Y. X. Xu, G. H. Miley, J. M. Martinez-Val, W. McKenzie, and J. Kirchhoff, "Road map to clean energy using laser beam ignition of boron-hydrogen fusion," *Laser Part. Beams*, **35**, 730–740 (2017).

[28] J. Pfeifle, V. Brasch, M. Lauermann, Y. Yu, D. Wegner, T. Herr, K. Hartinger, P. Schindler, J. Li, D. Hillerkuss, R. Schmogrow, C. Weimann, R. Holzwarth, W. Freude, J. Leuthold, T. J. Kippenberg, and C. Koos, "Coherent terabit communications with microresonator Kerr frequency combs," *Nat. Photon.*, **8**, 375–380 (2014).

[29] P. Marin-Palomo, J. N. Kemal, M. Karpov, A. Kordts, J. Pfeifle, M. H. P. Pfeiffer, P. Trocha, S. Wolf, V. Brasch, M. H. Anderson, R. Rosenberger, K. Vijayan, W. Freude, T. J. Kippenberg, and C. Koos, "Microresonator-based solitons for massively parallel coherent optical communications," *Nature*, **546**, 274–279 (2017).

[30] P. Ghelfi, F. Laghezza, F. Scotti, G. Serafino, A. Capria, S. Pinna, D. Onori, C. Porzi, M. Scaffardi, A. Malacarne, V. Vercesi, E. Lazzeri, F. Berizzi, and A. Bogoni, "A fully photonics-based coherent radar system," *Nature*, **507**, 341–345 (2014).

[31] S. T. Cundiff and A. M. Weiner, "Optical arbitrary waveform generation," *Nat. Photon.*, **4**, 760–766 (2010).

[32] A. M. Weiner, "Ultrafast optical pulse shaping: a tutorial review," *Opt. Commun.*, **284**, 3669–3692 (2011).

[33] S. A. Diddams, "The evolving optical frequency comb," *J. Opt. Soc. Am. B*, **27**, B51–B62 (2010).

[34] J. Ye and S. T. Cundiff *Femtosecond optical frequency comb: principle, operation and applications*, Springer Science & Business Media (2006).

[35] D. J. Jones, S. A. Diddams, J. K. Ranka, A. Stentz, R. S. Windeler, J. L. Hall, and S. T. Cundiff, "Carrier-envelope phase control of femtosecond mode-locked lasers and direct optical frequency synthesis," *Science*, **288**, 635–639 (2000).

[36] T. W. Hänsch, "Nobel lecture: Passion for precision," *Rev. Mod. Phys.*, **78**, 1297–1309 (2006).

[37] N. R. Newbury, "Searching for applications with a fine-tooth comb," *Nat. Photon*, **5**, 186–188 (2011).

[38] M. T. Murphy, T. Udem, R. Holzwarth, A. Sizmann, L. Pasquini, C. Araujo-Hauck, H. Dekker, S. D'Odorico, M. Fischer, T. W. Hänsch, and A. Manescau, "High-precision wavelength calibration of astronomical spectrographs with laser frequency combs," *Mon. Notices Royal Astron. Soc.*, **380**, 839–847 (2007).

[39] T. Steinmetz, T. Wilken, C. Araujo-Hauck, R. Holzwarth, T. W. Hänsch, L. Pasquini, A. Manescau, S. D'Odorico, M. T. Murphy, T. Kentischer, W. Schmidt, and T. Udem, "Laser frequency combs for astronomical observations," *Science*, **321**, 1335–1337 (2008).

[40] C.-H. Li, A. J. Benedick, P. Fendel, A. G. Glenday, F. X. Kärtner, D. F. Phillips, D. Sasselov, A. Szentgyorgyi, and R. L. Walsworth, "A laser frequency comb that enables radial velocity measurements with a precision of 1 cm s^{-1}," *Nature*, **452**, 610–612 (2008).

[41] J. L. Hall, "Nobel lecture: Defining and measuring optical frequencies," *Rev. Mod. Phys.*, **78**, 1279–1295 (2006).

[42] I. Coddington, N. Newbury, and W. Swann, "Dual-comb spectroscopy," *Optica*, **3**, 414–426 (2016).

[43] C. Reimer, M. Kues, P. Roztocki, B. Wetzel, F. Grazioso, B. E. Little, S. T. Chu, T. Johnston, Y. Bromberg, L. Caspani, D. J. Moss, and R. Morandotti, "Generation of multiphoton entangled quantum states by means of integrated frequency combs," *Science*, **351**, 1176–1180 (2016).

[44] F. Helmchen and W. Denk, "Deep tissue two-photon microscopy," *Nat. Methods*, **2**, 932–940 (2005).

[45] J. Cheng, C.-S. Liu, S. Shang, D. Liu, W. Perrie, G. Dearden, and K. Watkins, "A review of ultrafast laser materials micromachining," *Opt. Laser. Technol.*, **46**, 88–102 (2013).

[46] G. A. Mourou, T. Tajima, and S. V. Bulanov, "Optics in the relativistic regime," *Rev. Mod. Phys.*, **78**, 309–371 (2006).

[47] S. Arahira, Y. Matsui, and Y. Ogawa, "Mode-locking at very high repetition rates more than terahertz in passively mode-locked distributed-Bragg-reflector laser diodes," *IEEE J. Quantum Electron.*, **32**, 1211–1224 (1996).

[48] T. J. Kippenberg, R. Holzwarth, and S. A. Diddams, "Microresonator-based optical frequency combs," *Sciecne*, **332**, 555-559 (2011).

[49] G. Sobon, K. Krzempek, P. Kaczmarek, K. M. Abramski, and M. Nikodem, "10 GHz passive harmonic mode-locking in Er-Yb double-clad fiber laser," *Opt. Commun.*, **284**, 4203–4206 (2011).

[50] L. N. Binh *Photonic signal processing: techniques and applications*, CRC Press (2007).

[51] P. Wang, L. Zhan, Z. Gu, Q. Ye, X. Hu, and Y. Xia, "Arbitrary numerator rational-harmonic mode locking in fiber ring lasers," *J. Opt. Soc. Am. B*, **21**, 1781–1783 (2004).

[52] P. Petropoulos, M. Ibsen, M. N. Zervas, and D. J. Richardson, "Generation of a 40-GHz pulse stream by pulse multiplication with a sampled fiber Bragg grating," *Opt. Lett.*, **25**, 521–523 (2000).

[53] O. de Vries, T. Saule, M. Plötner, F. Lücking, T. Eidam, A. Hoffmann, A. Klenke, S. Hädrich, J. Limpert, S. Holzberger, T. Schreiber, R. Eberhardt, I. Pupeza, , and A. Tünnermann, "Acousto-optic pulse picking scheme with carrier-frequency-to-pulse-repetition-rate synchronization," *Opt. Express*, **23**, 19 586–19 595 (2015).

[54] G. Chang, C. Li, D. F. Phillips, A. Szentgyorgyi, R. L. Walsworth, and F. X. Kärtner, "Optimization of filtering schemes for broadband astro-combs," *Opt. Express*, **20**, 24 987–25 013 (2012).

[55] Y. Vidne, M. Rosenbluh, and T. W. Hänsch, "Pulse picking by phase-coherent additive pulse generation in an external cavity," *Opt. Lett.*, **28**, 2396–2398 (2003).

[56] J. Azaña and M. A. Muriel, "Temporal self-imaging effects: theory and application for multiplying pulse repetition rates," *IEEE J. Sel. Top. Quantum Electron.*, **7**, 728–744 (2001).

[57] R. Maram, J. Van Howe, M. Li, and J. Azaña, "Noiseless intensity amplification of repetitive signals by coherent addition using the temporal Talbot effect," *Nat. Commun.*, **5**, 5163 (2014).

[58] R. Maram, J. Van Howe, M. Li, and J. Azaña, "Lossless fractional repetition-rate multiplication of optical pulse trains," *Opt. Lett.*, **40**, 375–378 (2015).

[59] J. Azaña, "Spectral Talbot phenomena of frequency combs induced by cross-phase modulation in optical fibers," *Opt. Lett.*, **30**, 227–229 (2005).

[60] R. Maram and J. Azaña, "Spectral self-imaging of time-periodic coherent frequency combs by parabolic cross-phase modulation," *Opt. Express*, **21**, 28 824–28 835 (2013).

[61] A. Malacarne and J. Azaña, "Discretely tunable comb spacing of a frequency comb by multilevel phase modulation of a periodic pulse train," *Opt. Express*, **21**, 4139–4144 (2013).

[62] V. Ataie, D. Esman, B. P. Kuo, N. Alic, and S. Radic, "Subnoise detection of a fast random event," *Science*, **350**, 1343–1346 (2015).

[63] B. C. Smith *Fundamentals of Fourier transform infrared spectroscopy*, CRC Press (2011).

[64] D. Thornton, B. Stappers, M. Bailes, B. Barsdell, S. Bates, N. D. R. Bhat, M. Burgay, S. Burke-Spolaor, D. J. Champion, P. Coster, N. D'Amico, A. Jameson, S. Johnston, M. Keith, M. Kramer, L. Levin, S. Milia, C. Ng, A. Possenti, and W. van Straten, "A population of fast radio bursts at cosmological distances," *Science*, **341**, 53–56 (2013).

[65] R. C. Gonzalez *Digital Image Processing*, Pearson Education (2009).

[66] J. Kim and Y. Song, "Ultralow-noise mode-locked fiber lasers and frequency combs: principles, status, and applications," *Adv. Opt. Photon.*, **8**, 465–540 (2016).

[67] R. A. Probst, T. Steinmetz, T. Wilken, H. Hundertmark, S. P. Stark, G. K. L. Wong, P. S. J. Russell, T. W. Hänsch, R. Holzwarth, and T. Udem, "Nonlinear amplification of side-modes in frequency combs," *Opt. Express*, **21**, 11 670–11 687 (2013).

[68] N. R. Newbury and W. C. Swann, "Low-noise fiber-laser frequency combs," *J. Opt. Soc. Am. B*, **8**, 1756–1770 (2007).

[69] S. S. Haykin *Communication systems*, Wiley (2001).

[70] R. N. McDonough and A. D. Whalen *Detection of signals in noise*, Elsevier (1995).

[71] J. W. Goodman *Introduction to Fourier optics*, McGraw-Hill (1988).

[72] J. Als-Nielsen and D. McMorrow *Elements of Modern X-ray Physics*, Wiley (2011).

[73] K. B. Howell *Principles of Fourier analysis*, CRC Press LLC (2016).

[74] A. V. Oppenheim and A. S. Willsky *Signals and systems*, Prentice Hall (1997).

[75] G. P. Agrawal *Nonlinear fiber optics*, Academic Press (2012).

[76] Corning®, "SMF-28® Ultra Optical Fiber," PI1424 specification sheet (2014).

[77] H. F. Talbot, "LXXVI. Facts relating to optical science. No. IV," *Philos. Mag.*, **9**, 401–407 (1836).

[78] Lord Rayleigh, "XXV. On copying diffraction-gratings, and on some phenomena connected therewith," *Philos. Mag.*, **11**, 196–205 (1881).

[79] K. Patorski, "I The self-imaging phenomenon and its applications," *Progress in Optics*, **27**, 1–108 (1989).

[80] J. Wen, Y. Zhang, and M. Xiao, "The Talbot effect: recent advances inclassical optics, nonlinear optics, and quantum optics," *Adv. Opt. Photon.*, **5**, 83–130 (2015).

[81] A. R. Maripov and Y. Ismanov, "The Talbot effect (a self-imaging phenomenon) in holography," *J. Opt.*, **25**, 3 (1994).

[82] H. Hamam and J. L. de Bougrenet de la Tocnaye, "Programmable joint fractional Talbot computer-generated holograms," *J. Opt. Soc. Am. A*, **12**, 314–324 (1995).

[83] H. Dammann, G. Groh, and M. Kock, "Restoration of faulty images of periodic objects by means of self-imaging," *Appl. Opt.*, **10**, 1454–1455 (1971).

[84] H. Hamam, "Talbot imaging and unification," *Appl. Opt.*, **42**, 7052–7059 (2003).

[85] A. Isoyan, F. Jiang, Y. C. Cheng, F. Cerrina, P. Wachulak, L. Urbanski, J. Rocca, C. Menoni, and M. Marconi, "Talbot lithography: self-imaging of complex structures," *J. Vac. Sci. Technol. B Microelectron. Nanometer. Struct. Process. Meas. Phenom.*, **27**, 2931–2937 (2009).

[86] B. J. McMorran and A. D. Cronin, "An electron Talbot interferometer," *New J. Phys.*, **11**, 033 021 (2009).

[87] Y. Yu, D. Chassaing, T. Scherer, B. Landenberger, and H. Zappe, "The focusing and Talbot effect of periodic arrays of metallic nanoapertures in high-index medium," *Plasmonics*, **8**, 723–732 (2013).

[88] M. S. Chapman, C. R. Ekstrom, T. D. Hammond, J. Schmiedmayer, B. E. Tannian, S. Wehinger, and D. E. Pritchard, "Near-field imaging of atom diffraction gratings: The atomic Talbot effect," *Phys. Rev. A*, **51**, R14–R17 (1995).

[89] J. Ruostekoski, B. Kneer, W. P. Schleich, and G. Rempe, "Interference of a Bose-Einstein condensate in a hard-wall trap: From the nonlinear Talbot effect to the formation of vorticity," *Phys. Rev. A*, **63**, 043 613 (2001).

[90] X.-B. Song, H.-B. Wang, J. Xiong, K. Wang, X. Zhang, K.-H. Luo, and L.-A. Wu, "Experimental observation of quantum Talbot effects," *Phys. Rev. Lett.*, **107**, 033 902 (2011).

[91] T. Jannson and J. Jannson, "Temporal self-imaging effect in single-mode fibers," *J. Opt. Soc. Am.*, **71**, 1373–1376 (1981).

[92] H. Guillet de Chatellus, E. Lacot, W. Glastre, O. Jacquin, and O. Hugon, "Theory of Talbot lasers," *Phys. Rev. A*, **88**, 033 828 (2013).

[93] J. Azaña and M. A. Muriel, "Temporal Talbot effect in fiber gratings and its applications," *Appl. Opt.*, **38**, 6700–6704 (1999).

[94] J. Azaña and L. R. Chen, "General temporal self-imaging phenomena," *J. Opt. Soc. Am. B*, **20**, 1447–1458 (2003).

[95] D. Pudo, M. Depa, and L. R. Chen, "Single and multiwavelength all-optical clock recovery in single-mode fiber using the temporal Talbot effect," *J. Lightwave Technol.*, **25**, 2898–2903 (2007).

[96] B. H. Kolner, "Space-time duality and the theory of temporal imaging," *IEEE J. Quantum Electron.*, **30**, 1951–1963 (1994).

[97] J. H. Hannay and M. V. Berry, "Quantization of linear maps on a torus-fresnel diffraction by a periodic grating," *Physica D*, **1**, 267–290 (1980).

[98] M. V. Berry and S. Klein, "Integer, fractional and fractal Talbot effects," *J. Mod. Opt.*, **43**, 2139–2164 (1996).

[99] S. Matsutani and Y. Ônishi, "Wave-particle complementarity and reciprocity of Gauss sums on Talbot effects," *Found. Phys.*, **16**, 325–341 (2003).

[100] J. Caraquitena, M. Beltrán, R. Llorente, J. Martí, and M. A. Muriel, "Spectral self-imaging effect by time-domain multilevel phase modulation of a periodic pulse train," *Opt. Lett.*, **36**, 858–860 (2011).

[101] M. R. Schroeder *Number theory in science and communication*, Springer Science & Business Media (1997).

[102] C. R. Fernández-Pousa, "On the structure of quadratic Gauss sums in the Talbot effect," *J. Opt. Soc. Am. A*, **34**, 732–742 (2017).

[103] J. Azaña and H. Guillet de Chatellus, "Angular Talbot effect," *Phys. Rev. Lett.*, **112**, 213 902 (2014).

[104] R. Kashyap *Fiber Bragg gratings*, Academic Press (2009).

[105] J. Azaña and S. Gupta, "Complete family of periodic Talbot filters for pulse repetition rate multiplication," *Opt. Express*, **14**, 4270–4279 (2006).

[106] J. Azaña, "Temporal self-imaging effects for periodic optical pulse sequences of finite duration," *J. Opt. Soc. Am. B*, **20**, 83–90 (2003).

[107] M. G. Keller, J. Shaker, and Y. M. M. Antar, "Talbot effect applied to antennas," *IEEE Trans. Antennas Propag.*, **56**, 245–248 (2008).

[108] A. Berezovski, W.-X. Tang, and W. Wan, "Elastic wave Talbot effect in solids with inclusions," *Mech. Res. Commun.*, **60**, 21–26 (2014).

[109] F. Pfeiffer, T. Weitkamp, O. Bunk, and C. David, "Phase retrieval and differential phase-contrast imaging with low-brilliance X-ray sources," *Nat. Phys.*, **2**, 258–261 (2006).

[110] W. C. Navidi *Statistics for engineers and scientists*, McGraw-Hill Higher Education (2008).

[111] A. Yariv *Optical electronics*, Oxford University Press (1990).

[112] A. W. Lohmann and J. A. Thomas, "Making an array illuminator based on the Talbot effect," *Appl. Opt.*, **29**, 4337–4340 (1990).

[113] H. Hamam, "Design of Talbot array illuminators," *Opt. Commun.*, **131**, 359–370 (1996).

[114] H. Hamam, "Talbot array illuminators: general approach," *Appl. Opt.*, **36**, 2319–2327 (1997).

[115] C. R. Fernández-Pousa, R. Maram, and J. Azaña, "CW-to-pulse conversion using temporal Talbot array illuminators," *Opt. Lett.*, **42** (13), 2427–2430 (2017).

[116] R. Fleury and A. Alù, "Cloaking and invisibility : a review," *Prog. Electromagn. Res.*, **147**, 171–202 (2014).

[117] A. Alù and N. Engheta, "Achieving transparency with plasmonic and metamaterial coatings," *Phys. Rev. E*, **72**, 016 623 (2005).

[118] U. Leonhardt, "Optical conformal mapping," *Science*, **312**, 1777–1780 (2006).

[119] J. B. Pendry, D. Schurig, and D. R. Smith, "Controlling electromagnetic fields," *Science*, **312**, 1780–1782 (2006).

[120] D. Schurig, J. J. Mock, B. J. Justice, S. A. Cummer, J. B. Pendry, A. F. Starr, and D. R. Smith, "Metamaterial electromagnetic cloak at microwave frequencies," *Science*, **314**, 977–980 (2006).

[121] L. Li and J. B. Pendry, "Hiding under the carpet: a new strategy for cloaking," *Phys. Rev. Lett.*, **101**, 203 901 (2008).

[122] R. Liu, C. Ji, J. J. Mock, J. Y. Chin, T. J. Cui, and D. R. Smith, "Broadband ground-plane cloak," *Science*, **323**, 366–369 (2009).

[123] A. Alù and N. Engheta, "Multifrequency optical invisibility cloak with layered plasmonic shells," *Phys. Rev. Lett.*, **110**, 113 901 (2008).

[124] J. S. Choi and J. C. Howell, "Paraxial ray optics cloaking," *Opt. Express*, **22**, 29 465–29 478 (2014).

[125] U. Leonhardt and T. Tyc, "Broadband invisibility by non-euclidean cloaking," *Science*, **323**, 110–112 (2009).

[126] D. A. B. Miller, "On perfect cloaking," *Opt. Express*, **14**, 12 457–12 466 (2009).

[127] J. S. Choi and J. C. Howell, "Paraxial full-field cloaking," *Opt. Express*, **23**, 15 857–15 862 (2015).

[128] C. Qian, R. Li, Y. Jiang, B. Zheng, H. Wang, Z. Xu, and H. Chen, "Transient response of a signal through a dispersive invisibility cloak," *Opt. Lett.*, **41**, 4911–4914 (2016).

[129] F. Monticone and A. Alù, "Invisibility exposed: physical bounds on passive cloaking," *Optica*, **3**, 718–724 (2016).

[130] M. Selvanayagam and G. V. Eleftheriades, "Experimental demonstration of active electromagnetic cloaking," *Phys. Rev. X*, **3**, 041 011 (2013).

[131] J. S. Choi and J. C. Howell, "Digital integral cloaking," *Optica*, **3**, 536–540 (2016).

[132] S. Zang, C. Xia, and N. Fang, "Broadband acoustic cloak for ultrasound waves," *Phys. Rev. Lett.*, **106**, 024 301 (2011).

[133] Y. Li, X. Shen, Z. Wu, J. Huang, Y. Chen, Y. Ni, and J. Huang, "Temperature-dependent transformation thermotics: from switchable thermal cloaks to macroscopic thermal diodes," *Phys. Rev. Lett.*, **115**, 195 503 (2015).

[134] W. M. McCall, A. Favaro, P. Kinsler, and A. Boardman, "A spacetime cloak, or a history editor," *J. Opt.*, **13**, 024 003 (2011).

[135] M. Fridman, A. Farsi, Y. Okawachi, and A. L. Gaeta, "Demonstration of temporal cloaking," *Nature*, **481**, 62–65 (2012).

[136] J. M. Lukens, D. E. Leaird, and A. M. Weiner, "A temporal cloak at telecommunication data rate," *Nature*, **498**, 205–208 (2013).

[137] F. Li, Y. Park, and J. A. na, "Complete temporal pulse characterization based on phase reconstruction using optical ultrafast differentiation (PROUD)," *Opt. Lett.*, **32**, 3364–3366 (2007).

[138] J. Azaña, Y. Park, T.-J. Ahn, and F. Li, "Simple and highly sensitive optical pulse-characterization method based on electro-optic spectral signal differentiation," *Opt. Lett.*, **33**, 437–439 (2008).

[139] W. Heisenberg, "Über den anschaulichen Inhalt der quantentheoretischen kinematik und mechanik," *Z. Physik*, **43**, 172–198 (1927).

[140] D. A. B. Miller *Quantum mechanics for scientists and engineers*, Cambridge University Press (2008).

[141] D. Gabor, "Theory of communication," *J. IEE*, **93**, 429–441 (1946).

[142] D. Gabor, "Acoustical quanta and the theory of hearing," *Nature*, **159**, 591–594 (1947).

[143] M. Oberthaler and R. A. Höpfel, "Special narrowing of ultrashort laser pulses by self-phase modulation in optical fibers," *Appl. Phys. Lett.*, **63**, 1017–1019 (1993).

[144] C. Caspar, H. M. Foisel, A. Gladisch, N. Hanik, F. Kuppers, R. Ludwig, A. Mattheus, W. Pieper, B. Strebel, and H. G. Weber, "RZ versus NRZ modulation format for dispersion compensated SMF-based 10-Gb/s transmission with more than 100-km amplifier spacing," *IEEE Photon. Technol. Lett.*, **11**, 481–483 (1999).

[145] M. I. Hayee and A. E. Willner, "NRZ versus RZ in 10-40-Gb/s dispersion-managed WDM transmission systems," *IEEE Photon. Technol. Lett.*, **11**, 991–993 (1999).

[146] R. Ludwig, U. Feiste, E. Dietrich, H. G. Weber, D. Breuer, M. Martin, and F. Kuppers, "Experimental comparison of 40 Gbit/s RZ and NRZ transmission over standard singlemode fibre," *Electron. Lett.*, **35**, 2216–2218 (1999).

[147] R.-J. Essiambre, G. J. Foschini, G. Kramer, and P. J. Winzer, "Capacity limits of information transport in fiber-optic networks," *Phys. Rev. Lett.*, **101**, 163 901 (2008).

[148] R. Won, "View from... communication networks beyond the capacity crunch: is it crunch time?" *Nat. Photon.*, **9**, 424–426 (2015).

[149] A. D. Ellis, M. E. McCarthy, M. A. Z. A. Khateeb, M. Sorokina, and N. J. Doran, "Performance limits in optical communications due to fiber nonlinearity," *Adv. Opt. Photon.*, **9**, 429–503 (2017).

[150] S. T. Le, V. Aref, and H. Buelow, "Nonlinear signal multiplexing for communication beyond the Kerr nonlinearity limit," *Nat. Photon*, **11**, 570–576 (2017).

[151] I. Kang, M. S. Rasras, L. L. Buhl, M. Dinu, G. Raybon, S. Cabot, M. A. Cappuzzo, L. T. Gomez, Y. F. Chen, S. S. Patel, A. Piccirilli, J. Jaques, and C. R. Giles, "High-speed all-optical generation of advanced modulation formats using photonic-integrated all-optical format converter," *IEEE Journal of Selected Topics in Quantum Electronics*, **18**, 765–771 (2012).

[152] I. Kang, X. Liu, S. Chandrasekhar, M. Rasras, H. Jung, M. Cappuzzo, L. T. Gomez, Y. F. Chen, L. Buhl, S. Cabot, and J. Jaques, "Energy-efficient 0.26-Tb/s coherent-optical OFDM transmission using photonic-integrated all-optical discrete Fourier transform," *Opt. Express*, **20**, 896–904 (2012).

[153] J. van Weerdenburg, R. Ryf, J. C. Alvarado-Zacarias, R. A. Alvarez-Aguirre, N. K. Fontaine, H. Chen, R. Amezcua-Correa, Y. Sun, L. Grüner-Nielsen, R. V. Jensen, R. Lingle, T. Koonen, and C. Okonkwo, "138-Tb/s Mode- and Wavelength-Multiplexed Transmission Over Six-Mode Graded-Index Fiber," *Journal of Lightwave Technology*, **36**, 1369–1374 (2018).

[154] M. Seghilani, R. Maram, and J. Azaña, "Mitigating nonlinear propagation impairments of ultrashort pulses by fractional temporal self-imaging," *Opt. Lett.*, **42**, 879–882 (2017).

[155] J. Perez, Z. Ghassemlooy, S. Rajbhandari, M. Ijaz, and H. L. Minh, "Ethernet FSO communications link performance study under a controlled fog environment," *IEEE Commun. Lett.*, **16**, 408–410 (2012).

[156] M. L. Stevens and D. M. Boroson, "A simple delay-line 4-PPM demodulator with near-optimum performance," *Opt. Express*, **20** (5), 5270–5280 (2012).

[157] J. Hoxha, J. Morosi, S. Shimizu, P. Martelli, P. Boffi, N. Wada, and G. Cincotti, "Spectrally-efficient all-optical OFDM by WSS and AWG," *Opt. Express*, **23**, 10 986–10 996 (2015).

[158] P. D. Heyn, J. Luo, S. D. Lucente, N. Calabretta, H. J. S. Dorren, and D. V. Thourhout, "In-band label extractor based on cascaded Si ring resonators enabling 160 Gb/s optical packet switching modules," *J. Lightwave Technol.*, **32**, 1647–1653 (2014).

[159] A. Saljoghei, C. Browning, and L. P. Barry, "In-band insertion of RoF LTE services in OOK based PON's using line coding techniques," *Opt. Commun.*, **356**, 488–494 (2015).

[160] F. Nekoogar *Ultra-wideband communications: fundamentals and applications*, Prentice Hall PTR (2006).

[161] M. G. M. Hussain, "Ultra-wideband impulse radar-an overview of the principles," *IEEE Aerosp. Electron. Syst. Mag*, **13**, 9–14 (1998).

[162] W. Freude, R. Schmogrow, B. Nebendahl, M. Winter, A. Josten, D. Hillerkuss, S. Koenig, J. Meyer, M. Dreschmann, M. Huebner, C. Koos, J. Becker, and J. Leuthold "Quality metrics for optical signals: eye diagram, Q-factor, OSNR, EVM and BER," in *International Conference on Transparent Optical Networks (ICTON),* Coventry, UK (2012), paper **Mo.B1.5**.

[163] D. Norte and A. E. Willner, "All-optical data format conversions and reconversions between the wavelength and time domains for dynamically reconfigurable WDM networks," *J. Lightwave Technol.*, **14**, 1170–1182 (1996).

[164] C. W. Chow, C. S. Wong, and H. K. Tsang, "All-optical modulation format conversion and multicasting using injection-locked laser diodes," *J. Light. Technol.*, **22**, 2386–2392 (2004).

[165] C. W. Chow, C. S. Wong, and H. K. Tsang, "All-optical RZ to NRZ data format and wavelength conversion using an injection locked laser," *Opt. Commun.*, **223**, 309–313 (2003).

[166] L.-S. Yan, A.-L. Yi, W. Pan, B. Luo, and J. Ye, "Simultaneous NRZ-to-RZ format conversion and one-to-six error-free channel multicasting using a single pump in a highly nonlinear fiber," *Opt. Express*, **18**, 21 404–21 409 (2010).

[167] P. Groumas, V. Katopodis, C. Kouloumentas, M. Bougioukos, and H. Avramopoulos, "All-optical RZ-to-NRZ conversion of advanced modulated signals," *IEEE Photon. Technol. Lett.*, **24**, 179–181 (2012).

[168] Y. Ding, C. Peucheret, M. Pu, B. Zsigri, J. Seoane, L. Liu, J. Xu, H. Ou, X. Zhang, and D. Huang, "Multi-channel WDM RZ-to-NRZ format conversion at 50 Gbit/s based on single silicon microring resonator," *Opt. Express*, **18**, 21 121–21 130 (2010).

[169] Y. Ding, H. Hu, M. Galili, J. Xu, L. Liu, M. Pu, H. C. H. Mulvad, L. K. Oxenløwe, C. Peucheret, P. Jeppesen, X. Zhang, D. Huang, and H. Ou, "Generation of a 640 Gbit/s NRZ OTDM signal using a silicon microring resonator," *Opt. Express*, **19**, 6471–6477 (2011).

[170] M. Xiong, O. Ozolins, Y. Ding, B. Huang, Y. An, H. Ou, C. Peucheret, and X. Zhang, "Simultaneous RZ-OOK to NRZ-OOK and RZ-DPSK to NRZ-DPSK format conversion in a silicon microring resonator," *Opt. Express*, **20**, 27 263–27 272 (2012).

[171] J. D. Jackson *Classical Electrodynamics*, Wiley (2012).

Index

W